Flanders
State of
the Art

Modelling Belgian Coastal zone and Scheldt mouth area

Sub report 14: Scaldis-Coast model – Model setup and validation of the morphodynamic model

DEPARTMENT
**MOBILITY &
PUBLIC
WORKS**

www.flandershydraulics.be

Modelling Belgian Coastal zone and Scheldt mouth area

Sub report 14: Scaldis-Coast model – Model setup and validation of the morphodynamic model

Kolokythas, G.; Fonias, S.; Wang, L.; De Maerschalck, B.; Vanlede, J.

Flanders Hydraulics

Flanders State of the Art

Cover figure © The Government of Flanders, Department of Mobility and Public Works, Flanders Hydraulics

Legal notice

Copyright and citation

Document identification

Customer:	Vlaams-Nederlandse Scheldecomissie (VNSC)	Ref.:	WL2023R15_068_14
Keywords (3-5):	Coastal modelling, Comples Project Kustvisie, Waves, Tide, Morphology		
Knowledge domains:	Hydraulics and sediment > Hydrodynamics > Waves > Numerical modelling		
Text (p.):	217	Appendices (p.):	17
Confidentiality:	☒ No	☒ Available online	

Author(s):	Kolokythas, G., Wang, L., Fonias, S., De Maerschalck, B.

Control

	Name	Signature
Reviser(s):	Vanlede, J.	Getekend door:Joris Vanlede (Signature) Getekend op:2023-10-17 09:44:14 +02:0 Reden:Ik keur dit document goed — Vanlede Joris — Vlaamse overheid
Project leader:	De Maerschalck, B.	Getekend door:Bart De Maerschalck (Sig Getekend op:2023-10-17 09:38:30 +02:0 Reden:Ik keur dit document goed — De Maerschalck Bart — Vlaamse overheid

Approval

Head of Division:	Bellafkih, K.	Getekend door:Abdelkarim Bellafkih (Sign Getekend op:2023-10-16 13:28:27 +02:0 Reden:Ik keur dit document goed — Bellafkih Abdelkarim — Vlaamse overheid

CERTIFIED LR ISO 9001

Abstract

With the increasing awareness of sea level rise, the Flemish Authorities initiated the *Complex Project Kustvisie* (CPKV) in order to start together with all involved stakeholders to define the overall long-term coastal defence strategy for the Belgian Coast. In order to analyze the impact of sea level rise on the morphology of the coast and to assess proposed mitigation measures on their efficiency the need for a flexible coastal model for the Belgian coast and Scheldt mouth area was revealed.

Therefore, in 2015 it was decided to build an integral coastal model within the TELEMAC-MASCARET model suite. The present report describes the setup and validation of the sediment transport and morphodynamic part of the model. Scaldis-Coast consists of a morphodynamic module, a 2D TELEMAC hydrodynamic module and a TOMAWAC wave propagation module.

The Scaldis-Coast model is a highly efficient and flexible model that is applicable for short and long term morphodynamics both in the tidally driven off-shore and wave driven near-shore part of the Belgian coastal zone and Scheldt mouth area. The computational domain spans from the French coast near Calais to the Dutch coast between the Eastern Scheldt and the Grevelingenmeer, including the Eastern and Western Scheldt estuary. The offshore boundary is at at a distance of about 30 km from the coast. The resolution of the model varies from 750 m offshore to 25 m nearshore with automatic refinement around complex geometries like breakwaters, but also at locations with steep slopes in the bathymetry. With a morphological acceleration factor of twenty (MORFAC = 20) the computational cost is about 1,5 to 2 days on a 100-cores high performance computer for a ten years morphological run.

The long term coastal morphodynamics are validated against the historical evolution of the seabed in the large area around Zeebrugge after the extension of the outer port in 1986. In general, the large-scale trends are well represented. This is the systematic erosion in front of the extended port and the sedimentation at the sand bank of the Paardenmarkt. In the last decade both the erosive trends in front of Zeebrugge and the sedimentation trends at Paardenmarkt tend to slow down. This is less obvious in the model. This can be attributed to the presence of resistant mud layers in the surrounding of Zeebrugge, whereas the model is a pure sand model. First steps have been made in including cohesive sand dynamics in the model. Also, the formation of the Baai van Heist is not accurately represented. This is something that has been noticed before in other sand-based morphodynamic models for Zeebrugge, but also at other locations as IJmuiden. However, preliminary results of a combined sand-mud model show promising steps forwards for this complex morphodynamic behaviour.

With respect to the near- and onshore morphodynamics driven by the littoral drift, the model has been proven to perform well. On the midterm, i.e. annual erosion/sediment trends, the model has been validated against erosion trends at Wenduine and sedimentation trends of the fairway to the Blankenberge marina.

First steps have been made in implementing cross-shore sediment transport processes. However, at this moment they are not yet implemented in the Scaldis-Coast model. This makes the model less suitable for estimating beach and foreshore storm responses. Nevertheless, the extensive siltation of the Blankenberge marina access channel due to one storm event, was been reproduced accurately by the model.

Contents

List of tables

List of figures

1   Introduction

Within the *Complex Project Kustvisie* (CPKV) all involved stakeholders participate in process of defining the overall design of the long-term coastal defence of the Belgian Coast. The project was formerly known as project *Vlaamse Baaien* (Flemish Bays). The *Vlaamse Baaien* project was initiated in 2014 by the Flemish Authorities with the goal to protect the Belgian Coast from (extreme) sea level rise and climate change on the horizon 2050 – 2100. The goal of the project is to create an attractive and natural coast that is climate change resilient with economic benefits like estuarine traffic and renewable energy.

Within this project a wide variety of mitigation strategies can be considered, ranging from extra beach and foreshore nourishments, dunes on beaches to artificial offshore barrier islands. The evaluation of these interventions on currents, waves and morphology revealed the need for a flexible, accurate and versatile global coastal model for the Belgian coast and Western Scheldt mouth area.

Up till 2015, the available models for the Belgian coast, mostly restricted to selective stretches of the coast or ports, build for specific projects and limited in offshore direction, mostly based on structured grids. Or on the other hand large scale continental shelf models with little focus on the near- and onshore coastal area.

Therefore, it was decided to build an integral coastal model within the TELEMAC-MASCARET model suite. One of the main goals of this study is the development of a numerical model capable of predicting the morphological evolution both close to the coastline and at relatively deeper waters. The model aspires to represent the alongshore driven coastal morphological processes en the interaction with antropogenic interventions like port extensions, channel maintenance and beach and foreshore nourishments. Also special attention is paid to the more off-shore tidal driven morphodynamics like the decadal bed evolution around Zeebrugge after the completion of the seaward port extension in 1986. Efforts have been taken to introduce wave driven cross-shore sediment transport mechanisms. However, more research is required to come to a reliable model for practical use with respect to cross-shore driven transport phenomena like natural feeding of the beach and dune-food and storm induced shore retreatment.

The present report describes the setup and validation of the sediment transport and morphodynamic part of the model. The morphodynamic model is a coupled combination of the 2D TELMAC hydrodynamic model, the TOMAWAC wave propagation model and the SISYPHE sediment transport and bed update model. The setup and validation of the hydrodynamics and wave part of the model are described in separate reports.

A list of the preceding reports and memos delivered within project 15_068 is given in Table 1.

Table 1 – List of delivered FHR reports (R) and memos (M) within project 15_068.

Title	ID
Report: Modellering Vlaamse Baaien, Deelrapport 1: Hydrodynamische Modellering Scenario's Oostkust	WL2016R15_068_1
Report: Modellering Belgische Kustzone en Scheldemonding, Deelrapport 2: Morfologische analyse scenario's Vlaamse Baaien	WL2017R15_068_2
Report: Modellering Belgische Kustzone en Scheldemonding, Deelrapport 3: Modellering van de morfologische effecten na aanleg nieuwe Geul van de Walvischstaart	WL2017R15_068_3

Report: Modellering Belgische Kustzone en Scheldemonding, Rekennota: Berekening golfklimaat Vlaamse Baaien scenario's E4 en F1	WL2017R15_068_4
Report: Modellering Belgische Kustzone en Scheldemonding, Sub report 5: Progress report - Scenarios Vlaamse Baaien and model developments	WL2017R15_068_5
Report: Modelling Belgian Coastal zone and Scheldt mouth area: Sub report 6: Progress report 2 - Evaluation of numerical modelling tools and model developments	WL2018R15_068_6
Report: Modelling Belgian Coastal zone and Scheldt mouth area: Sub report 7: Progress report 3 – Model developments: Hydrodynamics, waves and idealized modelling	WL2018R15_068_7
Report: Modelling Belgian Coastal zone and Scheldt mouth area: Sub report 8: Progress report 4 – Model developments: Waves, idealized modelling and morphodynamics	WL2019R15_068_8
Report: Modelling Belgian Coastal zone and Scheldt mouth area: Sub report 9: Progress report 5 – Model developments: Waves, idealized modelling and morphodynamics	WL2019R15_068_9
Report: Modelling Belgian Coastal zone and Scheldt mouth area: Sub report 10 – Summary of the 2D TELEMAC morphodynamic model Scaldis-Coast: version 2020 developed for the Complex Projects Coastal Vision and Extra Container Capacity Antwerp	WL2020R15_068_10
Report: Modelling Belgian Coastal zone and Scheldt mouth area: Sub report 11: Progress report 6 – Model developments: Grid optimization, Morphodynamics, Dredging/dumping subroutines, Wave conditions	WL2020_R15_068_11
Report: Modelling Belgian Coastal zone and Scheldt mouth area: Sub report 12: Scaldis-Coast model – Model setup and validation of the 2D Hydrodynamic model	WL2020_R15_068_12
Report: Modelling Belgian Coastal zone and Scheldt mouth area: Sub report 12: Scaldis-Coast model – Model setup and validation of the wave model	WL2020_R15_068_13
Memo: Modelling Belgian Coastal zone and Scheldt mouth area	WL2016M15_068_1
Memo: Beschrijving scenario's Vlaamse Baaien: Oostkust	WL2016M15_068_2
Memo: Berekeningen golfklimaat scenario F1	WL2016M15_068_3
Memo: Gebruik van de rekencluster aMT voor Telemac berekeningen	WL2016M15_068_4
Memo: Modelling of bed morphology evolution at Knokke for a beach nourishment scenario (G2) by XBeach	WL2016M15_068_5
Memo: Berekeningen golfklimaat scenario E4	WL2016M15_068_6
Memo: Morfologische analyse scenario's Vlaamse Baaien	WL2016M15_068_7
Memo: Vlaamse Baaien: invloed eiland ten oosten van Zeebrugge op het Zwin	WL2016M15_068_8

Memo: Sediment transport formulation in XBeach and Delft3D	WL2016M15_068_9
Memo: Impact aanleg nieuwe vaargeul op de morfologie van de Schelde monding en estuarium: Een geïdealiseerde modelstudie	WL2016M15_068_10
Memo: Morfodynamische effecten aanleg nieuwe geul van de Walvischstaart	WL2016M15_068_11
Memo: Morfologische modellering m.b.v. TELEMAC - SISYPHE	WL2016M15_068_12
Memo: Geul van de Walvischstaart: samenvatting morfologisch onderzoek stabiliteit en baggerbeslag	WL2016M15_068_13
Memo: Artikel Tijdingen: Vlaamse Baaien	WL2016M15_068_14
Memo: Toelichting baggerbeslag Geul van de Walvischstaart	WL2017M15_068_15
Memo: Hydrodynamic modelling of 'Vlaamse Baaien' dunebelt scenarios I3 and I4	WL2017M15_068_16
Memo: Dunebelt scenario I4 – Scaldis vs Semi-circular Telemac3D	WL2017M15_068_17
Memo: Overview of existing Telemac hydrodynamic models: NSG-BCG and Scaldis	WL2017M15_068_18
Memo: CSM and ZUNO run of 2009 including 60, 90 and 200 cm sea level rise	WL2017M15_068_19
Memo: Sea level rise impact on Zeebrugge port accessibility - Telemac3D hydrodynamic modelling	WL2017M15_068_20
Memo: Bringing TELEMAC and Gmsh meshing tool closer	WL2017M15_068_21
Memo: Time step sensitivity analysis for TOMAWAC stand alone and TELEMAC3D-TOMAWAC coupled simulations	WL2017M15_068_22
Memo: Unstructured high resolution coastal model for the Belgian Coast and Scheldt Mouth: model requirements	WL2018M15_068_23
Memo: Telemac2D (and 3D) coupling with Sisyphe	WL2017M15_068_24
Memo: TOMAWAC test runs	WL2017M15_068_25
Memo: Bathymetry and Mesh Construction for ScaldisKust	WL2018M15_068_26
Memo: Scaldis-Coast model calibration: Bottom roughness tuning	WL2018M15_068_27
Memo: Preparing SDS wind file for CSM-ZUNO runs	WL2019M15_068_28
Memo: TELEMAC2D-TOMAWAC-SISYPHE coupled run for hydrodynamics and wave validation	WL2019M15_068_29
Memo: Nestor coupling with TELEMAC2D/SISYPHE and set-up	WL2019M15_068_30

Memo: Scaldis-Coast: Summary Coastal 2D TELEMAC morphodynamic model for the Belgian Coast and Scheldt mouth area (input CREST final report)	WL2019M15_068_31
Memo: Scaldis-Coast: Summary Coastal 2D TELEMAC morphodynamic model for the Belgian Coast and Scheldt mouth area for the Complex Project Coastal Vision	WL2020M15_098_32
Memo: Artikel tijdingen: Storm Ciara	WL2020M15_068_33
Memo: Suspended sediment transport using GAIA	WL2020M15_068_34
Memo: Test runs with new module GAIA in the TELEMAC-MASCARET system	WL2020M15_068_35

Table 2 – Conference proceedings/presentations

XBeachX 2017	MORPHODYNAMIC ANALYSIS OF INTERVENTION SCENARIOS AT THE BELGIAN COAST UNDER THE MASTERPLAN 'FLEMISH BAYS'	XBeach X Conference
ICCE 2018	IMPACT OF SEA LEVEL RISE ON THE ACCESSIBILITY OF COASTAL PORTS: A CASE STUDY OF THE PORT OF ZEEBRUGGE (BELGIUM)	International Conference on Coastal Engineering
TUC 2018	Neumann (water level gradient) boundaries in TELEMAC 2D and their application to wave-current interaction (Conference proceedings)	Telemac User Conference
EGU 2019	SCALDIS-COAST: AN INTEGRATED NUMERICAL MODEL FOR THE SIMULATION OF THE BELGIAN COAST MORPHODYNAMICS	EGU General Assembly
TUC 2019	TEL2TOM: coupling TELEMAC and TOMAWAC on arbitrary meshes	Telemac User Conference
VLIZ 2019	Scaldis-Coast: An unstructured next generation integrated model for the Belgian Coastal Zone	VLIZ Marine Science Day
IAHR 2020	Simulating the morphological evolution of the Belgian coast by means of the integrated numerical model SCALDIS-COAST	IAHR Europe Congress

2 Background: Available sediment formulations in TELEMAC

The present chapter describes all the parametric analyses and modifications that have been implemented within the TELEMAC-MASCARET suite in order to support the simulations that have been conducted using the Scaldis-Coast model Kolokythas *et al.* (2019). Those modifications are tested in simplified domains (Gaussian hump, Trench, Idealized model for Belgian coast etc.) and also in real subdomains of the Belgian coast.

2.1 Preliminary study for coupling TELEMAC and SISYPHE

The first attempt has been focused on coupling TELEMAC-2D (and 3D) with SISYPHE, in two simple geometric configurations:

- Propagation of a Gaussian hump in open channel flow
- Propagation of a (polynomial shape) trench in open channel flow

SISYPHE is a sediment transport and morphological model which is part of the hydro-informatics finite element and finite volume system TELEMAC-MASCARET. In SISYPHE, sediment transport rates, split into bedload and suspended load, are calculated at each node as a function of various flow (velocity, water depth, wave height, etc.) and sediment (grain diameter, relative density, settling velocity, etc.) parameters. The bedload is calculated by using classical sediment transport formulas from the literature. The suspended load is determined by solving an additional advection-diffusion equation for the depth-averaged suspended sediment concentration. The bed evolution equation (Exner equation) can be solved by using either a finite element or a finite volume formulation (Tassi & Villaret, 2014).

An extensive parametric analysis has been conducted in order to define which parameters (physical, numerical etc.) are affecting the sediment transport and bed morphology most. In the majority of the performed tests only bed load transport is considered. However, morphological evolution of both the hump and the trench cases due to suspended sediment transport is examined. In addition, a basic coupled 2D simulation is examined against a 3D one, in order to examine the differences occurring in a full 3D simulation. Interpretation of the additional simulations will provide further guidelines for coupling TELEMAC-2D (and 3D) with SISYPHE.

2.1.1 Uniform flow over a Gaussian hump

The first case under consideration is the uniform open channel flow over a bed in a shape of a Gaussian hump. The bed is movable and under the flow conditions the hump is expected to migrate along the direction of the flow. This case is quite simple in terms of establishing the flow and thus, comprehending the effect of each parameter considered for the simulations.

In addition, an approximation to an analytical solution (Schramkowski *et al.*, 2017) has been used to validate the model results in terms of the migration of the hump, to verify the reliability of the numerical solver. The goal is to determine the migration speed of the hump using different sediment transport formulae (for bed load and suspended load) and to identify possible software limitations.

Numerical configuration

Geometry

The numerical domain is an orthogonal box which is 2400 m long in the direction of the flow and 160 m in the transverse direction. The water depth is equal to 10 m, with the exception of the region where the Gaussian hump is considered (see Figure 1). The reference system is placed in the inflow of the channel, in the middle of the channel width and vertically on the position of the free surface. The expression of the hump geometry is given by the following expression in terms of local bathymetry:

$$d = d_o + n_o \exp\left(-\frac{(x - x_{mean})^2}{2\sigma^2}\right)$$

where d_o is the channel's bathymetry without the hump, n_o is the maximum value of the hump in the vertical axis, x_{mean} is the distance of the centre of the hump, and σ is a measure of the hump width and is equal to 450 m.

BOTTOM
-7.878
-8.108
-8.338
-8.568
-8.798
-9.028
-9.258
-9.488
-9.718
-9.948
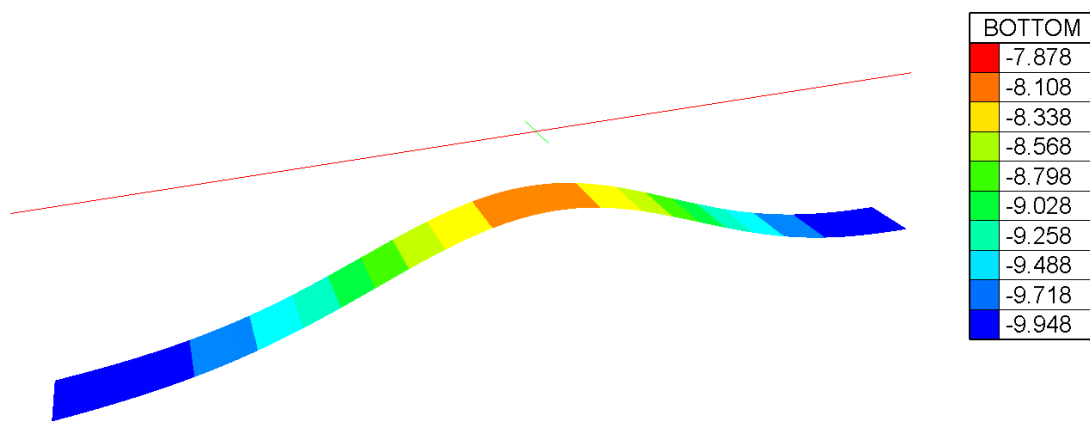
Figure 1 – Gaussian hump geometric configuration in terms of water depth (3D view).

Numerical parameters (TELEMAC-2D & SISYPHE)

The boundary conditions for the flow are defined in the boundary conditions (input) file (.cli) for TELEMAC-2D. For the inflow, a prescribed discharge boundary is used, whereas for the outflow a constant water level is used. The values are prescribed within the TELEMAC-2D steering file (.cas). The discharge at the inflow is Q = 1600 m^3/s, for a channel width equal to 160 m (or 10 m^2/s/m) and the prescribed water depth is 10 m at the outflow. The prescribed discharge creates a uniform flow with far field depth averaged flow velocity equal to u = 1 m/s. Even though some of the advection schemes do not require stability criteria, for all the simulations a Courant-Friedrichs-Lewy (CFL) number (u · Δt/Δx, where u is the flow velocity, Δt the time step and Δx the length interval) equal to 0.3, is considered. The total simulated period is 62.5 days. The solver used for the hydrodynamic propagation step follows the GMRES (Generalised Minimum RESidual) method.

For the bottom friction, the Chézy law has been considered and friction coefficient is taken equal to 60 (> 50, the default value). Since the friction effects from the side boundaries would be undesirable because the hump needs to propagate in the same manner along the width of the channel, no friction has been imposed on their surface. This creates pseudo-periodical boundary conditions along the width of the open channel which is equivalent to an infinitely wide channel configuration.

For the turbulence modelling, a constant viscosity, the k-epsilon and the Smagorinsky models are used in order to examine the differences they produce in the flow field. TELEMAC-2D offers the possibility of using a variety of models for turbulence.

The boundary conditions for the morphological simulation, are defined in the boundary conditions (input) file (.cli) for SISYPHE. To prevent the model from resulting into unwanted erosion at the inflow boundary, it is important to define fixed bed elevation (zero evolution) in the boundary conditions file. This can be achieved by assigning LIEBOR=5 for the inflow nodes (8th column in .cli file).

In SISYPHE, the bed update is calculated by a residual distribution scheme. For the advection of the suspended sediment, multiple numerical schemes are available either based on residual distribution schemes or the method of characteristics. The critical evolution ratio is set equal to 0.1. This means that for evolution to water depth ratio lower than 0.1, the water depth does not perceptibly modify the current field distribution.

The sediment considered in the present study is sand with diameter of grains equal to d_{50} = 250 μm and sediment-to-fluid density ratio equal to S = 2.65. This gives a critical Shields number Θ_c computed by:

$$D_* = d_{50} \left[(S-1) \frac{g}{\nu^2} \right]^{1/3} = 5.93$$

$$\Theta_C = 0.14 D_*^{-0.64} = 0.0448$$

This value will be computed by the code. However, a lower value can be assigned in order to intensify the erosion/deposition phenomena, potentially. For sediment transport, total load is considered using the formula by Engelund & Hansen (1967) (30).

Finally, the effect of a series of other parameters are examined, such as avalanching, slope effects, different advection schemes, etc.

Simulated test cases and results

Validation

The simulation of flow over a Gaussian hump will be validated against the analytical solution. For clarity, we mention below the common numerical parameters used since they will be modified, during the parametric investigation.

Mesh S001:	triangular uniform, edge length 40m
Initial flow conditions:	still water (cold start)
Courant-Friedrichs-Lewy number:	0.3
Advection Scheme:	Method of Characteristics
Law of bottom friction:	Chézy
Friction law on side walls:	no friction
Turbulence model:	Smagorinsky
Sediment transport:	Bed load
Bed load transport formula:	Engelund & Hansen (1967) (30)
Bed porosity:	0.4
Avalanching:	NO

The analytical expression of the bed load formula of Engelund and Hansen (30) utilized in TELEMAC and considering a drag coefficient defined by Chézy coefficient C, is the following:

$$q_x = 0.05 \, (S-1)^{-2} d_{50}^{-1} g^{-2} \left(\frac{g}{C^2} \right)^{3/2} u^5 (= m u^b)$$

where q_x is the sediment transport, S is the sediment-to-fluid density ratio, d_{50} is the sediment diameter, g the gravitational acceleration and u is the depth-average propagation velocity. Each of the bed points on the hump is propagating with a speed that is approximated by the expression:

$$c = \frac{bmQ^b(WD)^{-b-1}}{1-e}$$

where, WD is the local water depth over the bed and e is the sediment porosity. It has to be highlighted that this is not an exact analytical solution but an approximation. For this solution the water motion is calculated from the continuity equation, there are no changes in the free surface level and a constant friction coefficient is used in the sediment transport equation. The above solution is based on characteristic method and it is only valid in the initial stage, before the hump starts to break.

The aforementioned expression is used to evaluate the performance of TELEMAC-2D - SISYPHE model comparing the numerical results to the analytical ones (see Figure 2).
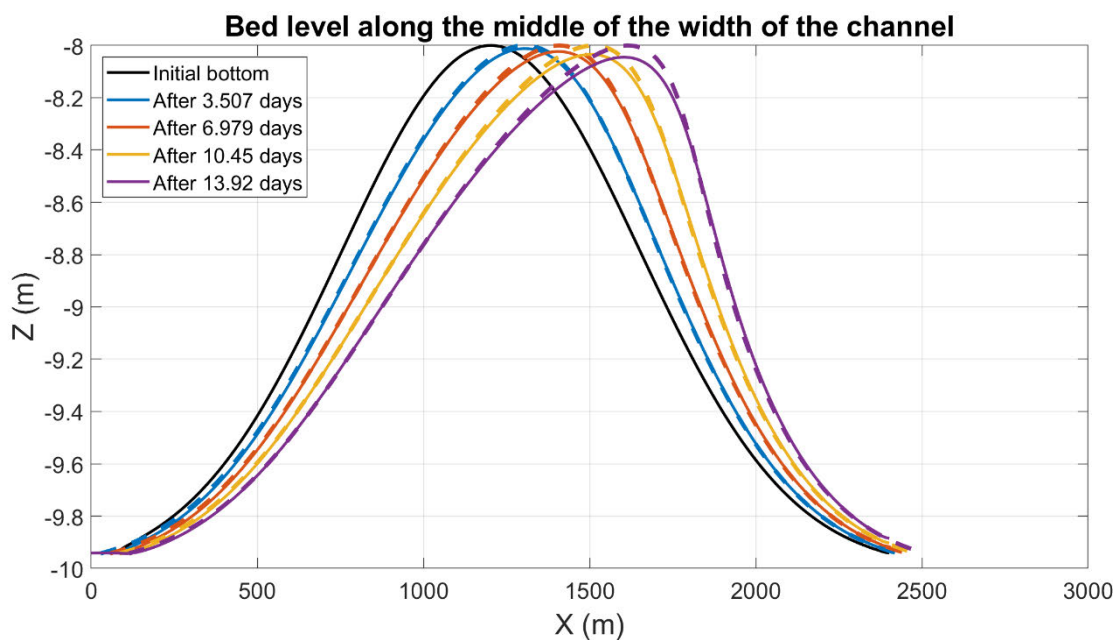
Figure 2 – Comparison of numerical (solid lines) against analytical solution (dashed lines) in terms of middle-width sections of bed level in different time instances.

Grid Convergence Analysis

The simulation of flow over a Gaussian hump is examined using different numerical configurations and models in order to examine their effect. Firstly, a Grid Independence Analysis is conducted in order to define if the results converge as the numerical grids are refined. So we set up (Table 3) the following simulations:

Table 3 – Grid Independence Analysis simulation cases

Case	Triangle edge length (m)	Number of elements	Time step (s)
S001	40	480	12.0
S002	20	2156	6.0
S003	10	9094	3.0

It can be observed (Figure 3), that even after *t* = 20.87 days, there are no significant differences in the bedform. It is obvious that the difference between medium (S002) and fine (S003) mesh is lower than between coarse (S001) and medium (S002) mesh, which means that a convergence is actually achieved. Thus, the following simulations will be performed using the medium mesh and only in certain cases the coarse mesh will be used explicitly for computational speed up.

Table 4 – Computation time for Grid Independence Analysis.

Case	Number of elements (W)	Computation time T (s)	Efficiency E=T/W
S001	480	1254	2.6
S002	2 156	3 244	1.5
S003	9 094	8 815	1.0

Concerning the total required computation time for the three different computational meshes, Table 4 shows that the model efficiency (defined as the ratio of calculation time to number of cells) increases with the number of cells.
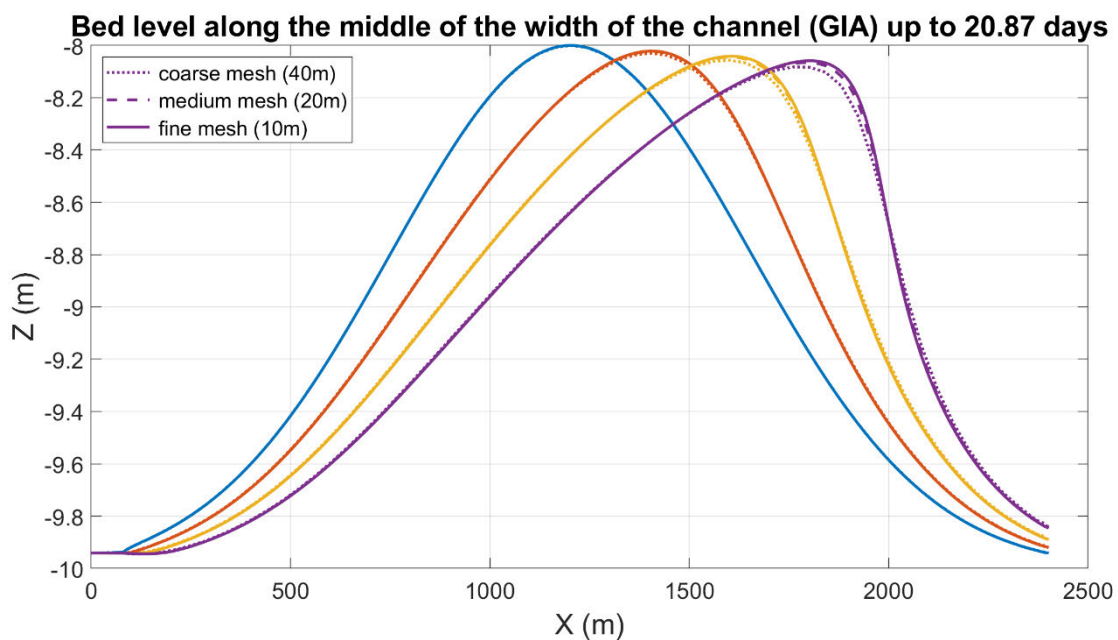
Figure 3 – Middle-width sections of bed level in different time instances (blue lines at 0 days, red lines at 6.97 days, yellow lines at 13.92 days and purple lines at 20.87 days) for coarse-S001 (dashed-dotted line), medium-S002 (dashed) and fine-S003 (solid line) meshes.

Investigation of domain dimensions effect

At this section, the horizontal domain dimensions will be examined in terms of the effect on the flow and the propagation of the Gaussian hump. Apart from test case S001 with the coarse mesh, two more cases are now simulated, and their results are compared. One with double width (S004) to examine whether a longer transverse dimension results in higher spanwise variation, one with double streamwise dimension (S005) to examine the outflow effect and one case (S006) which is just like case S005 but the outflow boundary condition is set to free surface elevation at -0.067 m to establish the same friction slope with the flow case in the short domains (see Table 5). The slope is computed using the Chézy coefficient as $S_f = (1/R_h)(U/C)^2$, where R_h is the hydraulic radius and U the uniform flow velocity. The head loss is equal to the friction product of the friction slope by streamwise length and thus it will be double for a double streamwise domain.

Table 5 – Horizontal domain effects simulation cases.

Case	Domain dimensions (m)	Outflow BC
S001	2 400 x 160	0.0 m
S004	2 400 x 320	0.0 m
S005	4 800 x 160	0.0 m
S006	4 800 x 160	-0.067 m
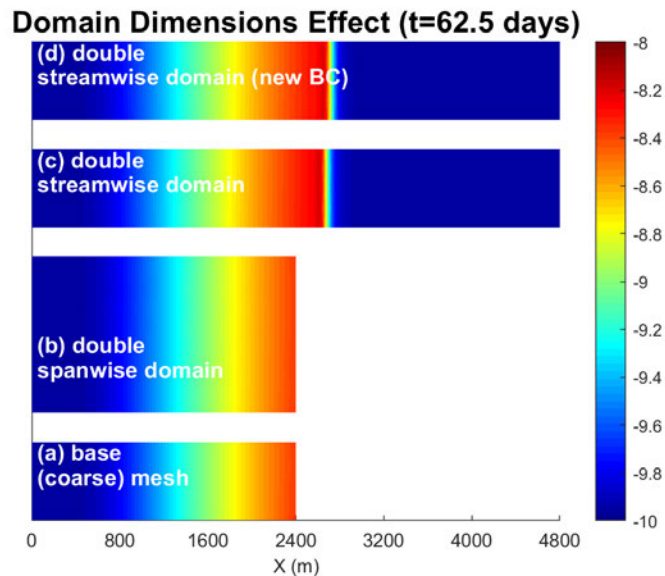
Figure 4 – Contour plots of bed level over the propagating Gaussian Hump for (from bottom to top): the base (coarse) mesh domain S001, double spanwise domain (S004), double streamwise domain (S005) and double streamwise domain with corrected hydraulic slope (S006).

Bed level along the middle of the width of the channel (domain effects) up to 62.53 days
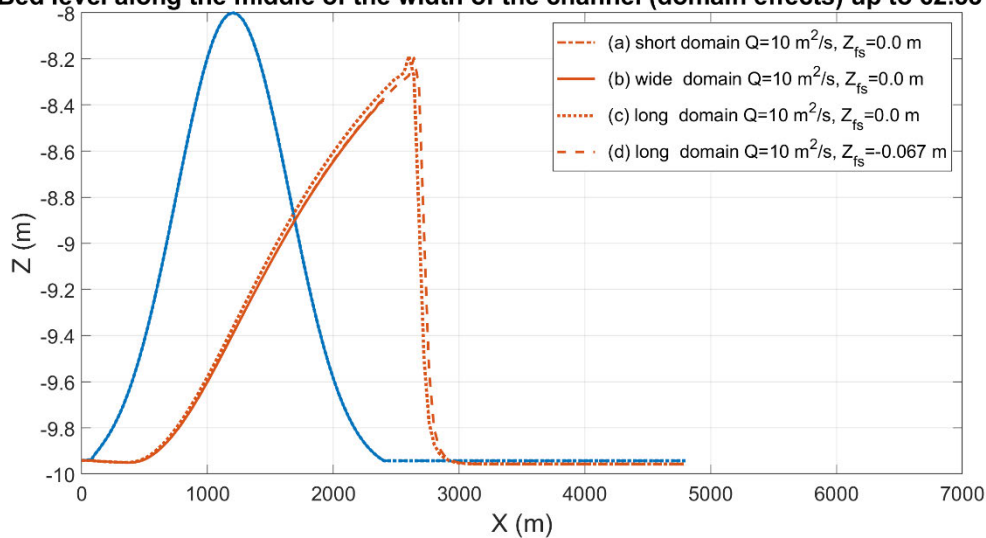
Figure 5 – Middle-width sections of bed level in different time instances for the base (coarse) mesh domain S001 (dash-dot-dotted line), double spanwise domain S004 (solid line), double streamwise domain S005 (dotted line) and double streamwise domain with corrected hydraulic slope S006 (dashed line).

From the contour plots of water depth on Figure 4, there is no visible difference for consideration of a longer or wider domain. In Figure 5, it can be observed that cases (a) and (b) result in slightly faster propagation of the hump in comparison with case (c). This is attributed to the alteration of the flow's hydraulic slope, which is milder in the case of the extended model. This has been proven by case (d), where the hydraulic conditions become identical by applying a free surface -0.067 m at the outflow boundary. This way, the propagation speed becomes also the same in cases (a), (b) and (d).

Turbulence model effect

TELEMAC-2D offers the possibility of using different models for turbulence. In this section, three cases are considered based on the consideration of different models: constant viscosity, Smagorinsky and k-epsilon models. In addition, Smagorinsky model is chosen for two simulations, one for the short and one for the long numerical domain (see Table 6).

Table 6 – Cases for investigation of turbulence model effects (simulations performed with coarse mesh)

Case	Domain dimensions (m)	Turbulence model
S001b	2400 x 160	Constant viscosity
S001	2400 x 160	Smagorinsky
S005	2400 x 160	Smagorinsky
S007	4800 x 160	k-epsilon

Figure 6 indicates that the only difference observed among the different test cases is the one attributed to the different hydraulic slope between short and long domain. Hence, the small differences are attributed to the domain effects and not in the turbulence model considered.
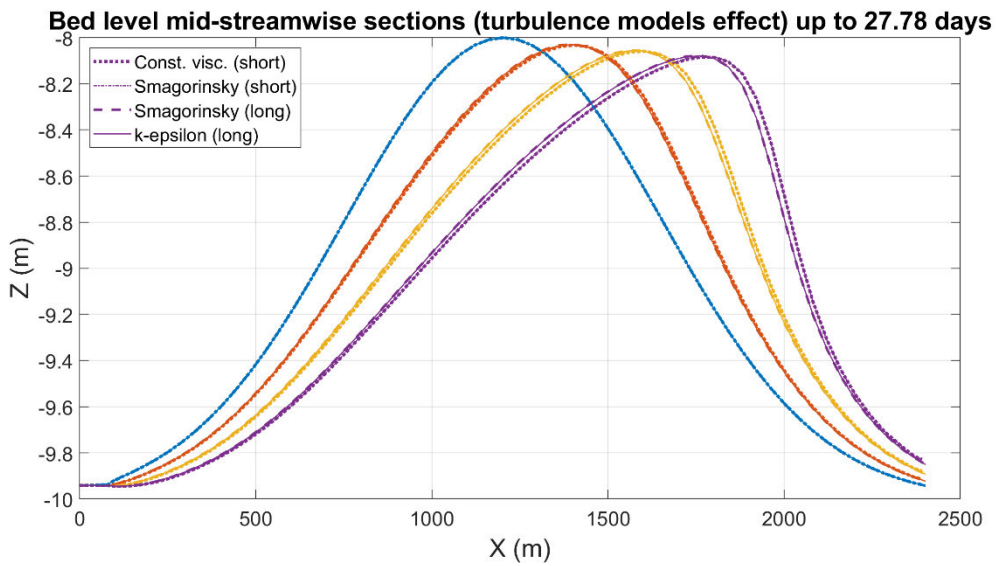
Figure 6 – Middle-width sections of bed level in different time instances. Constant viscosity turbulence model S001b (dotted line), Smagorinsky turbulence model S001 (dash-dot-dotted line), Smagorinsky turbulence model S005 in longer domain (dashed line) and k-epsilon turbulence model S007 in longer domain (solid line).

Advection scheme effect (velocity)

Even though the default advection scheme which is based on the Method of Characteristics is unconditionally stable, at this point different advection schemes will also be investigated. The test cases are summarized on Table 7. Some of the schemes are stable under CFL condition (cases S008 and S009) or they are not mass conservative (cases S002 and S008) or they are computationally expensive (case S010).

Table 7 – Test cases for investigation of different advection schemes (medium mesh considered).

Case	Advection Scheme
S002	1-Method of characteristics
S008	2-Centred semi implicit scheme + SUPG
S009	3-Upwind explicit finite volume
S010	5-PSI distributive scheme, mass-conservative
S020	15-ERIA scheme
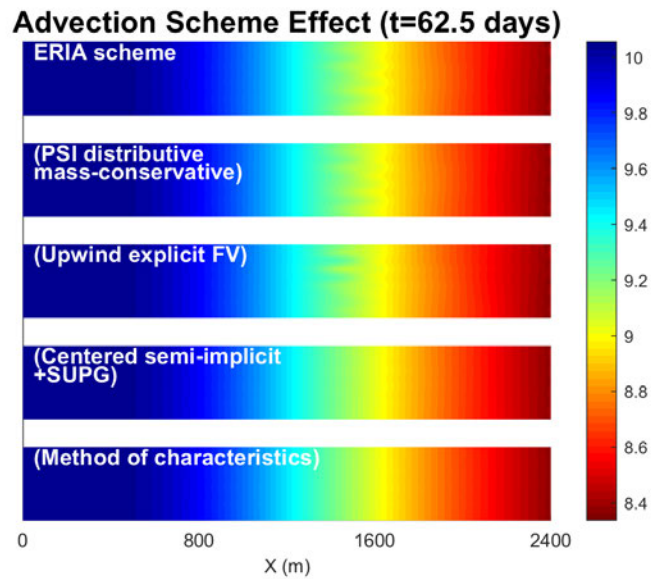
Figure 7 – Water depth contours for the Gaussian hump propagation for different advection schemes,
at the end of the simulation (medium grid, cold start).
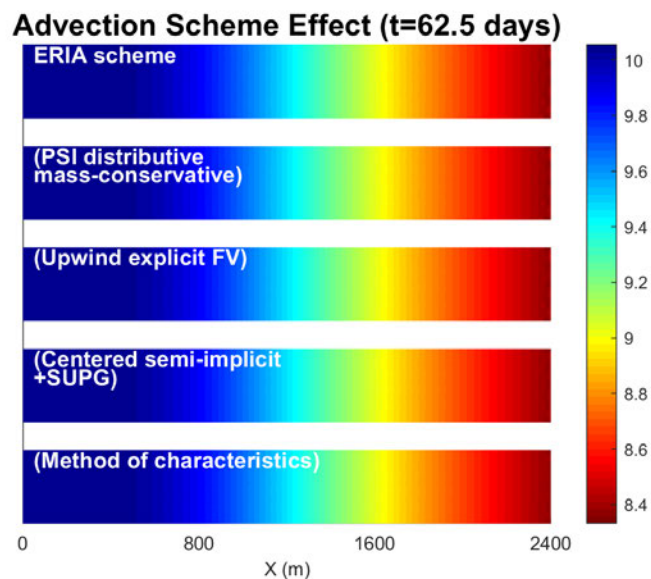
Figure 8 – Water depth contours for the Gaussian hump propagation for different advection schemes,
at the end of the simulation (hot start).

As it can be seen from Figure 7, all the advection schemes results in the hump propagation with the same speed. However, the upwind explicit finite volume (S009), the PSI distributive scheme (S010), mass-conservative and ERIA scheme (S020) demonstrate spatial instabilities along the channel's width when started with a cold start, which cannot be justified for the present application. The Method of Characteristics and the Centred Semi Implicit Scheme + SUPG demonstrate show almost the same smooth behaviour.

However, since the unstable behaviour of the advection schemes is not expected, and may be attributed to the cold start (starting from zero flow) conditions, the last set of simulations are performed once more with hot start conditions starting from a point where the flow is already established and converged. In Figure 8, it is evident that the bed evolution is highly sensitive in the initial conditions combined with the advection schemes. Consequently, if the simulations are initiated within converged flow conditions, no differences in the final solution is given regardless of the advection scheme considered.

At this point it must also be pointed out that for the case S008 different upwind factors were considered (i.e. 0.01, 0.1, 0.5, 1.0 and 2.0). Simulations with those different values did not indicate any kind of different behaviour neither for the flow nor for the bed morphology basically due to the simple case under consideration.

Investigation of different bed-load transport formulas

Within this section, different (than the one used so far) total load transport models, are tested and their effect is discussed under the same flow conditions. These models are the Bijker's formula (Bijker, 1992) (ICF=4 in SISYPHE), the Soulsby & van Rijn formula (Soulsby, 1997) (ICF=5 in SISYPHE) and the formula of Van Rijn (Leo C. van Rijn *et al.*, 2007) (ICF=71, applied as an additional option in SISYPHE). The simulations are conducted based on the S002 test case. The Engelund & Hansen formula results show (Figure 9) that for a total of 50 days, the hump propagates with a speed of approximately 0.32 mm/s. It can be observed that the Bijker's formula (Figure 10Figure 9) is the least active model, and it appears that the lower stoss side of the hump propagates with lower speed than the rest of the hump that propagates with a speed of about 0.17 mm/s. The models results by Soulsby & van Rijn and van Rijn (2007) are shown in Figure 11 and Figure 12, respectively. Those models are the most active concerning the propagation of the hump in time. Soulsby & van Rijn model results in a propagation speed of about 0.64 mm/s, whereas van Rijn (2007) results in a speed of about 0.51 mm/s.
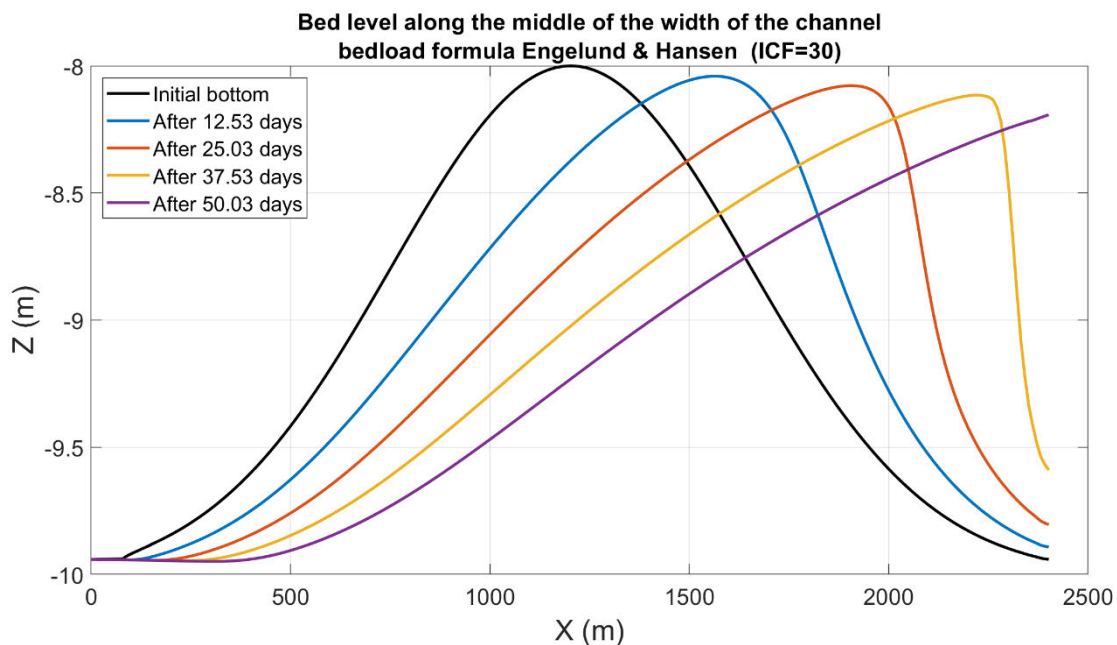
Figure 9 – Numerical solution in terms of middle-width sections of bed level in different time instances for the Engelund & Hansen (ICF=30) total load transport model for a total of 50 days.
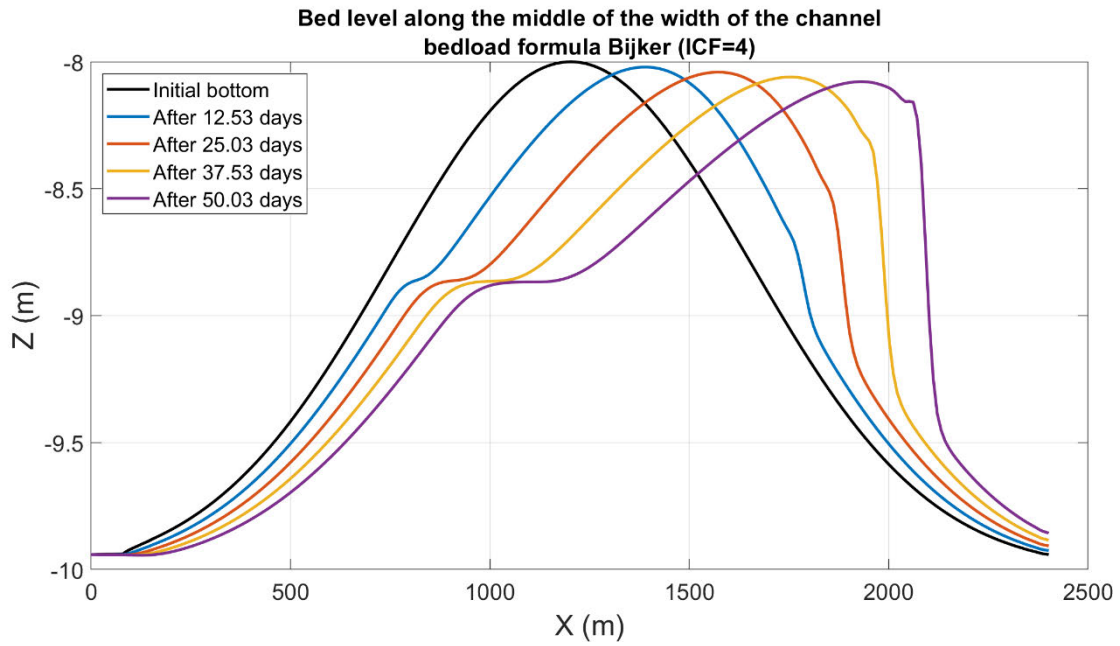
Figure 10 – Numerical solution in terms of middle-width sections of bed level in different time instances for the Bijker (ICF=4) bed-load transport model for a total of 50 days.
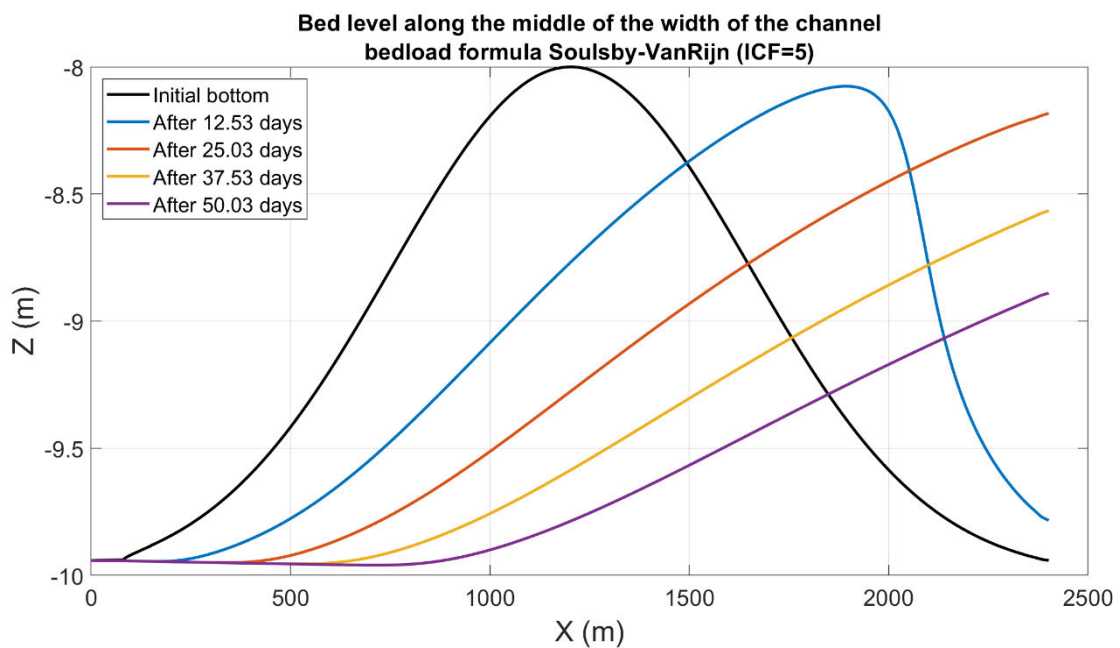
Figure 11 – Numerical solution in terms of middle-width sections of bed level in different time instances for the Soulsby & van Rijn (ICF=5) bed-load transport model for a total of 50 days.
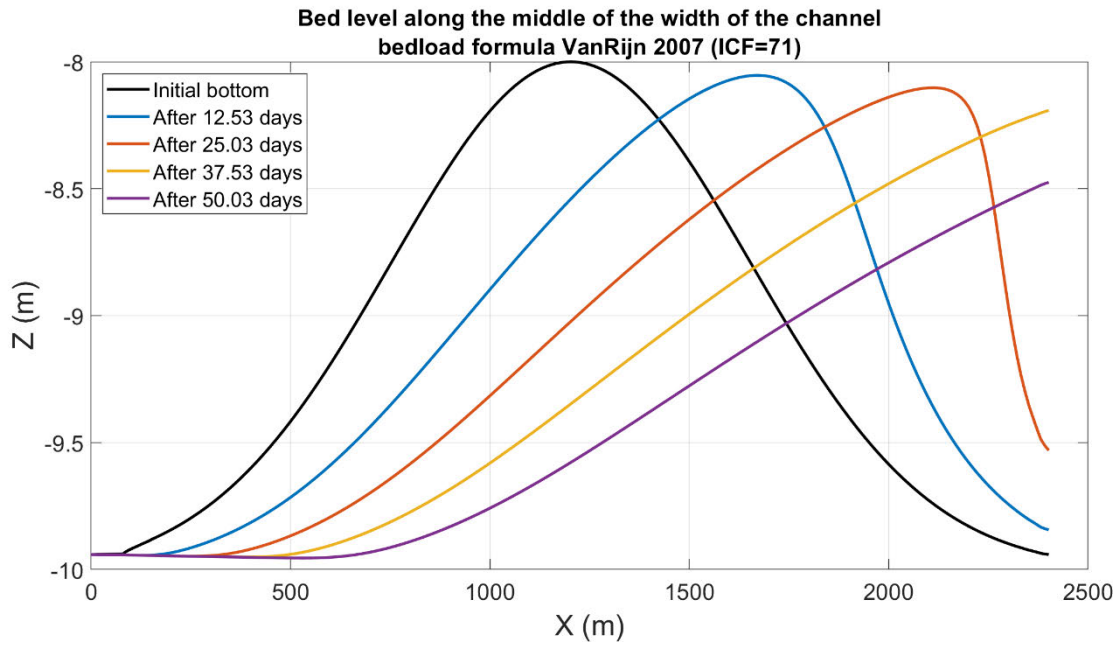
Figure 12 – Numerical solution in terms of middle-width sections of bed level in different time instances for the Van Rijn (2007) (ICF=71) bed-load transport model for a total of 50 days.

Investigation of Slope Effect

A sloping bottom causes an increase bed-load transport rate in the downslope direction, and the reduction in upslope bed-load direction. For taking into account the bed slope effect it is possible to use the Koch & Flokstra (1981) formula. As indicated in SISYPHE user manual, this effect of bed slope is similar to adding a diffusion term in the bed evolution equation. It tends to smooth the results and is often used to reduce instabilities. The corrected magnitude of the sediment transport is given by:

$$Q_b^* = Q_b \left(1 + \beta \frac{\partial z_b}{\partial s} \right)$$

where z_b is the bed level, s is the flow direction and β or beta s an empirical factor accounting for the streamwise bed slope effect (= 1:3 by default). It is suggested that the beta parameter of the model should be calibrated depending on the case under examination Saberi & Zenz (2016).

The correction on the solid transport rate density is applied in this section in order to account the slope effect. The test cases considered are given in Table 8 all based on the coarse long mesh case. It has to be mentioned that in all the previous cases the beta parameter was equal to zero since the SLOPE EFFECT was set to NO.

Table 8 – Cases for investigation of slope effects in propagation of a Gaussian hump (medium mesh).

Case	Beta parameter
S005	0.0
S012	1.3
S013	2.5
S014	5.0
S015	10.0
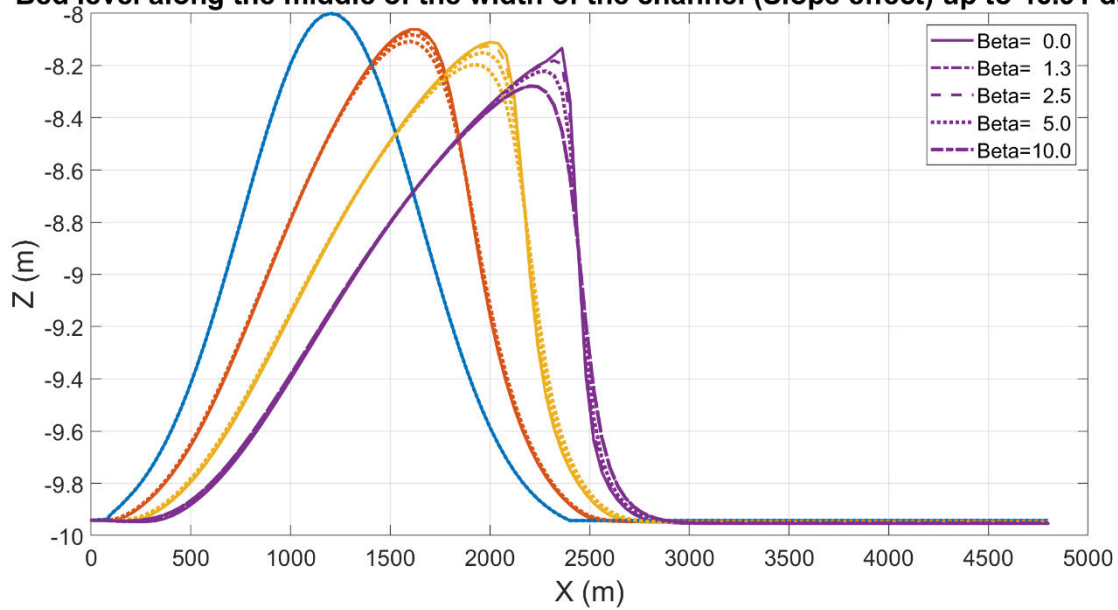
Figure 13 – Middle-width sections of bed level in different time instances (coarse long grid) for different beta parameter of Koch & Flokstra (1981) formula for the propagation of a Gaussian hump.

As it can be seen in Figure 13, the application of a higher beta parameter results in smoothening and dispersion of the hump. The default value of beta = 1.3 is not resulting in any significant differences compared to the case without considering slope effects for this testcase.

Effect of the Morphological Factor (MOFAC)

The simulation of flow over the Gaussian Hump, is conducted for different morphological factors ranging from 1 (default) up to 100 in order to speed up the morphological processes. The results are given in terms of morphodynamic times. The hydrodynamic times are 625 days for case S016 with MOFAC=1, 62.5 days for case S017 with MOFAC=10, 31.25 days for case S021 with MOFAC=20, 12.5 days for case S022 with MOFAC=50 and 6.25 days for case S018 with MOFAC=100.

Table 9 – Simulation cases for different morphological factors.

Case	MOFAC
S016	1
S017	10
S018	100
S021	20
S022	50

Bed level along the middle of the width of the channel (Morphological factor effect)
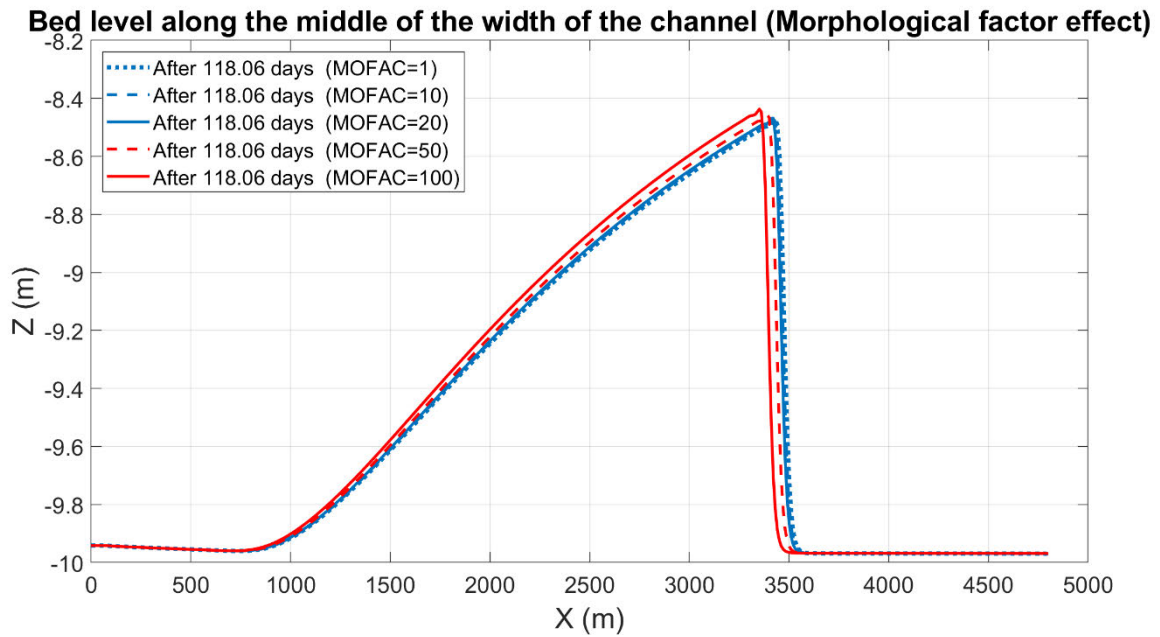
Figure 14 – Gaussian hump position after 118 days (upper figure) and 243 days (lower figure) in morphological time for MOFAC=1 in case S016 (dotted blue line), MOFAC=10 in case S017 (dashed blue line), MOFAC=20 for case S021 (solid blue line), MOFAC=50 for case S022 (dashed red line) and MOFAC=100 in case S018 (solid red line).

From the results of Figure 14 it can be concluded that for morphological factor 20, the results are the same without consideration of morphological factor. This is undeniably a factor that can also contribute in computational speed up, which has to be treated with caution, as in a different problem and configuration, the morphological factor that provides similar results may be higher or lower. Morphological factor equal to 100 results in a lower propagation speed for the hump.

Gaussian Hump propagation due to suspended sediment transport

The simulation of flow over the Gaussian hump is also performed for consideration of only suspended load transported (case S019) by means of the two-dimensional advection-diffusion equation. Equilibrium inflow concentration (EQUILIBRIUM INFLOW CONCENTRATION=YES) has been considered, computed by Van Rijn formula (3). For SISYPHE, options for no diffusion and no correction on convection velocity have been chosen. The choice of type of advection was the ERIA scheme (15).
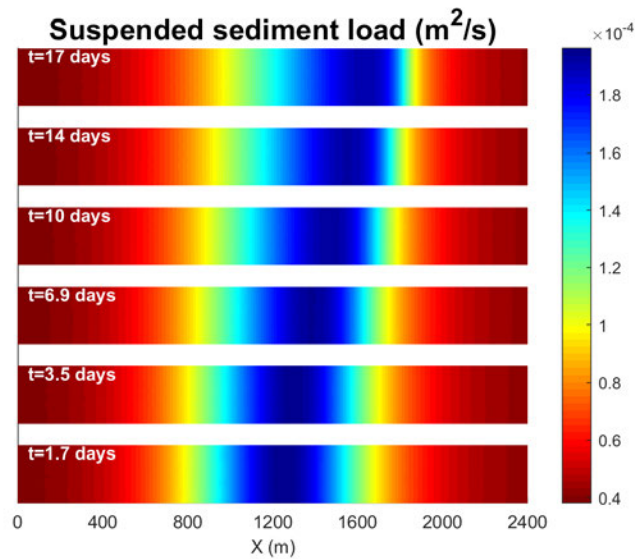
Figure 15 – Suspended sediment load contour plots for flow over a Gaussian hump (with equilibrium inflow concentration computed by Van Rijn's formula), in different time instances (S019).
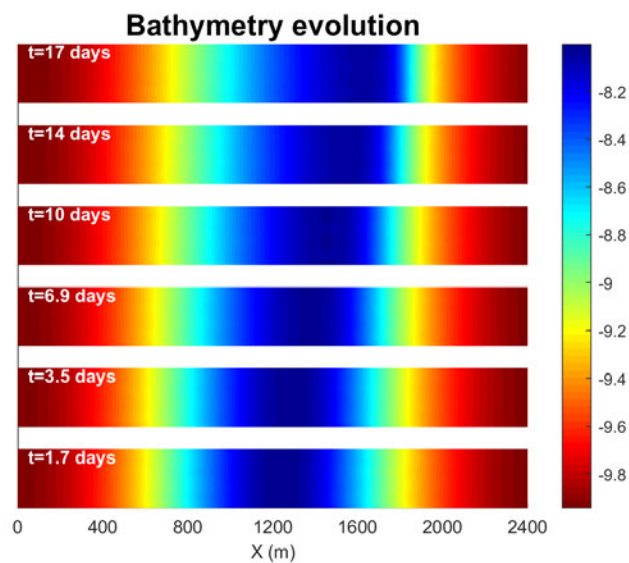
Figure 16 – Bathymetry contour plots for flow over a Gaussian hump for suspended sediment motion in different time instances (S019).

Different types of advection schemes have been investigated in this particular case, starting from the one that has been used by default based on the Method of Characteristics (1). This advection scheme resulted in non-evolving bathymetry at the lateral boundaries, whereas the hump was migrating in accordance with the imposed flow. Advection scheme 14 resulted in negligible migration of the hump $O(10^{-4})$. Finally, advection schemes 3, 4, 5, 15 seem to provide the most reasonable results. The results are exactly the same for advection schemes 3, 4 and 5 with those presented for ERIA advection scheme (15) in Figure 15 and Figure 16 and the hump propagation is uniform in the spanwise direction.

2D vs 3D numerical results on Gaussian Hump propagation

The aforementioned results concern the results coupling TELEMAC-2D and SISYPHE. Results concerning coupling of TELEMAC-3D and SISYPHE are compared in this section. The number of the vertical planes are chosen to be equal to 20. The horizontal turbulence model is the Smagorinsky (4), and the vertical is the mixing length model (2) by Nezu and Nagakawa (3). In addition, the numerical domain chosen for the 3D simulations has been extended 2 400 m upstream and downstream so that there is enough space before the hump for the development of the flow and also after the hump to make sure that there will be no effects from the outflow boundary.
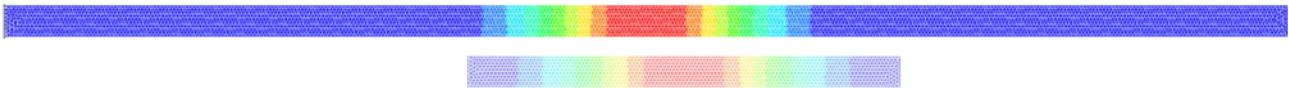
Figure 17 – Upper figure: domain dimensions for the 3D simulation with TELEMAC-3D and lower figure: domain dimensions for the 2D simulations with TELEMAC-2D.
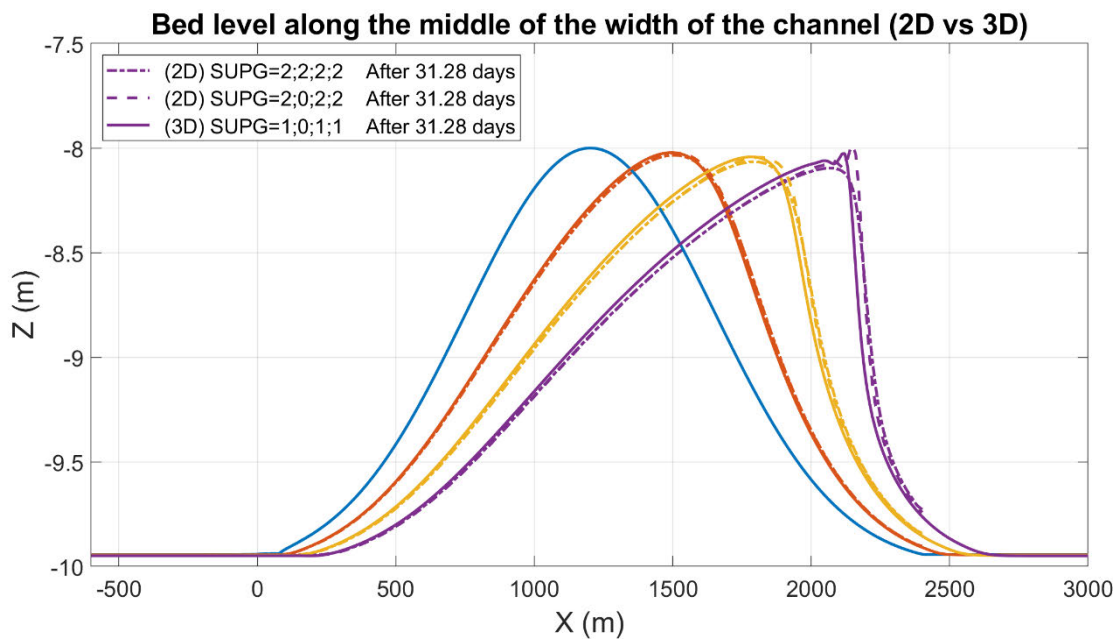
Figure 18 – Middle-width sections of bed level in different time instances: 2D with SUPG=2;2;2;2 (case S002), 2D with SUPG=2;0;2;2 (case S002_supg) and 3D with SUPG=1;0;1;1 (case S002_3d).

Results are compared in terms of sections of bed level in different time instances in the middle of the channel width (Figure 18) where the hump seems to propagate with the same speed in both cases. It can be seen that the 3D solution includes wiggles on the hump's crest as the hump propagates. Those wiggles are not present neither to the 2D cases shown in Figure 18 with domain equal to 2 400 m, nor to the 2D cases shown in Figure 5 and Figure 13. This issue has been attempted to be tackled by finer vertical resolution close to the solid bed with no different behaviour. It has been found that the SUPG OPTION default parameters, are different in TELEMAC-2D and TELEMAC-3D. SUPG OPTION is a table of 4 integers relating, in order, to the velocities,

depth, tracer and k-Epsilon model. For TELEMAC-2D the default values are 2;2;2;2 whereas for TELEMAC-3D is 1;0;1;1. The default value 0 for the advection scheme concerning depths in TELEMAC-3D corresponds to a non-upwind scheme and is responsible for the observed wiggles. The 2D case with SUPG=2;0;2;2 in Figure 18 results in similar wiggled form of the hump. SUPG is an option that can prevent the formation of spurious numerical oscillations. However, since the scheme is also more diffusive, steep slopes can be smoothed out.

2.1.2   Migrating trench

Numerical configuration

Geometry

The numerical domain is rectangular, 4800 m long in the horizontal plane in the direction of the flow and 160 m long in the transverse direction. The water depth is constant equal to 10 m, with the exception of the region that the trench is considered (see Figure 19).
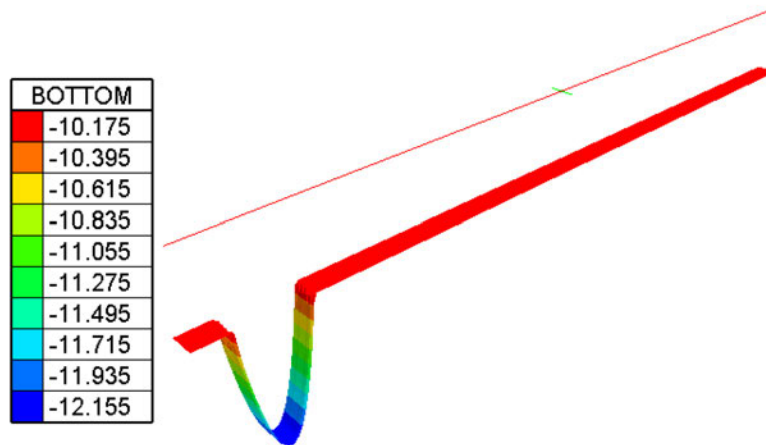
Figure 19 – Trench geometric configuration in terms of water depth (3D view).

The reference system is placed in the inflow of the channel, in the middle of the channel width and vertically on the position of the free surface. The expression of the trench geometry is given by the following expression in terms of local bathymetry:

$$d = 10^{-20}x^3 + 5 \cdot 10^{-5}x^2 - 0.0395x - 4.3535$$

This expression is valid for 200 < x < 600. Rest of the domain has constant bathymetry d_o = -10 m.

Numerical parameters (TELEMAC-2D - SISYPHE)

All the numerical parameters and sediment characteristics are identical to the previous base computations so that there can be common ground for comparisons. The computational domain considered here is 4800 m long and 160 m wide. In addition, uniform flow conditions at Q = 1600 m³/s have been considered, similar to the Gaussian hump case.

Simulated test cases and results

Investigation of Slope Effect

In the present case, the slope effect from the Koch & Flokstra (1981) formula has also been examined. The test cases under consideration have different beta parameters as shown in Table 10.

Table 10 – Cases for investigation of slope effect in propagation of a trench (medium mesh considered).

Case	Beta parameter
T001	0.0
T002	1.3
T003	2.5
T004	5.0

As it can be observed in Figure 20, a beta value equal to 0 or the default value (beta = 1.3) results into an unnatural instability in the back side of the trench. Higher values of the beta parameter result in faster dispersion of the trench. It seems that consideration of a slightly higher value of beta = 2.5 can yield almost similar results without the previously mentioned instability in the back side of the trench.
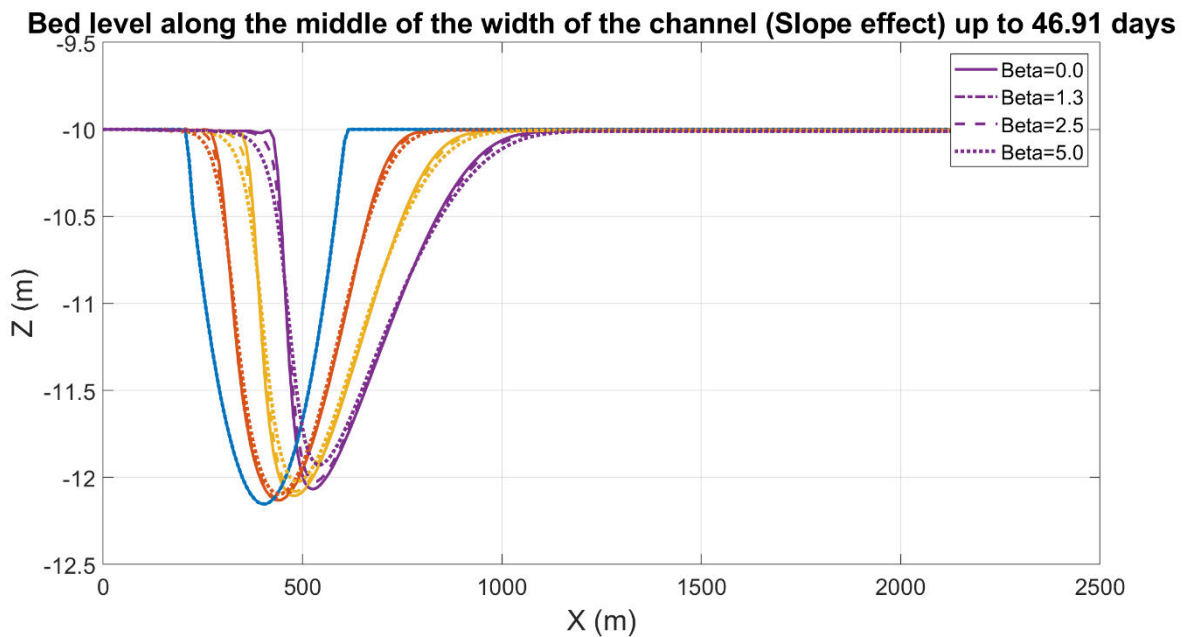
Figure 20 – Middle-width sections of bed level in different time instances (medium grid) for different beta parameter of (Koch & Flokstra, 1981) formula for the propagation of a trench.

Effect of the Morphological factor (MOFAC)

The simulation of flow over the trench, is conducted for different morphological factor from 1 (default) up to 100 in order to speed up the morphological processes. The results are given in terms of morphodynamic times. The hydrodynamic times are 625 days for case T005 with MOFAC=1, 62.5 days for case T006 with MOFAC=10, 31.25 days for case T009 with MOFAC=20, 12.5 days for case T010 with MOFAC=50 and 6.25 days for case T007 with MOFAC=100.

Table 11 – Simulation cases for different morphological factors.

Case	MOFAC
T005	1
T006	10
T007	100
T009	20
T010	50
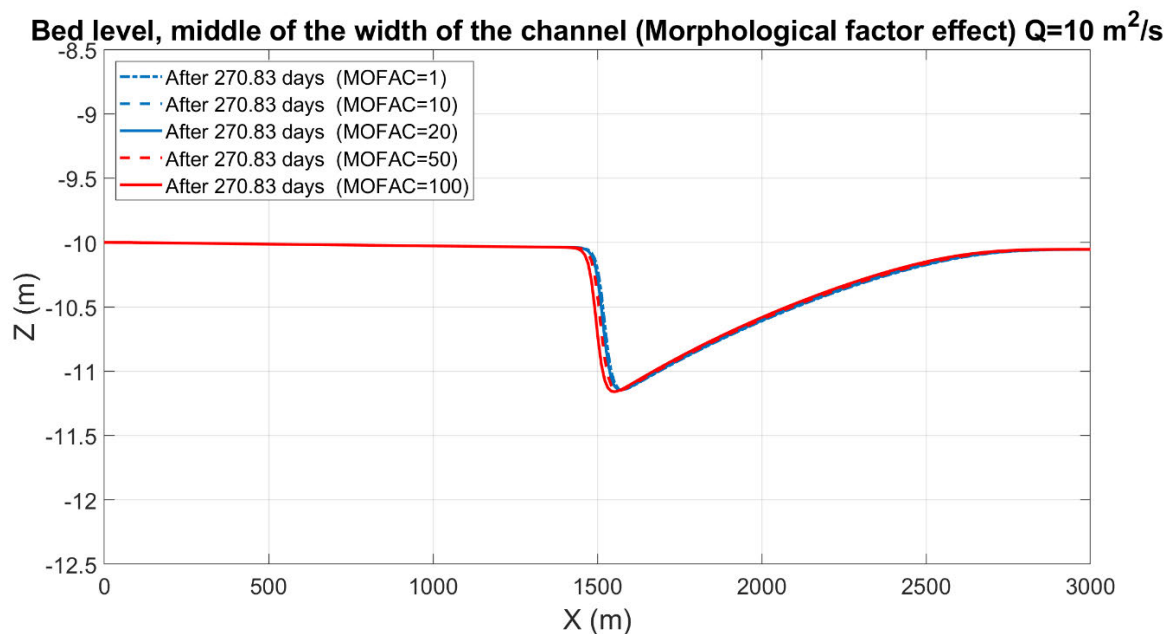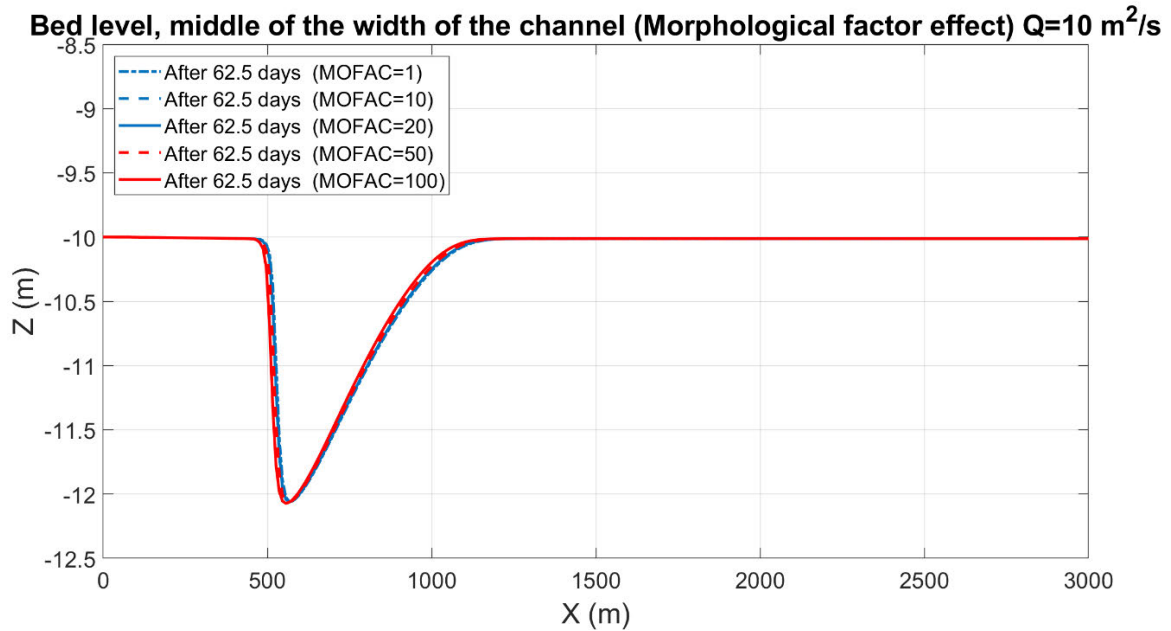
Figure 21 – Trench position position after 62.5 days (upper figure) and 270 days (lower figure) in morphological time for MOFAC=1 in case T005 (dotted blue line), MOFAC=10 in case T006 (dashed blue line), MOFAC=20 for case T009 (solid blue line), MOFAC=50 for case T010 (dashed red line) and MOFAC=100 in case T007 (solid red line)..

From the results (Figure 21) it can be concluded that for morphological factor up to 20, the results are the same without consideration of morphological factor. Similar to the case of the Gaussian hump, this parameter can speed up computations but taking into account that morphological factor effect depends on the specific case to be simulated.

Trench propagation due to suspended sediment transport

The simulation of flow over the trench is also performed for consideration of only suspended load (case T008) transported by means of the 2-dimensional advection-diffusion equation. Equilibrium inflow concentration (EQUILIBRIUM INFLOW CONCENTRATION=YES) has been considered, computed by Van Rijn formula (3). For SISYPHE, options for no diffusion and no correction on convection velocity have been chosen. The choice of type of advection was the ERIA scheme (15) just like in the case of the Gaussian hump. From the results shown in Figure 22 it can be seen that in the spanwise direction the flow starts as uniform but as the trench propagates, it appears that there is a spanwise effect similar to the Gaussian hump case. Similar behaviour can be observed for suspended load (see also Figure 23). The trench is not propagating fast due to the sediment diameter of 250 µm used in the simulations.
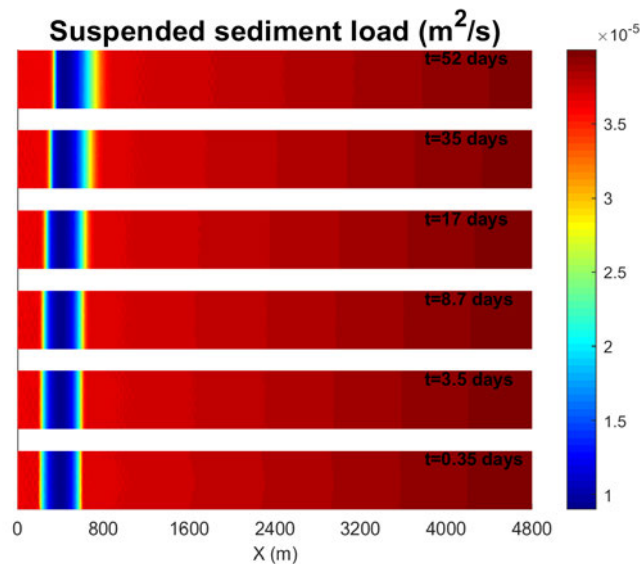
Figure 22 – Suspended sediment load contour plots for flow over a trench (m²/s), in different time instances (T008).
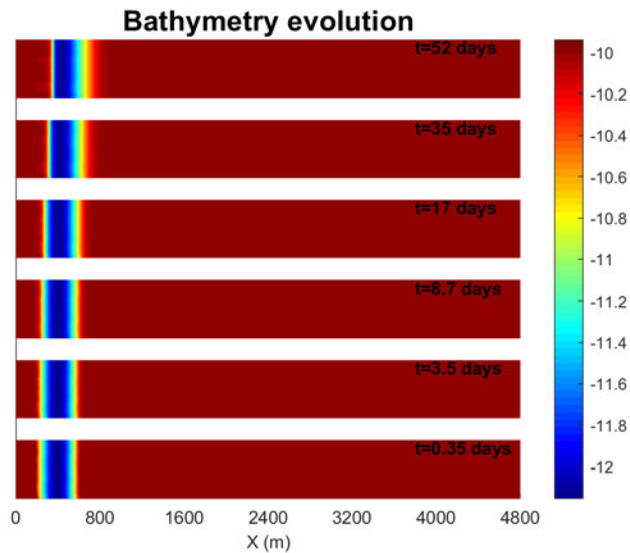
Figure 23 – Bathymetry contour plots for flow over a trench for suspended sediment motion in different time instances (T008).

2D vs 3D numerical results on Trench propagation

The above mentioned results concern the results using TELEMAC-2D and SISYPHE coupled. Results concerning coupling of TELEMAC-3D and SISYPHE are compared in this section. The number of the vertical planes are chosen to be equal to 20. The horizontal turbulence model is the Smagorinsky (4), and the vertical is the mixing length model (2) by Nezu and Nagakawa (3).

Results are compared in terms of water depth contours (Figure 24) and sections of bed level in different time instances in the middle of the channel width (Figure 25). The 2-dimensional solution is somewhat different than the 3-dimensional solution. Even though the trench propagates with the same speed, in 3-dimensional simulation there are wiggles in the bed morphology (Figure 24) similar to those observed at the crest of the Gaussian hump in bed level middle width sections (Figure 25). Once more this behaviour is attributed to the SUPG default values for the advection of depth in TELEMAC-2D (SUPG=2;2;2;2) and TELEMAC-3D (SUPG=1;0;1;1).
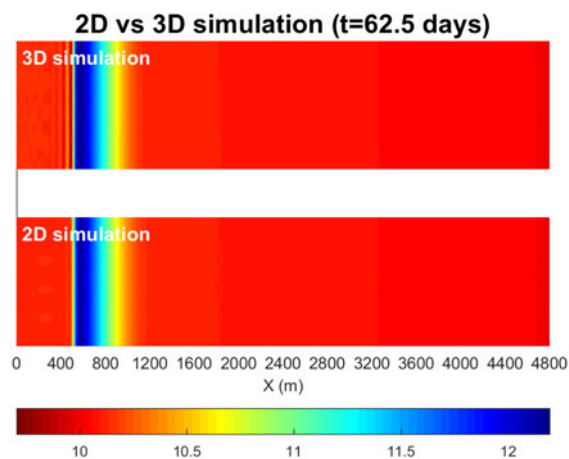
Figure 24 – Water depth contour plots for flow over a trench for suspended sediment motion (2D, case T001 vs 3D, case T001_3d).
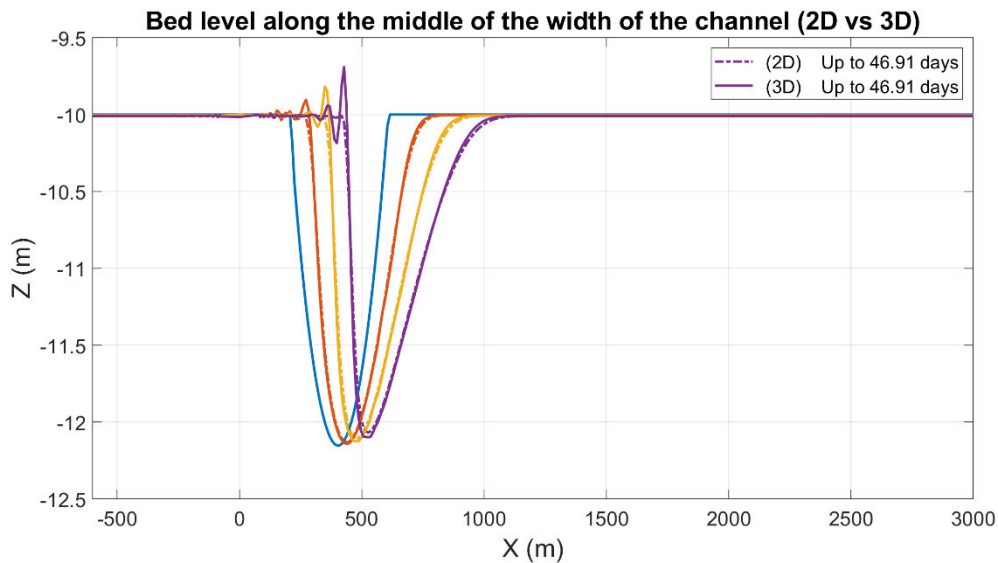
Figure 25 – Middle-width sections of bed level in different time instances (2D vs 3D).

2.1.3 Conclusions

From the morphological simulations driven by a uniform flow over a Gaussian hump and a trench, a certain number of conclusions can be extracted. It has to be mentioned that the results of the present preliminary work should be considered as a guide and not as definite rules in every other application.

Note that these testcases are for stationary flow, whereas the intended application has non-stationary (tidal) flow and waves.

- A grid of O(20-40 m) elements can capture the mean flow quantities at an acceptable level for the Gaussian hump and the migrating trench applications examined, as no significant differences in the flow results occur. Coarsening the grid resolution by a factor of 2 results in computational time reduction by a factor of ≈ 1.61.

- Turbulence schemes do not affect the bed evolution for the applications examined.

- In numerical parameters, the advection schemes for the velocities (along with upwinding technique) have no effect on the bed evolution solution. Certain advection schemes are affected however by the initial conditions creating instabilities in the bed morphology. It is advisable to start the morphological simulation from a converged flow solution (hot start).

- Sloping effects can smoothen the unnatural instabilities and wiggles produced by the numerical model. In the present application of trench propagation, it has been proved that consideration of beta parameter equal to 2.5 can erase instabilities. Although, one must keep in mind that the beta factor is a calibration factor, rather than a numerical stabilisation factor. Changing the slope factor might change the equilibrium slopes of trenches, sand bars or beaches. It might influence dredging numbers as well.

- Different formulas for bed load transport have been examined, i.e. the original Engelund and Hansen formula (1967), the Bijker's formula (Bijker, 1992), the Soulsby & van Rijn formula (Soulsby, 1997) and the formula of Van Rijn (Leo C. van Rijn *et al.*, 2007). The least active is Bijker's formula followed by Engelund and Hansen formula. Soulsby & van Rijn and Van Rijn (2007) are the most active in propagation of the Gaussian hump.

- Morphological factor is a useful parameter for speeding up the morphological calculations but must be treated with caution. It has been shown here that a morphological factor up to 20 produces same results with no consideration of morphological factor. A factor 100 leads to deviating migrations speeds.

- Suspended sediment results in the propagation of the bathymetric structures. However, even if the morphology initiates evolving uniformly, with time it appears that more sediment is gathered in lateral boundaries than in the middle of the channel. The problem is solved by using a different advection scheme (15) and deactivating diffusion terms.

- 2-dimensional simulations result in same propagation speed of the Gaussian hump and the trench with the 3-dimensional simulation results. However, some wiggles (in the 3D simulations) have been observed in the lee side of the hump, and the upstream end of the trench, which is attributed to the different upwind configuration of the advection scheme of TELEMAC-2D and 3D.

2.2   Idealized model for the Belgian coast

In this section, an idealized simplified model is developed for the Belgian coast for the simulation of flow due to tide and wave interaction. This model consists of an offshore water level boundary, and a Neumann boundary condition for the lateral boundaries.

Then, the basic features of the TEL2TOM functionality will be presented. This is a knew featured develop by the project team which allows the simulation of coupled TELEMAC-2D - TOMAWAC on different independent meshes. This way, the TOMAWAC domain can cover a larger domain area for the proper wave propagation and have coarser mesh than the domain of TELEMAC-2D. This way, significant computational speed up can be achieved with the same level of accuracy. This functionality will also be applied in simulations on the idealized model.

2.2.1   Application of Neumann boundaries in a schematic coastal model

Neumann boundary conditions allow to predefine the longshore water level gradients at the boundaries without the need to know the velocities and water levels itself. Due to wave run-up and wave induced currents exact water levels and velocities at the lateral boundaries are not known beforehand near the shoreline. Implying inconsistent water levels or velocities at the boundaries leads to stability problems or unrealistic flows. Therefore, within the current project, a methodology to implement Neumann type boundary conditions for water level gradients within the TELEMAC-2D model suite has been developed and programmed into the software. For additional methodology and mathematical background on the implementation of Neumann boundary conditions, the reader is referred to Breugem *et al.* (2018), which has been presented at the Telemac User Conference 2018 (see Appendix A).

In subsection 2.2.1, a fully schematized case will be implemented, describing the key features of the model and to demonstrate the robustness and efficiency of the methodology. In section 2.2.2 this model will be applied to validate the nearshore velocities due to tidal and wave action at Mariakerke (measuring campaign of period 23/09/2015 – 14/11/2015 (Montreuil *et al.*, 2015). Finally, a second validation case will be examined in section **Fout! Verwijzingsbron niet gevonden.** in order to estimate the wave driven currents measured on the field by drifters (drifters deployment on 11/06/2012 (Dan *et al.*, 2017)).

Model setup

The domain for the application of the Neumann boundary condition implementation is an idealized bathymetry of the Belgian coast west of Zeebrugge port (Figure 26).

The bathymetry of the numerical domain has a constant slope of 1:50 from the coastline towards the offshore for a length of 1.1 km and the rest of the offshore bathymetry is flat at -17.33 m. The vertical level reference is Mean Sea Level (MSL). A detail of the bathymetry formation is given by section A-A at Figure 27. The numerical domain (see Figure 28) is discretized using a channel type mesh in the nearshore region with elements of 60 m long along the coastline and 20 m wide in the other direction. This has been chosen since the flow patterns are not expected to demonstrate strong variations in the longshore direction. In the rest of the domain (offshore) a triangular mesh is used with minimum element size equal to 60 m and expansion ratio of 7%.

Figure 26 – Numerical domain of the schematic coastal model application.
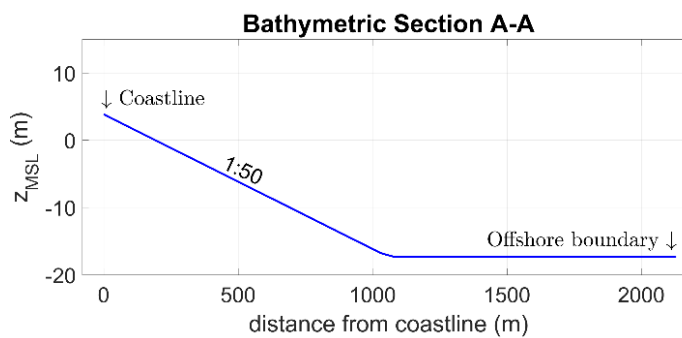
Figure 27 – Bathymetric Section A-A for the schematic coastal model application.

Concerning the boundary conditions of the numerical domain, two separate boundary conditions (.cli) files are considered, one for TELEMAC-2D and one for TOMAWAC. In both files the coastline side is considered as a solid boundary. For TELEMAC-2D the offshore boundary is an Open boundary with prescribed water level H, whereas for the east and west lateral boundaries the Neumann-type boundary conditions with prescribed water level gradients were chosen. For TOMAWAC, the lateral boundaries and offshore boundary are considered as Open boundaries.
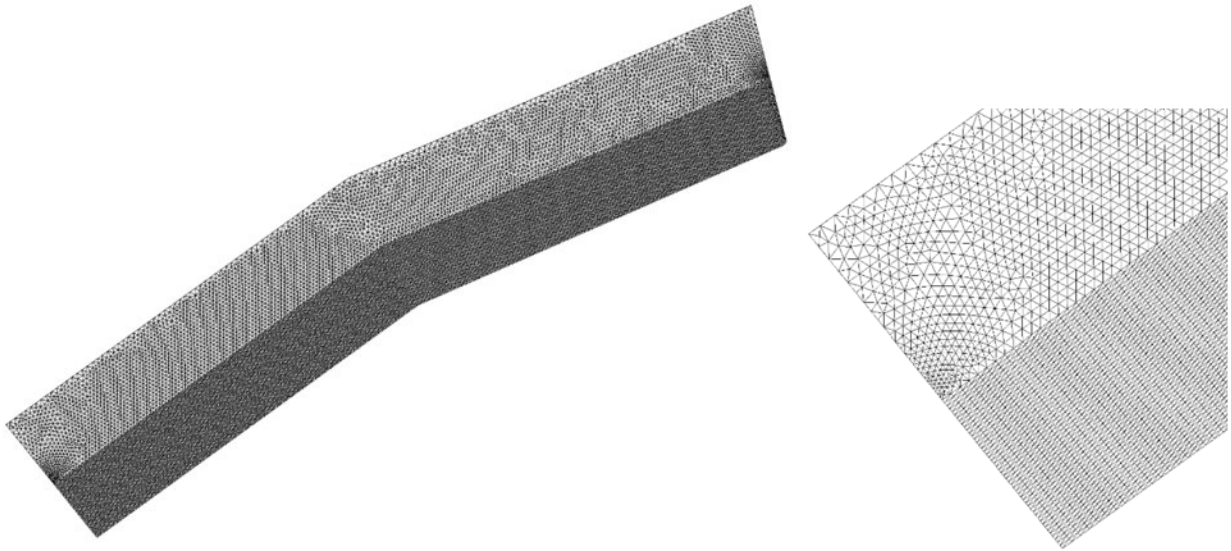
Figure 28 – Computational mesh for the idealized Belgian coast application (left figure) and detail of the west boundary area (right figure).

Model settings

Within the aforementioned numerical configuration, flows consisting of tide and/or wave action have been simulated. The tidal flow is introduced by means of a sinusoidal free surface elevation in time and space according the expression:

$$h = h_o sin\left[2\pi\left(\frac{t}{T} - \frac{x}{L}\right)\right] \tag{1}$$

where h_o = 2 m is the tidal amplitude, T = 12 hr is the tidal period and the tidal wavelength is $L = T \cdot \sqrt{g \cdot z_{max}} = 43\,200\,s \cdot \sqrt{9.81\,m/s^2 \cdot 17.33m} = 563\,241\,m$. The above free surface expression is applied along the offshore boundary of the numerical domain and the length x is equal to 0 m on the east corner of the offshore domain and it increases along the offshore up to the maximum value of 13 092 m on the west corner of the offshore domain. Those temporally variable values on the offshore nodes of the domain are included within the FORMATTED DATA FILE 1 required to assign the offshore boundary conditions in TELEMAC-2D. For the implementation of Neumann boundary conditions, a LIQUID BOUNDARIES FILE is required to assign the free surface spatial gradient $\partial h/\partial x$ according to:

$$\frac{\partial h}{\partial x} = -2\pi\frac{h_o}{L}cos\left[2\pi\left(\frac{t}{T} - \frac{x}{L}\right)\right]\hat{n} \tag{2}$$

where $\hat{n}$ is the unit normal vector to the boundary, pointing outside of the numerical domain. This means that for the east boundary the value $\partial h/\partial x$ is assigned, whereas for the west boundary the value $(-\partial h)/\partial x$ is assigned. Finally, the OPTION FOR LIQUID BOUNDARIES has to be assigned with one value for each of the open boundaries. For the implementation of Neumann boundary conditions, the value 3 must be assigned to the corresponding boundaries. For the numerical solution of TELEMAC-2D a constant timestep of 10 s is considered.

For TOMAWAC boundary conditions, a constant wave attack from North is considered with significant wave height H_s = 2.0 m and peak period T_p = 6.32 s. TOMAWAC will be coupled with the TELEMAC-2D and a timestep of 10 min is considered for the computation of the source terms and the propagation time step is equal to 1 min. Non-linear interactions between frequencies, white capping dissipation, depth induced breaking dissipation (NUMBER OF BREAKING TIME STEPS = 20) and triad interactions have also been considered along with stationary wind conditions and fully grown waves from north with velocity equal to 12.24 m/s, Wilson (1965).

TELEMAC-2D will be used independently for the simulation of tidal flow, or coupled with TOMAWAC either for wave driven currents or combination of tidal flow and wave driven currents. The total simulation time for each case was equal to one week.

Results on tidal flow

The simulation results for the tidal flow with TELEMAC-2D are presented in Figure 29. Contour plots of velocity magnitude along with velocity vector fields throughout the last simulated tidal cycle (first half) around the High Water (HW) of tide every 1.5 hr. The velocity vectors are interpolated in a coastline adapted grid for clearer view. It can be observed that throughout the tidal cycle, the side boundaries along with the implemented Neumann boundary conditions allow the tidal velocities to exit and/or enter the numerical domain. In addition, the formation of the boundary layer along the coastline and its temporal variation throughout the tidal cycle can be observed. At the snapshot at HW + 1.5 hr the separation of the nearshore flow from the offshore can be observed as well. This application indicates that the implementation of the Neumann boundary conditions on lateral boundaries works smoothly for simulating tidal flow, while it was observed that water level boundary conditions lead to severe instabilities in the near shore as presented by Breugem *et al.* (2018).
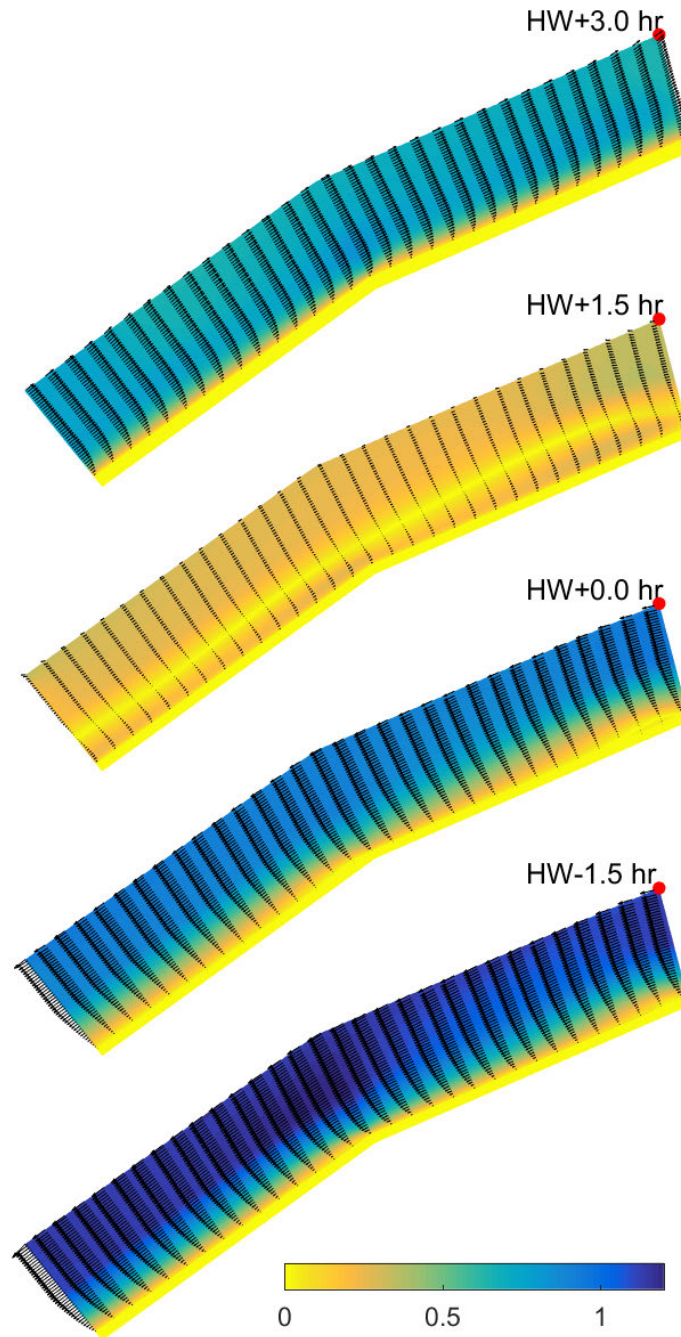
Figure 29 – Contour plots of velocity magnitude (m/s) and velocity vector fields for tidal flow every 1/8 of the half tidal cycle (only tidal forcing, no waves included. Contour colours indicate the velocity magnitude).

Results for wave driven currents

In this section, the results of online coupling of TELEMAC-2D with TOMAWAC considering only wave action as described above, will be presented. The difference with the above considerations is that the timeseries for Neumann conditions used here in LIQUID BOUNDARIES FILE is equal to 0. This consideration for the value $\partial h/\partial x = 0$ is not the most appropriate but is the best possible approximation. There is no tidal forcing, the water level is constant in time and the currents are only induced by the waves. The occurring velocity vectors and velocity magnitude contour plot is shown in Figure 30. The formation of the longshore current can be clearly observed in the surf zone. However, certain velocity disturbances are evident along the east and west boundaries. They are mainly attributed to the selected value of $\partial h/\partial x$. Nevertheless, the effect on the currents inside the domain is limited.
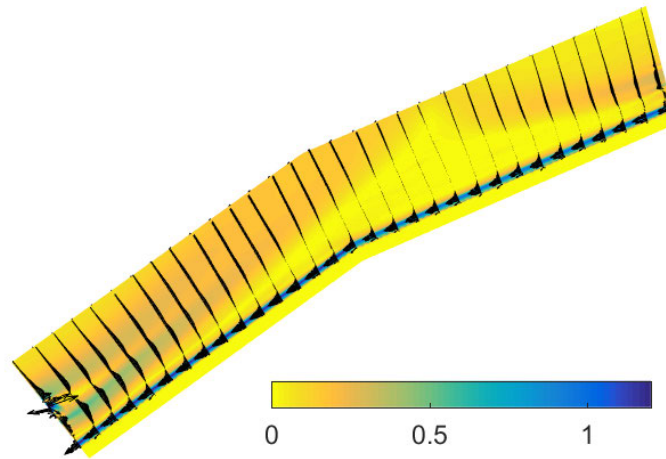
Figure 30 – Contour plots of velocity magnitude (m/s) and velocity vector fields for wave driven currents.

Results for combined tides and wave driven currents

In the last simulated case, TELEMAC-2D and TOMAWAC are coupled to simulate the combined action of tide and waves on this idealised coastal area. The values of the Neumann boundary conditions in this test case is determined by Equation 2, and the results are demonstrated in Figure 31. The longshore wave driven current is evident throughout the whole tidal cycle and in the offshore, the tidal velocities can be observed. The flow separation is also observed here at HW + 1.5 hr, but the separation region is pushed more to the nearshore and the flow velocity magnitude is clearly smaller in comparison with the tidal case. Finally, slight disturbances in the flow field are observed in the Neumann boundaries in the velocity profiles. This is attributed to the boundary condition file of TOMAWAC which is not fully compatible with the current Neumann configuration implemented in TELEMAC-2D. However, even in this case, those disturbances do not seem to have any effect within the inner nodes of the numerical domain.
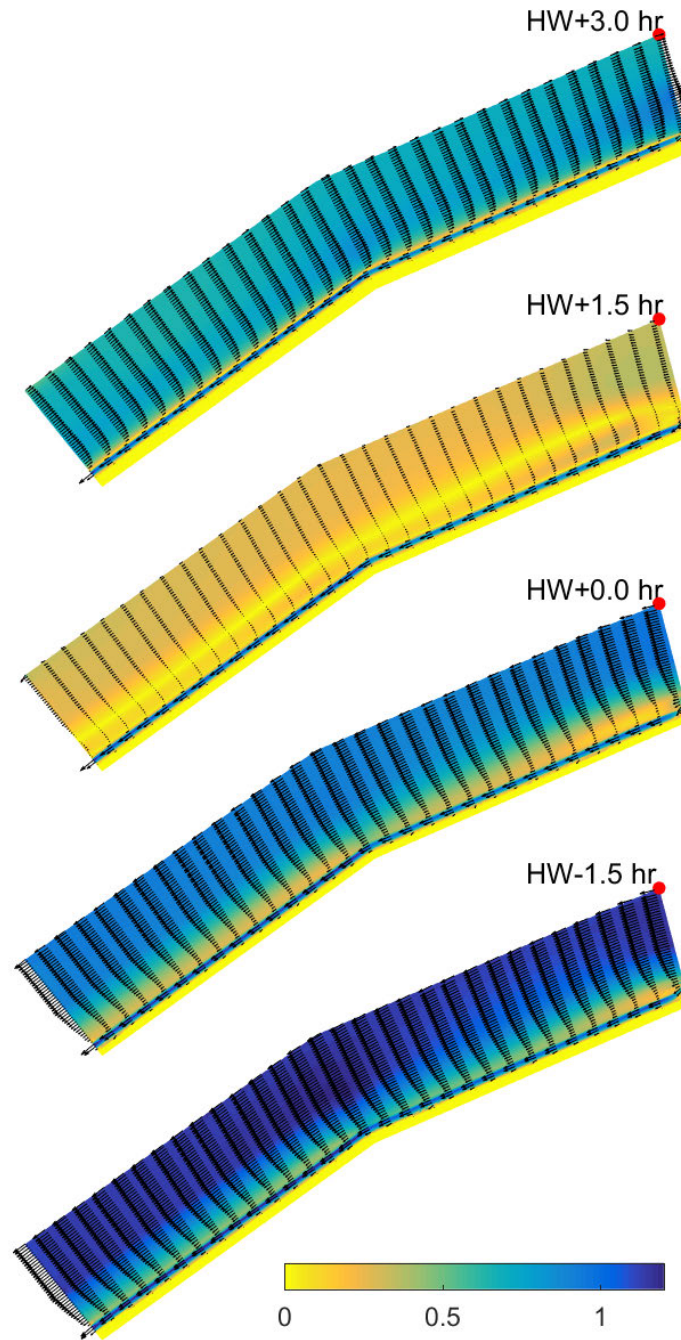
Figure 31 – Contour plots of velocity magnitude (m/s) and velocity vector fields for combined action of tidal flow and wave driven currents every 1/8 of the half tidal cycle (velocity vectors are exaggerated for visual purposes).

2.2.2 Validation against Mariakerke flow data

In this section, a submodel for the simulation of coastal flow (due to tidal and wave action) between Oostende and Nieuwpoort is created. The simulation is performed considering a similar to 2.2.1 numerical configuration concerning the boundary condition of the submodel. The offshore boundary will have predefined water level and in the east and west boundaries (connecting offshore boundary with the coastline) the Neumann boundary condition will be imposed. The TELEMAC-2D results will be compared against field measurements for the field measuring campaign of period 23/09/2015 – 14/11/2015 at Mariakerke (Montreuil *et al.*, 2015). The aim of this submodel is to validate the velocity measurement timeseries at specific locations within the computational domain for the considered campaign.

The first validation model contains the coastal region between the Nieuwpoort and Oostende ports. The bathymetric data is from year 2015. The offshore boundary is placed about 5 km far from the coastline and the length of the coastline is around 16 km. Within the area of interest depicted in Figure 32, a triangular mesh is created that adapted to the position of the groins in the coastal region. The minimum grid size is 20 m that extends till the half of the offshore distance and the rest of the grid size has a linear expansion of 7% (see Figure 33). In the present TELEMAC2D model, water level boundary conditions are imposed on the offshore boundary and wave conditions to all the open boundaries coming from the nearby tidal gauges of Newport and Ostend, and Kwintebank wave buoy.
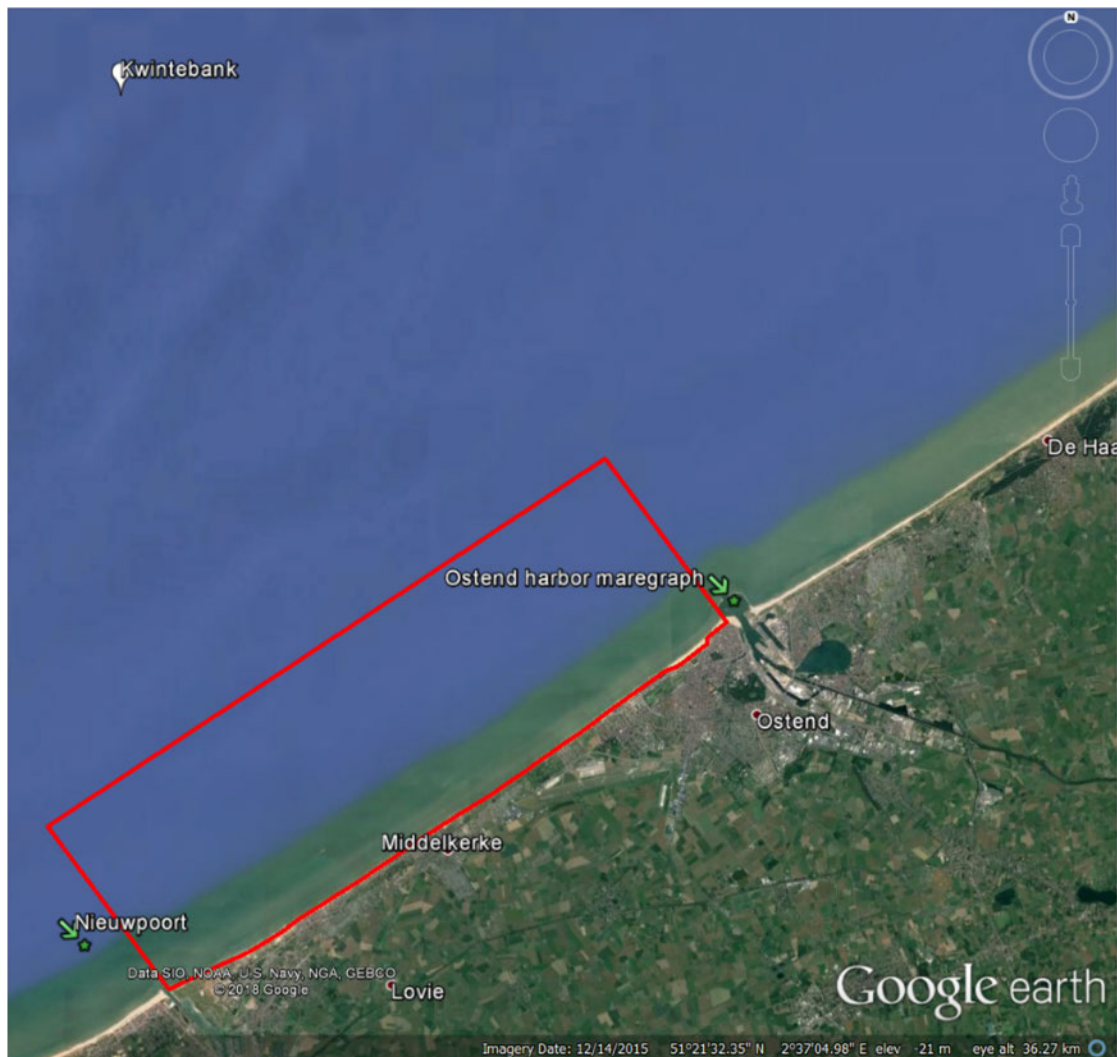
Figure 32 – Limits of the numerical domain for Validation case 1.
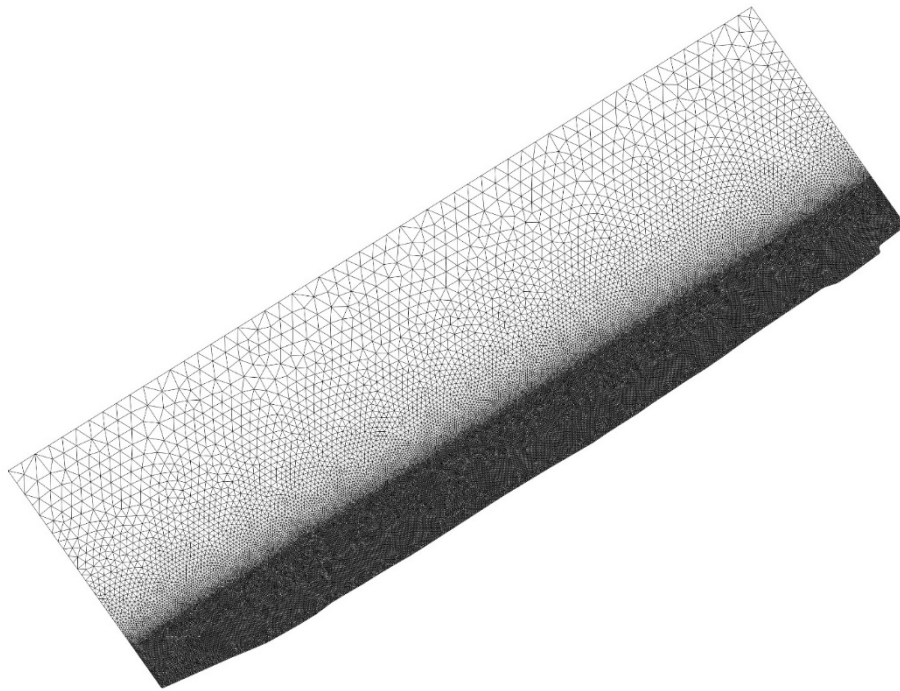
Figure 33 – Computational mesh for Validation case 1.

Tidal Input

For the proper consideration of the temporal variation of the water level of the offshore boundary, a FORMATTED DATA FILE 1 is created. The tidal signals from Nieuwpoort and Oostende for the specific period have been considered (https://meetnetvlaamsebanken.be/). The locations of the tidal signals are given (in RD Paris) in Table 12.

Table 12 – Location of tidal gauges (RD Parijs)

Location	X	Y
Ostend harbor maregraph	-17489	363946
Nieuwpoort	-33609	355920

The weighted effect on both signals has been considered for the offshore water levels temporal variation. Neumann boundary conditions are imposed on the lateral boundaries. Each boundary has a uniform value, varying in time. This value is equal to the water level gradient of the two last grid nodes of the offshore boundary. Thus, for Neumann boundary conditions on the lateral boundaries, the two last grid nodes in the eastern and western sides are used to compute the slope of the water level in the longshore direction (slope facing inwards). This slope is the value of the Neumann boundary condition computed separately for the east and west boundaries. The value of the Neumann boundary condition is spatially uniform along each lateral boundary and temporally changes based on the temporal variation of the offshore water level.

TELEMAC-2D results

Using the tidal data of the previous section, a comparison with velocity measurements at stations at Mariakerke is performed. The measuring campaign under consideration is between 23/09/2015 and 14/11/2015. However, the simulation with TELEMAC-2D is performed for the first 21 days and results are gathered every 10 minutes. The measuring campaign included two stations in the section 104 (see Table 13 and Figure 34) namely Hercules and Hylas I. Although the depth (of deployment/retrieval) of the measuring stations is reported, a crosscheck with the local water depth in the created bathymetry has been conducted. Hercules is actually at a depth equal to -6.5 m TAW, but Hylas I in the considered bathymetry, is found at depth equal to -2.7 m TAW, although more than -3.5 m TAW depth was reported in (Montreuil *et al.*, 2015).

Station		Geographical coordinates (WGS84)		Geographical coordinates (RD Parijs)		Date	Depth (m TAW)
		Longitude	Latitude	X	Y		
Hercules/M1	Deployment	2°52.38'E	51°13.25'N	-20624	362070	23/09/2015	-6.5 m
	Retrieval	2°52.38'E	51°13.25'N	-20624	362070	03/12/2015	-6.5 m
Hylas I/M3	Deployment	2°52.47E	51°13.17'N	-20524	361920	23/09/2015	-3.5 m
	Retrieval	2°52.47E	51°13.17'N	-20524	361920	03/12/2015	-3.5 m

<p align="center">Table 13 – Location of measuring stations under consideration</p>
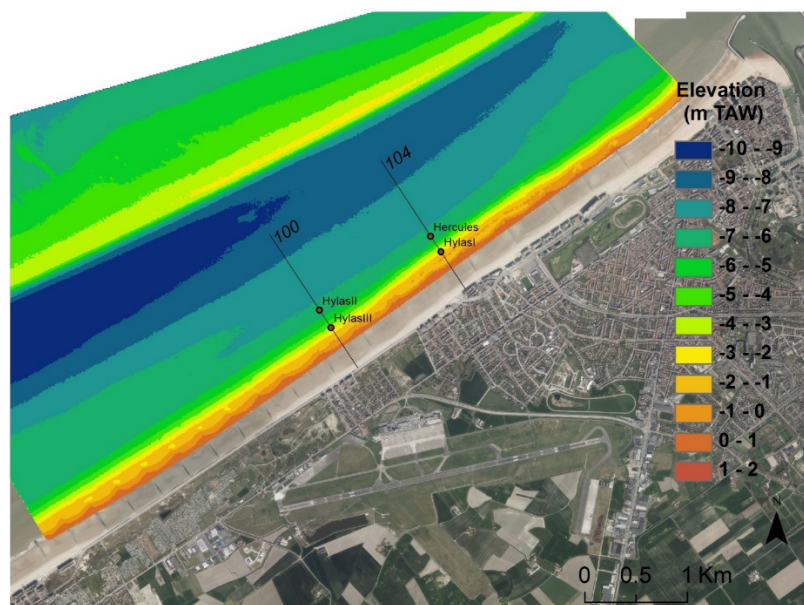
Figure 34 – Topographic map in 2015 and location of the measuring instruments. Figure from (Montreuil *et al.*, 2015)

The velocity signals at those stations have been measured by means of Acoustic Wave and Current meter (AWAC-W). The level of agreement between the field measurements and the numerical results can be observed in terms of eastward U and northward V velocity components in Figure 35 and Figure 36. It can be observed that a satisfactory agreement with the field measurements is achieved. Furthermore, comparison in terms of velocity magnitude and direction can be seen at Figure 37 and Figure 38. Although the model tends to underestimate the maximum flood velocities.

Contour plots of velocity magnitude and velocity vectors in fractions of the period of M2 tidal component (equal to 12 hours and 25.2 minutes) every 1/4 of the period (high water is defined by the point in the east side of the offshore boundary) can be observed at Figure 39. The tidal current is visible and also the separation of the coastal boundary layer, although this is less obvious than in Figure 29.
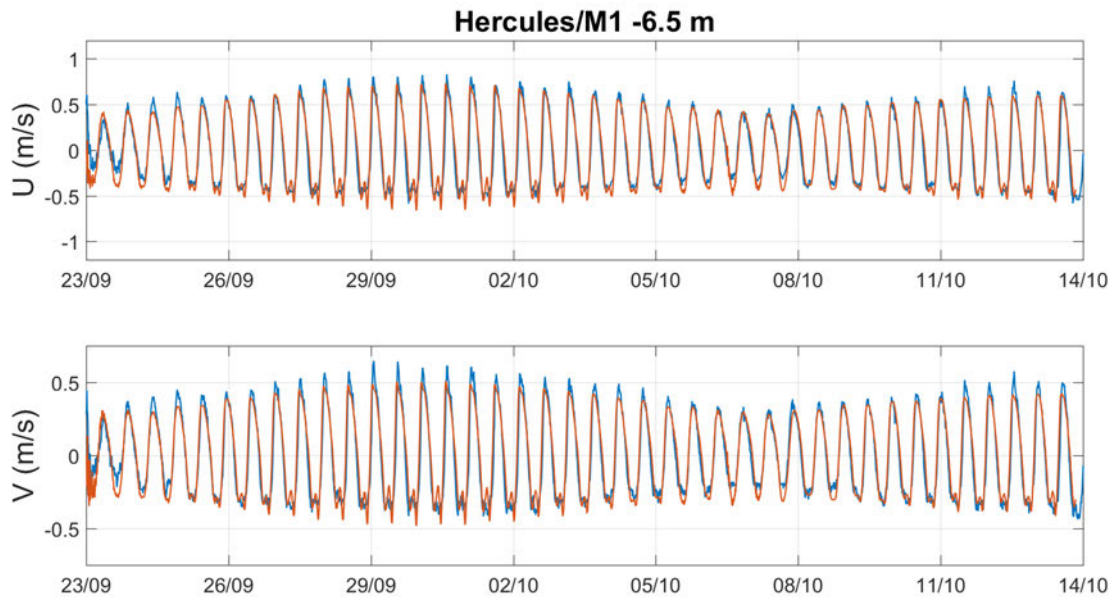
Figure 35 – Eastward U and northward V velocity components in measuring station Hercules (deployed at depth -6.5 m TAW). Field measurement with blue line and model results with orange line.
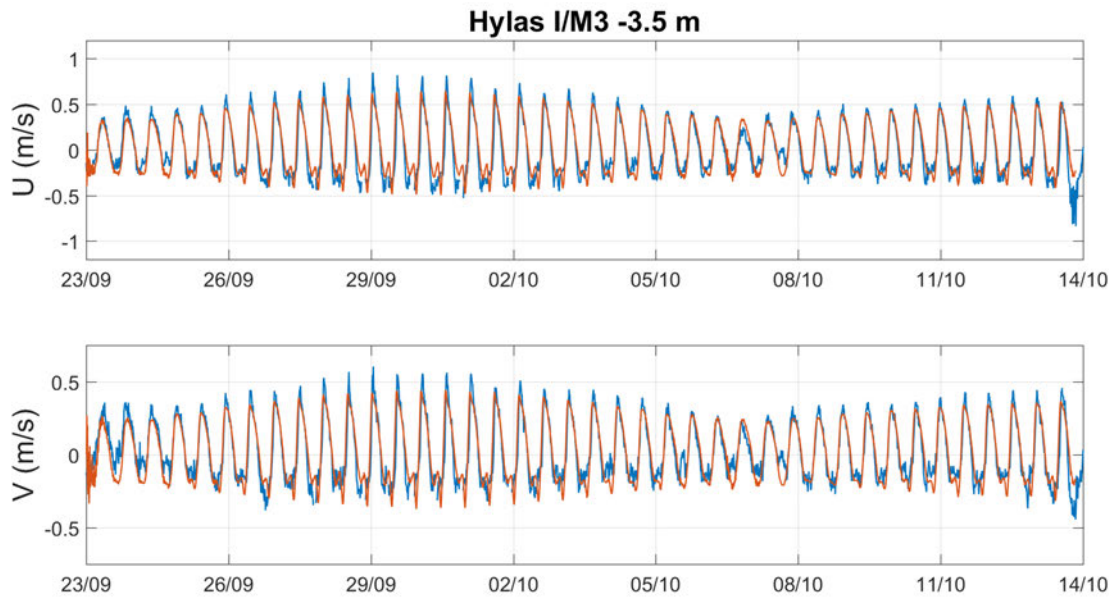
Figure 36 – Eastward U and northward V velocity components in measuring station Hylas I (deployed at depth -3.5 m TAW). Field measurement with blue line and model results with orange line.
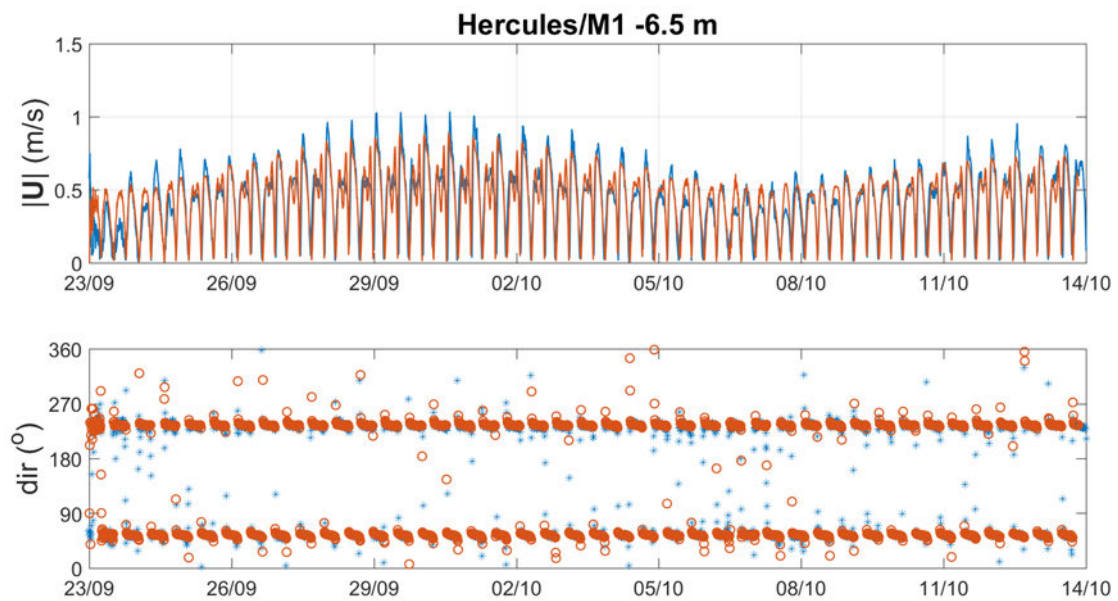
Figure 37 – Velocity magnitude and direction in measuring station Hercules (deployed at depth -6.5 m TAW). Field measurement with blue color and model results with orange color.
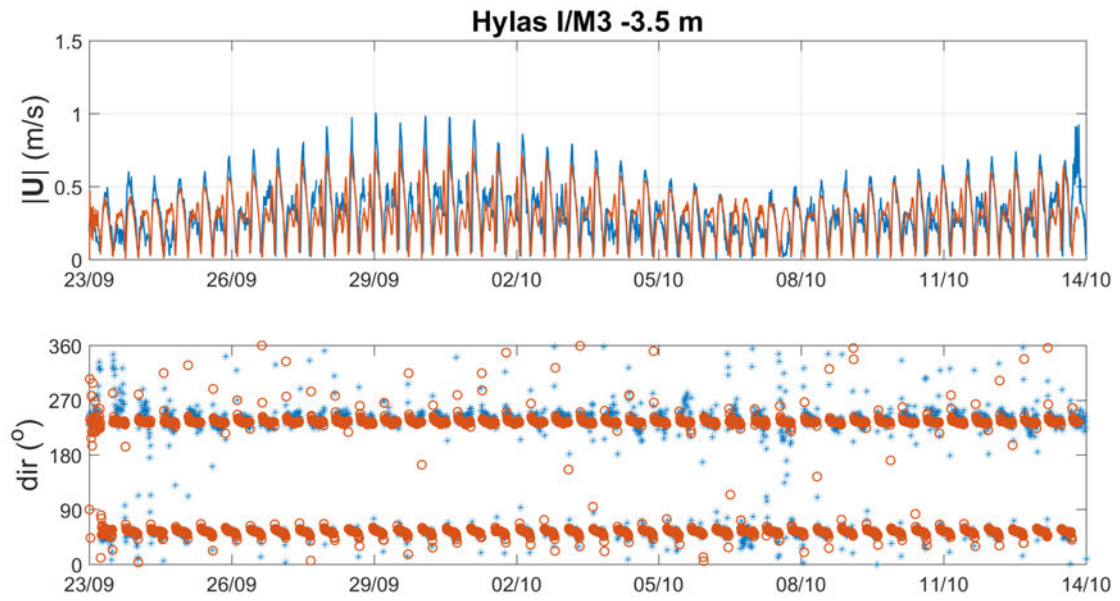
Figure 38 – Velocity magnitude and direction in measuring station Hylas I (deployed at depth -3.5 m TAW). Field measurement with blue color and model results with orange color.
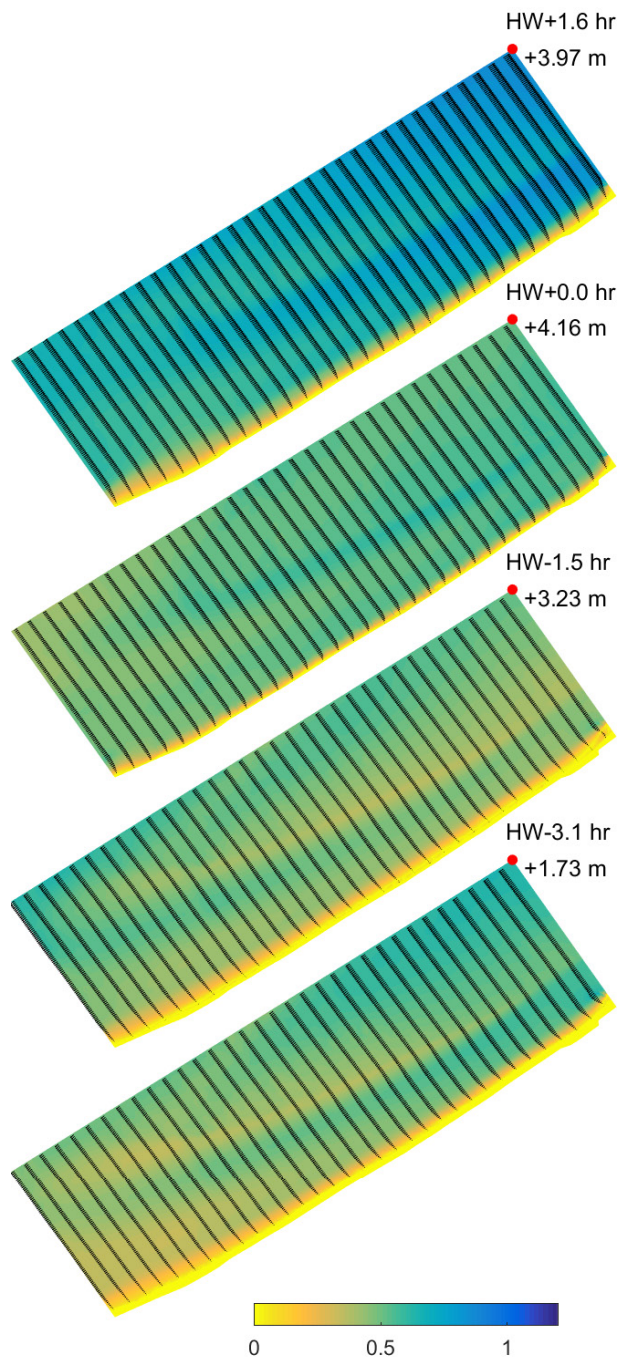
Figure 39 – Contour plots of velocity magnitude and velocity vector fields for tidal flow every 1/8 of the half tidal cycle (period of M2 tidal component).

Wave Input

Concerning the wave data in the area of interest, we used the input from Kwintebank (buoy: Datawell - Directionele Waverider) located at (X,Y) = (-31963, 376860) (see Figure 32). The significant wave height and peak period signals can be seen in Figure 40. The wave data propagate from the location of the wave-buoy to the domain boundary for time equal to $\Delta x_{min}/\sqrt{g \cdot d}$, where Δx_{min} is the minimum distance from the buoy to the domain boundary, and d is the local water depth in the domain boundary location closest to the buoy. Since the wave data comes from a station placed on a sand bar (shallow depth), the TYPE OF BOUNDARY DIRECTIONAL SPECTRUM is equal to 6, which corresponds to JONSWAP spectrum.
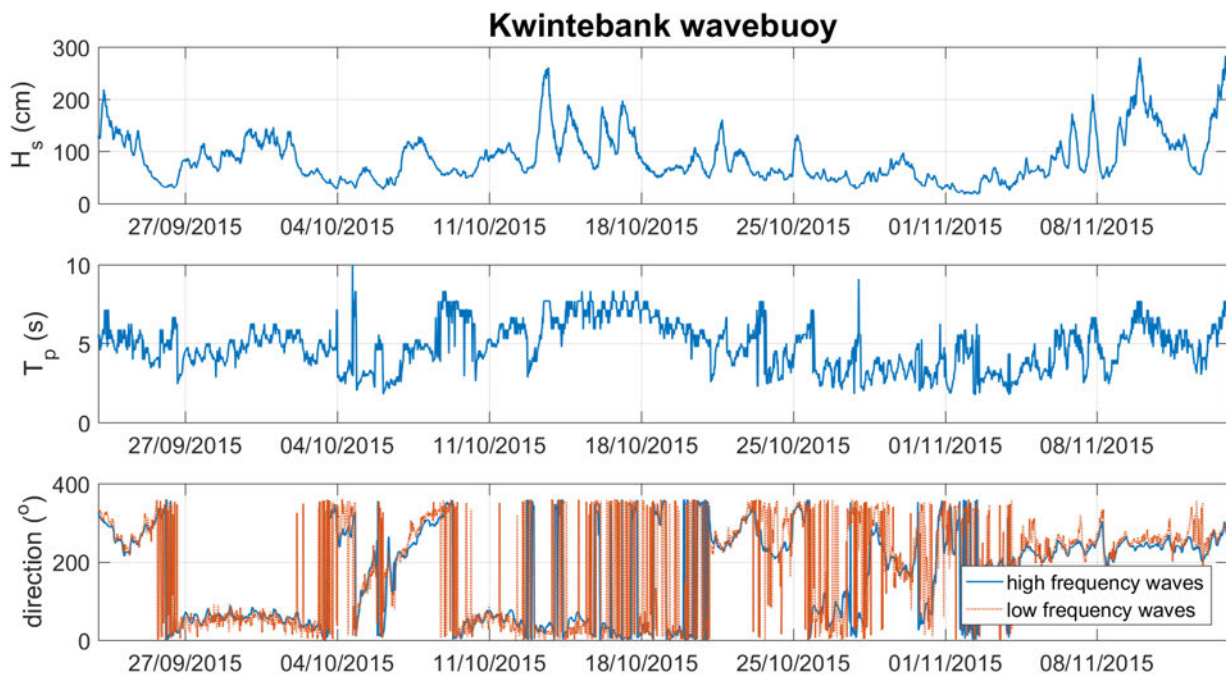
Figure 40 – Wave data input for TOMAWAC from Kwintebank (Boei: Datawell - Directionele Waverider) used in the simulation.

This way, a file ***waveObc.txt*** is created that includes the wave boundary conditions for the present model in every timestep.

Coupling TELEMAC-2D – TOMAWAC results

Using also the wave data as described in the previous section, a coupled simulation of TELEMAC-2D with TOMAWAC is performed. The simulation is performed for one week like before, and the coupling period for TELEMAC-2D and TOMAWAC is set to 60 (ratio of TOMAWAC time step to TELEMAC-2D time step). This application aims at demonstrating whether the current model can produce the wave-driven currents.
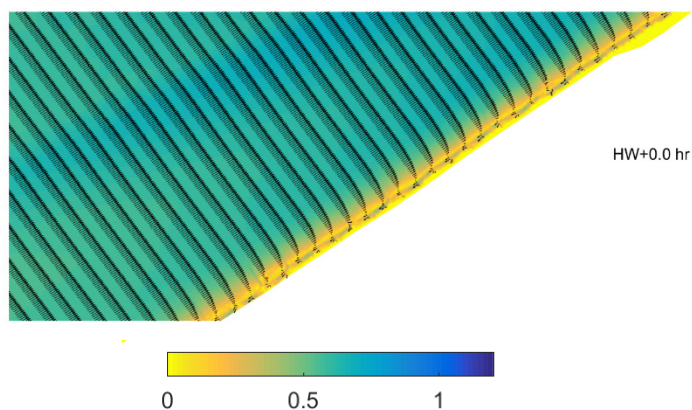
Figure 41 – Contour plots (detail) of velocity magnitude and velocity vector fields for combined action of tidal flow and wave driven currents nearshore detail of formation of the longshore current and the groynes effect.

The results in terms of velocity magnitude contour plots and velocity vectors for the combined action of tidal flow and wave driven currents can be observed in the nearshore region at Figure 41 and in the whole domain at Figure 42. Once again, results are demonstrated as of the period of M2 tidal component (equal to 12 hours and 25.2 minutes) every 1/4 of the period (High Water HW is defined by the point in the east side of the offshore boundary). The coast separation pattern of the flow is slightly changing compared to Figure 39 (for purely tidal flow). In addition, the longshore current contribution created is only visible in close proximity of the coastline. The longshore current is spatially demonstrating modification in the sequence of profiles, attributed to the existence of the groynes.
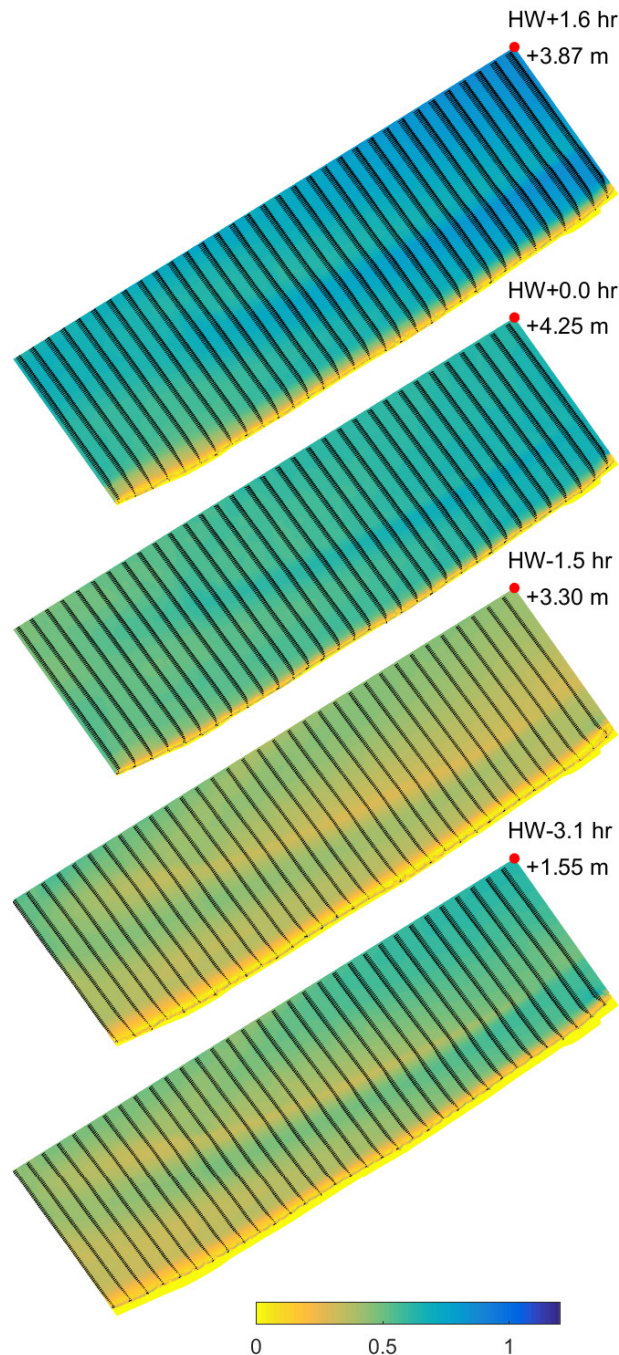
Figure 42 – Contour plots of velocity magnitude and velocity vector fields for combined action of tidal flow and wave driven currents every 1/8 of the half tidal cycle (period of M2 tidal component).

2.2.3 Application of the TEL2TOM functionality: Extended wave domain

Typically, the wave model and the hydrodynamical model demand different constraints with respect to model size and grid resolutions. In large scale models the wave model typically is the limiting factor with respect to wall clock time, although the wave model often requires in large parts of the domain less high resolution than the hydrodynamic model. On the other hand, often it is wanted to have the boundaries of the wave model farther away from the domain of interest in order to have a smoothly varying wave field at the boundary of the hydrodynamic model.

So far in TELEMAC-TOMAWAC is was only possible to couple a hydrodynamic and wave model when both models share identical grids. Coupling different domain extends and grid resolutions would be advantageous both with respect to model quality as to computation times. For that purpose, the TEL2TOM functionality has been developed. According to that, two different domains are considered: one for TELEMAC-2D/SISYPHE and one for TOMAWAC. There is a connectivity list between the two models that indicates which node of TOMAWAC mesh is connected to the TELEMAC-2D mesh (TOM2TEL) and vice versa (TEL2TOM). The parameters TOM2TEL and TEL2TOM are computed using Matlab scripts and are assigned to the GEO-Selafin input files of TELEMAC-2D and TOMAWAC, respectively. The advantages of this approach are the following:

- TOMAWAC can have coarser mesh than the TELEMAC-2D mesh so that computational speed is achieved without compromising on accuracy.

- There is no more any conflict on boundary conditions between TELEMAC-2D and TOMAWAC.

In this section, different parametric investigations will be conducted in the idealized model for the Belgian coast.
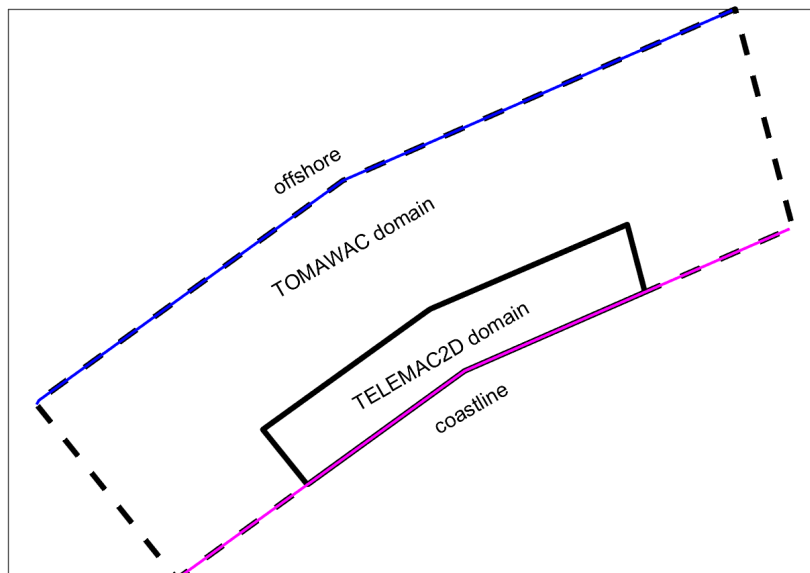
Figure 43 – Configuration of TEL2TOM for the Schematic model of the Belgian coast with TELEMAC-2D domain (solid line), TOMAWAC domain (dashed line), offshore boundary (blue line) and coastline (magenta line).

The features of the schematized model have been described in the previous section. For that purpose, the TELEMAC-2D domain includes a coastline of ≈ 12 km, extending offshore at ≈ 2.2 km (solid line of Figure 43). The TOMAWAC domain occurs by offsetting the TELEMAC-2D domain for ≈5 km in the coastline (magenta line) and offshore boundary (blue line). As indicated before, the bathymetry has a constant nearshore slope of 1:50 for half of the TELEMAC-2D domain width (≈1.1 km) and the rest of the domain has a flat bathymetry at -17.33 m (vertical reference level is TAW). Bathymetry including meshing can be seen in Figure 44. A set of 9 groynes have also been considered in order to check their effect on the simulated flow.

In this particular application, the nodes of the TELEMAC-2D mesh coincide with TOMAWAC mesh nodes. However, in the general case communication between the two modules is achieved by means of a user defined interpolation, e.g. nearest neighbour, linear, inverse distance, ... This functionality can become handy because TOMAWAC in general, does not require very fine resolution in order to provide accurate results whereas TELEMAC-2D needs fine resolution, especially in the nearshore. This indicates that higher computational speed can be achieved in many applications.
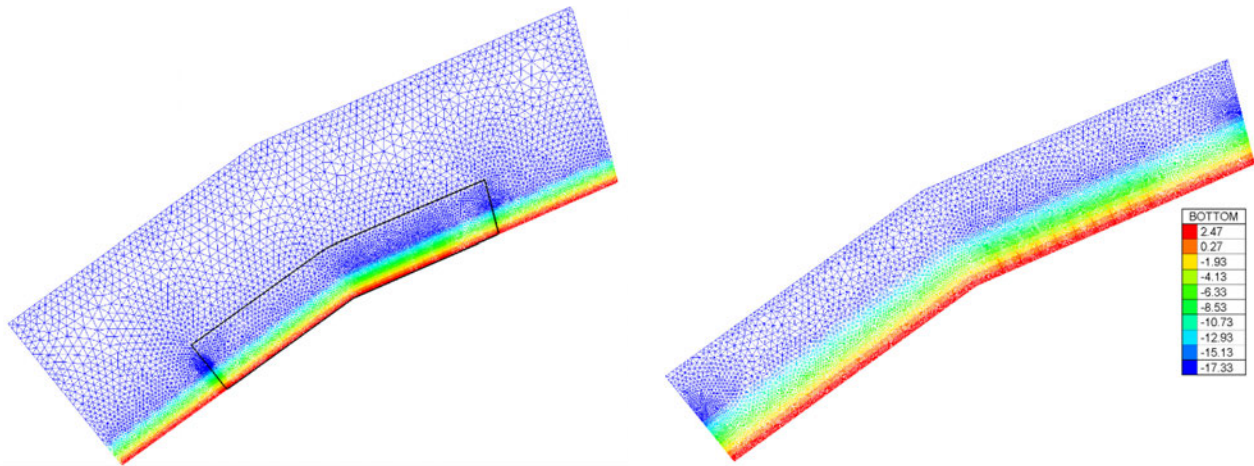
Figure 44 – (left) TOMAWAC mesh with bathymetry and TELEMAC-2D outline (black solid line)
and (right) TELEMAC-2D mesh with bathymetry.

Application parameters and results for coupled TELEMAC-2D - TOMAWAC simulation

Simulation parameters

The coupled TELEMAC-2D-TOMAWAC case under consideration is simulated for ≈12 days. The TELEMAC-2D timestep is 10 s, the TOMAWAC timestep is 2 minutes and the coupling period is set to 30 min minutes (COUPLING PERIOD FOR TOMAWAC = 180).

The tidal flow is established by a tidal component with period equal to 12 h (similar to S2) which is assigned by a formatted file of spatio-temporal variation of free surface elevation assigned at the offshore boundary of the TELEMAC-2D domain. At the lateral open boundaries of TELEMAC-2D domain, a time-dependent Neumann boundary condition is assigned by a "liquid boundaries" file. The Neumann boundary values are the local offshore free surface gradient normal to the lateral boundaries.

The wave action is accounted for by JONSWAP spectrum with significant wave height H_s = 2 m, peak period T_p = 6.32 s. Two different wave angles of attack have been examined, north (N) and north-west (NW) in order to look into the different flow effects in the nearshore due to the wave-driven currents. Based on the wave direction, constant wind has been considered with velocities V_x= 0 m/s and V_y=-12.24 m/s for north wave attack, and V_x= 8.655 m/s and V_y=- 8.655 m/s for north-west wave attack.

CPU time tests

It is clear from previous investigations that TOMAWAC is the most computationally consuming module in coupled TELEMAC-2D - TOMAWAC simulations. Consequently, in this section different meshes for TOMAWAC will be examined in order to see how much the computation time increases when TOMAWAC mesh gets finer. Thus, different meshes have been generated in order to investigate the level of computational speed-up that can be achieved. The different meshes are distinguished by the resolution of triangles in the nearshore region, ranging from 25 m for the fine mesh up to 200 m for the coarse mesh (see Table 14).

It has to be mentioned that those cases are only tested in terms of CPU time and not in terms of accurate representation of hydrodynamics due to the fact that TELEMAC-2D and TOMAWAC nodes do not coincide and thus, communication between the two modules is done by means of nearest neighbour interpolation which alters quite significantly the formation of the wave driven currents in the nearshore region. Hydrodynamic efficiency of TEL2TOM will be discussed extensively in the next section.

Table 14 – Test Cases for computational speed-up investigation.
Resolution for each module refers to the minimum nearshore resolution.

Case	TELEMAC-2D min resolution	TELEMAC-2D number of nodes	TOMAWAC min resolution	TOMAWAC number of nodes
G001	25	10786	25	16498
G002	25	10876	50	11750
G003	50	7057	50	11750
G004	50	7057	100	4823
G005	50	7057	200	2550

The required CPU time for each of the cases G001-G005 is shown in Figure 45. It appears that a 1:1 scaling is achieved when using a coarser mesh for TOMAWAC. Test case G002 requires lower simulation time than case G001, since there are fewer nodes in TELEMAC-2D. Comparing case G002 with G001, which has the same TOMAWAC grid, case G002 requires approximately slightly smaller time per timestep in TOMAWAC module. For those reasons, case G002 is reported but it is not part of the line shown in Figure 45.
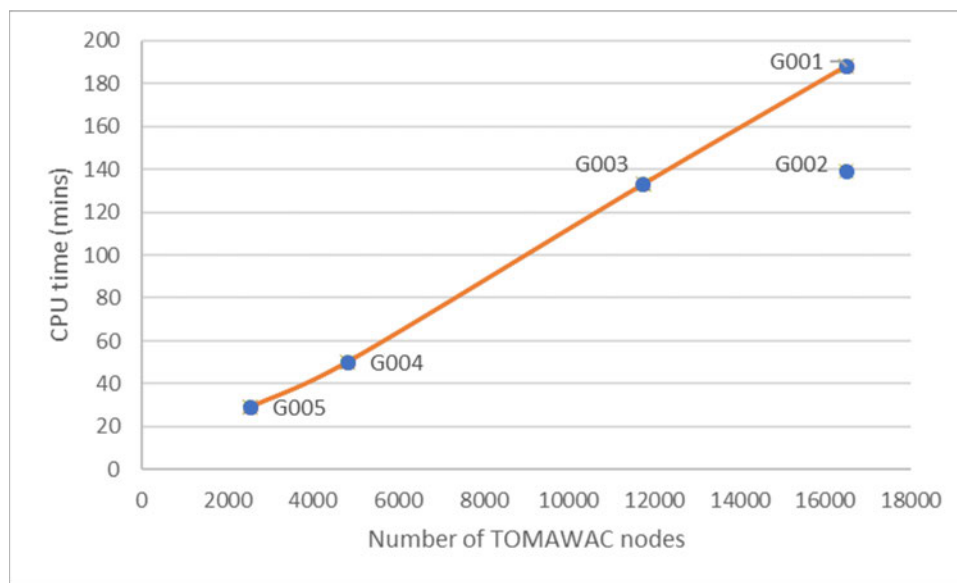
Figure 45 – Comparison of CPU time against number of nodes for TOMAWAC for simulation of waves and currents in the schematized case of Belgian coast. Case G002 which has finer resolution for TOMAWAC than in TELEMAC-2D is reported separately.

Accuracy of the hydrodynamics

At this point the capability of the test cases to demonstrate the wave driven currents and the flow in the nearshore region needs to be examined. In order to tackle the errors emerging from the nearest neighbour interpolation, in the considered meshes the TELEMAC-2D grid points have the same location with those of TOMAWAC mesh in the same region, so that the communicated values of velocities and water levels are referring exactly to the same locations for the two modules. The two cases considered, are summarized in Table 15.

Table 15 – Test Cases for grid sensitivity. Resolution for each module refers to the minimum nearshore resolution.

Case	TELEMAC-2D min resolution	TELEMAC-2D number of nodes	TOMAWAC min resolution	TOMAWAC number of nodes	Waves-wind direction
G001b	25	24332	25	33251	N
G001c	25	24332	25	33251	NW
G003b	50	7161	50	11650	N

Figure 46 gives a contour plot of the TOMAWAC domain with zooming in the TELEMAC-2D region for case G001b at the end of the simulation. The reduction of the wave height can be evident especially in the west part of the nearshore region, where no groynes exist to affect the wave propagation.

In the current approach a one-way coupling for the currents is applied: i.e. radial stresses and shear stresses are passed from the TOMAWAC module to the TELEMAC module to generate wave driven currents. From the hydrodynamic module, only the water levels are sent to the wave model. So, waves are not directly influenced by the currents. It was found out that a two-way current-wave coupling would lead to small fluctuations from the expected value of the significant wave height H_s = 2 m the regions close to the offshore TELEMAC-2D domain. The decoupling of flow velocities from TOMAWAC can be achieved, by setting the flow velocities equal to zero by modifying the routine wac.F.
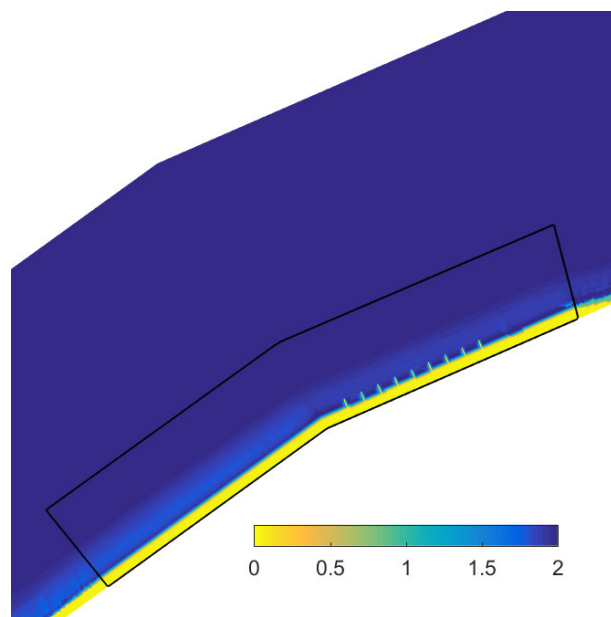
Figure 46 – Contour plot of significant wave height for case G001b at the end of the simulation.

The hydrodynamic results for case with the coarser mesh G003b can be seen in Figure 47. Different instantaneous contour plots of velocity magnitude along with velocity vectors are shown every 1/8 of the tidal cycle. The wave driven current is evident in every snapshot with direction to the west, since the waves and wind come from the north and propagate towards the coast. What is of vital importance is the significant eradication of disturbances in the east and west, similarly to those observed in Figure 30. Those disturbances emerged from the fact that the same boundary, the one of TELEMAC-2D in the current investigation, was assigned different and non-compatible boundary conditions for the two different modules.

For TELEMAC-2D Neumann conditions in the lateral boundaries and defined values of free surface elevation in time and space for the offshore boundary. On the other hand, defined zero elevation boundary condition used to be assigned in TOMAWAC. This resulted in intense flow in the side regions of the TELEMAC-2D domain. Using the TEL2TOM functionality, we consider different domains and this can tackle this issue as it can be seen from the hydrodynamic results. It is important to emphasise that although these numerical instabilities act local at the boundary of the domain of interest, in morphological runs, local disturbances will effect on the median or long-term large parts of the domain and therefore should be threated carefully.
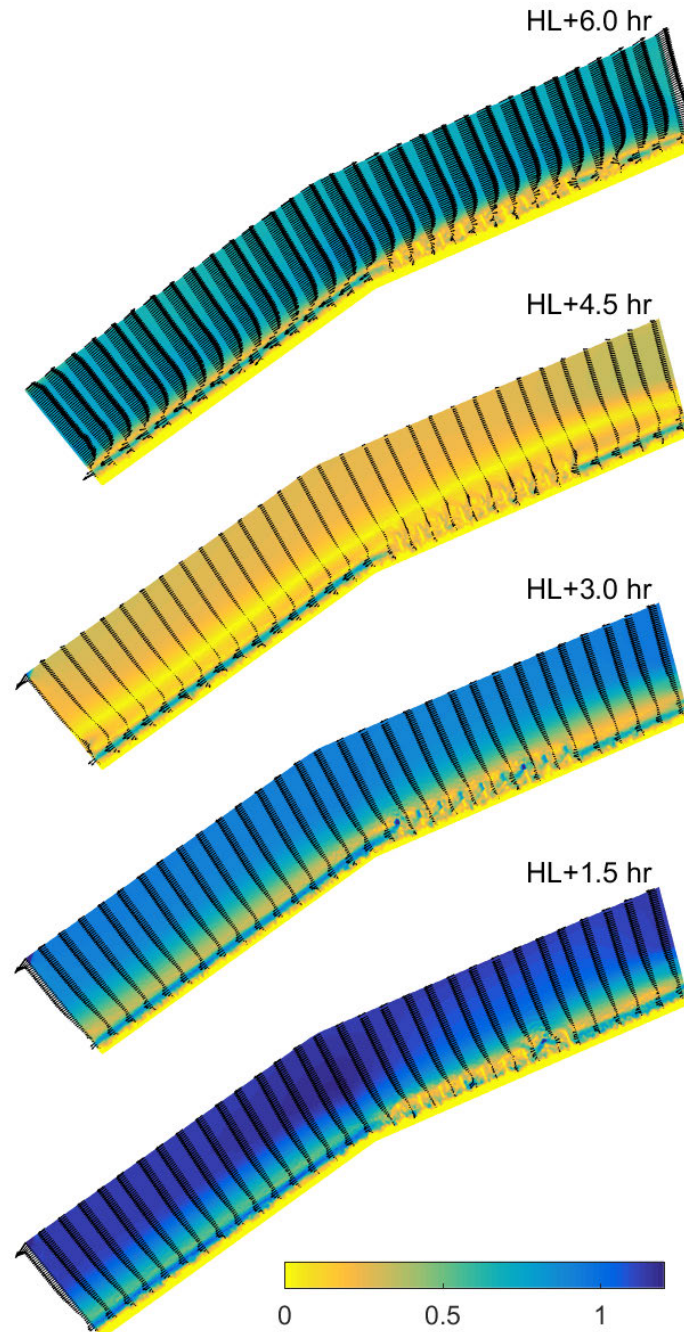
Figure 47 – Contour plots of velocity magnitude and velocity vector fields for tidal flow every 1/8 of the half tidal cycle (tidal period equal to 12 hr) for case G003b.

Test case G003b indicates that the width of the wave driven currents is ≈250 m. Since the nearshore resolution considered in this case is 50 m, it provides a quite adequate level of accuracy. However, the flow within the groynes is not fully resolved as indicated in Figure 48 where flow results using meshes G003b (coarse) and G001b (fine) are compared. Possible high velocity vectors usually seen onto the position of the groynes can be explained by the drying/flooding occurring onto the groynes.
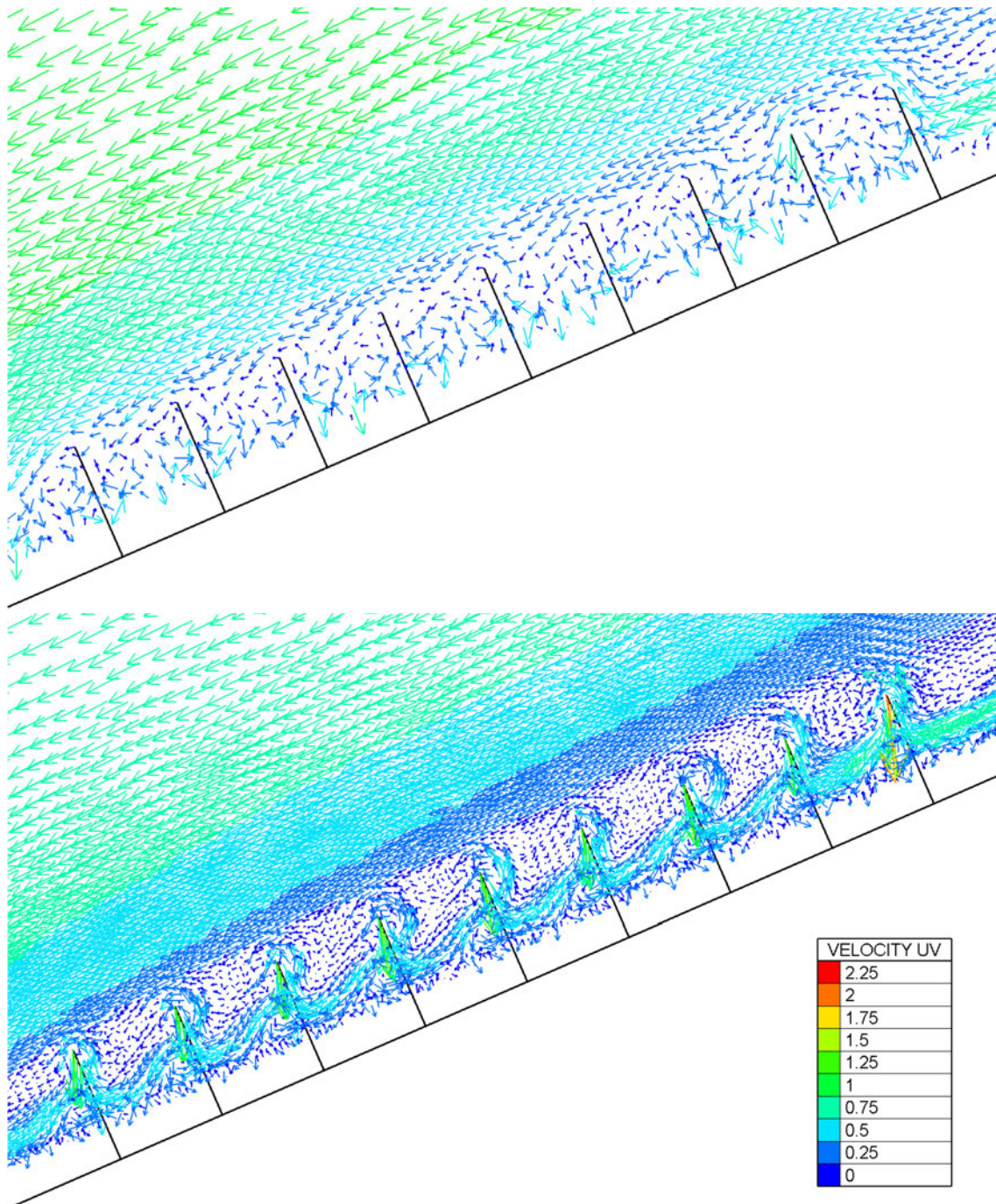
Figure 48 – Snapshot of the velocity vectors in the vicinity of the groynes for case G003b (upper figure) and G001b (lower figure) for coarse (50 m resolution nearshore) and fine meshes (25 m), respectively, at the same time instance.

Full hydrodynamic results from test case G001b for a finer resolution of 25 m in the nearshore, for coupled TELEMAC-2D and TOMAWAC simulation are shown in Figure 49. The results demonstrate no significant difference for the representation of the wave driven currents in terms of width and velocity magnitude. However, the flow resolving near the groynes requires this level of refinement as demonstrated before. This can provide us with the conclusion that a resolution of 25 m will be adequate to account for the nearshore flow in domains with similar geometric characteristics with the Belgian coast.

The above test cases have been simulated for different incident wave directions. In some cases, shear instabilities have been observed in the wave-driven longshore current. As it can be seen at Figure 50 for test case G001c simulated with incident waves from the north-west (NW) it appears that eddies between the longshore current and the outer flow concerning the horizontal velocity. Those values were reported also by Roelvink and Reniers (2011). The cross-shore distribution of the wave-driven longshore current may allow low-frequency modulations in the horizontal velocities. Sometimes the velocity perturbations can grow, resulting in the shear instabilities expressed in terms of vortices like those demonstrated here.

It must be highlighted at this point that no such behaviour has been observed in simulations with coarse meshes. This is an additional indication that a resolution of 25 m is necessary for accurate capture of the flow features.
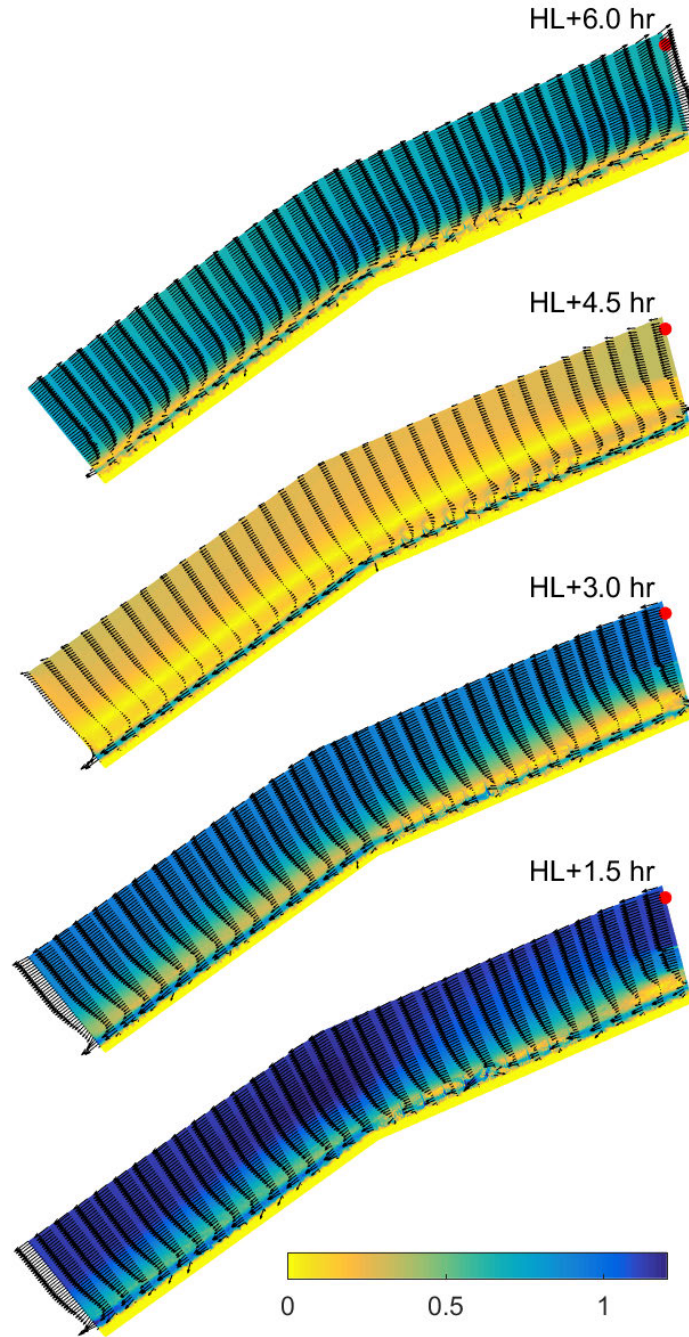
Figure 49 – Contour plots of velocity magnitude and velocity vector fields for tidal flow every 1/8 of the half tidal cycle (tidal period equal to 12 hr) for case G001b.
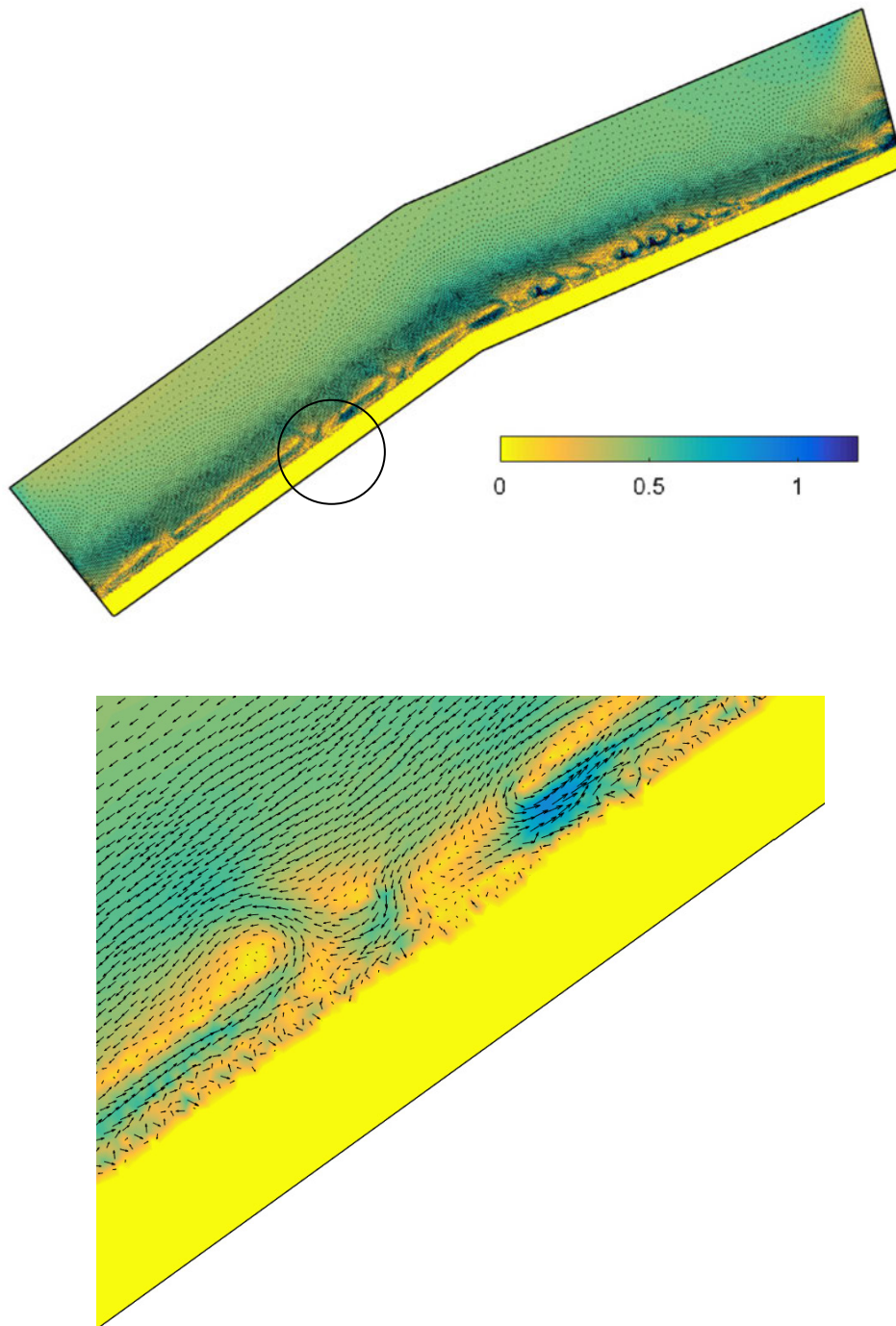
Figure 50 – Up: Shear instabilities observed in the west side of the nearshore domain for case G001c with incident waves and wind from north-west (NW). Down: detail of the velocity vector field in the vicinity of the observed shear instabilities.

Application parameters and results for coupled TELEMAC-2D - TOMAWAC - SISYPHE simulation

Simulation parameters for SISYPHE

The ultimate target of the TEL2TOM approach is to simulate bed morphology evolution under the influence of tide and waves. Consequently, the previous simulation for the coarse grid (case G003b) is repeated with the SISYPHE module active.

For the preliminary bed morphology simulations, we consider sediment of diameter equal to 300 μm and various bedload transport formulas (see Table 16) including Soulsby & van Rijn (Soulsby, 1997), Soulsby (1997) and van Rijn 2007 (Leo C. van Rijn *et al.*, 2007). The morphodynamic factor is set equal to 1. A spin up period of one day is considered before switching on SISYPHE in order to avoid cold start instabilities and velocity gradients. Finally, non-erodible beds for the groynes and the East and West TELEMAC-2D domain edges have been defined.

A full parametric investigation has been conducted since high velocity values occur on the groynes as a result of drying and flooding, which results in intense erosion/deposition for SISYPHE and instabilities in TOMAWAC. Different options for consideration of tidal flats and minimum depths have been examined. It was concluded that only the FREE SURFACE GRADIENT COMPATIBILITY equal to zero could provide the most stable results throughout the simulation. The key idea behind this option is that the free surface gradient has a linear part and a piecewise constant part. This consideration aims at breaking the rigorous compatibility between water depth and velocity components which verify the continuity equation. Thus, spurious oscillations that can appear in areas with high topographic gradients can be dampened.

Table 16 – Bed morphology simulations based on case G003b (coarse mesh).

Case	MIN. DEPTH FOR BEDLOAD	SLOPE EFFECT (Koch & Flokstra, 1981)	Coupling period TELEMAC-2D - TOMAWAC	Bedload transport model
H003a	10 cm	-	30 min	Soulsby & van Rijn - 5
H003a_1	10 cm	1.3	30 min	Soulsby & van Rijn - 5
H003a_2	10 cm	5.0	30 min	Soulsby & van Rijn - 5
H003b	20 cm	-	30 min	Soulsby & van Rijn - 5
H003c	50 cm	-	30 min	Soulsby & van Rijn - 5
H003a_1a	10 cm	1.3	15 min	Soulsby & van Rijn - 5
H003a_1b	10 cm	1.3	6 min	Soulsby & van Rijn - 5
H003a_1_Bail	10 cm	1.3	30 min	Bailard - 8
H003a_1_VR07	10 cm	1.3	30 min	van Rijn 2007 - 71 (addition)

Moreover, the effect of several parameters was examined in the bed morphology results. Firstly, different values for MINIMUM DEPTH FOR BEDLOAD were tested, namely 10 cm (case H003a), 20 cm (case H003b) and 50 cm (case H003c), to cancel sediment fluxes to and from dry points.

(a)

(b)

(c)
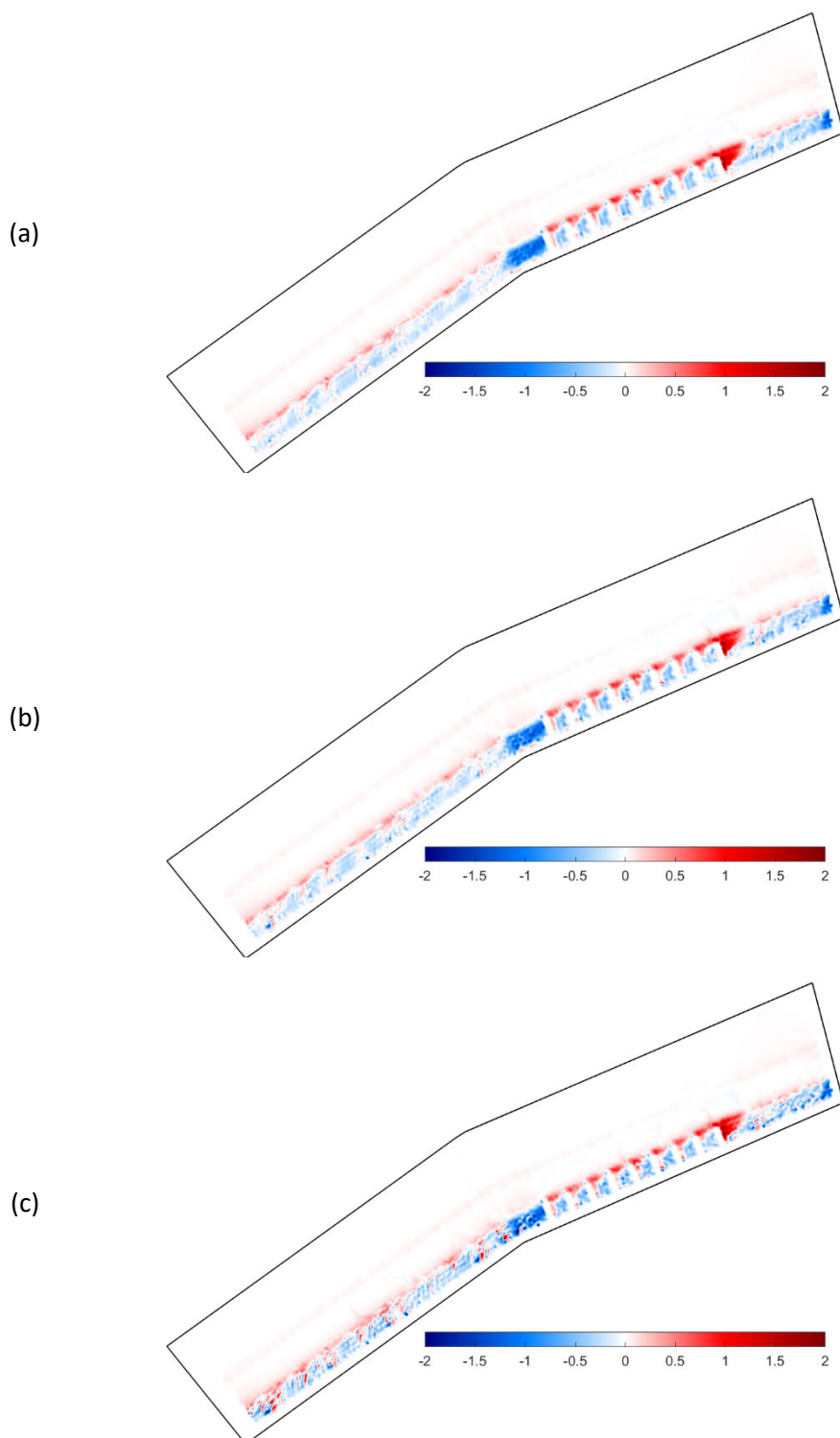
Figure 51 – Contour plots of bed evolution in the end of the simulation for different values of MINIMUM DEPTH FOR BEDLOAD (from top to bottom): (a) 10 cm (case H003a), (b) 20 cm (case H003b) and (c) 50 cm (case H003c)

The simulation results for different values of MINIMUM DEPTH FOR BEDLOAD are shown in Figure 51. It can be seen that consideration of higher minimum values of minimum depths result in more intense patterns of erosion/deposition in the nearshore region except the region of the groynes, even within the very limited amount of morphodynamic time of 12 days considered here. This indicates that consideration of a reasonable minimum depth can result in avoiding cases of unnatural erosion/deposition, but higher values can possibly intensify those phenomena.

Next investigation was conducted by switching on the SLOPE EFFECTS, using the model by (Koch & Flokstra, 1981). Two different beta parameters were examined, beta=1.3 (default) case H003a_1, beta=5.0 case H003a_2 and the results were compared with case H003a without slope effects. It must be mentioned at this point that for all the morphodynamic simulations, SEDIMENT SLIDE option has been switched on with a threshold at 40° angle (default value). Nevertheless, this option has no effect due to the mild slopes in the considered domain.

(a)

(b)
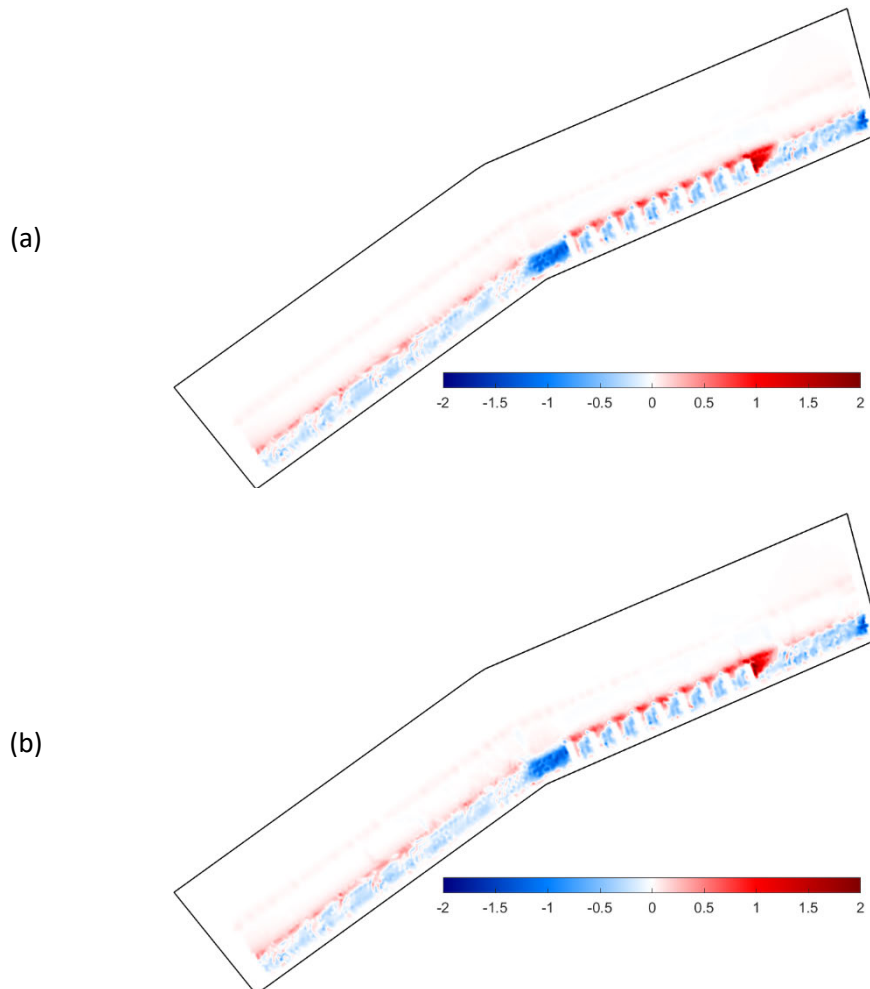
Figure 52 – Contour plots of bed evolution in the end of the simulation for different values of beta parameter in (Koch & Flokstra, 1981) model for slope effects: (a) beta=1.3 (case H003a_1) and (b) beta=5.0 (case H003a_2).

It appears in Figure 52, that the effect of this parameter is also not intense, since only minor depositions in the west coast occur considering a higher value of beta parameter. For beta=1.3 which is the default value of the slope effect model, there is no difference between this case and case H003a that does not consider slope effects.

Finally, the results of three different bedload transport models suitable for combined effect of waves and currents is examined at this point: Soulsby & van Rijn (Soulsby, 1997) in case H003a_1, (Bailard, 1981) in case H003a_1_Bail and van Rijn 2007 (Leo C. van Rijn *et al.*, 2007) in case H003a_1_VR07, that was programmed in addition to the existing bedload transport models. Figure 53 demonstrates the erosion/deposition patterns for the three different runs.

(a)

(b)

(c)
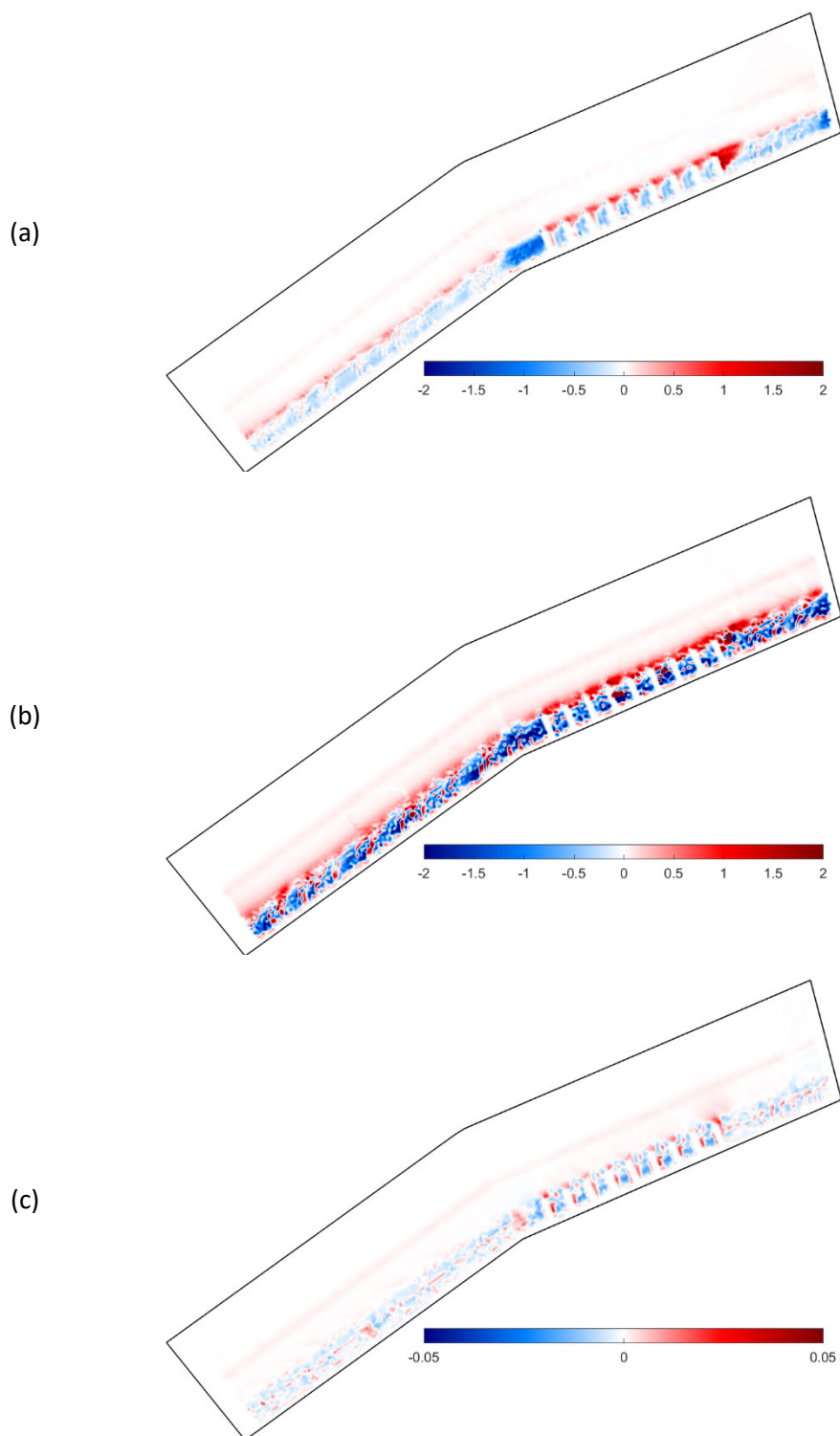
Figure 53 – Contour plots of bed evolution in the end of the simulation for different bedload transport models: (a) Soulsby & van Rijn, (b) Bailard and (c) Van Rijn 2007

The model of Bailard demonstrates the highest erosion/deposition patterns, whereas the van Rijn 2007 formula shows the smallest patters (order of maximum ±5 cm) compared to the model of Soulsby & van Rijn. Notice that this is in line with the findings for the migrating Gaussian hump in Section 2.1.1.

The significant differences between the transport formula emphasise the importance of validating the model for real cases whenever there are available data. This way there will be a more correct choice of bedload transport model, suitable for the area of study.

2.2.4 Application of the TEL2TOM functionality in the idealised model: applying different grid resolutions for the wave and the hydrodynamic model

In this section, the most updated results of the TEL2TOM functionality for linear interpolation between the nodes of TELEMAC-2D and TOMAWAC domains is applied in the idealized model for the Belgian coast. This allows the use of a coarser TOMAWAC grid combined with a high resolution TELEMAC-2D grid. This combination allows for a cost-efficient coupled model without compromising on accuracy, which is required for long term morphological modelling of the coastal zone.

The reader is referred to (Breugem *et al.*, 2019), which has been presented at the Telemac User Conference 2019 and is included in the appendix of the Final report Wave propagation model. This article provides further information on the implementation of the functionality. In addition, it is utilized within Scaldis-Coast model which will be discussed in detail in chapter 5.

Table 17 – Simulation cases of the idealized model using the TEL2TOM functionality.

Test case	TELEMAC-2D min grid size (m)	TOMAWAC min grid size (m)	TELEMAC-2D num. of nodes	TOMAWAC num. of nodes	Simulation time (hours)
C1	50	50	7161	11650	3.35
C2	25	25	24332	33251	10.87
C3	25	50	24332	11650	3.08

Application of TEL2TOM has been implemented in the idealised model. A TOMAWAC domain has been considered by offsetting the open boundaries of the TELEMAC-2D domain by ≈5.0 km. Three different cases have been considered including coarse meshes (minimum grid size 50 m) for TELEMAC-2D and TOMAWAC (C1), fine meshes (minimum grid size 25 m) for TELEMAC-2D and TOMAWAC (C2), and one case with fine TELEMAC-2D mesh and coarse TOMAWAC mesh (C3) as shown in Table 17. The bathymetry of the idealised case and the coarse meshes are shown in Figure 54. In the testcases C1 and C2 although the models have a different stretch for the wave and hydrodynamics, inside the boundaries of the TELEMAC-2D model, the grid nodes of the two models coincide. In the C3 testcase, both grids are completely independent.
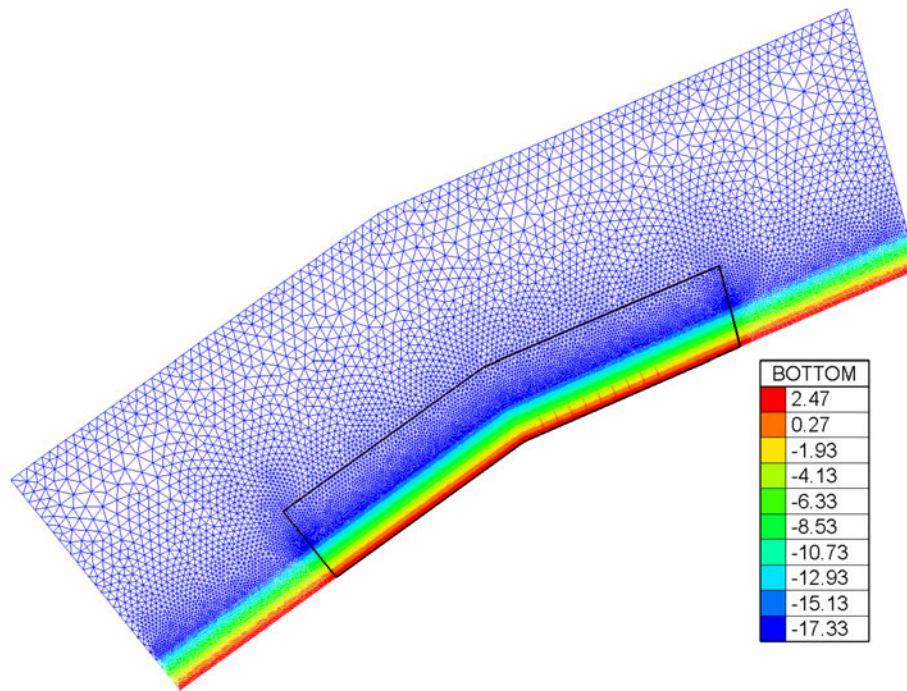
Figure 54 – TOMAWAC domain and mesh for test case C1. TELEMAC-2D domain area is indicated with black solid line.

The tidal data occurred from assigning a sinusoidal tide along the offshore boundary of the TELEMAC-2D domain (indicated with black line in Figure 54). The wave data for TOMAWAC occurred by considering waves with significant wave height equal to 2 m and peak wave period equal to 6.32 s coming from north. In addition, constant wind has also been considered from north with wind velocity -12.24 m/s. The total simulation time was equal to ≈13 days.
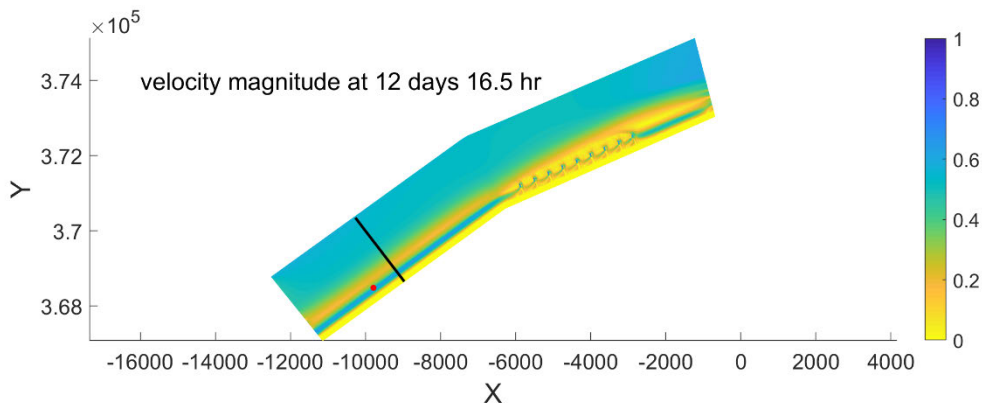
Figure 55 – Snapshot of the velocity magnitude after 12d 16.5h of full simulation of tides and waves for test case C3. Black line corresponds to the cross-shore section considered for comparing the hydrodynamic data for each test case. Red point corresponds to the location considered to compare timeseries of velocity magnitude for each test case.

The objectives of the above mentioned set of simulations are to determine the reduction of the simulation time along with the level of accuracy in representing the wave driven currents in the west side of the nearshore area. It has been already known that the resolution in the vicinity of groynes is as accurate as the level of refinement increases around the groynes, which is not within the objectives of this group of simulations.

Figure 55 depicts a snapshot of the velocity magnitude in the TELEMAC-2D domain. In the west nearshore area, a first impression of the wave-driven currents is given. In addition Figure 56 gives cross-shore profiles of the velocity magnitude for test cases C1 (coarse meshes for TELEMAC-2D and TOMAWAC), C2 (fine meshes for TELEMAC-2D and TOMAWAC) and C3 (fine mesh for TELEMAC-2D and coarse mesh for TOMAWAC). It can be concluded that the results occurring with case C3 demonstrate discrepancies smaller than 5% with those of case C2. In this case we can conclude that TEL2TOM functionality works properly and that it can accurately reproduce velocity magnitudes in the nearshore region and thus, the occurring wave-driven currents.
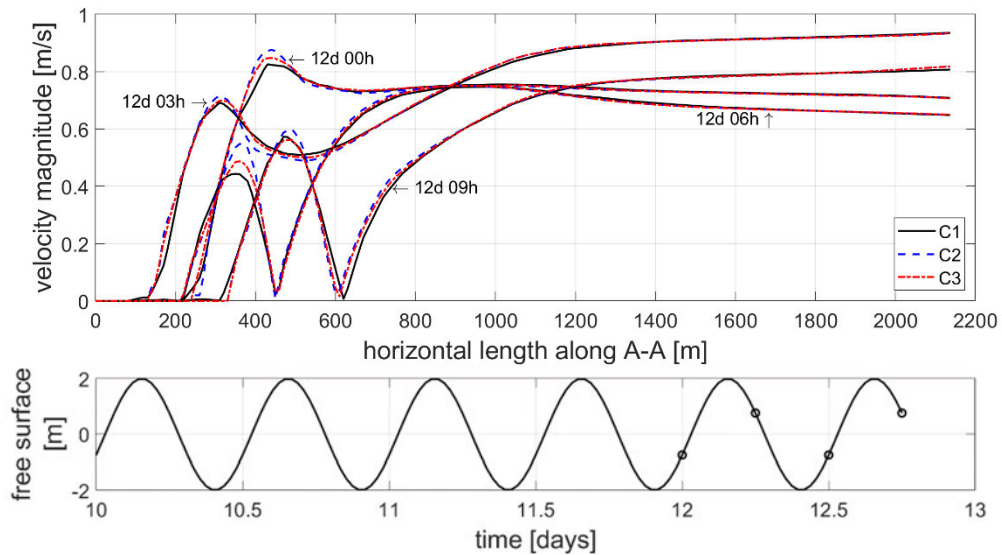
Figure 56 – Upper figure: Cross-shore profiles (section indicated with black solid line in Figure 55) of the velocity magnitude within fractions of one tidal cycle for test cases C1 (black solid line), C2 (blue dashed line) and C3 (red dash-dotted line). Lower figure: tidal signal in the offshore boundary of the section (solid line) and time instants of the fractions of the tidal cycle (black circles).

Moreover, based on the above-mentioned profiles, we have taken timeseries of the velocity magnitude in one location indicated with a red point in Figure 55. The results shown in Figure 57 and we can see that TEL2TOM configuration results (case C3) demonstrate much smaller discrepancies with the case C2 of the fine meshes, especially in capturing the troughs and the second harmonic of the timeseries. The bars are clearly captured with almost zero discrepancy.
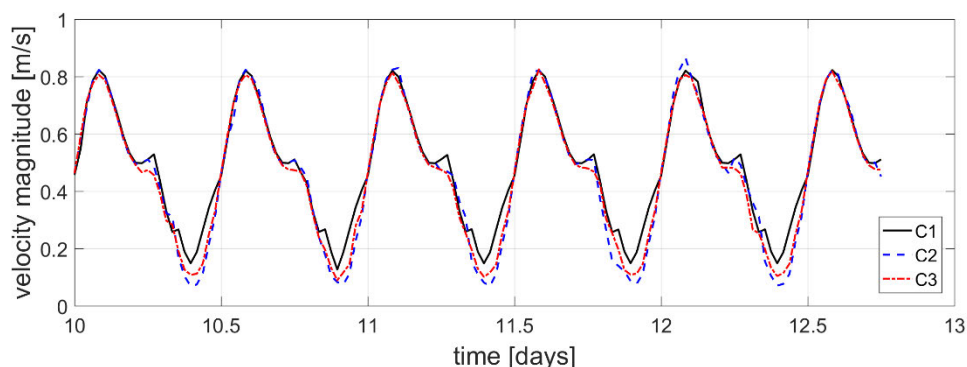
Figure 57 – Timeseries of velocity magnitude at a specific location 370 m far from the coastal boundary of TELEMAC-2D domain) for test cases C1 (black solid line), C2 (blue dashed line) and C3 (red dash-dotted line).

From the above mentioned analysis, it can be safely concluded that the TEL2TOM functionality can be a tool that can provide stability in the hydrodynamic results (wave-driven currents) by considering a much coarser TOMAWAC domain. This can also contribute in significant level of computational speed up (see Table 17). It can be observed that the required time for simulating case C3 is even smaller than the time for case C1. This is based on the fact that with the coarse TOMAWAC grid and the accurate hydrodynamic input of TELEMAC-2D, the required number of iterations for the source terms is kept low at the same level for the two test cases.

2.2.5   Conclusions

On Neumann Boundary conditions:

- The implementation of the Neumann boundary conditions for the connection of offshore with the nearshore boundaries combined with providing the water level as offshore boundary condition appears to give reliable results for tidal currents.
- For the validation case against Mariakerke flow data, the use of Neumann boundary conditions in the lateral boundaries allows to capture the nearshore flow velocities due to the tide at a satisfactory level.
- The coupling of TELEMAC-2D and TOMAWAC still can create local instabilities in the solution on the boundaries that the Neumann conditions are implemented. These instabilities come from the incompatibility of boundary conditions for TELEMAC-2D and TOMAWAC (in .cli files). However, these instabilities don't tend to be advected into the inner model domain, i.e. the domain of interest, nor do they tend to grow in time to blow up the simulation. But they can affect on the longer term the bed evolution inside the domain of interest in case of a morphodynamic run. The TEL2TOM module can overcome this boundary instabilities by selecting a larger domain for the wave model than for the hydrodynamic model.
- Concerning the quantification of marine currents measured by the drifters deployed in the campaign of 11/06/2012, it appears that the results are different than the depth average velocities. This happens because drifters measure only at a level -1 m from the free surface. Wave data coming from a buoy places far from the area of interest may also contribute in the observed deviations. It appears that consideration of wind is not modifying significantly the wave driven currents for this testcase.

On the implementation of TEL2TOM with an extended wave domain:

- The application of the TEL2TOM model for the idealized model of the Belgian coast managed to minimize the disturbances in the velocity field of the TELEMAC-2D domain in the region of the side boundaries. This occurs because TELEMAC-2D and TOMAWAC have different domains and communicate only the required information for the proper coupling, without applying incompatible boundary conditions in the same boundaries as it used to happen.
- Test cases conducted for different resolution of the TOMAWAC domain indicated that there is almost a 1:1 relationship between the number of TOMAWAC grid nodes increase and CPU time increase.
- It can be concluded that a nearshore resolution of 25 m can be sufficient to accurately reproduce the wave driven currents in terms of the width and velocity magnitude in the nearshore of a straight coastline. Finally, the flow between the groynes is represented with more detail the higher the grid resolution is. However, it requires further investigation to determine the max required grid resolution to reproduce fully the flow patterns.
- For simulation of bed morphology evolution, it appears that the TEL2TOM approach results in eradication of unnatural erosion/deposition patterns gathering at boundaries like those observed in previous simulations considering the same domains for TELEMAC-2D and TOMAWAC. Different bedload transport model, produce different levels of bed evolution, even for the small morphodynamic time examined.

On the implementation of TEL2TOM for different grid resolutions:

- The application of the TEL2TOM model for the idealized model of the Belgian coast can provide accuracy in the hydrodynamic results (wave-driven currents) and substantial speed up, attributed to considering a much coarser TOMAWAC domain. The combination of a fine TELEMAC-2D domain coupled with a coarse TOMAWAC domain resulted in lower number of required iterations for the source terms.

3   Representative tide

An input reduction technique named as 'representative tide' is implemented for the generation of simplified tidal forcing suitable for the long-term morphological simulations performed by Scaldis-Coast model.

3.1   The representative tide concept

The reduction of hydrodynamic input data of a tide-dominated numerical model aims to contribute in the computational cost reduction by finding a satisfactory way to represent a long tidal period by only one (or a small number of) 'representative' tide(s). The concept of input data reduction in long-term morphological simulations under tidal action followed here, was proposed and successfully implemented by Latteux (1995). According to Latteux, this representative tide must lead to the same elementary (flood and ebb) and residual transport as the actual set of natural tides.

The numerical experiments reported in Latteux (1995), were performed also by TELEMAC-2D (one of its earliest versions) coupled with a morphology module known as TSEF. In those experiments it was found that the predicted bed evolution of a yearly tidal cycle, for the case of a schematized estuary, compared quite well to the one resulting from a schematized forcing of one year using one representative or else 'morphological' tide. The representative tide found to be in between mean tide and mean spring tide. More recently the representative tide technique was also implemented for the calibration of the Oostende-Knokke hydrodynamic and sediment transport model (OKNO) by Zimmermann *et al.* (2013).

Apart from the input reduction, the technique of representative tide helps in the safer increase of the morphological time-step, when this is implemented through a morphological acceleration factor (MOFAC). This is because, applying a relatively high MOFAC in morphodynamic simulations forced by realistic hydrodynamic climate, affects substantially the chronology of events resulting into unrealistic clustering of high-impact events that may lead, in turn, to non-reversible, unrepresentative changes. Thus, using morphological acceleration coupled with the implementation of a representative tide decreases the unwanted effects of chronology.

3.2   Coupling TELEMAC-2D & SISYPHE: Model set-up

The procedure for the extraction of the representative tide described in the previous section, is implemented in the present study by coupled simulations of TELEMAC-2D with SISYPHE. The aim is to select a reduced tidal forcing suitable for the evaluation of the morphodynamic model.

3.2.1   Basic settings

The coupled hydrodynamic and the morphodynamic simulations are performed on a common computational grid of Scaldis-Coast model. The coupling of the two modules takes place at every time-step of the computation (COUPLING PERIOD FOR SISYPHE=1), or in other words, the hydrodynamic and the morphodynamic time-steps are identical. Note that the latter statement is valid only for the simulations where no morphological acceleration is considered.

The settings of the calibrated hydrodynamic model, presented in chapter 3 of the Progress Report 3 (Kolokythas *et al.*, 2018b), are also applied in the present coupled simulations. Table 18 summarizes the most important settings of both modules, TELEMAC-2D and SISYPHE. Note that the coupling of the hydro- and morphodynamic modules initiates after a spin-up of the hydrodynamic module for a short simulation period of four days, so that a fully developed flow field occupies the computational domain.

As for the computational time, the coupling of the hydrodynamic module with the morphodynamic one does not cost much more than a standalone hydrodynamic simulation, as long as one of the total load formulae is applied for the sediment transport calculation and, thus, suspended load is not calculated separately. In this case a typical morphodynamic simulation of one year takes around 22 hours on 32 CPUs. On the other hand, the computational time is doubled if the advection-diffusion equation for suspended load is solved. Notice that only tide is considered for these simulations. The model is not yet coupled with a wave model, which is by far the most expensive part of the simulation.

Table 18 – Main settings of the morphodynamic Scaldis-Coast model.

	Parameter	Value
TELEMAC-2D	Time step	10 s
	Initial conditions	developed flow field after spin-up of 4 days
	Version of TELEMAC	TELEMAC V2P2R2
	Wind	On
	Coriolis / coefficient value	YES / $1.13522 \cdot 10^{-4}$ s^{-1}
	Salt transport	Off
	Roughness formula	Manning
	Bed roughness value	varying roughness distribution (run D18)
	Option for treatment of tidal flats	1: equations solved everywhere with correction on tidal flats
	Treatment of negative depths	2: flux control
	Free surface gradient compatibility	0.9
	Horizontal turbulence model	4: Smagorinski
	Scheme for advection of velocities	1: method of characteristics
	Scheme for advection of depth	5: conservative scheme
	Scheme for diffusion of velocities	1: implicit (1 is default; 0 cancels the diffusion)
	Solver	7: Generalized Minimum Residual (GMRES) method
SISYPHE	Total load transport formula	30: (Engelund & Hansen, 1967)
	Suspension	NO
	Slope effect	YES
	Formula for slope effect	1: Koch & Flokstra (1981) / BETA = 1
	Median grain diameter (D_{50})	250 μm

3.2.2   Simulation period

The simulation period covers almost the whole year 2014 (from 06/01/2014 to 31/12/2014) in order to extract the representative tide of the specific year.

3.2.3   Offshore boundary conditions

The hydrodynamic model is forced by time-series of the water level and velocities (of time-step equal to 10 minutes) calculated by the ZUNOv3 model. A correction of the harmonic components is calculated based on the comparison of the harmonic components of the ZUNO results and measurements for a period of the year. The correction is based on the average differences in harmonic components (ZUNO vs. measurements) found for several stations in the Belgian and Dutch Coastal zone for the M2, M4, S2 phases (see Table 19). After decomposition and correction, the water level signal is re-synthesized in order an unbiased time series to be applied at the boundary of Scaldis-Coast model. Note that for the year 2014 there was no need for correction of the zero harmonic (Z0) component.

Table 19 – Correction of harmonic components of water level variation for the year 2014.

Harmonic component	Correction
Phase M2	+4°
Phase M4	-6°
Phase S2	+5°

3.2.4   Wind forcing

Wind time series presented in Figure 58 is imposed uniformly on the computational domain through the subroutine meteo.f. For the parameterization of the wind drag the formulation of Flather (1976), default in TELEMAC2D, was employed.
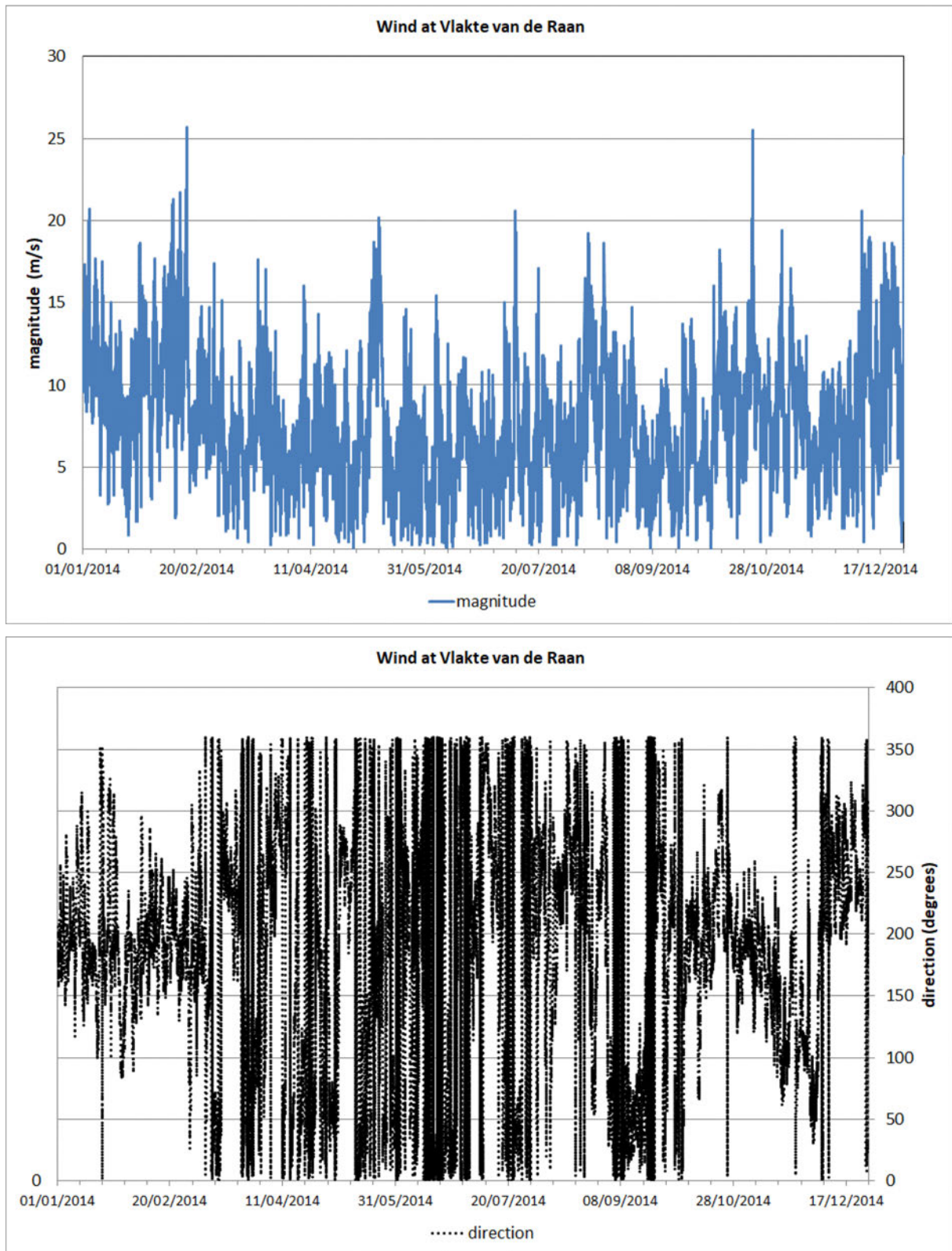
Figure 58 – Wind magnitude (above) and direction (below) time series at Vlakte van de Raan for the year 2014.

3.2.5   SISYPHE Inflow/Outflow boundary conditions

No bottom change is considered at the inflow boundaries. According to the SISYPHE manual, at the outflow boundary, bedload doesn't require any particular boundary condition. In case the advection-diffusion equation is solved for the suspended load concentration, a zero gradient condition is applied at the outflow boundaries.

3.3   Representative tide selection

The criterion for the selection of the representative tide of the considered year (2014) is the best agreement between the mean sediment transport, resulting from the tested representative tide and the one from the yearly water level time-series. Specifically, the procedure includes to following steps:

- The coupled hydrodynamic and sediment transport model is run for the considered simulation period of one year, imposing frozen bottom, i.e. no bottom updating, and without imposing morphological acceleration (MOFAC=1).
- The two components of the sediment transport rate, Q_x and Q_y (x and y directions) are calculated at every single node of the domain and summed at every time-step of the calculation.
- The two components of the mean sediment transport rate, Q_{xmean} and Q_{ymean}, are calculated by averaging the instantaneous sediment transport rates for each set of two consecutive tidal cycles covering the full year 2014.
- Finally, the set of two tides which best represents the magnitude (lowest RMSE) and the patterns (high correlation) of each of the yearly mean Q_x and Q_y components is selected.

Thus, when we refer to the representative tide we actually mean two successive tides and a time period of 24 hours 50 minutes. Note also that using the mean sediment transport rate as a criterion for the selection of the representative tide is equivalent as using the net sediment transport, as the first can be easily converted to the second by simply multiplying it by the duration of the period of averaging.

In Figure 59, the yearly averaged and the representative tide-averaged sediment transport rate Q_x are shown in the top and the bottom plot, respectively. The same plots for the y-component of the mean sediment transport (Q_y) are shown in Figure 60. Visual inspection of the two figures shows that the sediment transport patterns are in excellent agreement. This observation is also valid for the sediment transport magnitude. The set of the two consecutive tides selected as the representative tide are found to be in between the neap and the spring tide dating at the beginning of August (from 31/07/2014 23:30 to 02/08/2014 00:20) as shown in Figure 61 for a computational node close to Westhinder station (Tide No. 202). At the specific location the mean tidal range of the representative tide equals to 3.71 m, which is somewhat larger than the yearly mean tidal range that equals 3.63 m.
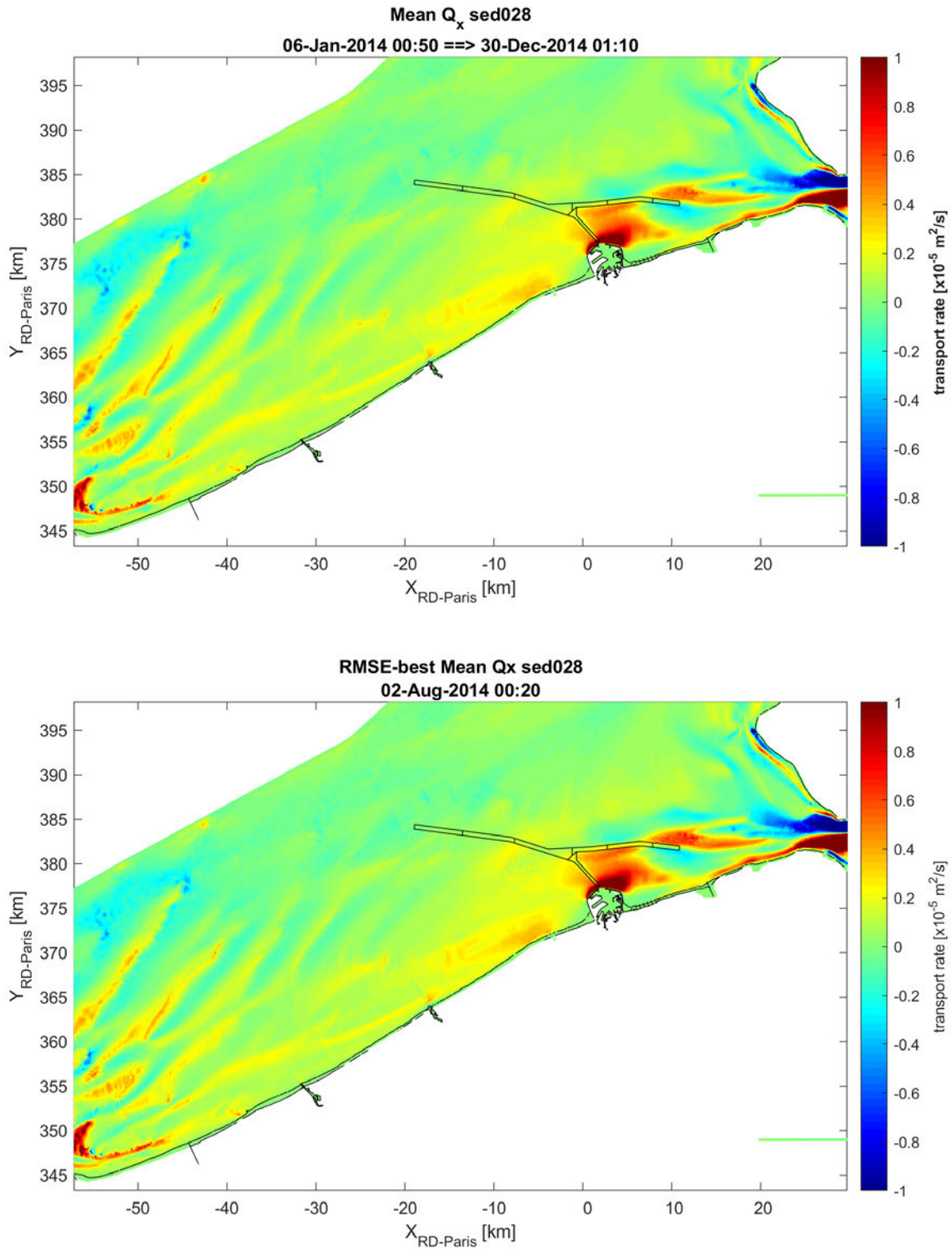
Figure 59 – Yearly averaged sediment transport rate Q_x (above) and the representative tide-averaged Q_x (below).
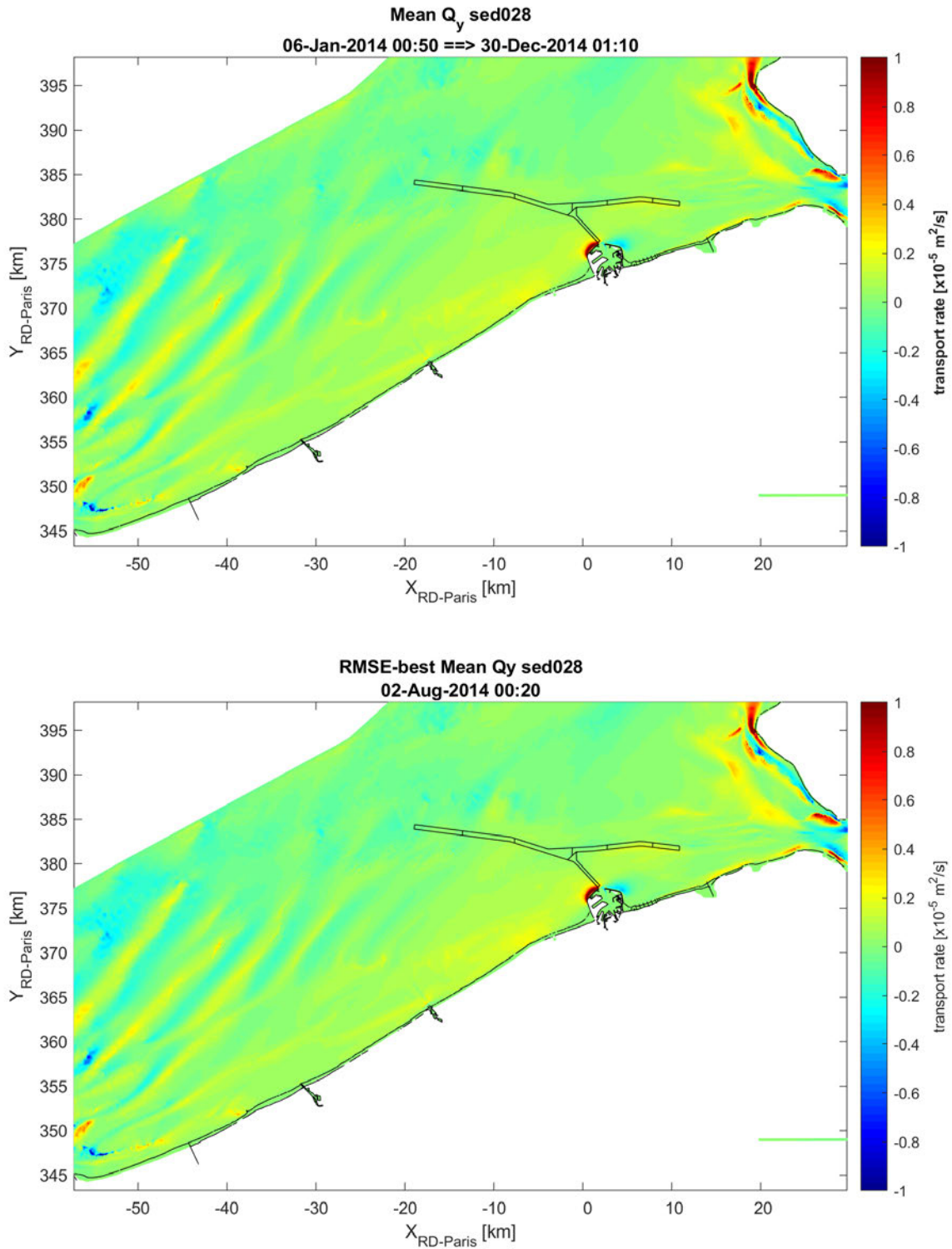
Figure 60 – Yearly averaged sediment transport rate Q_y (above) and representative tide-averaged Q_y (below).
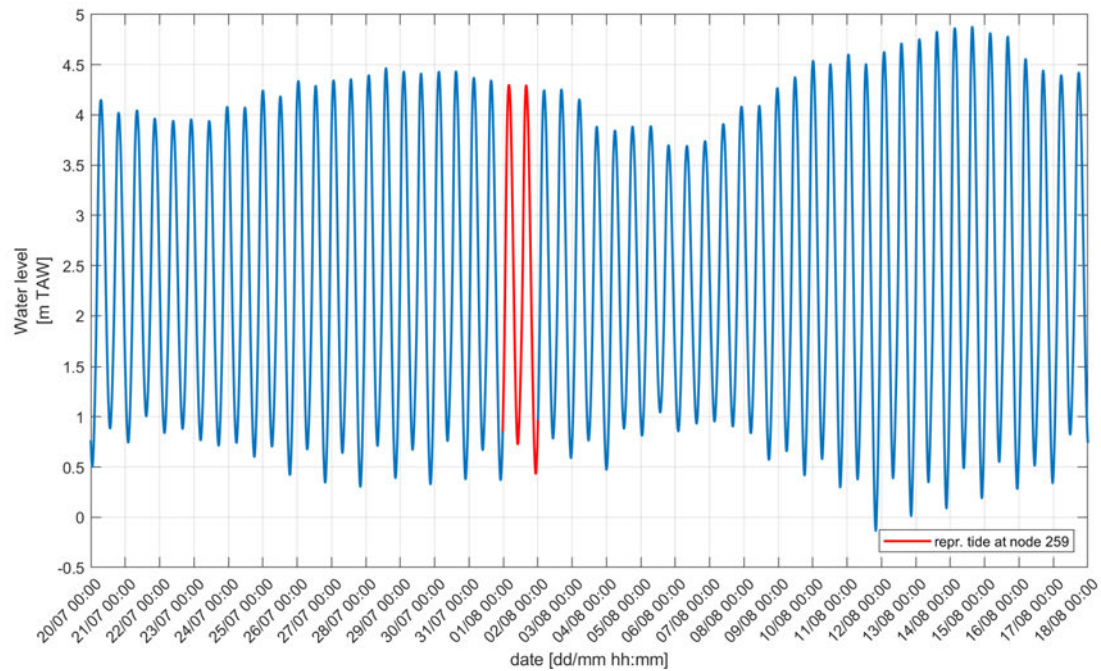
Figure 61 – Tidal variation for a full spring-neap tidal cycle that contains the selected representative tide (set of two successive tides) at a computational node close to Westhinder station.

As mentioned before, the criterion for the selection of the representative tide was the Root Mean Square Error (RMSE) in the comparison of the yearly averaged and tide-averaged sediment transport rates. In Figure 62 the results of this comparison are depicted for the two components Q_x and Q_y in the two top plots. It is found that the tidal cycle with the lowest RMSE for both Q_x and Q_y leads to very high (Pearson's) correlation coefficients (R) too. The highest R values are achieved for another tidal cycle (number 87) but they are only slightly different than those corresponding to the lowest RMSE values, as shown in the bottom plots of Figure 62. In the latter plots, it is shown that the magnitudes of the sediment transports are not any more in very good agreement as previously.

Note that this comparison was performed only for the computational nodes located in the subdomain depicted in Figure 59 and Figure 60, which corresponds to an extensive area of interest of this study. Moprhological changes beyond the French border, at the Eastern Scheldt, or at upstream Western Scheldt are excluded from this study.

The Pearson's correlation coefficient of two random variables is a measure of their linear dependence. If each variable has N scalar observations, then the Pearson correlation coefficient is defined as

$$R(A, B) = \frac{1}{N-1} \sum_{i=1}^{N} \left(\frac{\overline{A_\iota - \mu_A}}{\sigma_A} \right) \left(\frac{B_i - \mu_B}{\sigma_B} \right)$$

where μ_A and σ_A are the mean and standard deviation of A, respectively, and μ_B and σ_B are the mean and standard deviation of B.
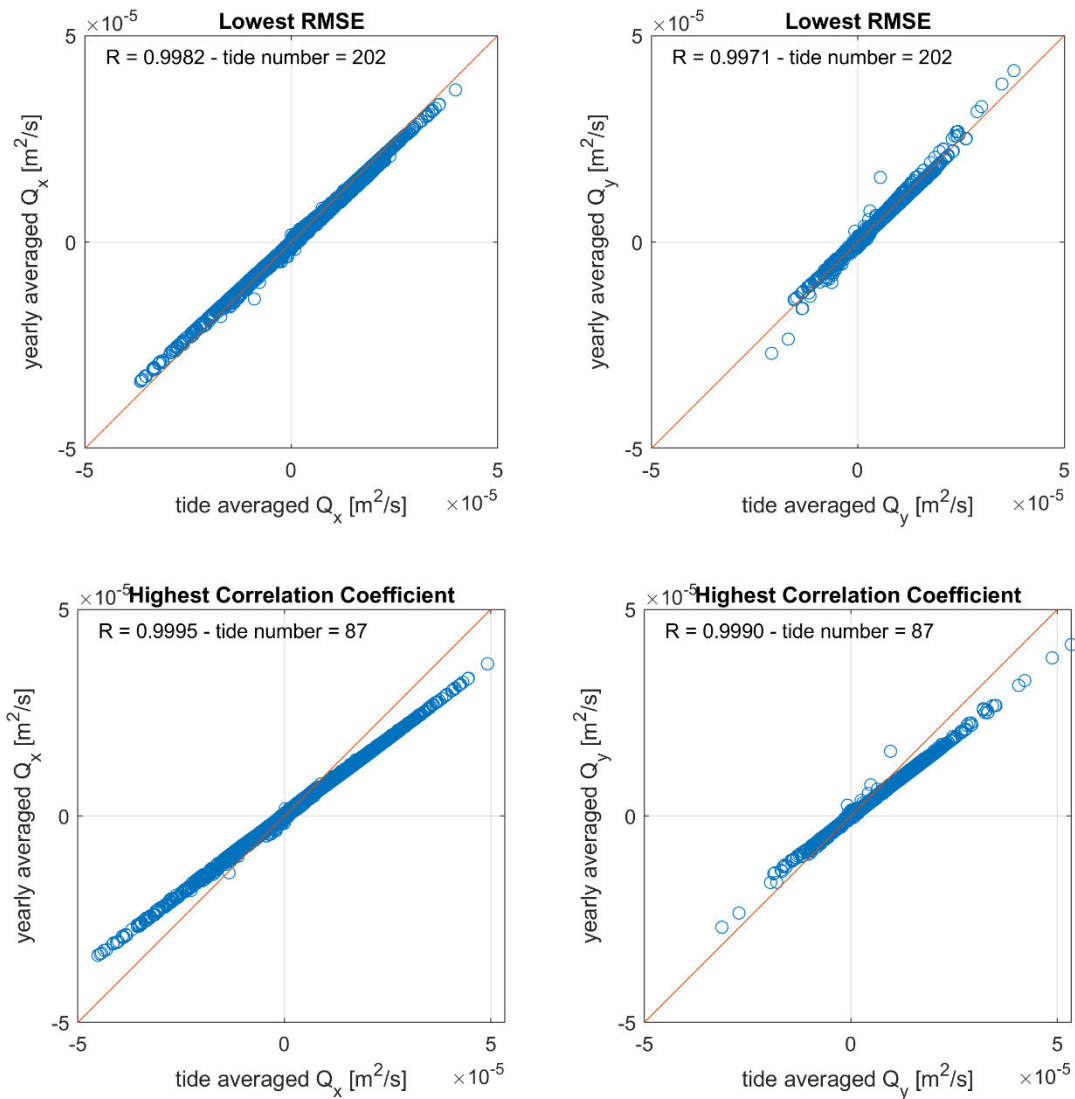
Figure 62 – Node to node comparison of yearly averaged vs. tide-averaged sediment transport rates Q_x (left plots) and Q_y (right plots) for the tidal cycle that leads to lowest RMSE (top plots) in bed evolutions and the tide that gives the best correlation between the bed evolutions (bottom plots).

The same procedure for the selection the representative tide was repeated considering other available total load (bed load and suspended) formulas in SISYPHE, in order to investigate their influence on the selection of the appropriate representative tide. To this end, apart from the Engelund & Hansen formula (Engelund & Hansen, 1967), the formula of Van Rijn (Leo C. van Rijn *et al.*, 2007) and the Bijker's formula (Bijker, 1992) were considered. In Table 20, the top 7 representative tides which performed better in fulfilling the aforementioned criterion of the lowest RMSE and simultaneously presenting high correlation coefficients, are shown for the three considered total load formulas. The selection of the most appropriate tidal cycle was repeated considering sediment transport rates within two different sub-domains of Scaldis-Coast, i.e., one large sub-domain that includes the offshore Flemish Banks and a smaller one that focuses on the area around Zeebrugge port and the mouth of Western Scheldt. For the large sub-domain, a general remark is that Engelund & Hansen and Bijker formula present similar 'preference' in representative tide (RT202), while for Van Rijn's formula the couple of tidal cycles dating from 11/06/2014 06:40 to 12/06/2014 07:30 (RT153) scores best.

For the small sub-domain, the three considered formulas show preference to RT137 (25/05/2014 17:20 to 26/05/2014 18:10). Precisely, RT137 is the second best (in terms of RMSE) for Van Rijn's formula, but still very close the one that scores best. Note that RT137 is also included in the top 5 of representative tides for all considered formulas in the large sub-domain calculation, meaning that it could potentially used also for the Flemish Banks morphodynamics study. On the other hand, RT202 could be considered in general when using Engelund & Hansen or Bijker's formula, but should rather be avoided when using formula of Van Rijn. Furthermore, RT153, should rather be avoided when Bijker's formula is considered. Lastly, it is worth mentioning that the higher RMSE values observed for Van Rijn's formula, compared to the other two formulas, are due to the fact that the first leads to substantially larger sediment transport rates than the other two.

Table 20 – Representative tide performance based on the lowest RMSE between the yearly-averaged and the tide-averaged sediment transport rate (Q_{mean}) for three total load formulae available in SISYPHE. Considered Scaldis-Coast subdomains for statistics: (1) Belgian continental shelf (sand banks included), and (2) Zeebrugge and Western Scheldt mouth area.

Belgian continental shelf (sand banks included); [x_{min}, x_{max}, y_{min}, y_{max}] = [-57.0, 30.0, 343.0, 397.0] (km)						
	Engelund & Hansen		**Bijker**		**Van Rijn 2007**	
Ranking	**Tide no.**	**RMSE x 10^{-7}**	**Tide no.**	**RMSE x 10^{-7}**	**Tide no.**	**RMSE x 10^{-7}**
1	202	2.70	202	2.76	153	6.61
2	172	2.92	172	2.88	173	7.48
3	*137*	2.93	153	3.01	80	7.49
4	153	2.95	*137*	3.11	172	7.80
5	143	3.26	143	3.17	*137*	8.34
6	173	3.26	173	3.38	144	8.56
7	203	3.36	80	3.48	202	8.70
Zeebrugge and Western Scheldt mouth; [x_{min}, x_{max}, y_{min}, y_{max}] = [-10.0, 40.0, 370.0, 398.0] (km)						
	Engelund & Hansen		**Bijker**		**Van Rijn 2007**	
Ranking	**Tide no.**	**RMSE x 10^{-7}**	**Tide no.**	**RMSE x 10^{-7}**	**Tide no.**	**RMSE x 10^{-7}**
1	137	3.03	137	4.17	80	8.18
2	203	4.50	*202*	4.81	137	8.42
3	80	4.87	203	5.29	173	9.35
4	*202*	5.09	80	5.66	88	9.68
5	153	5.13	173	5.83	*153*	10.02
6	173	5.14	172	5.92	203	11.27
7	144	5.57	144	6.05	116	11.41

3.4   Performance evaluation

After the selection of the representative tide, two morphodynamic simulations were performed in order to evaluate the performance of the selected representative tide:

- the morphodynamic simulation with the realistic tidal forcing of the year 2014 was repeated allowing bottom updating this time
- a morphodynamic simulation which was forced by a schematized tidal forcing of 357 successive representative tides for a simulation period of one year

Then, the sedimentation and erosion patterns at the end of the simulation period were compared in order to evaluate the performance of the reduced (schematized) forcing. The results from the case of the Engelund and Hansen formula are presented here as indicative of all the tested formulas.

The bed evolution after a full (realistic) year is shown in Figure 63, while the bed evolution difference between the reduced input simulation and the full year simulation is shown in Figure 64. The dashed box denotes the extensive area of interest, where statistical analysis for the evaluation of the reduced forcing took place. It can be observed that differences in the area of interest are limited. On the other hand, at regions of low resolution such as the French continental shelf and the entrance of Eastern Scheldt, which is characterized by high speed currents, there observed noticeable differences of order of magnitude ±0.5 m. Noticeable differences are also observed at some locations in the Western Scheldt. It is also reminded that these regions were not considered in the procedure of the representative tide selection.

In Figure 65, the comparison of bed evolution between the full-year forcing and the reduced forcing simulations is presented. The performance statistical parameters given in this figure confirm the very good representation of the tidal forcing by the reduced input data. Specifically, the RMSE is very close to zero the Pearson's correlation coefficient (R) is very close to one, while the relative Mean Square Error (MSE) is also very low. The latter parameter is indicative of the error in bed evolution and it is computed as the ratio of the mean quadratic deviation between reference and schematized simulations of bed changes to mean quadratic bed changes.
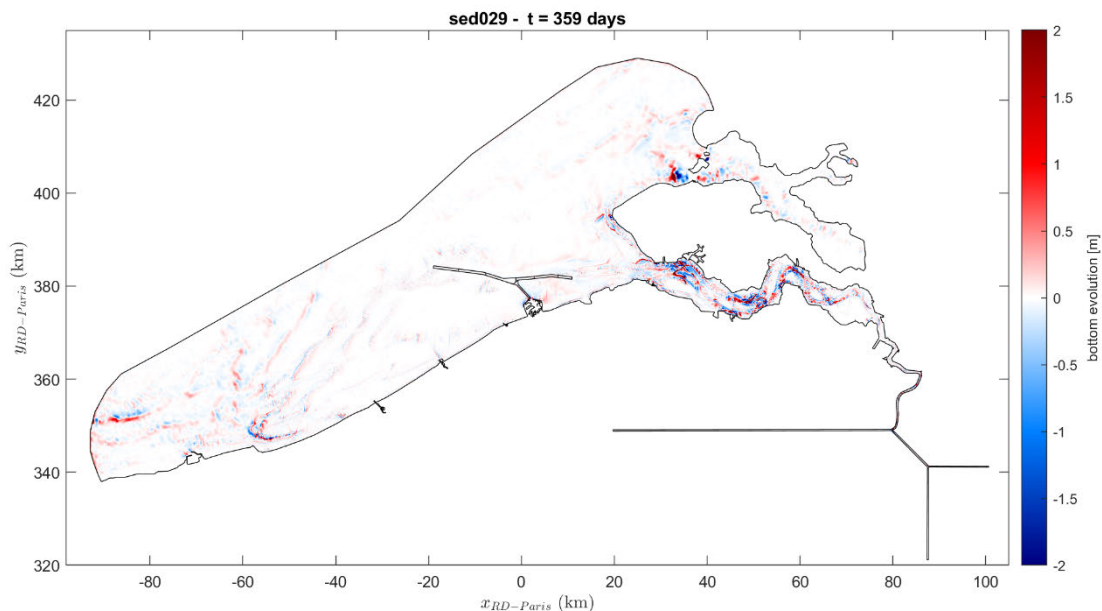
Figure 63 – Sedimentation/erosion patterns after one year under realistic hydrodynamic forcing [Engelund & Hansen formula].
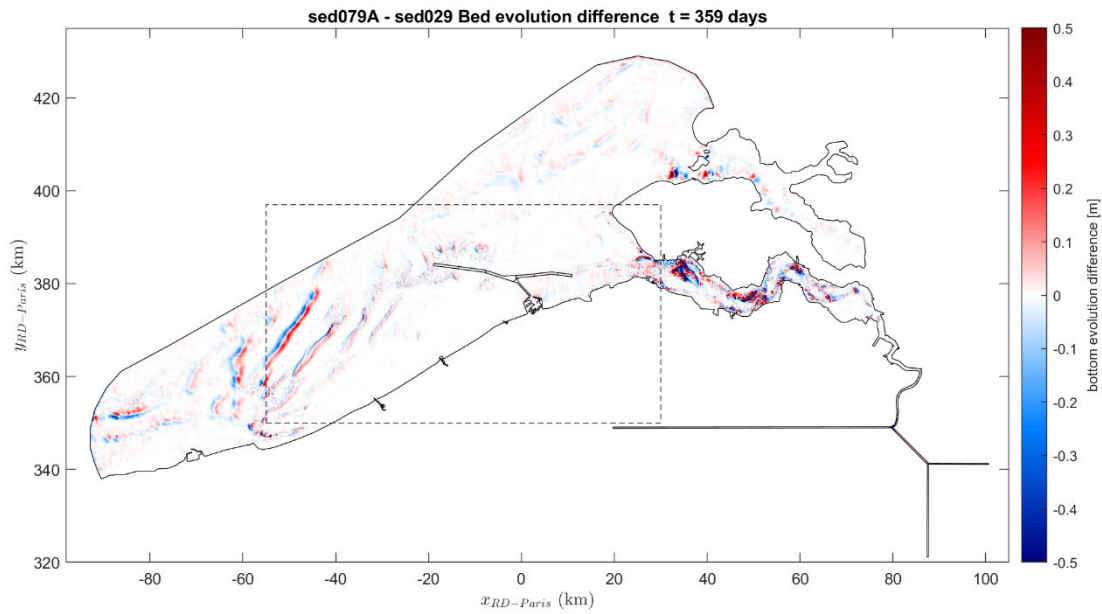
Figure 64 – Bed evolution difference between the simulation with successive representative tides and the simulation with full year tidal forcing [Engelund & Hansen formula]. The dashed box denotes the region where statistical analysis took place.
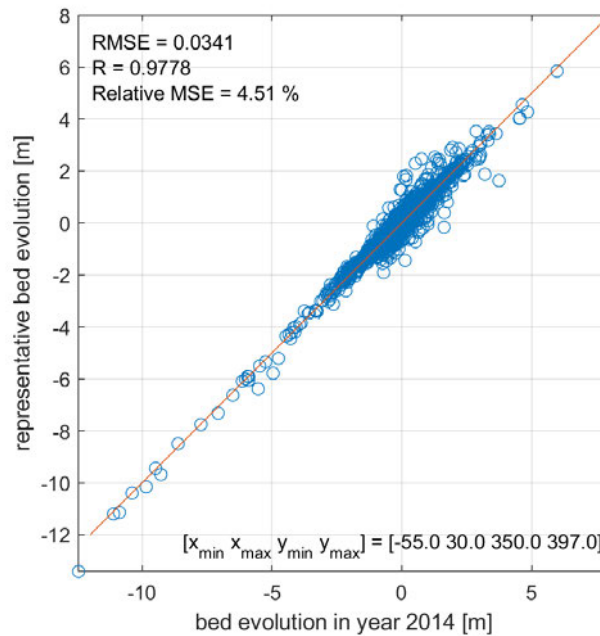
Figure 65 – Comparison of bed evolution between the simulation with successive representative tides and the simulation with full year tidal forcing by use of Engelund & Hansen formula. The coordinates of the box in the domain where statistical analysis took place are given in the bottom of the figure.

4 Representative wave conditions

Generally, in morphodynamic modelling analogue to the input reduction for the tide, also the wave input is reduced to a limited set of representative wave conditions. This is to allow a higher morphological acceleration factor necessary to simulate long term morphodynamic evolution. The waves have a major impact on the shallow near- and on-shore bed evolution. The Belgian coast is characterised by a mean littoral transport from west to east. The annual alongshore transport will be used as validation parameter for the representative wave climate, i.e. the annual longshore transport modelled by a representative wave climate should be in close agreement to the brute force long term mean longshore transport.

A limited set of schematized wave conditions based on equal wave energy was derived for a one-year period 2014-2015. It was shown that the limited set of schematized wave conditions gave a similar annual net longshore transport for the selected period 2014-2015 as the full year timeseries of waves.

However, when applying the method to a pre-selected representative one-year period for which the derived schematized wave conditions were similar to the schematized ones reduced from 10-year times series, it was turned out the schematized wave conditions did not give the same annual net transport as the one-year timeseries. It showed that generally, the method was not applicable for the Scaldis-Coast model. This is discussed in Section 0 and 4.3.

Therefore, it was decided to run 10-year sediment transport simulations forced by wave boundary conditions and wind conditions which are both collected at the measuring station Westhinder. The simulations show that the annual net longshore transport can differ significantly from one year to another. Based on the 10-year simulations, a one-year and a half-year period has been respectively selected to represent as close as possible the annual mean longshore transport along the Belgian Coast. This is discussed in detail in Section 4.4.

The table below firstly summarizes the simulations which are introduced in this chapter.

Table 21 – Summary of the simulations presented in Chapter 4

runID	Mesh	TOM2TEL	MorFac	Transport formula	Grain size
HSW015a	D2	NO	0	Soulsby-van Rjin	250µm
HSW019	D2	NO	0	Soulsby-van Rjin	250µm
HSW036	D2	NO	0	Soulsby-van Rjin	250µm
HSW037	D2	NO	0	Soulsby-van Rjin	250µm
HSW071	G01	NO	1	Soulsby-van Rjin	250µm
HSW087	G01	NO	0	Soulsby-van Rjin	250µm
HSW091	G01	NO	0	Soulsby-van Rjin	250µm
HSW092	G01	NO	0	Soulsby-van Rjin	250µm
HSW110	D4	YES	20	Bijker	200µm, 500µm

4.1 Schematization of wave/wind climate

4.1.1 Wave reduction

Following the wave reduction method of Benedet *et al.* (2016), the Belgian Coast is firstly split into two parts by the black dash line in Figure 66. For the wave reductions, the wave direction is projected to a new reference system in which the black dashed line in Figure 66 is defined as zero degree (starting point) of the wave direction. This is the direction perpendicular to the coast. Then 1-year complete wave climate is schematized to 12 blocks in Figure 67. Each block has equal wave energy flux according to the formula below.

$$E_f = \frac{\rho g^2 H_s^2 T_p}{64\pi}$$

where ρ is water density, g is gravity acceleration, H_s is significant wave height and T_p is peak wave period.

One wave condition can be derived from one block by the formulae blow.

$$\overline{H_s} = \sqrt{\frac{64\pi \cdot \overline{E_f}}{\rho g^2 \overline{T_p}}}$$

where $\overline{H_s}$ is representative significant wave height of each block, ρ is water density, g is gravity acceleration, $\overline{E_f}$ is mean wave energy flux of each block and $\overline{T_p}$ is mean peak wave period of each block.
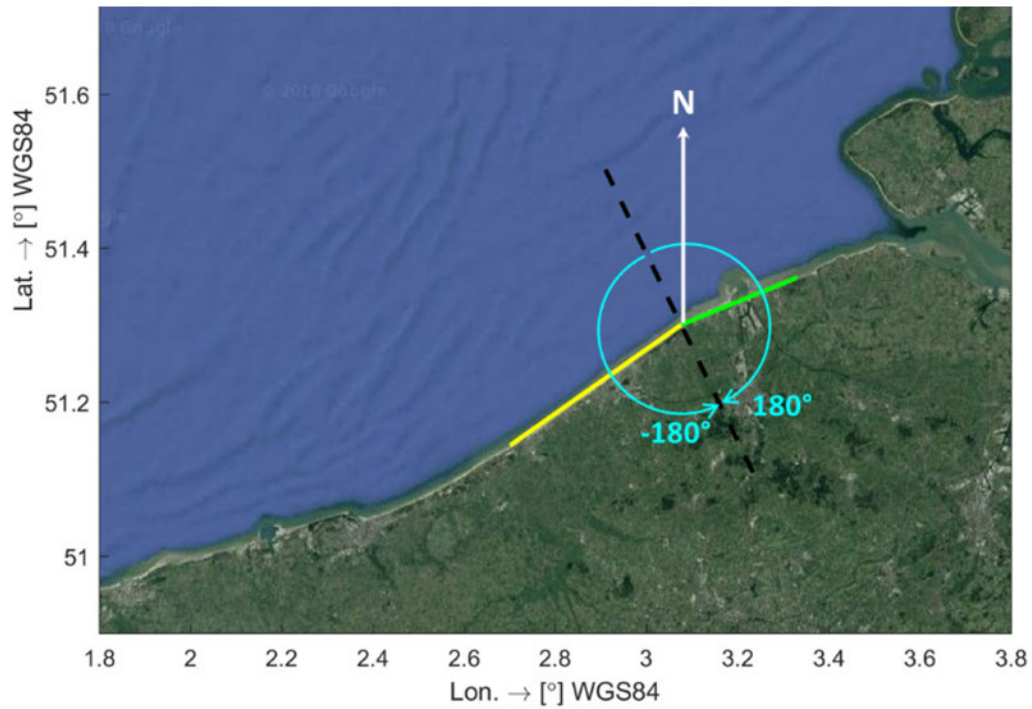
Figure 66 – New definition of wave direction (from 0° to -180° and from 0° to 180°, black dash line indicates the 0°).
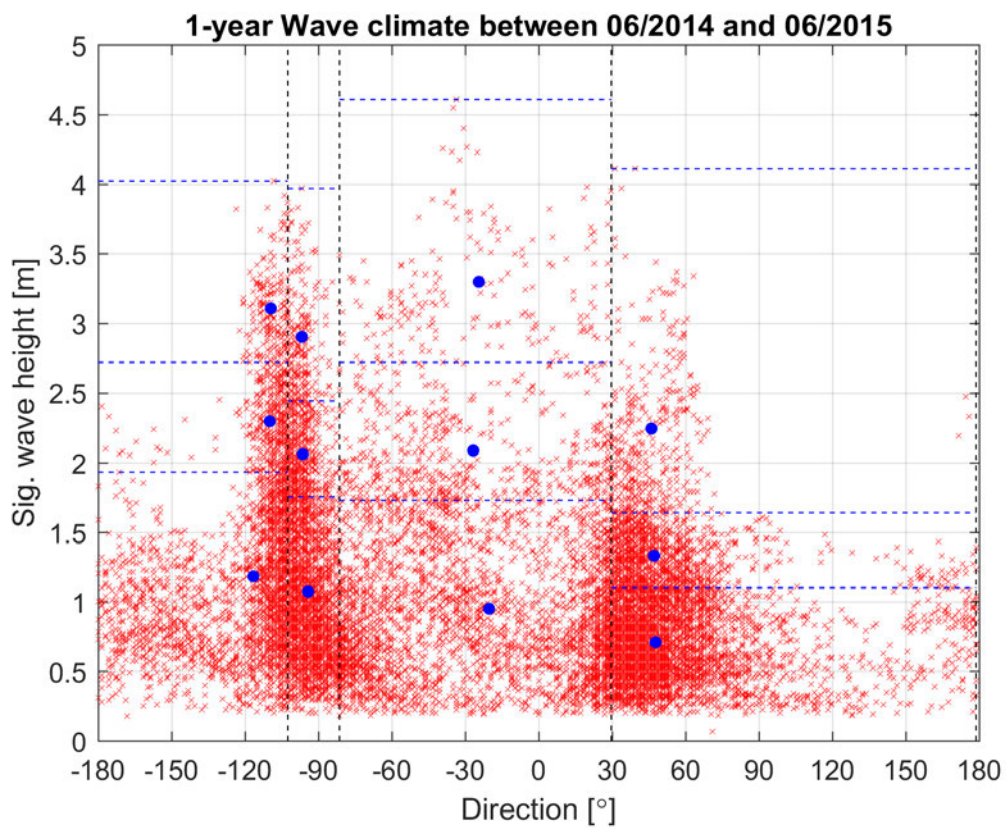
Figure 67 – Wave schematisation for full wave climate of the period between 01 June 2014 and 01 June 2015, and each blue dot represents the schematized wave condition of each block (runID: HSW019).

With respect to sediment transport and morphodynamics, the wave climate has the largest contribution to the literal transport which for the Belgian coast is the major driving factor for the beach and foreshore morphology. Therefore, the wave and wind reduction method is validated for the coastal longshore transport. At first instance, the bed update is not activated in the model to avoid any possible disturbance from morphological changes. Together with the representative tide and schematized wind conditions, the set of 12 schematized wave conditions is verified by 1-year simulation (runID: HSW015a) with brute force which consists of time series tide, wave and wind. The method to reduce wind conditions will be introduced in next section.

The model (runID: HSW019) was run with the 12 schematized wave conditions individually for two diurnal tidal cycles (2 x 24h50min). The first tidal cycle is used for spin-up of the model, and the net longshore sediment transport was computed during the second tidal cycle. In Figure 68, the pink box indicates the domain within which the net longshore transport was calculated with integration over cross-shore profiles. According to the yearly occurrence rate of each wave condition, see

Table 22, the net longshore transport produced by each wave condition in one year can be derived from the net longshore transport computed by each run. Then the total annual net longshore transport is obtained by summation of the yearly net longshore transport produced by all 12 schematized wave conditions, and shown by the blue line in

Figure 69. The red line shows the annual net longshore transport produced by the brute force computation.
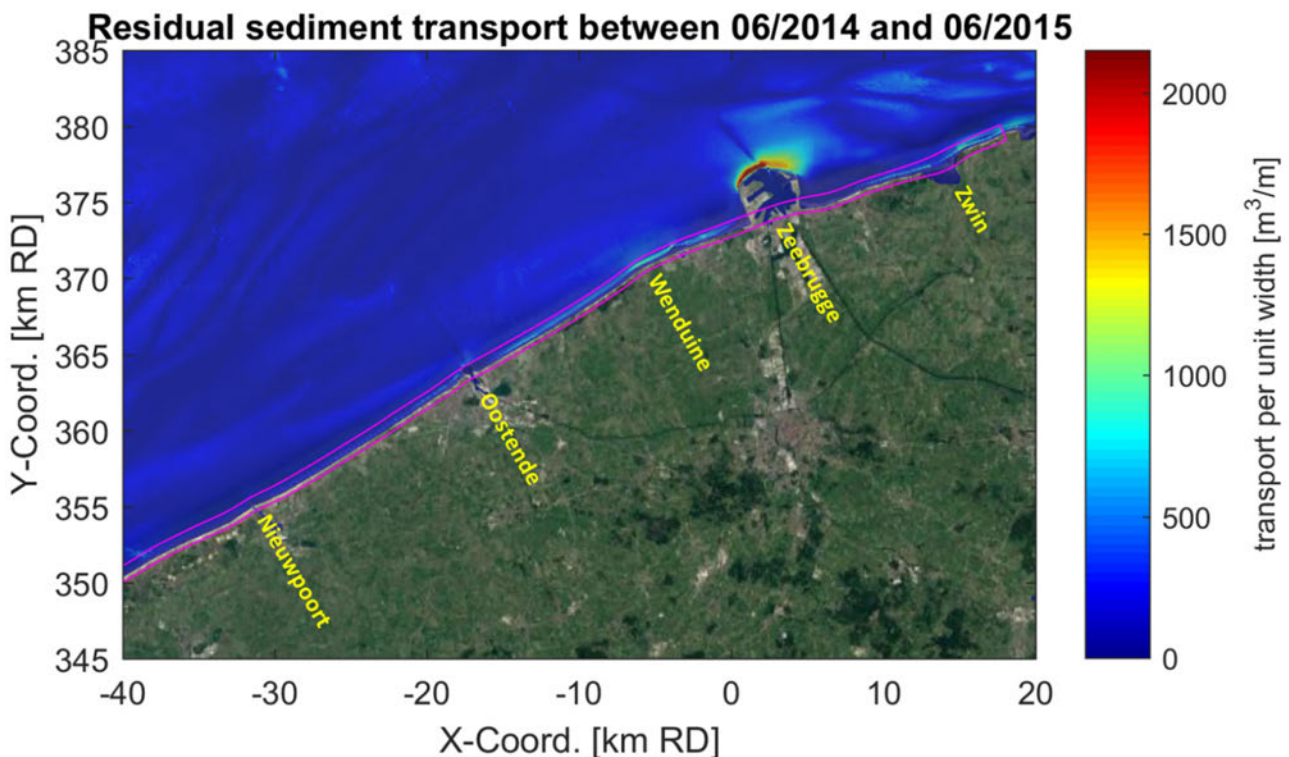
Figure 68 – Residual sediment transport with 1-year brute force, the pink box indicates the domain to compute longshore transport integrated over cross-shore profiles (runID: HSW015a).

Table 22 – 12 schematized wave conditions reduced from the wave climate between 06/2014 and 06/2015 ($\overline{U_w}$ is the representative wind speed of each block, wind/wave direction follows nautical convention)

$\overline{H_s}$ [m]	$\overline{T_p}$ [s]	$\overline{U_w}$ [m/s]	wind/wave direction [°]	occurrence rate [%]
1.18	4.48	9.68	217.98	13.53
2.30	6.62	14.12	224.66	2.41
3.11	7.38	17.13	225.11	1.19
1.07	4.77	8.83	240.36	15.36
2.06	6.31	13.64	238.16	3.15
2.90	7.14	16.91	237.79	1.40
0.95	5.01	7.07	314.30	18.69
2.09	5.99	12.36	307.81	3.24
3.30	7.13	16.93	310.08	1.08
0.71	5.65	5.54	22.31	29.66
1.33	6.02	8.14	21.70	7.91
2.24	7.03	11.79	20.62	2.38
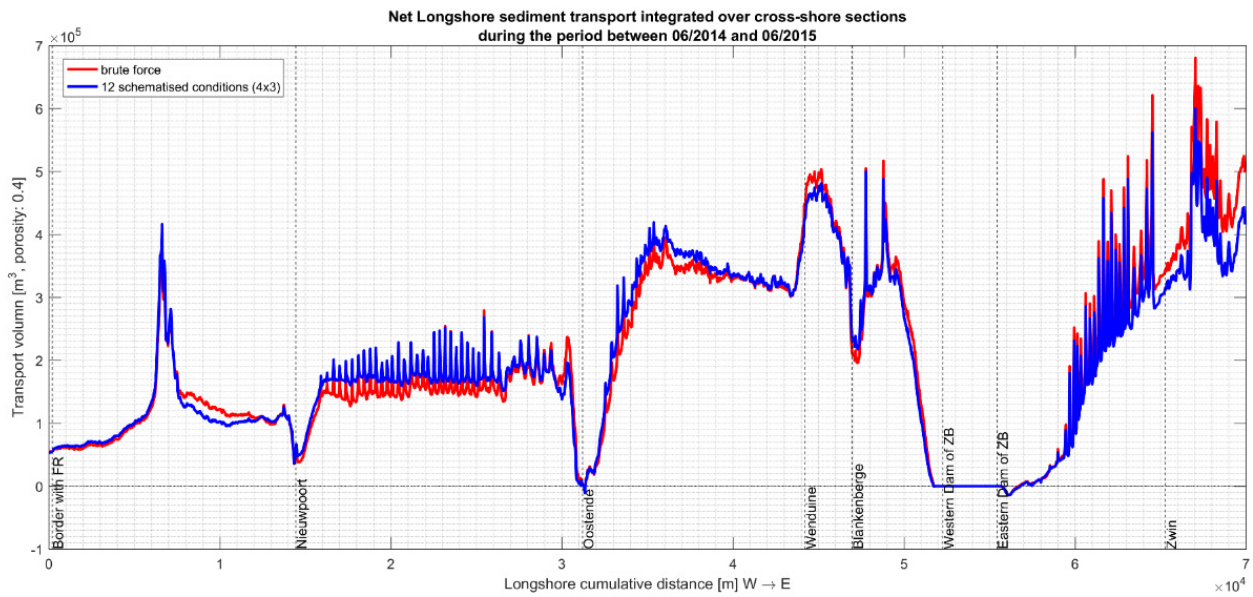
Figure 69 – Modelled net longshore sediment transport integrated over the cross-shore profiles during one year from 01 June 2014 to 01 June 2015 (red: HSW015a, blue: HSW019).

4.1.2   Pre-selection of the representative year

The method of wave reduction has been approved by the comparison between the schematized wave conditions and brute force. The objective of this study is to simulate 10-year morphology of the Belgian Coast, and thus the reduction method is further applied to 10-year wave climate as shown in Figure 70, and the 12 schematized wave conditions are given in Table 23.
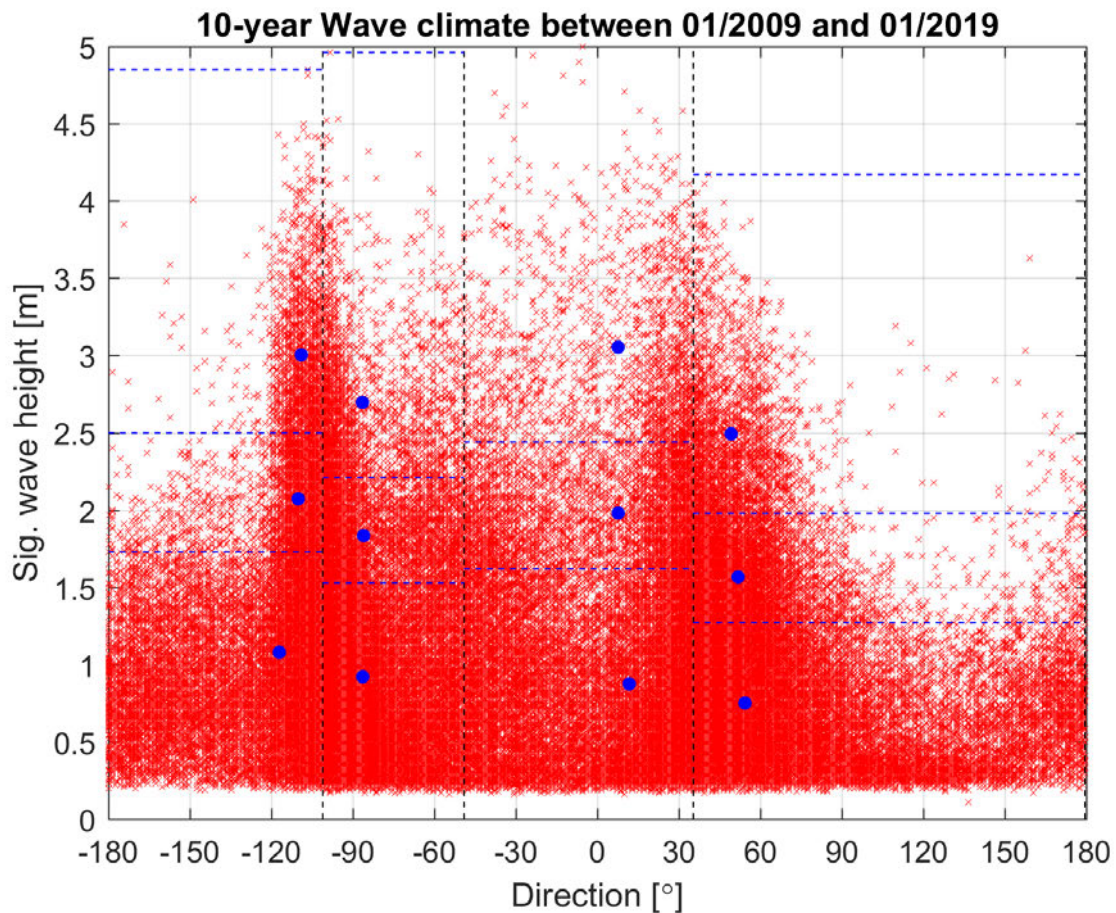
Figure 70 – Wave schematisation for full wave climate of the period between 01 January 2009 and 01 January 2019, and each blue dot represents the schematized wave condition of each block (runID: HSW036).

Unlike SWAN, TOMAWAC needs transition time for a new wave condition on the boundary to reach equilibrium in the model domain from last wave condition. When merging the individual schematised wave conditions to an artificial time series, the transition time will have an impact on the morphodynamic results. This makes the model extra sensitive to choices in how the artificial time series is built up, leading to unwanted extra model uncertainty. With the objective to perform simulations of 10-year morphology or more, it was decided to force the model with a one-year measured timeseries which should be representative for the long-term wave climate with respect to littoral transport. To select the one-year representative period, called the representative year, iteratively a one-year subset is selected from the ten-year measured timeseries. The schematized wave conditions are compared to the schematized wave conditions of the 10-year period. It was found that for the period April 17th, 2017 till April 17th, 2018 the schematized wave conditions are closest to those in Table 23. This period was then selected as the representative year.µ

Table 23 – 12 schematized wave conditions reduced from 10-year wave climate ($\overline{U_w}$ is the representative wind speed of each block, wind/wave direction follows nautical convention)

$\overline{H_s}$ [m]	$\overline{T_p}$ [s]	$\overline{U_w}$ [m/s]	wind/wave direction [°]	occurrence rate [%]
1.08	4.49	9.85	217.43	15.20
2.07	6.29	14.28	224.41	2.94
3.00	7.25	17.93	225.52	1.22
0.92	4.64	8.53	248.16	20.20
1.83	5.96	13.33	248.49	3.97
2.70	6.86	16.90	248.06	1.60
0.88	5.88	6.54	346.28	17.68
1.98	6.53	11.53	342.20	3.11
3.05	7.53	15.62	342.17	1.13
0.75	5.40	6.37	28.87	26.12
1.57	6.34	10.05	26.33	5.11
2.49	7.47	13.45	23.79	1.72

Figure 71 displays the 12 schematized wave conditions of the selected representative year. In Figure 72, it could be observed that there is a fairly good agreement on the annual net longshore transport produced by the 12 schematized wave conditions between the representative year (runID: HSW037) and 10 years (runID: HSW036). Therefore, the representative year was expected to simulate 10-year morphology in combination with morphological acceleration factor 10.
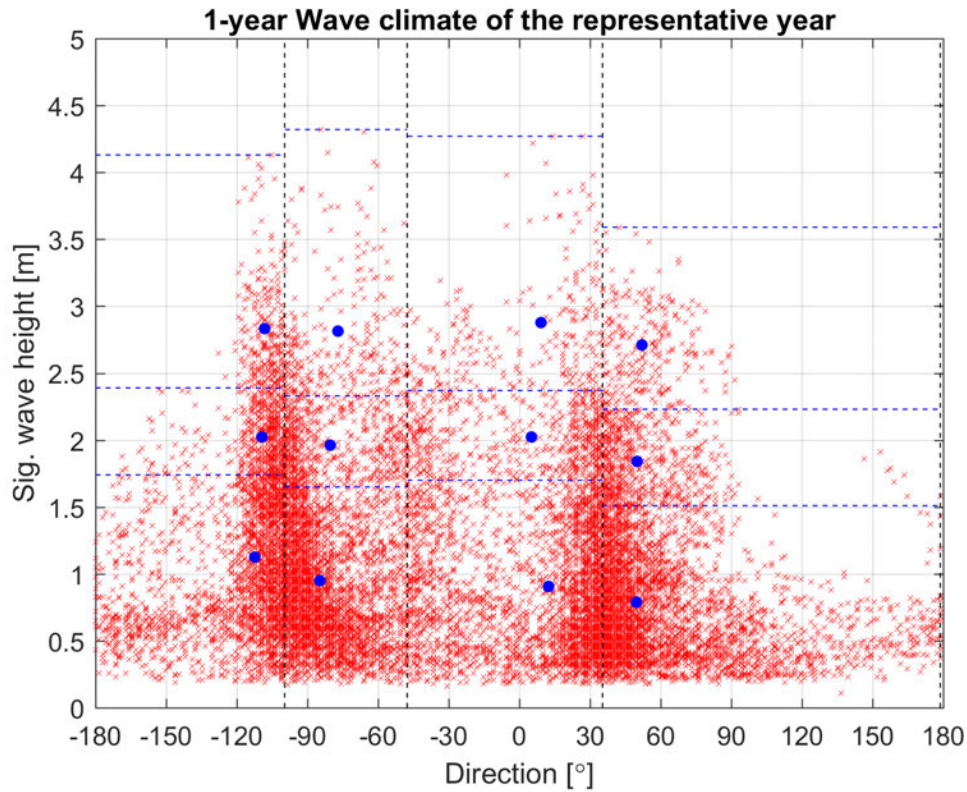
Figure 71 – Wave schematisation for full wave climate of the representative year, and each blue dot represents the schematized wave condition of each block (runID: HSW037).
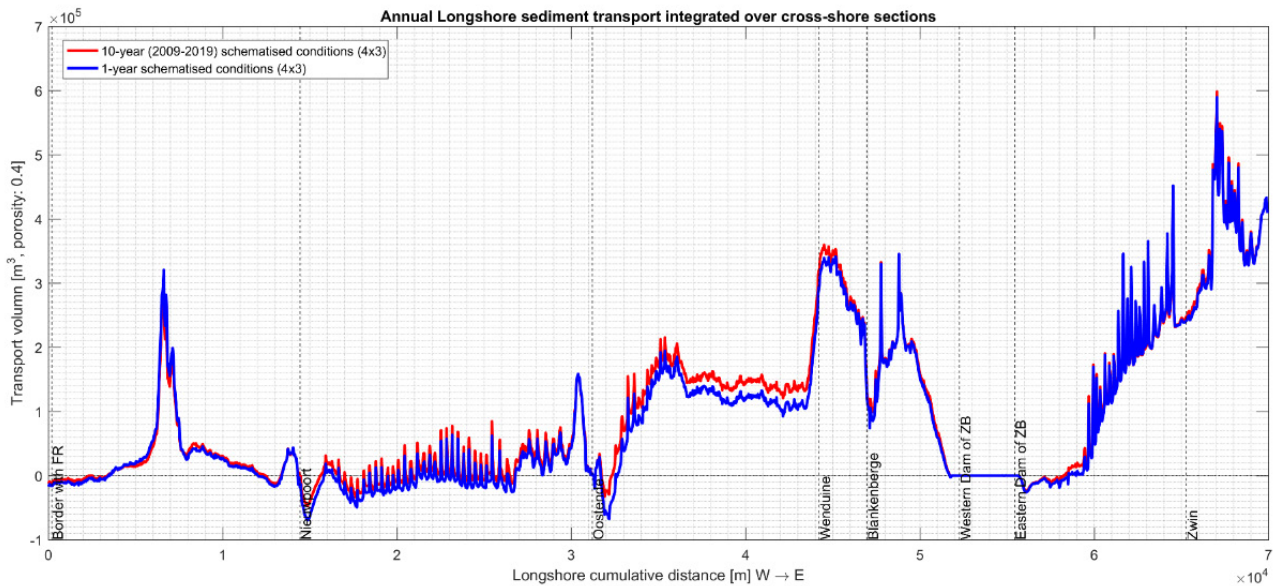
Figure 72 – Modelled annual net longshore sediment transport integrated over the cross-shore profiles with schematized wave conditions (red: HSW036, 12 wave conditions derived from 10 year data, see Table 23, blue: HSW037, 12 wave conditions derived from one year, Figure 71)

4.1.3   Wind reduction

Time series of wind data are available from the measurement station Westhinder, of the *Meetnet Vlaamse Banken* (MVB). According to Zimmermann *et al.* (2013), the wind and wave direction are reasonably well correlated, so the wind direction in the model is chosen equal to the wave direction applied at the boundaries.

Figure 73 shows the correlation between the wind speed and the significant wave height at the measurement station for the first wave condition in Table 23 (within the most left lower wave block in Figure 70). The black line delimits the significant wave height of a fully developed sea as a function of the wind speed according to the formula of Sverdrup-Munk-Bretschneider (SMB). The SMB criterion states that wave growth stops when the wave phase velocity is equal to the wind speed. Such a linear regression has been done for all 12 schematized wave condition blocks from Figure 70. With the linear regression, $\overline{U_w}$ is derived from $\overline{H_s}$ for each wave condition (Table 23).
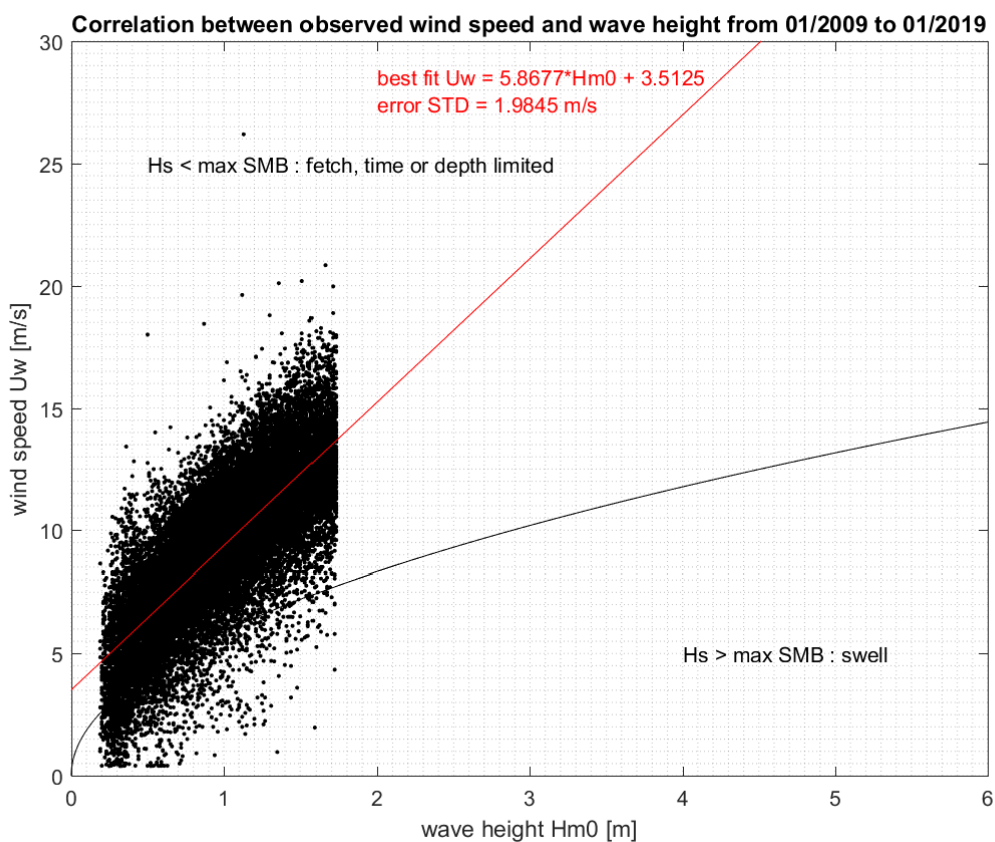
Figure 73: Significant wave height vs. wind speed within the most left lower wave block in Figure 70. The black line delimits the significant wave height of a fully developed sea as a function of the wind speed according to the formula of Sverdrup-Munk-Bretschneider (SMB).

4.2   Unsuccessful application of wave/wind reduction

In Section 4.1, the reduction method of wave climate has been successfully applied to the period between 06/2014 and 06/2015, which is called validation year because the erosion volume of nourishment has been validated by the model with brute forces (see Section 5.3.1).

The representative year between 04/2017 and 04/2018 was firstly selected based on the 10-year wave climate in Section 4.1. To further confirm robustness of the reduction method, the reduction method has been also applied to the pre-selected representative year, the transport model (runID: HSW071) has been run with brute forces for the same period.

However, a quite different transport volume was obtained, compared with that generated by the 12 schematized wave conditions which are reduced from the wave climate of the pre-selected representative year (Figure 74). The reduction method seems to be not solid for every year, and the pre-selected representative year based on the reduction method becomes also questionable. Next section is going to reveal the cause for the unsuccessful application of the reduction method.
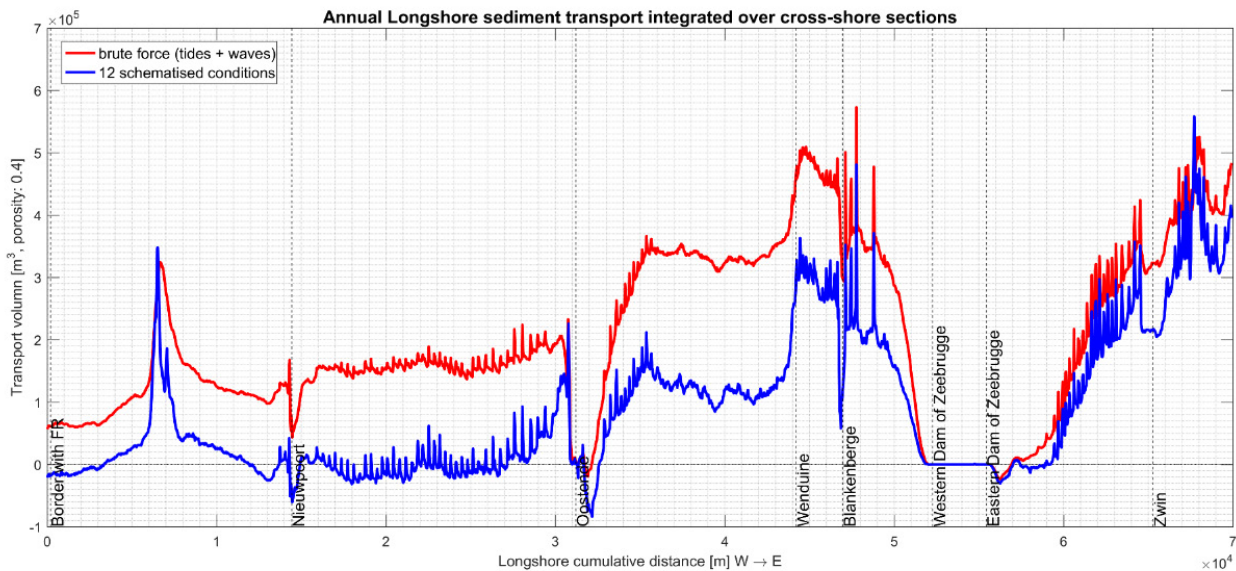
Figure 74 – Modelled net longshore sediment transport integrated over the cross-shore profiles during the representative year from 19 April 2017 to 19 April 2018, red: brute force wind and wave forcing (HSW071), blue: schematised wind and wave conditions (HSW037).

4.3 Effects of wind reduction

Before efforts are focused on effects of wind reduction, insufficient representative conditions of the wave climate were guessed as the primary reason for the unsuccessful application of the reduction method. The number of the schematized conditions has been increased to 160 with directional resolution 22.5° and size resolution 0.5m. However, the schematized 160 wave/wind conditions still failed to reproduce the alongshore transport volume produced by the brute force (G. Kolokythas *et al.*, 2020). The insufficient schematized conditions of the wave climate do not seem to be the reason for the unsuccessful application of the reduction method.

In contrast with the stationary computational mode which is normally used by the wave model SWAN, the wave model TOMAWAC employed in this project has only nonstationary computational mode for simulation. However, the nonstationary computational mode was also found to be not a cause for the unsuccessful application of the reduction method (G. Kolokythas *et al.*, 2020).

With the aim to thoroughly understand the reason why the reduction method cannot be successfully applied in this study, the time series schematized conditions are further investigated (Figure 75).
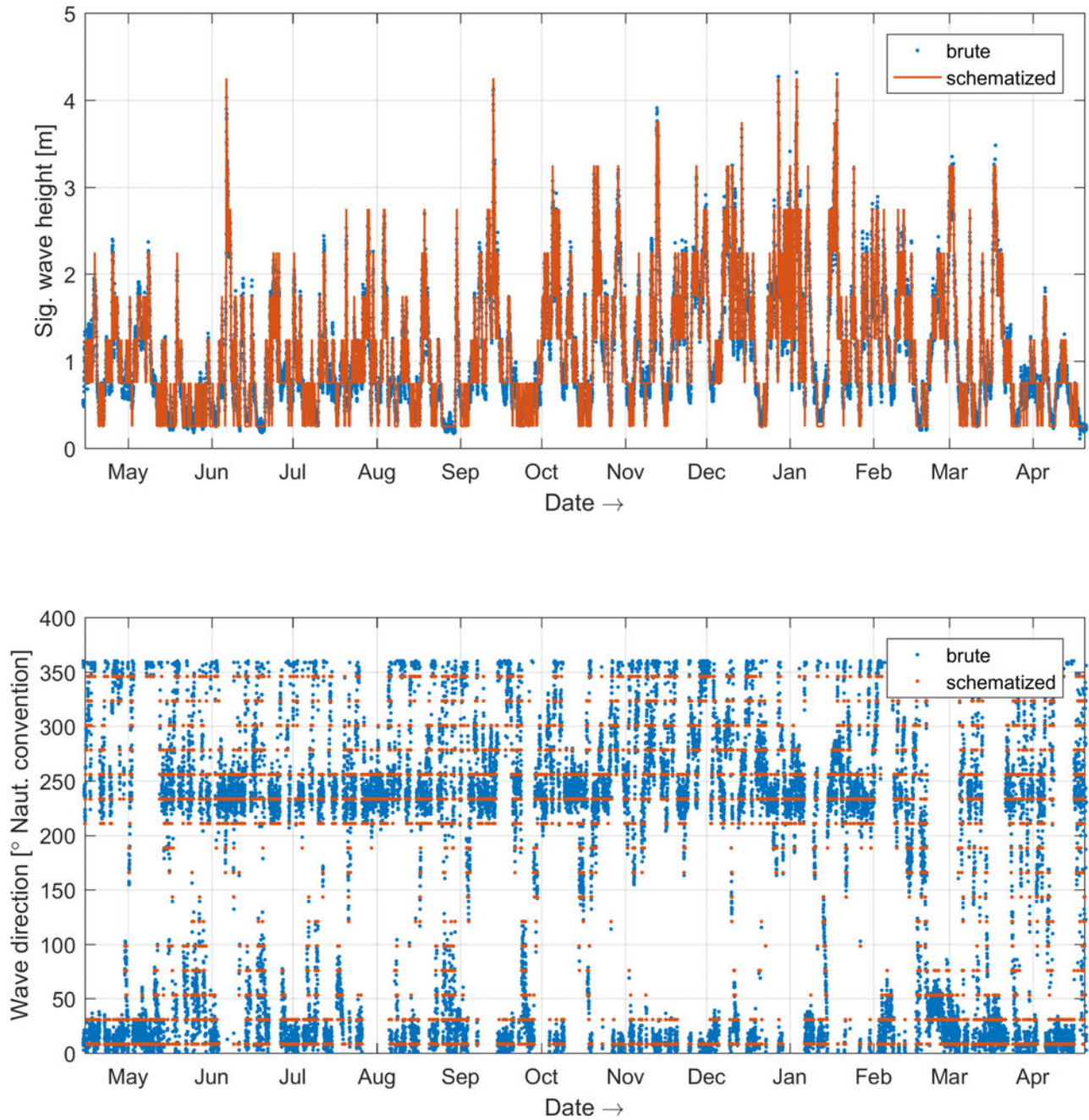
Figure 75 – The time series brute and schematized wave conditions (significant wave height and wave direction) of the representative year between 04/2017 and 04/2018.

A short period around one month is selected used for simulations with time series brute forces and schematized conditions. The time series schematized significant wave height, peak wave period and wave direction are replaced by the time series brute ones separately (runID: HSW087). When the schematized wind conditions, both wind speed and direction, are replaced by observed timeseries, also called brute force wind forcing, the net alongshore transport volume produced by the time series representative wave conditions and brute wind force is almost identical to that produced by the full brute wave and wind forcing (Figure 76). Therefore, the failure of the reduction method could be attributed to the schematization of the wind.

In order to further clarify effects of the wind reduction, the simulation with time series brute wave direction and wave speed is performed respectively. As shown as the purple and green lines in Figure 76, the schematization of wind direction seems to be the major reason for the failure of the reduction method. Therefore, it is not appropriate to assume an identical direction for the wave and wind conditions in this study.
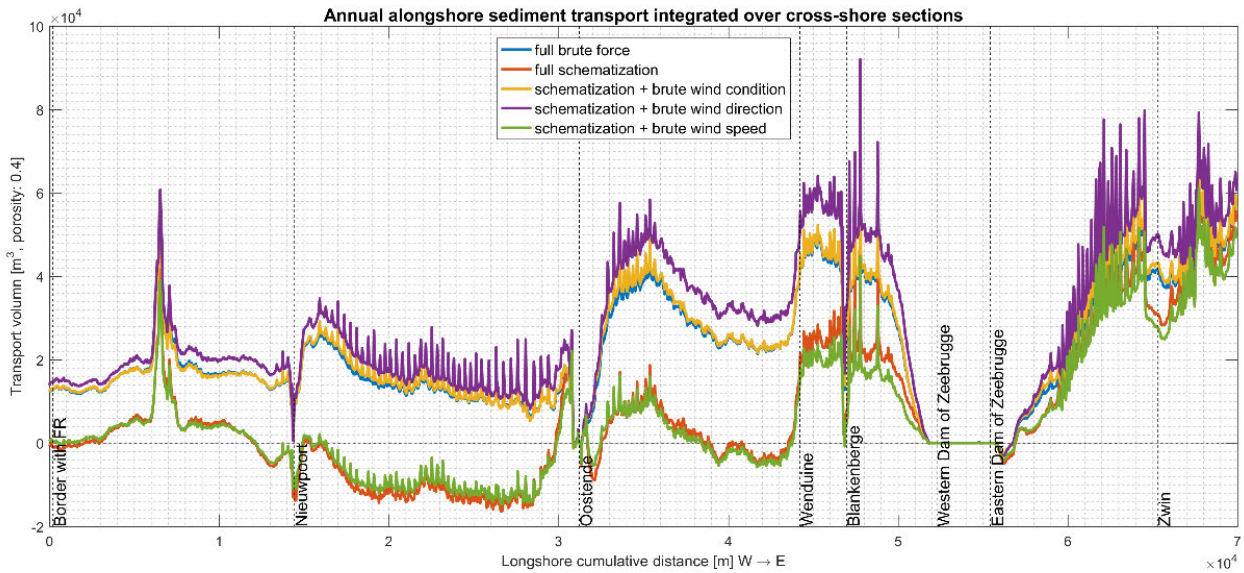
Figure 76 – Modelled net longshore sediment transport integrated over the cross-shore profiles with brute forces and different schematizations combined with brute forces (runID: HSW087).

In addition to the schematization of wind direction, the schematization of the wind speed seems to also play a certain role in the error compared to net alongshore transport volumes produced by the full brute forces because the purple line is still visibly larger than the blue line. To quantify the effect of wind speed on the net alongshore transport volume, the wind speed is increased by 10% and 20%. It could be found that the net alongshore transport volume is also quite sensitive to the wind speed (Figure 77). When the wind speed is increased by 20%, the net alongshore transport volume is already doubled.
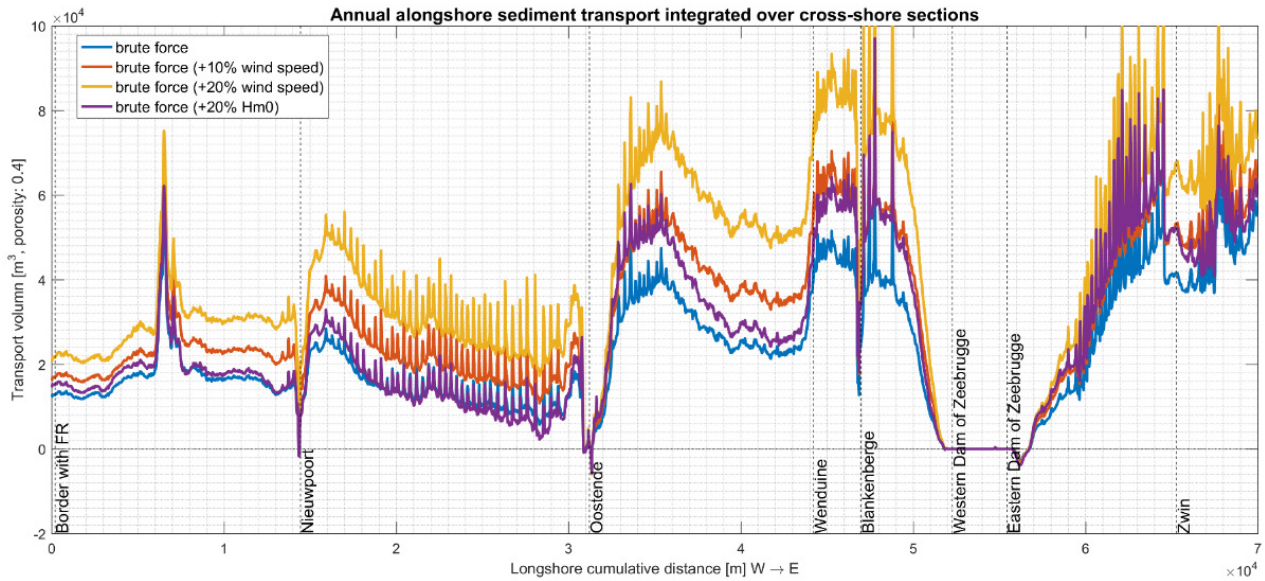
Figure 77 – Modelled net longshore sediment transport integrated over the cross-shore profiles with sensitivity tests of wind speed (runID: HSW087).

It was found that due to the size and direction of the model, internally generated waves have a significant contribution to the net longshore annual transport. Especially for winds coming from the west, the fetch-length in the model is sufficiently long, knowing that the west to south-west is the dominating wind direction. Wind-directions are not always in line with the wave direction at the offshore boundary, e.g. Westhinder station.

4.4   Selection of the representative periods

4.4.1   Representative one year

Although the cause for the failure of the reduction method has been detected, there seems to be no good solution to fix this issue. Therefore, the transport model (runID: HSW091 and HSW092) has been run with 10-year brute force wind and wave conditions, and the mean annual net alongshore transport was derived (Figure 78). Strong fluctuations in annual net transport are shown to take place from year to year. The annual net transport of the year 2009 was even observed in opposite direction for large parts of the Belgian Coast. The fluctuation east of Zeebrugge is less pronounced. This section of the coast is sheltered for waves from the north by the coast of Walcheren. Northern waves are often related to stormy conditions. It was noticed that even a little number of rough conditions can have an impact on the annual net transport.

Ideally the net alongshore transport produced in the representative year should be close to the mean annual one as much as possible. Based on this criterion the period between 30 November 2015 and 30 November 2016 was selected as the representative year (Figure 79).
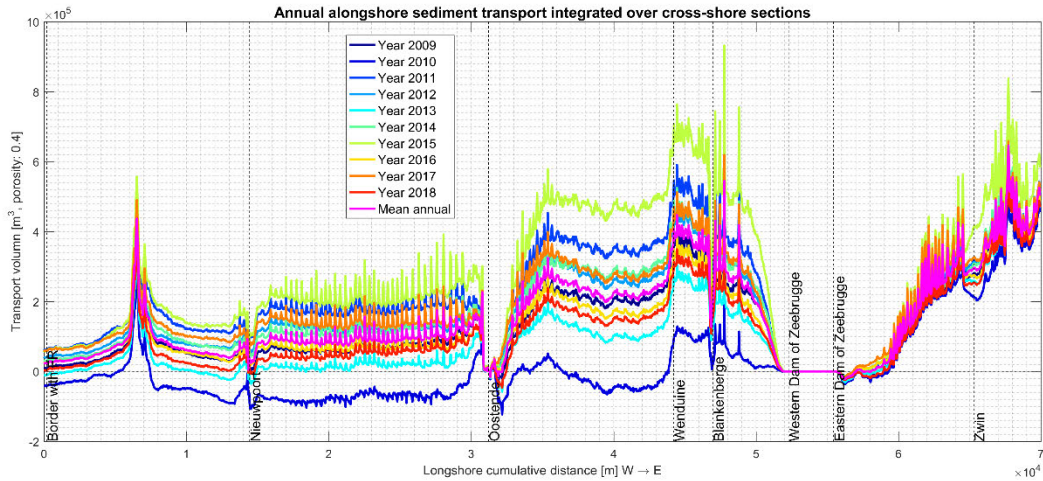
Figure 78 – Modelled annual net longshore sediment transport integrated over the cross-shore profiles with 10-year brute forces (runID: HSW091 and HSW092).
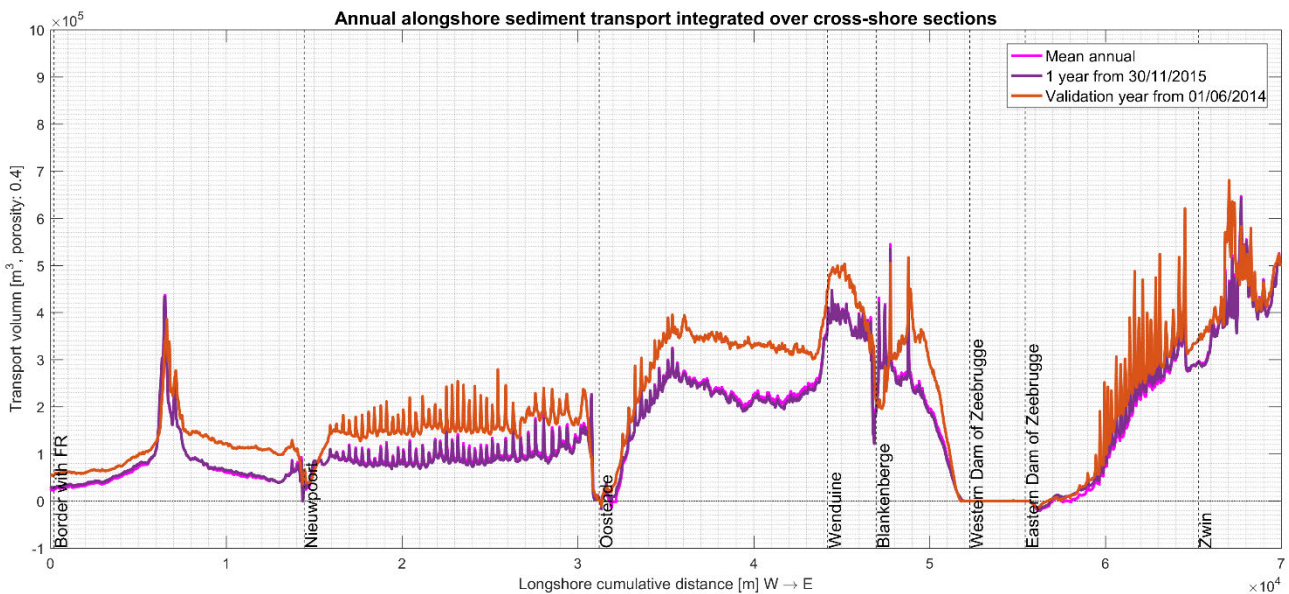
Figure 79 – Comparison among mean annual net transport derived from the 10-year modelling, modelled net transport of the selected representative year from 30 November 2015 to 30 November 2016, and modelled net transport of the validation year from 01 June 2014 to 01 June 2015.

4.4.2 Representative half year

In order to further reduce the computational time for the 10-year morphological simulation, a larger morphological acceleration factor (Morfac) has to be used. A representative half year is expected to perform the 10-year morphological simulation with Morfac =20. Following the last criterion for selection of the representative year, the double of net alongshore transport produced in the representative half year should be close to the mean annual one as much as possible (Figure 80). The half-year period starting from 07 November 2013 was selected as the representative half year for the 10-year morphological simulation.
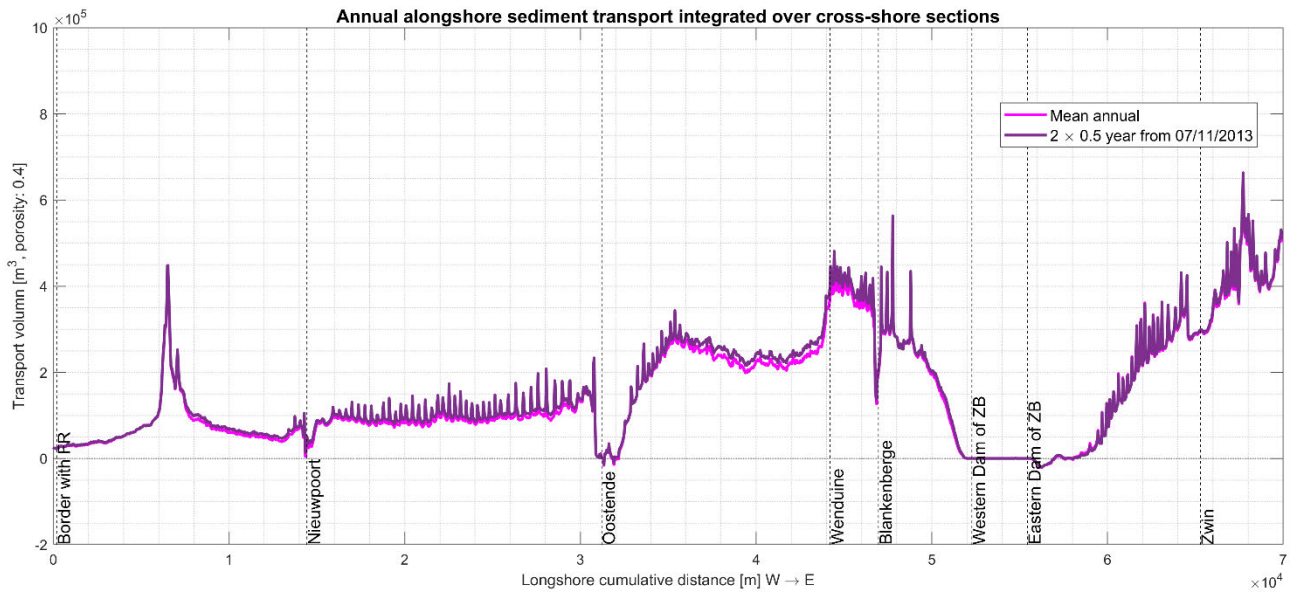
Figure 80 – Comparison between mean annual net transport derived from the 10-year modelling and modelled net transport of the selected representative half year from 07 November 2013.

4.4.3   Comparison representative half year and schematized wave conditions

In the next section the morphodynamic evolution of the Belgian Coastal zone in the vicinity of the Zeebrugge port after the seaward extension of the port will be compared between the model and observations. However, at the time being in the progress of the project, at that time the model was drive by the derived schematized wave conditions in Table 22. Therefore, in this section the effect of the forcing, schematised versus representative (half) year, on the large scale morphodynamics is investigated.

The 10-year morphological simulation was forced by wave/wind conditions of the representative half year with Morfac = 20 (runID: HSW110). Identical model setting are applied in a second run, but now with the schematized wave conditions of Table 22, one-year run, MORFAC 10 (ref003). The schematized wave conditions have been compiled to an artificial timeseries of wave climate as in Figure 81, which has been repeated ten times during the simulation.
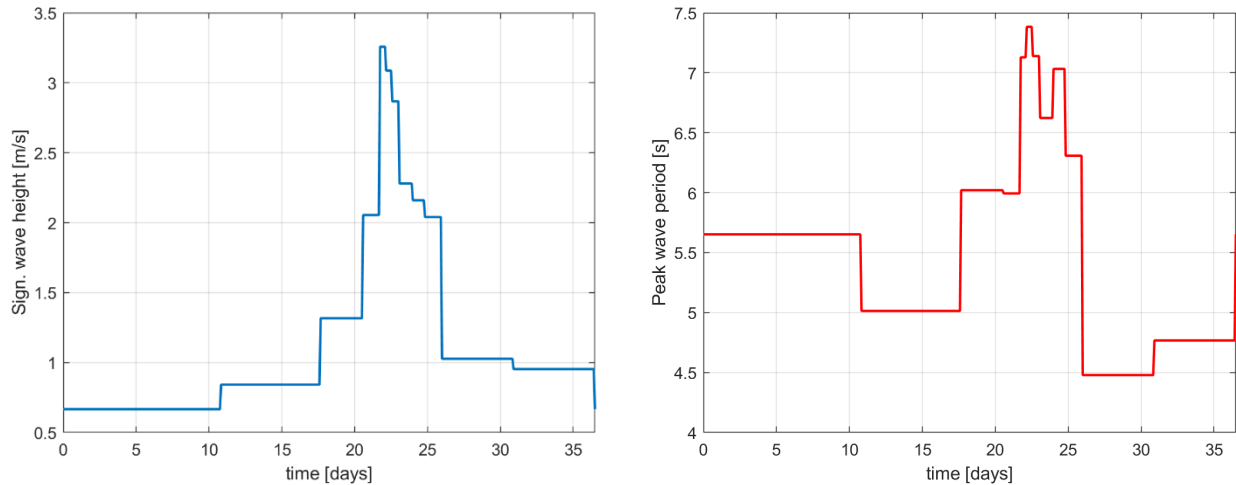
Figure 81 – Schematized wave conditions applied 10 times successively (blue line: Hmo; red line: Tp).

A qualitative comparison is given in Figure 82. It could be found that from the modelled sedimentation/erosion maps the major pattern produced by the two simulations is quite similar along the Belgian Coast (Figure 82). The waves, and particularly the wave direction has a less pronounced impact on the off-shore morphodynamics than on sediment transport in the surf zone.

However, even when zooming in on the area of Wenduine in Figure 83, Even there a good agreement on the morphological pattern could be still found between the two simulations. A quantitative comparison was even made based on the modelled net erosion volume within the closed pink box. The simulation driven by the brute force of the representative half year gives the net erosion about 223 100 m^3, which is only 1.0% less than the one produced by the simulation ref003: 225 400 m^3.

Therefore, it is argued that for the hind cast simulations, nevertheless it is advised in the future to make use of the representative (half) year wind and wave forcing, the schematized wave conditions still give reliable results.
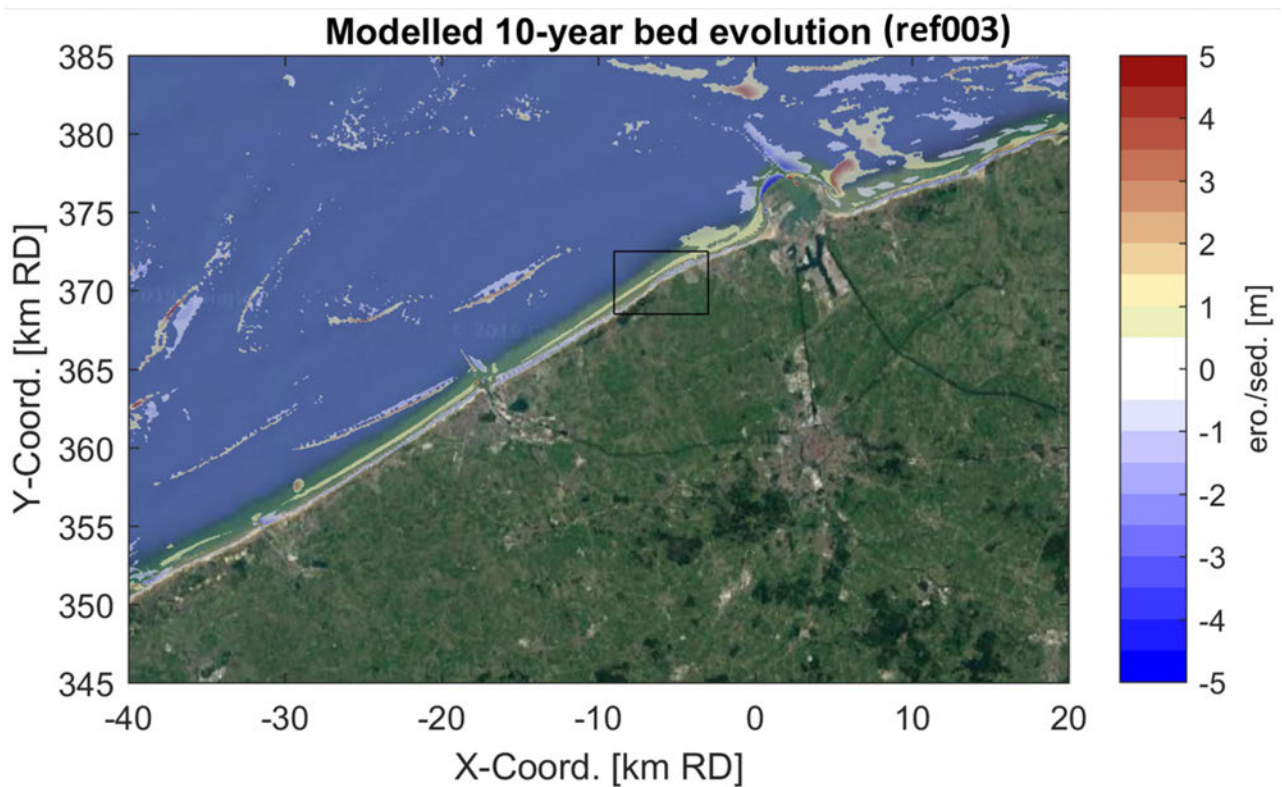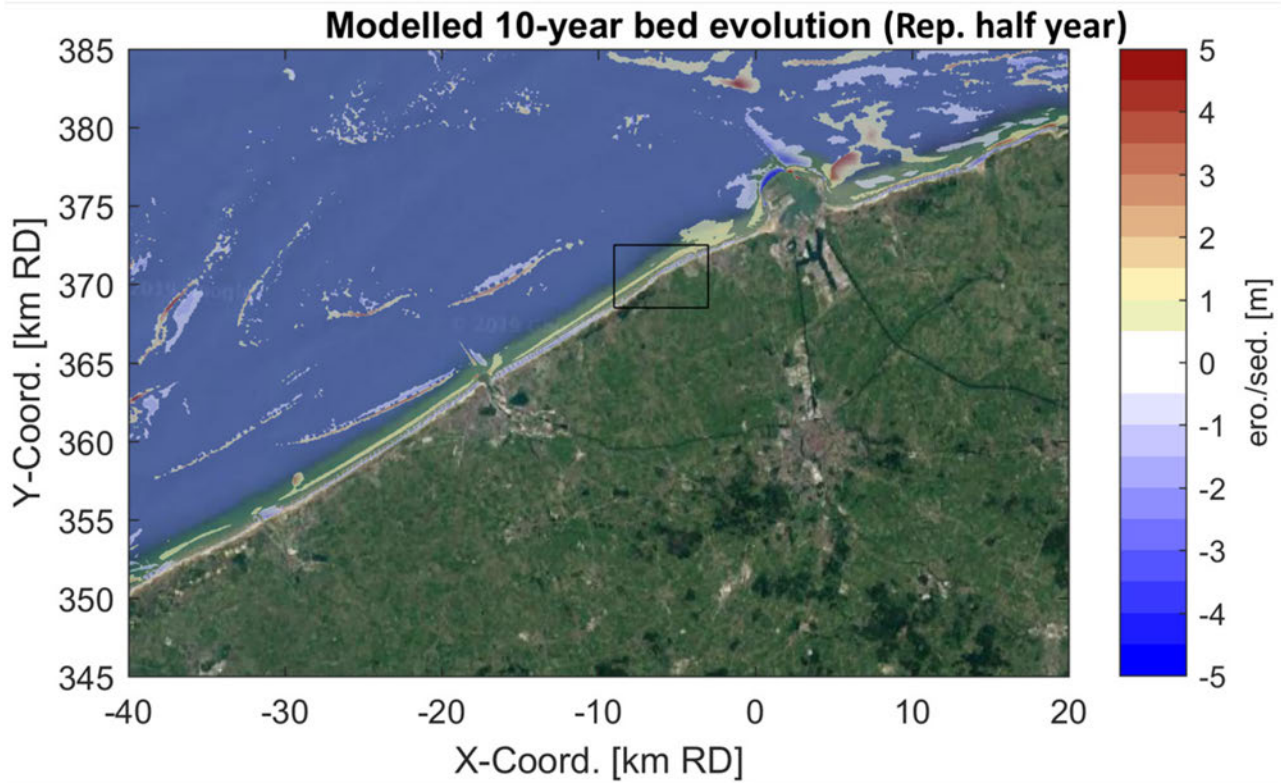
Figure 82 – Modelled 10-year morphological change within the Belgian Continental Shelf (upper: HSW110, simulation of the representative half year with Morfac =20; lower: simulation ref003).
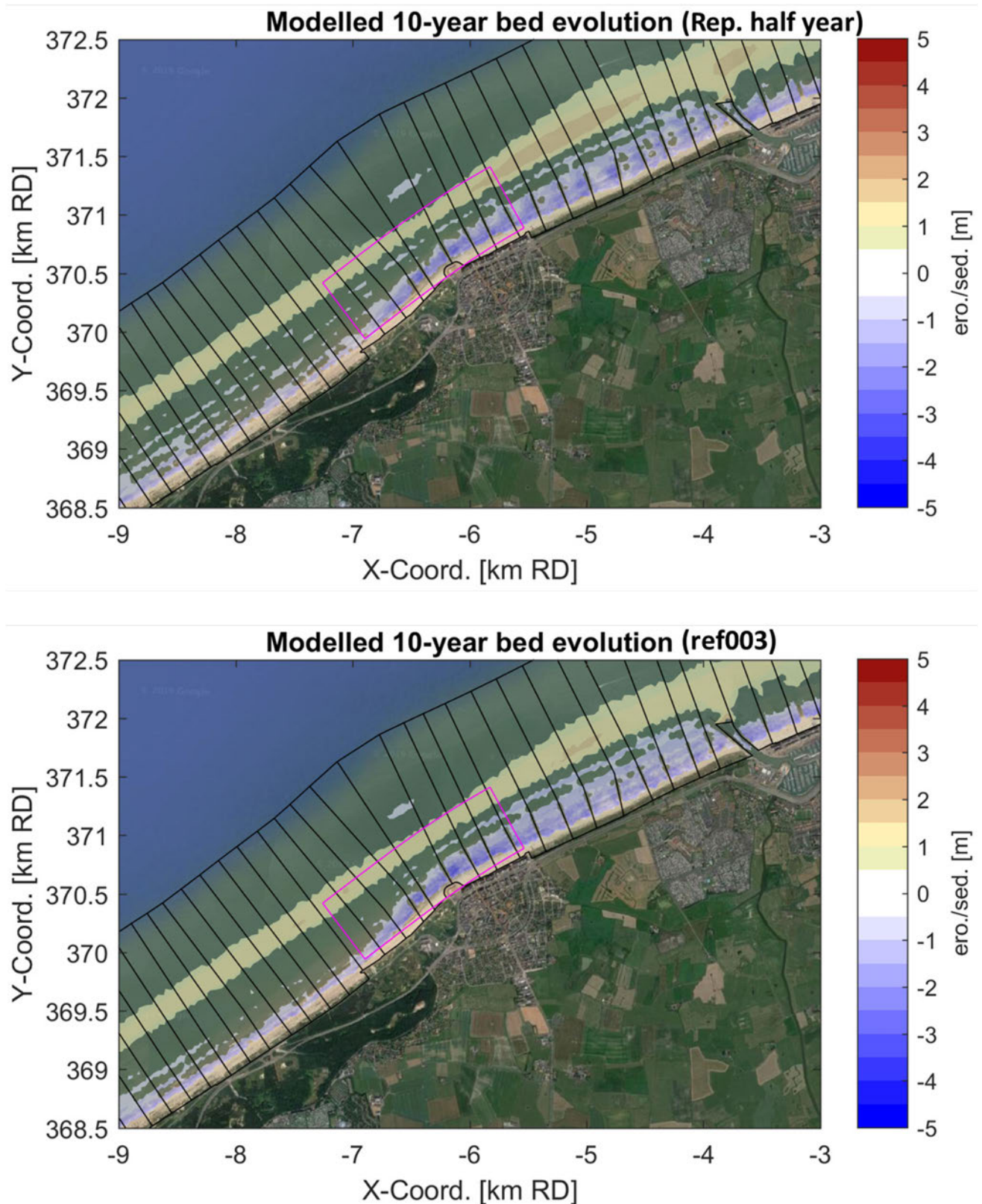
Figure 83 – Modelled 10-year morphological change at Wenduine (upper: HSW110, simulation of the representative half year with Morfac =20; lower: simulation ref003).

5 Morphodynamic modelling

In order to analyse the model sensitivity to numerical and physical parameters and to validate the model a hindcast starting from the extension of the port of Zeebrugge has been performed, see Section 5.1. Apart from the bathymetric evolution also the capability of the model to reproduce the historical and current maintenance dredging volumes is investigated in Section 5.2. Finally the longshore transports is validated by the beach evolution at Wenduine and siltation of the navigation channels of Blankenberge in 5.3.

5.1 Long-term morphological hindcasting

The performance of the morphodynamic model is evaluated by a long-term morphological hindcasting applied on the computational domain of the Scaldis-Coast model. Note that the term 'hindcasting', in the present study, corresponds only to the introduction of historical bathymetric data in the model whereas the hydrodynamic forcing is imposed using the input reduction technique, i.e. therepresentative tide presented in section 3.3 and a schematized wave condition as discussed in section 4.1. As in the case of the representative tide, the use of schematized wave conditions helps in the safer increase of the morphological time-step, avoiding a possible unrealistic clustering of high-impact events that may lead to non-reversible, unrepresentative changes, and thus, decreasing the unwanted effects of chronology.

The introduced historical bathymetry is a compilation of data from or around the year 1986, depending on the availability. This period coincides with the completion of the extension of the port of Zeebrugge (construction of breakwaters), which affected substantially the morphological equilibrium of the surrounding area. The morphodynamic version of Scaldis-Coast aspires to adequately represent the morphological changes triggered by this important human intervention at the coast.

Next, sensitivity tests of various model parameters (numerical and physical) and formulations are conducted aiming to improve the performance of the model in hindcasting sedimentation-erosion patterns and sand volume transfer at the area of interest.

5.1.1 Historical bathymetric data

The search of historical bathymetric data able to cover the entire computational domain was a difficult task and, thus, not entirely successful. Hence, the reference bathymetry of the model for the hindcasting comes from merging of the historical data at the extensive area of interest and the current bathymetry. The regions where historical data around the year 1986 were interpolated on the Scaldis-Coast grid are denoted in Figure 84 (left), being limited by four dashed polygons, i.e. the regular *vaklodingen* from the Dutch Ministry of Waterways and Transportation. Any bathymetric data outside the boundaries of these polygons is identical to the present bathymetry which is also shown in Figure 84 (right). Detailed information about the origin of the historical bathymetric data is given in Progress Report 4 (Kolokythas *et al.*, 2019).
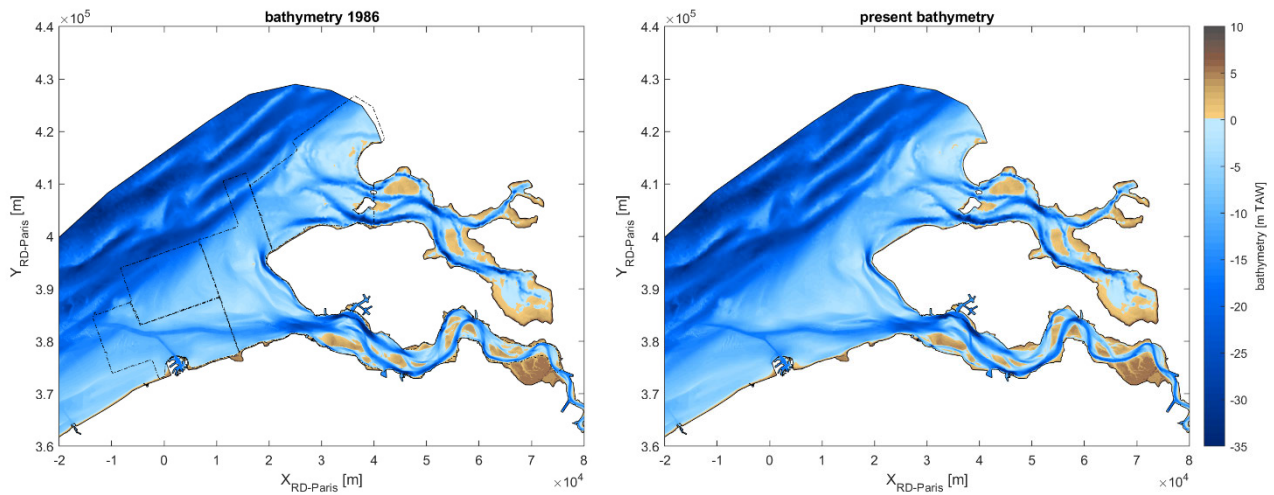
Figure 84 – Historical bathymetric data around the year 1986 (left) and present bathymetry (right) of the Scaldis-Coast model. The historical data occupy only the areas enclosed by the four dashed polygons (left figure).

In the same manner, the bathymetric data around the years 1996 and 2005 are interpolated on the computational grid in the areas enclosed by the dashed polygones shown in Figure 85. Note that these two historical bathymetries are used only for comparison against the numerical results of the hindcasting model, i.e. they are not used in the construction of other historical models.
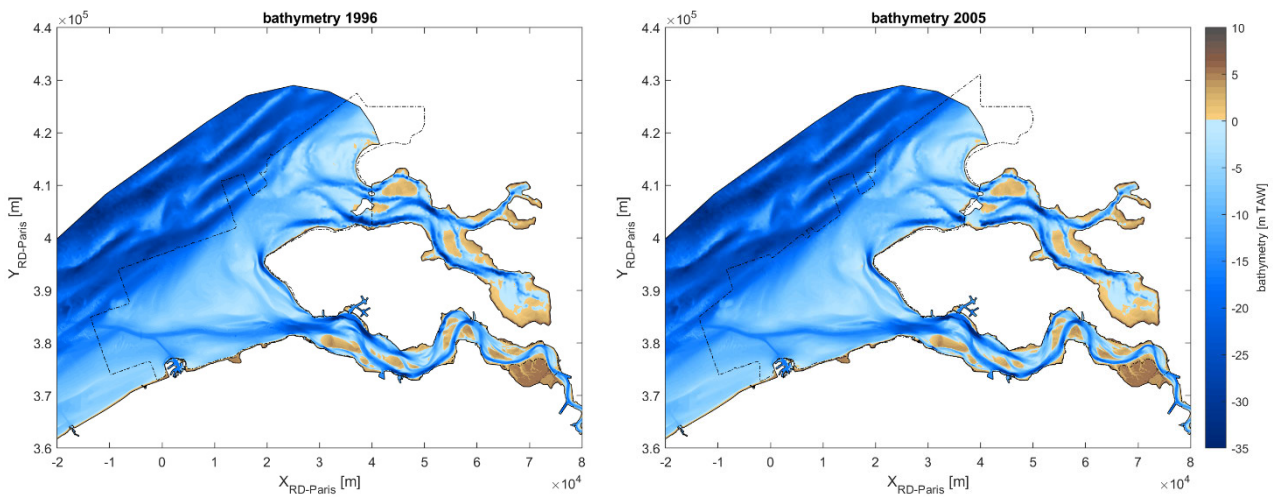
Figure 85 - Historical bathymetric data around the year 1996 (left) and 2005 (right). The historical data occupy only the areas enclosed by the dashed polygons.

The difference of historical bathymetries of the years 1996, 2005 and the current bathymetry against the reference historical bathymetry of the year 1986, are presented in Figure 86. A general observation that comes from a quick overview of the three subfigures is that the shape of main sedimentation-erosion patterns do not change substantially over the passing years, whereas the accumulated and eroded volumes seem to become larger over time (blue and red filled contours become darker over time). Among the patterns of great interest is the pit formed at the entrance of the port of Zeebrugge,

which is obviously connected with the sedimentation at the areas of Paardenmarkt (east of Zeebrugge port) and Bay of Heist (next to the eastern breakwater of Zeebrugge port). The aforementioned patterns are directly related to the coastal works of the extension of the port. The erosion of the navigation channels of Pas van Zand and Schaar-Wiellingen is due to capital and maintenance dredging works and not due to natural mechanisms. Strong sedimentation-erosion patterns are also observed at the mouth of Western Scheldt such as sedimentation at Breskens and erosion of the Geul van Walvischstaart. Large accumulation of sediment is observed at the bank from Rassen to Elleboog, while the opposite (deepening) is observed at Oostgat. Finally, strong morphodynamic activity is observed at the channels and banks between Vlissingen and Hooge Platen. To give an idea about the magnitude of sedimentation-erosion patterns developed over a 30-year period, it is noted that the order of magnitude of bed level change at the surroundings of Zeebrugge port is ±3 m, ±5 m at the area of the mouth and ±10 m at the channels and banks of the Western Scheldt. It is reminded that these bed level changes include both human and natural morphological activities.

5.1.2 Hindcasting: Reference simulation settings and results

For the reference morphodynamic simulation (SED069) the following considerations were taken into account:

- The model settings are identical to those presented in Section 3.2 of the present report. The only difference is the spin-up period, which now equals to four representative tides instead of four days of realistic forcing.
- The bathymetry of the year 1986 is considered at the temporal starting point (t=0) of the simulation.
- A schematized tidal forcing consisting of 1 080 successive representative tides, i.e. 1 102.5 days (about 3 years), was applied in the hydrodynamic module. For the reference run RT202 was selected.
- A MOFAC equal to 10 was considered in the morphological module, resulting to a simulation period of 11 025 days (10 times the hydrodynamic time) or else about 30 morphological years.
- Waves were not considered in this first modelling attempt. In the reference run the Engelund Hansen transport formula is used. The effect of waves is not considered in this formula. It is assumed the bed evolution in the (offshore) vicinity of the port and mouth aera is tidally driven.

In Figure 87, the sedimentation and erosion patterns of the bed evolution after 10 years (top figure), 19 years (middle figure) and 30 years (bottom figure). The specific snapshots were selected in order to make feasible a direct visual comparison with the corresponding bathymetry difference plots of Figure 86. The main observations that come from the visual inspection of the compared snapshots are roughly the following:

- The erosion pattern at the entrance of port of Zeebrugge (pit) is more or less captured by the model.
- Strong sedimentation at Paardenmarkt (and the surroundings) is numerically predicted by the model. The pattern presents differences compared to the measured bathymetries.
- In the difference plots of the measurements strong accumulation of sediment is observed at all instants at Bay of Heist, while in the model sedimentation can be observed a bit more off-shore east of the eastern harbor breakwater (Figure 89). The model seems to be incapable of reproducing the specific pattern, even though in the 30-years snapshot serious amount of sand has been transferred closer to Bay of Heist. This discrepancy can be attributed to possible differences in the composition of the transferred material, which in reality contains a large fraction of mud. Notice that in this run, waves are not taken into account. However, it has been noticed before with other models, including waves, that it seems not possible to reproduce the sedimentation at Bay of Heist without including fine sediments (Wang *et al.*, 2015).
- The model predicts accumulation of sand in the navigational channels (e.g. Pas van Zand and Schaar-Wiellingen). In the measured difference plots deepening of the channels is observed over the years, due to dredging works and not due to natural mechanisms. In the first refence runs, dredging and dumping module is not yet activated. The dredging and dumping module will be discussed in the next section.

- The real sedimentation/erosion patterns at the bank from Rassen to Elleboog, the Geul van Walvischstaart and the surroundings are reasonably reproduced by the model.
- Sedimentation patterns at Vlakte van de Raan (and at the north) are reasonably predicted by the model.
- On the other hand, the accumulation of sediment at Breskens is not well represented by the model.
- The strong morphodynamic activity observed at the channels and banks between Vlissingen and Hooge Platen can be roughly reproduced by the model, but there is room for improvement. The human interventions in the area must also be taken into account. It has to be mentioned here that the Spijkerplaat is one of the most dynamic shoals in the Western Scheldt. Due to the migration of the bank to the north, locally bed level differences up to ten meters in one year have been measured here (De Maerschalck *et al.*, 2017).

In order to have a clear view of how the sea bed evolved due to the occurrence of the aforementioned morphological changes, the predicted bottom levels at the area of interest 10 years, 19 years and 30 years after the beginning of simulation are shown in Figure 88 and Figure 89. For comparison with the reference situation the bottom level at t=0 is also given in Figure 88. It has to be mentioned that the predicted morphological patterns (ridge-shaped formations) mainly observed in 30-year evolution figure (bottom panel of Figure 89) at the area of Paardenmarkt, do not actually correspond to realistic formations. As it will be discussed later on, in the quantitative evaluation of the model, the uncertainty of the model seems to increase substantially for numerical predictions over 10 morphological years. Besides, the development of such unnatural bed undulations may be encountered by implementation of the right bed smoothing technique, such as the SUPG treatment presented in section 5.1.7.
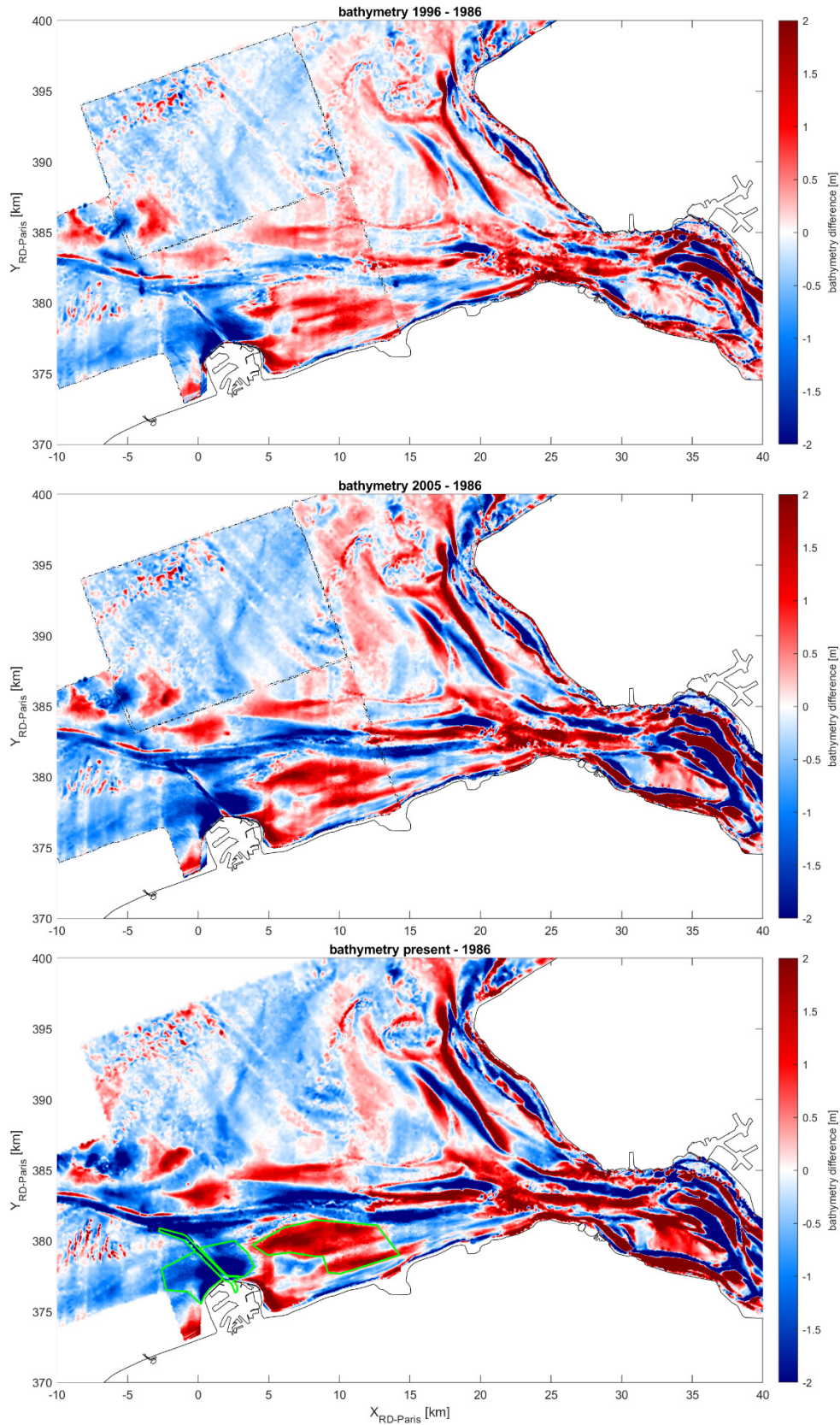
Figure 86 – Difference plots between historical and present bathymetries using as reference the bathymetry of the year 1986. Blue is erosion
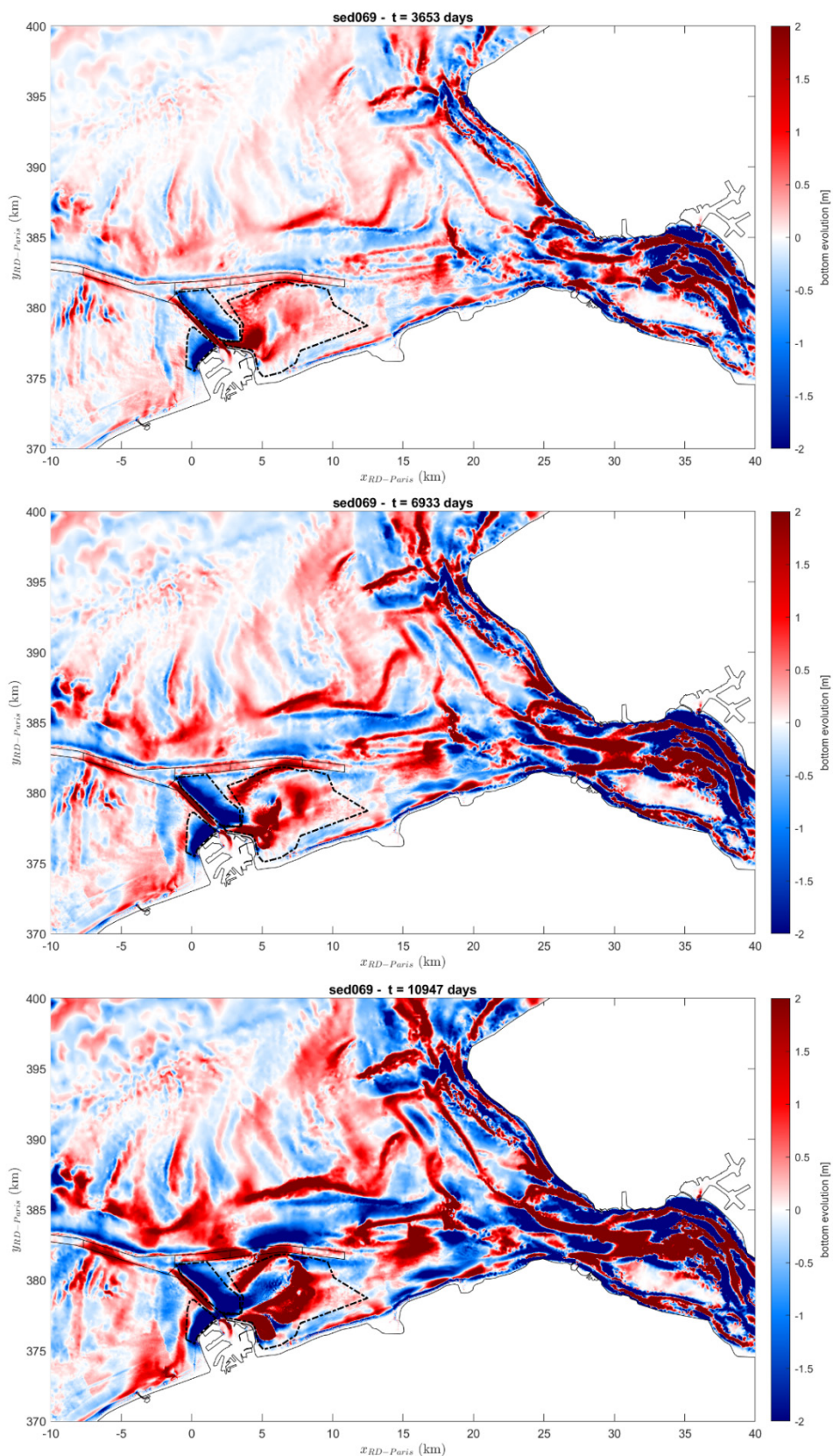
Figure 87 – Sedimentation/erosion patterns of the bed evolution resulting from the reference simulation after 10 years (top figure), 19 years (middle figure) and 30 years (bottom figure). Polygons indicate the areas where volume change is calculated.
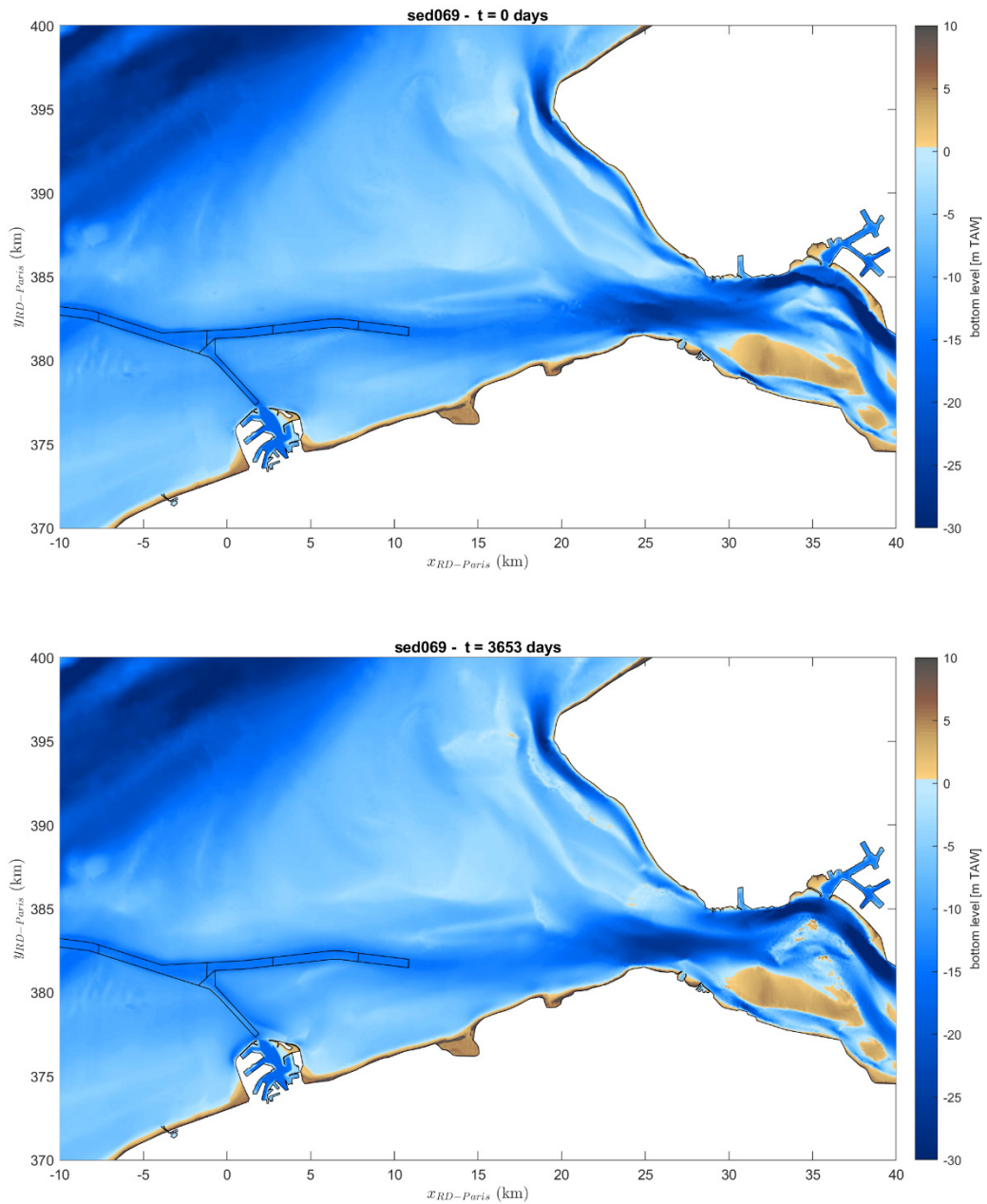
Figure 88 – Bottom level at the area of interest at the beginning of the simulation period [t=0] (top figure) and after 10 years (bottom figure).
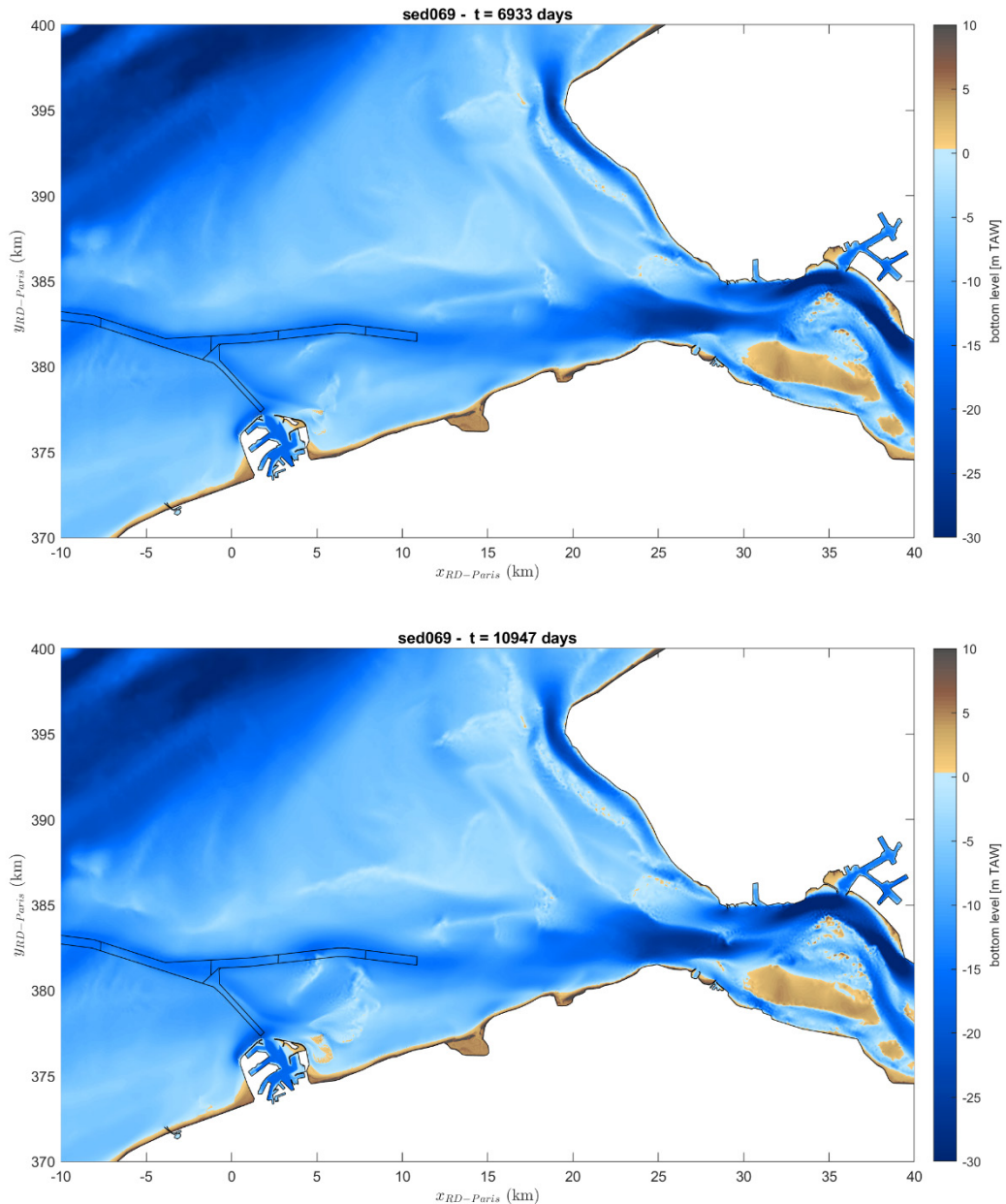
Figure 89 – Bottom level at the area of interest 19 years (top figure) and 30 years (bottom figure) after the beginning of simulation.

In order to quantify the performance of the reference model in predicting morphological changes at specific coastal areas of interest, sediment volume changes with respect to the (starting) year 1986 were calculated and compared with the corresponding ones coming from the measured bathymetries. The areas considered in this comparison are enclosed in the three polygons shown in Figure 87, and correspond to the highly eroded areas in front of Zeebrugge port breakwaters and the extensive area around Paardenmarkt. The polygons were sketched so that they roughly enclose the numerically predicted morphological patterns.

In Figure 90 the numerically predicted sediment volume changes over the simulation period are compared to the measured ones at each of the selected areas. It is indicated that the model performs very good in predicting the volume changes after 10 years at the considered areas. At the end of the simulation period volume changes seem to be highly overestimated by the model at the area eastern of Zeebrugge (Paardenmarkt) and overestimated at the area in front of the western breakwater. On the other hand, the predicted volume change at the area of the eastern breakwater seems to be in very good agreement with measurements over the whole simulation period.
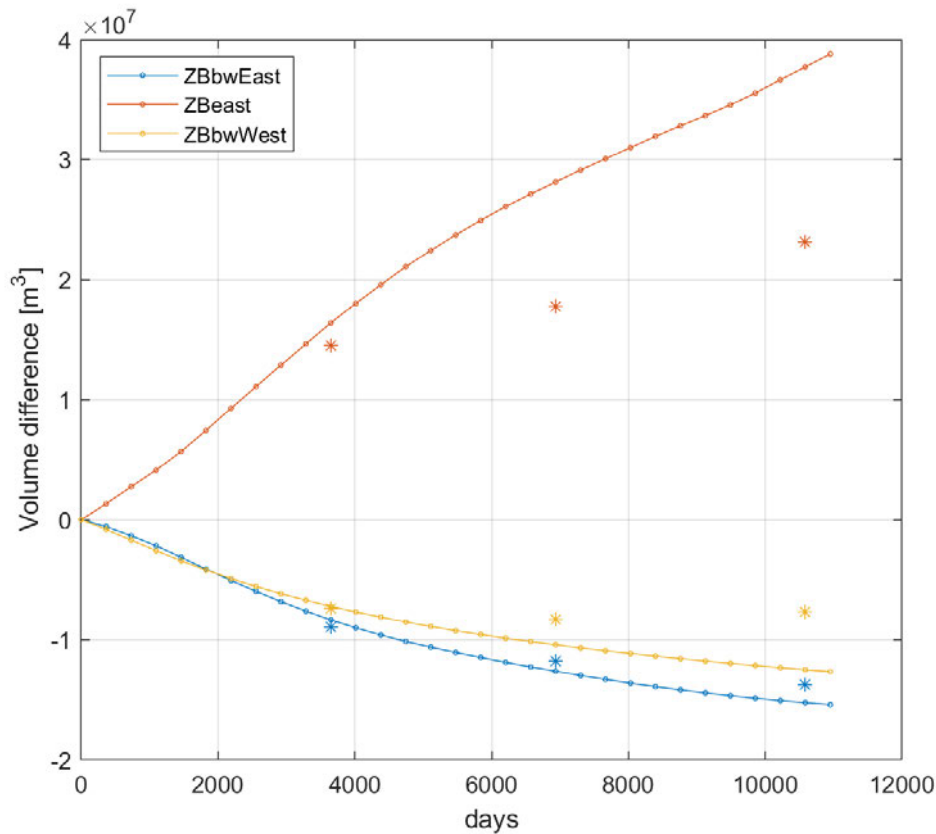
Figure 90 – Measured (asterisks) and numerically predicted (lines) volume change with respect to the year 1986 for the three polygons depicted in Figure 87. ZBbwEast = Zeebrugge eastern breakwater; ZBbwWest = Zeebrugge western breakwater; ZBeast = Paardenmarkt and surroundings;

Then, for the sake of completeness, the volume change enclosed in polygons based on the <u>measured</u> morphological patterns at the area around Zeebrugge port (see last subfigure in Figure 91). In Figure 92, the numerically predicted sediment volume changes over the simulation period are compared to the measured ones at each of the selected areas. This time summations of the eroded volumes in the two polygons in front of the port and the accumulated volumes at the polygons of Pas van Zand and Paardenmarkt are calculated. The latter summation has been done under the assumption that the dredged material from Pas van Zand is stored at Paardenmarkt. It is found that the model predicts the trend of increasing volume changes over the entire period, but significantly underestimates the magnitude of volume change in the area of Paardenmarkt.
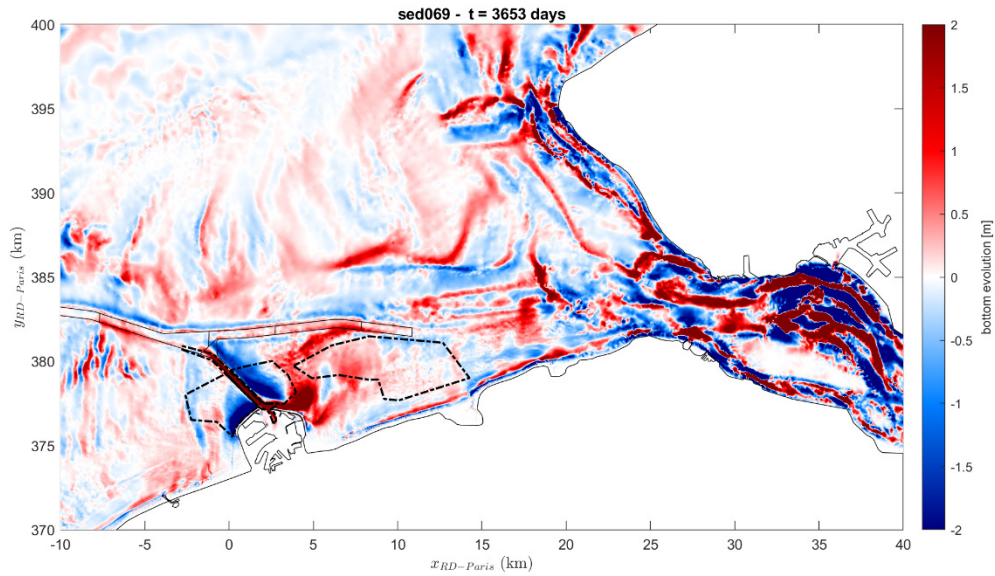
Figure 91 - Sedimentation/erosion patterns of the bed evolution resulting from the reference simulation after 10 years, with the polygons indicating the areas where volume change is calculated.
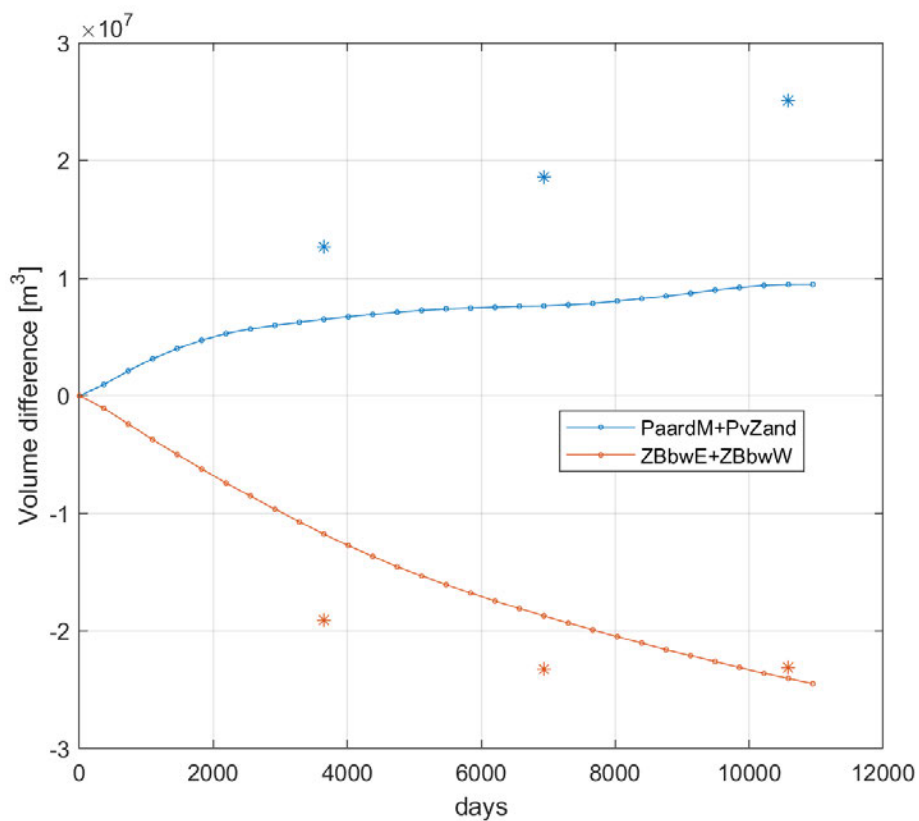
Figure 92 - Measured (asterisks) and numerically predicted (lines) volume change with respect to the year 1986 for the polygons depicted in Figure 91. ZBbwEast = Zeebrugge eastern breakwater; ZBbwWest = Zeebrugge western breakwater; PaardM = Paardenmarkt; PvZand = Pas van Zand.

5.1.3 Influence of transport formula

The classic Engelund & Hansen (1967) formula (ICF=30) which accounts for the total load transport, was initially compared to the modified Engelund & Hansen (which accounts for sand dunes) total load formula (ICF=3) and the Van Rijn's bed load formula (ICF=7) along with the advection-diffusion equation for the suspended load. It is found that the modified Engelund & Hansen formula substantially overestimates the volume that accumulates at the area around Paardenmarkt, while the coupled Van Rijn's-suspension formulation underestimates the eroded/accumulated volumes at the eastern breakwater region and at Paardenmarkt, respectively. The results were presented in Progress Report 4 (Kolokythas *et al.*, 2019) and they are not repeated here.

Since the final goal of the project is to create an integrated morphodynamic model for the coast (including waves and currents), the use of a formula for wave- and current-induced transport is mandatory. Two formulas that can account for coupled wave- and current-induced sediment transport in SISYPHE, are those of Soulsby- Van Rijn (ICF=5) and the one of Van Rijn (2007) are also tested. Note that the latter formula is not included in the utilized version of SISYPHE (7p2r2) and it is first implemented in this project.

The bed level change after a simulation period of about 10 years for the reference transport formula (Engelund & Hansen, sed069) and for Soulsby-Van Rijn (SVR, sed070b) and Van Rijn (VR07, sed070c) formulas, is presented in Figure 93. In general, both of the tested formulas lead to similar but by far more pronounced sedimentation-erosion patterns compared to the reference one, but obviously the SVR formula is more active compared to the VR07. Even though the two tested formulas present many similarities in terms of sed/ero patterns, noticeable differences are observed at the area between Paardenmarkt and Scheur van Wielingen and also at the mouth of Western Scheldt close to Breskens. Table 28 gives the sediment volume changes inside the polygons depicted in Figure 93 (top plot) for the period 1986-1996, for each of the implemented formulation. It is found that both the SVR and the VR07 formulas substantially overestimate the volume that accumulates at the area around Paardenmarkt, and the eroded volumes in front of the breakwaters.

Table 24 – Sediment volume changes inside the polygons of Figure 93 for the period 1986-1996 (10 morphological years). Comparison between the measurements and the numerical results of three different sediment transport formulations. EH-30 = Engelund & Hansen; SVR = Soulsby-Van Rijn; VR07= Van Rijn (2007).

Area (Polygon)	Volume change 1996-1986 [x10^6 m^3]			
	Measured	EH-30	SVR	VR07
ZBbwEast	-9.0	-8.35	-17.0	-14.6
ZBbwWest	-7.4	-7.2	-14.0	-12.3
ZBeast	+14.5	+16.4	+42.2	+35.1
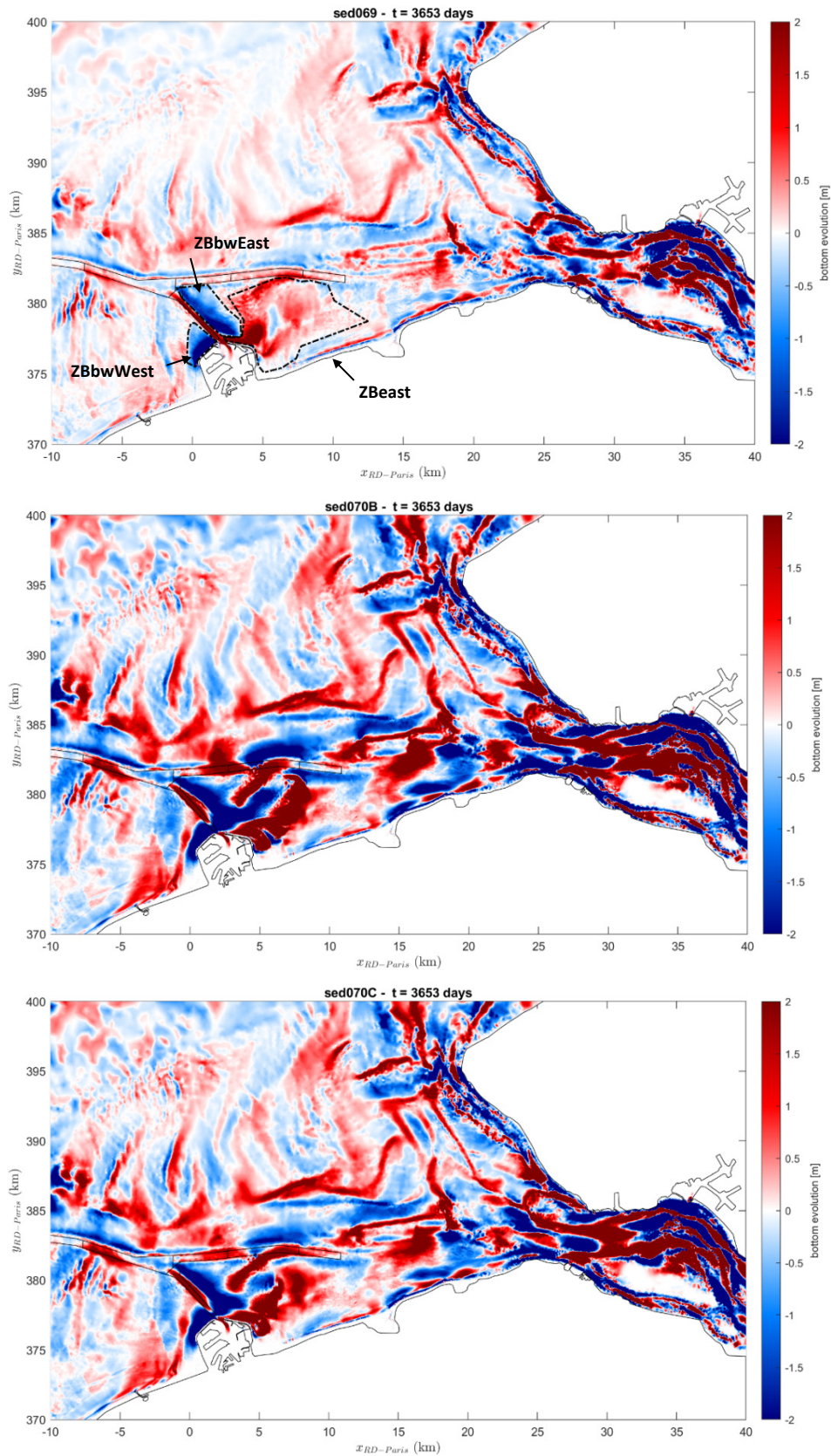
Figure 93 – Bed level change [m] obtained by use of three different sediment transport formulations after a simulation period of 10 years; (top) Engelund & Hansen – [30], (middle) Soulsby – Van Rijn [5], (bottom) Van Rijn (2007).

5.1.4 Influence of morphological tide

The bed level change after a simulation period of 10 years considering the Van Rijn's formula, VR07, for two representative tides, RT202 and RT153, is presented in Figure 94. Recall from Table 20 on page 71 that RT153 is considered as most appropriate for the Van Rijn 2007 formula, when considering the whole Belgian Coast. RT202 is the best for Engelund and Hansen but still scores well for VR07. It is found that the two representative tides lead to very similar results in terms of sed/ero patterns and their magnitude. It is worth mentioning, though, that RT202 (top plot) seems to move the sed/ero patterns slightly faster in time compared to RT153 (bottom plot). For example, the sedimentation pattern east of Zeebrugge harbor, which is driven by the flood dominated transport, has moved more westwards for RT202 simulation than for RT153 simulation.
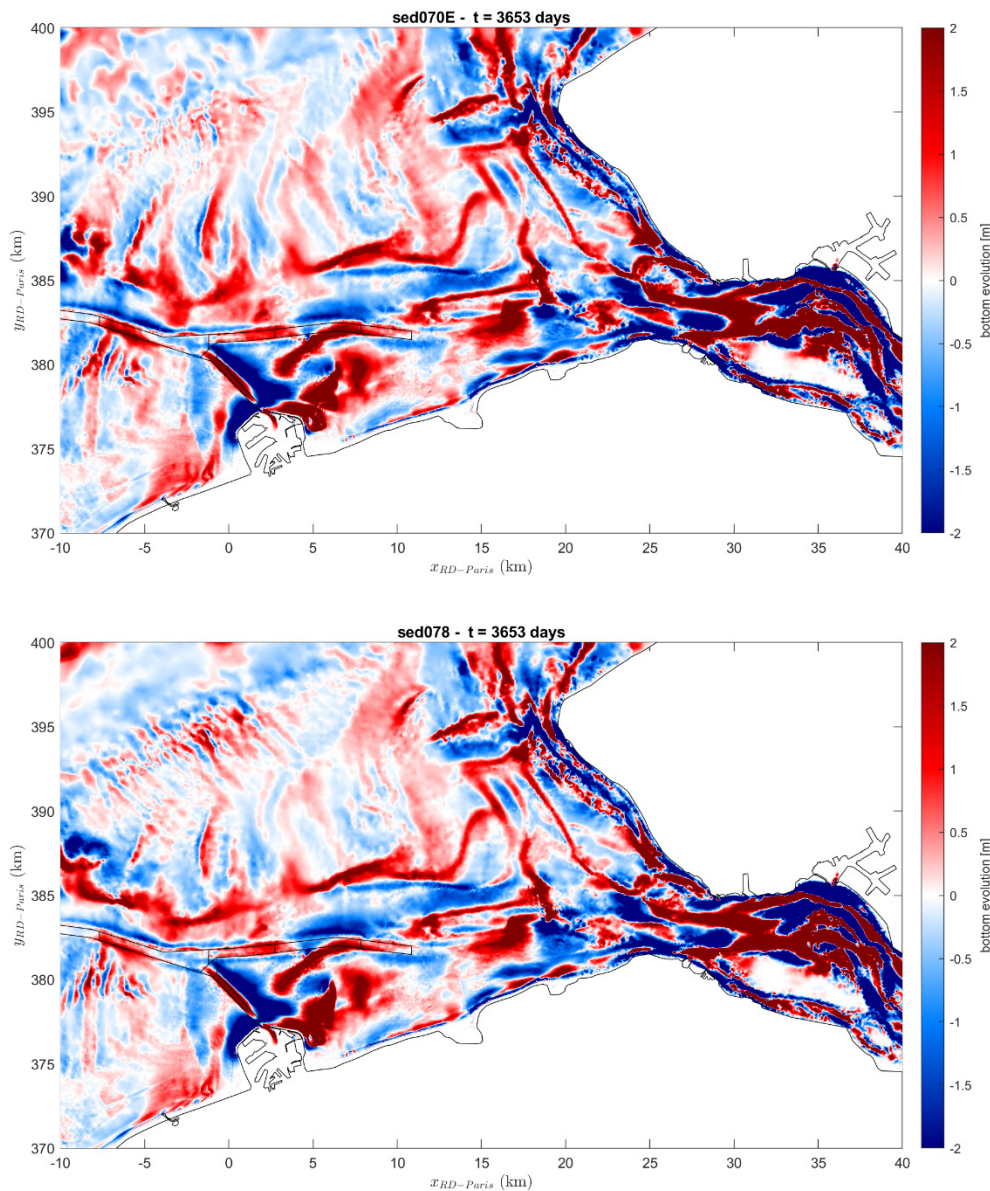
Figure 94 – Bed level change [m] obtained after a simulation period of 10 years by use of the Van Rijn's total load formula [VR07B] and two different representative tides; (top) RT202, (bottom) RT153.

The behaviour of the model at the area of the Flemish banks is also of interest. The representative tide seems to affect substantially the formation of the sed/ero patterns and therefore the morphological evolution of the Flemish banks. In Figure 95, it is shown that for the case of RT153 (bottom plot) the Oostdyck crest seems to migrate towards the offshore direction in contrast to what is observed for the RT202 (top plot). This behavior can be possibly explained by the differences in the tidal asymmetries of RT153 and RT202. In addition to this, the sed/ero patterns of the western sand banks, such as the Buiten Ratel, present substantial differences between the two simulations with different representative tides. Specifically, in the case of RT153 the sed/ero patterns are found to be much weaker than in the case of RT202.

Note that apart from the implemented morphological tide, other parameters that have substantial influence on the evolution (or the stability) of the Flemish banks, such as propagating waves (not considered in this test) and the sediment composition of the local seabed, are incorporated in the model in the following sections. Also a numerical stabilization technique, i.e. the SUPG method (Streamline Upwind Petrov-Galerkin), presented in section 5.1.7, contributes in the stabilization of the Flemish Banks.
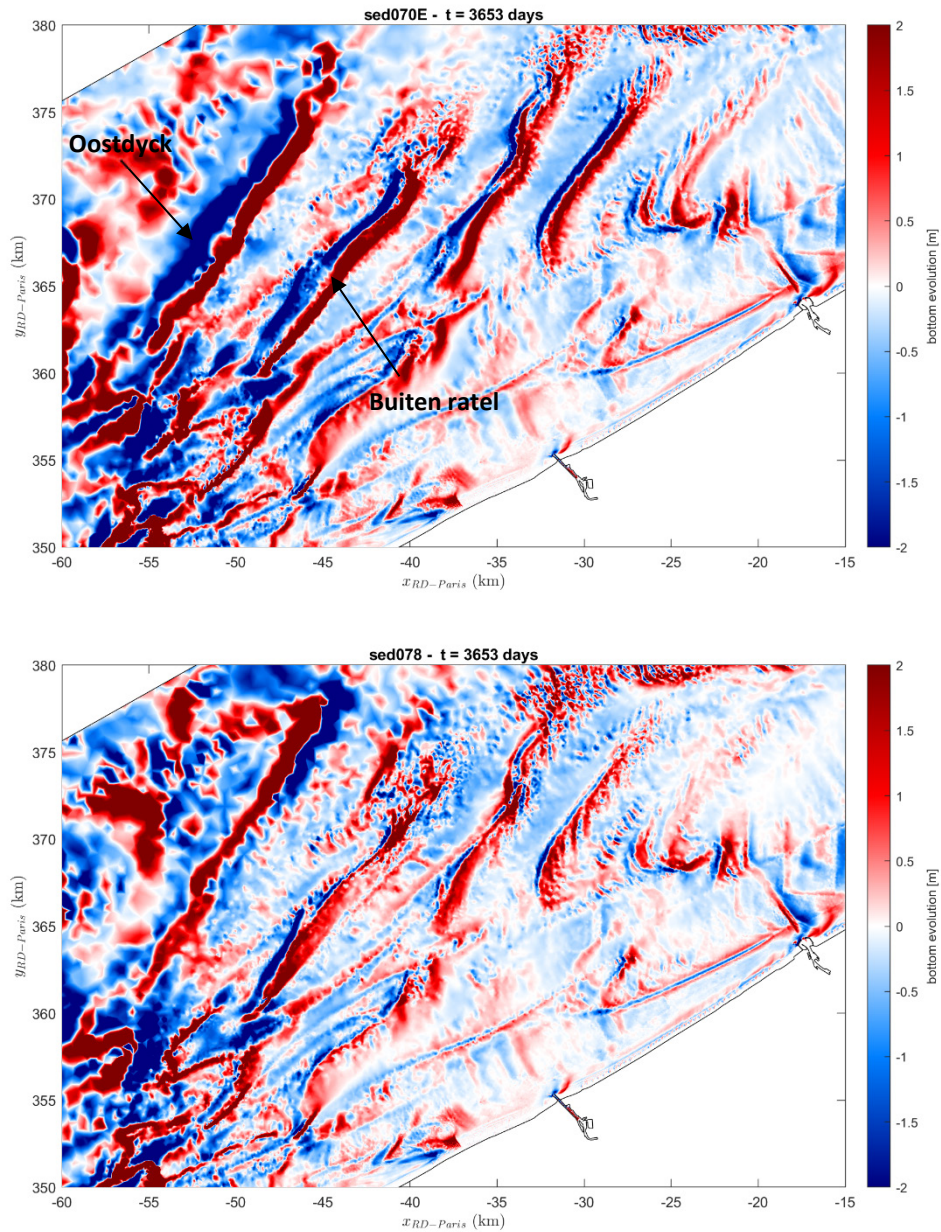
Figure 95 – Bed level change [m] obtained after a simulation period of 10 years by use of the Van Rijn's total load formula [VR07B] and two different representative tides; (top) RT202, (bottom) RT153.

5.1.5   Variable grain size

In all the morphodynamic simulations presented so far, sand of uniform median grain diameter, d_{50}, was considered as the transported bed material. The corresponding sensitivity tests performed within the hindcasting exercise, led to the selection of sand with d_{50} = 250 µm (Kolokythas *et al.*, 2019a). However, it is known that the consideration of a uniform d_{50} value for the entire model area is very simplistic and far from reality, since sediment size presents substantial variation at the investigated area. This is clearly indicated in Figure 96 and Figure 97 where the spatial distributions of the d_{50} of the sand fraction in the model domain, coming from two different published research studies, are presented.

The high-resolution data (250 m x 250 m) of Figure 96, which was reported in the thematic maps of MAREBASSE project (Van Lancker *et al.*, 2007), are only limited within the Belgian Continental Shelf (BCS). Since Scaldis-Coast domain extends beyond the BCS boundaries, the low-resolution data (0.125° x 0.125°) of Figure 97, which is part of the map of the northwest European Continental Shelf sedimentary environment (R. Wilson *et al.*, 2017), was utilized to complete the d_{50} map for our model, as the best available option for the time being. The main reason for selecting the specific low-resolution data, was the fact that the two datasets presented reasonable compatibility at the overlapping (BCS) area.

The main observations from the high-resolution dataset are:

- Very fine (<150 μm) to muddy (≈60 μm) sediment is located around Zeebrugge port.
- Fine sand (150-250 μm) is distributed along the (west) Belgian coast. Medium sand (300-400 μm) is observed, locally, at the transverse sand ridges of Koksijde.
- Medium sand of d_{50} = 300-350 μm is found at the deeper regions of the BCS up to the offshore boundary of the Scaldis-Coast domain. Local variation is observed at the Flemish sandbanks, where coarse sand (500-550 μm) can also be found.
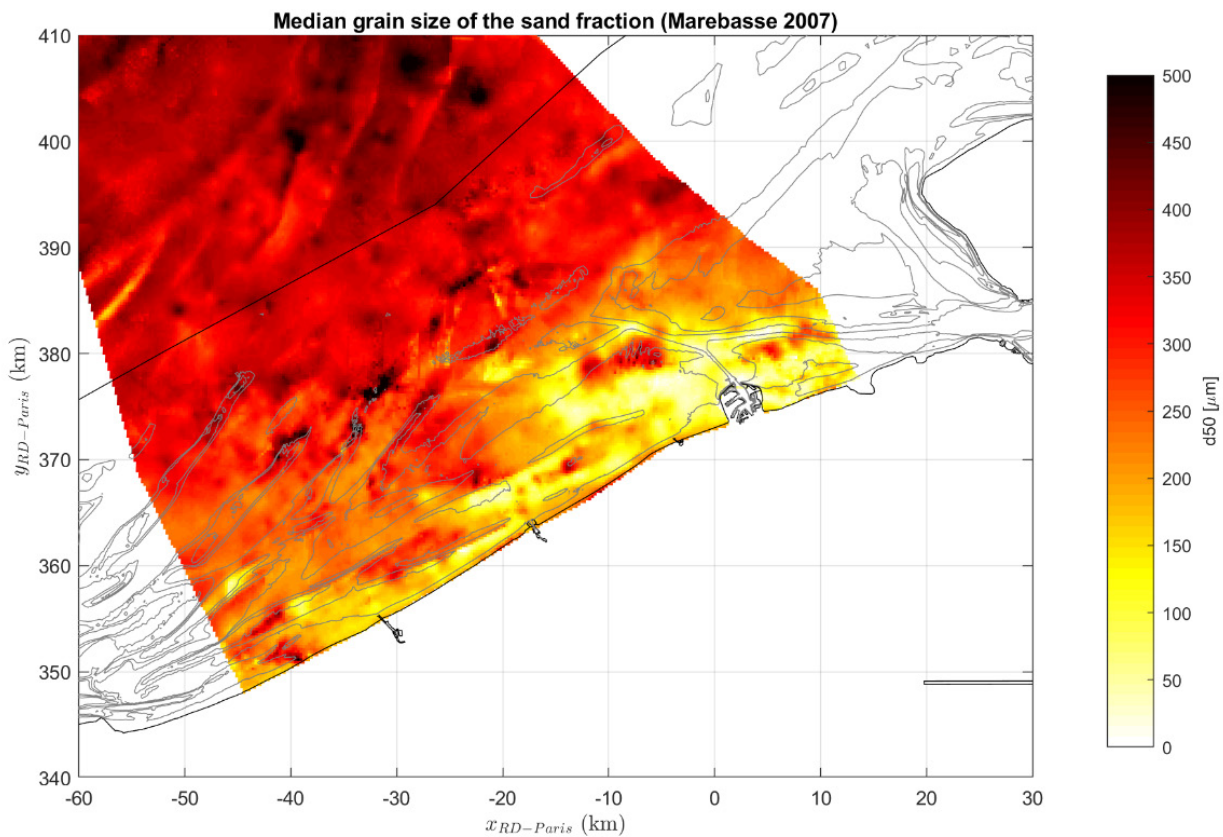
Figure 96 – Median grain size (d_{50}) distribution within the Belgian Continental shelf as reported in Van Lancker *et al.* (2007).

The main observations from the low-resolution dataset are:

- The sand is becoming coarser as we move westwards of the BCS domain towards the French continental shelf, where medium-coarse sand is found. The opposite behaviour is observed as we move eastwards of BCS towards the Dutch continental shelf, where medium-fine sand is found.
- At the area of Vlissingen medium-coarse sand is found, as shown by the limited data in the Western Scheldt.
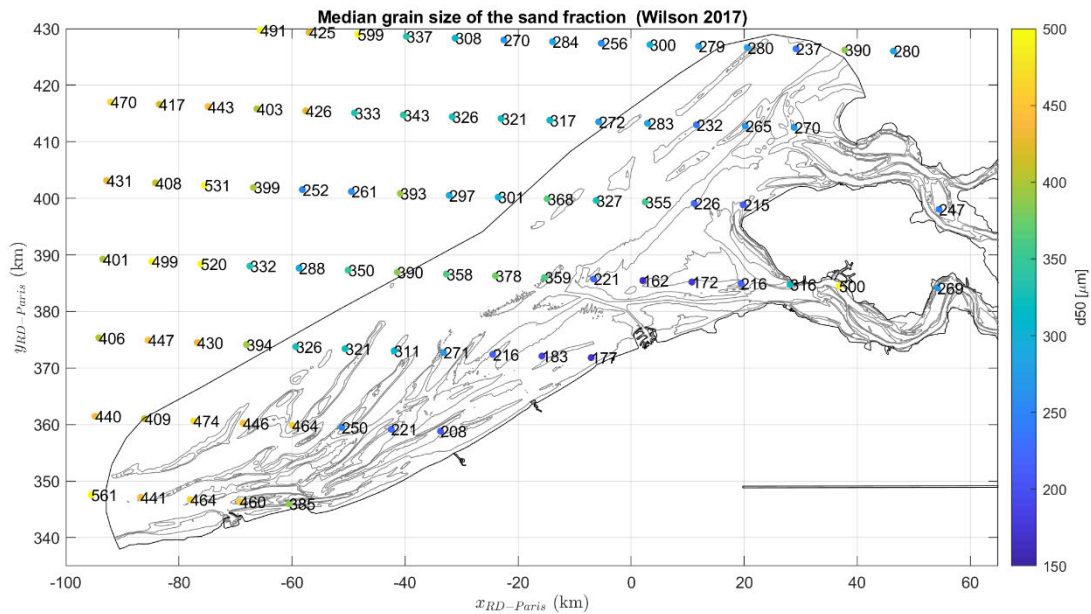
Figure 97 – Median grain diameter (d50) distribution at the southern North Sea region as reported in Wilson et al. (2017).

Sediment transport calculations with bed material of spatially varying d_{50} are possible in Scaldis-Coast under certain considerations and slight modifications in the source code of SISYPHE. In order to perform this objective, the capability of SISYPHE in coping with sediment mixtures, which may consist of two up to twenty classes, is being exploited.

By default, no vertical stratification of the classes is considered. Instead, the active layer concept is implemented, i.e., the composition of the movable bed layer is utilized for the calculation of the sediment transport rates for each class of sediment, leading to the weighted total sediment transport:

$$Q_{tot} = \sum_{i=1,N_{cl}} Avail(i)Q(i) \tag{3}$$

where N_{cl} is the number of classes, *Avail(i)* is the percentage of the class *i* in the active layer.

Briefly, the steps followed in SISYPHE for the calculation of bed morphology evolution, in case of sediment mixtures, are:

- Sediment transport rates are computed separately for each class by use of one of the provided bed (or total) load transport formulas
- The Exner equation is solved for each sediment class
- The total bed evolution is calculated by summing the individual bed evolutions of each class
- At the end of each time-step the new bed composition *Avail(i)* of the active layer is computed, ensuring the mass conservation of each class. The new composition is simply calculated based on the ratio of the evolution of each sediment class over the total evolution within one time-step.

However, in order to achieve spatially-varying d_{50} transport calculation in the Scaldis-Coast model, the concept of equivalent sediment transport is implemented. The number of classes in the active bed layer is limited, in this case to two classes, a fine and a coarse class, even though the Continental Shelf is characterized by a broad range of classes. The idea is to calculate the transport rate of material with specific d_{50} by summing the transport rates of two sediment classes, one of minimum d_{50} and one of maximum d_{50}. The reason that d_{50} values from sediment maps cannot be used directly in the calculations, is that sediment transport rates are calculated for each considered d_{50} in SISYPHE, which makes this direct implementation practically impossible.

As mentioned before, two sediment classes are considered, i.e., one for fine sand (d_{min} = 150 μm) and a second one for coarse sand (d_{max} = 500 μm). The minimum and maximum values of d_{50} were selected based on the grain size distribution maps in the model's domain, depicted in Figure 96 and Figure 97. Then, the percentage (availability) of each of the two selected classes (variable *Avail* in Eq. 3) in every grid node is calculated, so that their total transport rate is identical to the transport rate of the real d_{50} value (from the sediment map). The percentage calculation is based on:

1. the available grain size distribution maps
2. the selected sediment transport formula

The latter of the above parameters has to be taken into account, as long as the relation between transport rate Q and d_{50} is not linear. In the hypothetical case of a linear relation between Q and d_{50} the percentage of each class would be calculated by linear interpolation (e.g. d_{50} = 375 μm would correspond to 50% availability of each of the two selected classes). For the total load formula which has been considered in this exercise, i.e., the Engelund-Hansen formula, the percentage, *Avail*(1) of d_{min} = 150 μm in the sediment mixture of two classes, is calculated based on the relation $Q \sim 1/d_{50}$, leading to the availability curve depicted in Figure 98. Specifically, the percentage of the fine sediment in the mixture is given by the following expression:

$$Avail(1) = (1/d_{max} - 1/d_{50})/(1/d_{max} - 1/d_{min}) \qquad (4)$$

Apparently, the percentage of d_{max} = 500 μm in the mixture will be *Avail*(2) = 1- *Avail*(1).
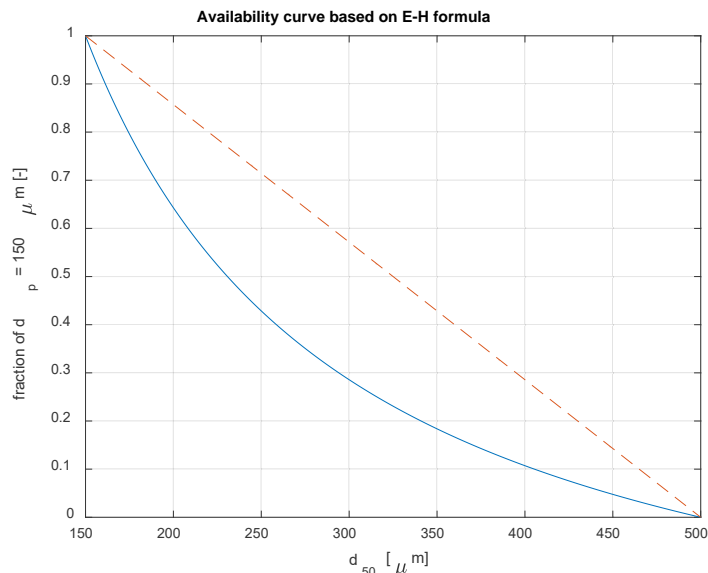
Figure 98 – Percentage of fine sand (dmin = 150 μm) in the sediment mixture of two classes (150 & 500 μm) based on the Engelund & Hansen formulation.

Then, the availability map (percentage of d_{min}) presented in Figure 99, is generated in order to be used as input for the spatially-varying d_{50} simulations.
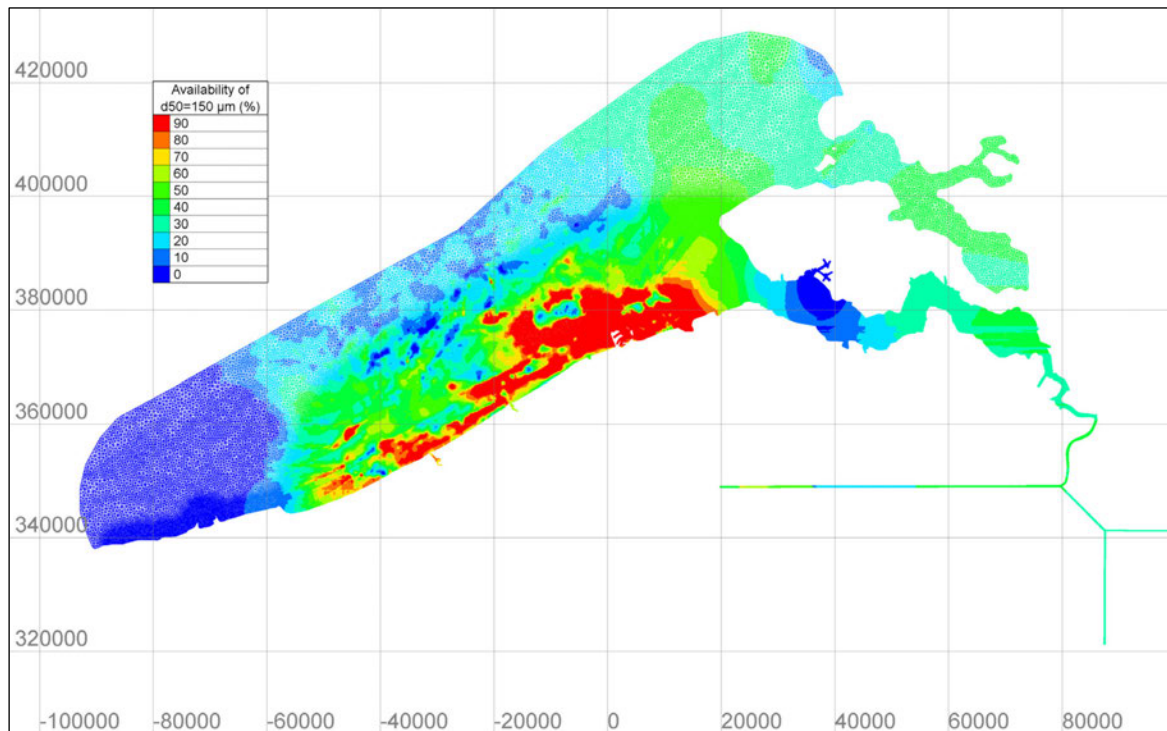
Figure 99 – Percentage of fine sand (dmin = 150 µm) in the sediment mixture of two classes (150 & 500 µm) within the Scaldis-Coast domain, based on the sediment maps of Figure 96 – Figure 97 and the Engelund & Hansen formulation.

The effect of varying d_{50} on the long-term morphological evolution in the Scaldis-Coast domain is evaluated through the well-known hindcasting exercise. The bed level change at the end of the simulation period, due to current-induced transport calculated by the Engelund-Hansen's formula, for the case of varying d_{50} is compared to that of the uniform grain size (d_{50} = 250 µm) in Figure 100. The main morphological patterns predicted by the varying d_{50} simulation (bottom figure), present many similarities with those of the uniform d_{50} case. However, due to the fact that the medium-sized sand (250 µm) has been replaced by fine sand (150 µm) at the area around Zeebrugge (according to Figure 96), the magnitude of the sed/ero patterns is now relatively larger. Larger eroded volumes in front of Zeebrugge breakwaters and stronger accumulation at Paardenmarkt, are found. Moreover, the sed/ero patterns formed close to the eastern breakwater of Zeebrugge, indicate that the local reduction of the grain size results into faster movement of these patterns eastwards. This is a desired behaviour if we take into account the corresponding measured patterns of Figure 102 (bottom). At the mouth of Western Scheldt, the morphological patterns are relatively weaker for the case of varying d_{50} due to the increase of the local grain size of sediment.
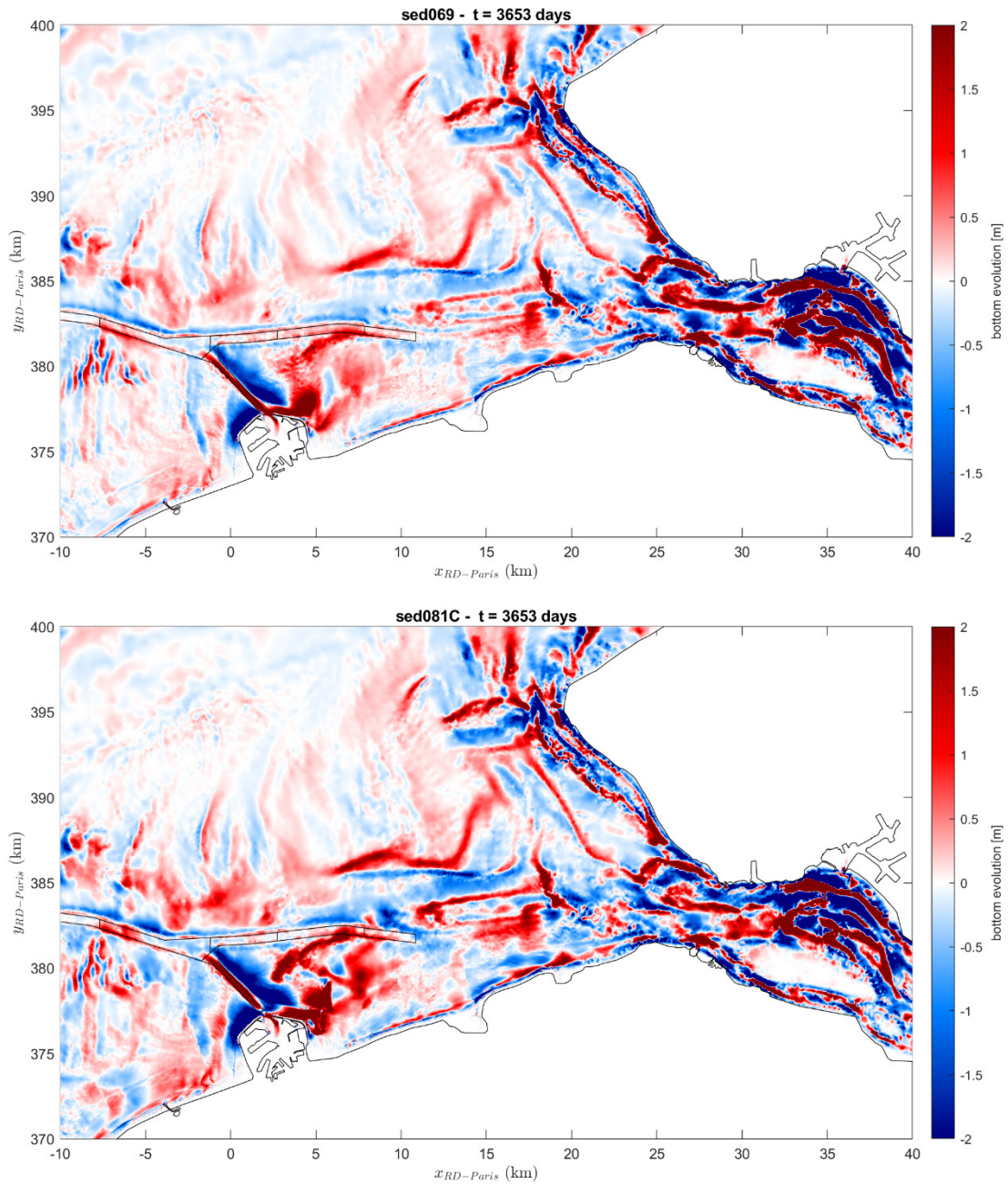
Figure 100 – Bed level change [m] obtained by use of Engelund & Hansen's sediment transport formula and two different d50 configurations after a simulation period of 10 years; (top) uniform d50 = 250 μm, (bottom) spatially-varying d50. [RT202, no waves]

5.1.6   Influence of waves

One of the main goals of this study is the development of a numerical model capable of predicting the morphological evolution both close to the coastline and at relatively deeper waters. Thus, the selection of a sediment transport formula that responds well to combined wave and current forcing, both at shallow waters (where wave-driven transport can be dominant) and at deeper areas, remain of high importance.

Testing of two other formulas that account for waves, i.e. the Soulsby van Rijn (SVR) and the Van Rijn's 2007 (VR07) formula, has showed reasonable agreement with the measured morphological patterns along the coast (Kolokythas *et al.*, 2019b). However, both formulas (SVR and VR07) tend to substantially overestimate the magnitude of the morphological patterns at deeper areas, as shown in section 5.1.3. Therefore, the investigation for a transport formula with balanced behavior both close to the coast and at deeper areas when driven by waves and currents, is continued with the evaluation of Bijker's formula (1992) in coupled wave and current simulations.

Wave- and current-induced sediment transport is considered through the application of the Bijker's formula in the hindcasting simulations. In order to get a clear view of how wave-induced currents affect the morphological patterns at the end of the simulation period, the bed level change plots of simulations, with and without wave forcing, 10 years after the expansion of Zeebrugge port, are presented in Figure 101. As mentioned before, the schematized wave conditions presented in section 4.1 were utilized for this exercise. In general, the shape of the sed/ero patterns developing at the broader area east of Zeebrugge are similar in the bed evolution maps of both simulations. However, the magnitude of the patterns resulting from the simulation with waves (swc011) is substantially larger than that of the currents-only simulation. Furthermore, major differences between the two simulations can be observed along and very close to the coastline, where the wave-induced transport is expected to be dominant. The simulation with wave forcing predicts strong erosion at Knokke beach and around Blankenberge harbour, while it gives strong accumulation at both sides of the Zeebrugge port. The aforementioned patterns are absent from the predictions of the currents-only simulation. Noticeable differences are also found in the Western Scheldt and specifically at the area of Vlissingen.

The bed level change at the end of the simulation period for the Bijker's transport formula coupled with RT137 tidal forcing against the measured bed level change (bathymetry 1996 – 1986), is presented in Figure 102. The main 'offshore' morphological patterns (these that are found in a distance from the coastline) predicted by Bijker's formula, present many similarities with those of the reference sediment transport formula (Engelund & Hansen) which was tested under tidal forcing only and were presented previously. The added value of including wave-induced sediment transport in the model is expected to be expressed through the reproduction of morphological patterns close to the coastline. The accumulation of sand at Bay of Heist, even though it is not accurately captured by the model, is now more evident. The same applies for the accumulation of sand at the west side of Zeebrugge port. The difficulties of numerical models in predicting sedimentation at Bay of Heist is a known issue, mainly attributed to the non-consideration of the muddy composition of the transferred material. The reduction of mean diameter, based on corresponding sediment distribution maps, is a first step to improve the performance of Scaldis-Coast, before incorporating sand-mud sediment transport simulation. In addition to the previous improvements from wave-induced transport consideration, strong erosion observed along Knokke beach is also better reproduced by the model.
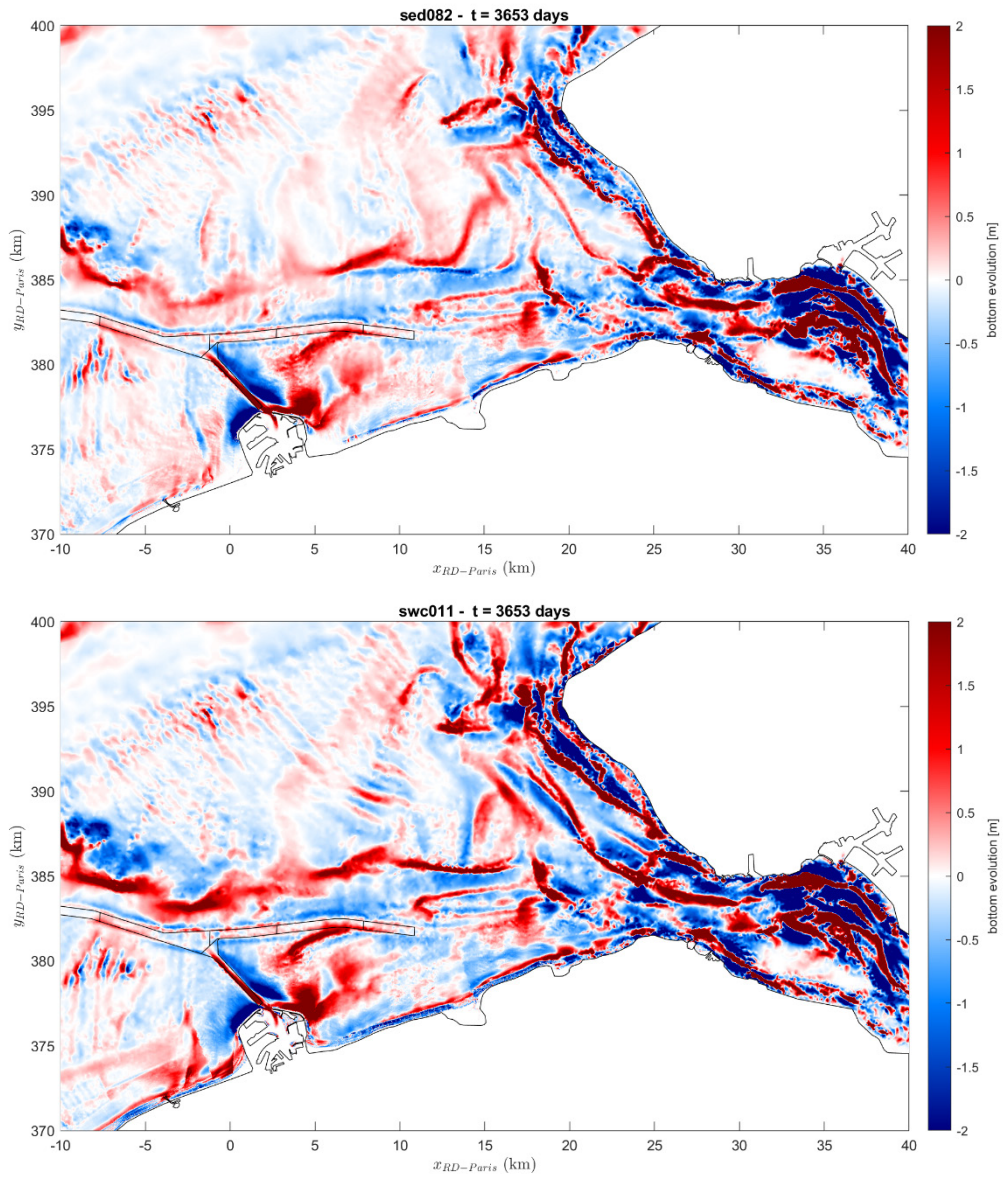
Figure 101 – Bed level change [m] obtained by use of Bijker's [b=5] sediment transport formula and RT153 after a simulation period of 10 years; (top) wave effect is deactivated, (bottom) wave effect is activated.
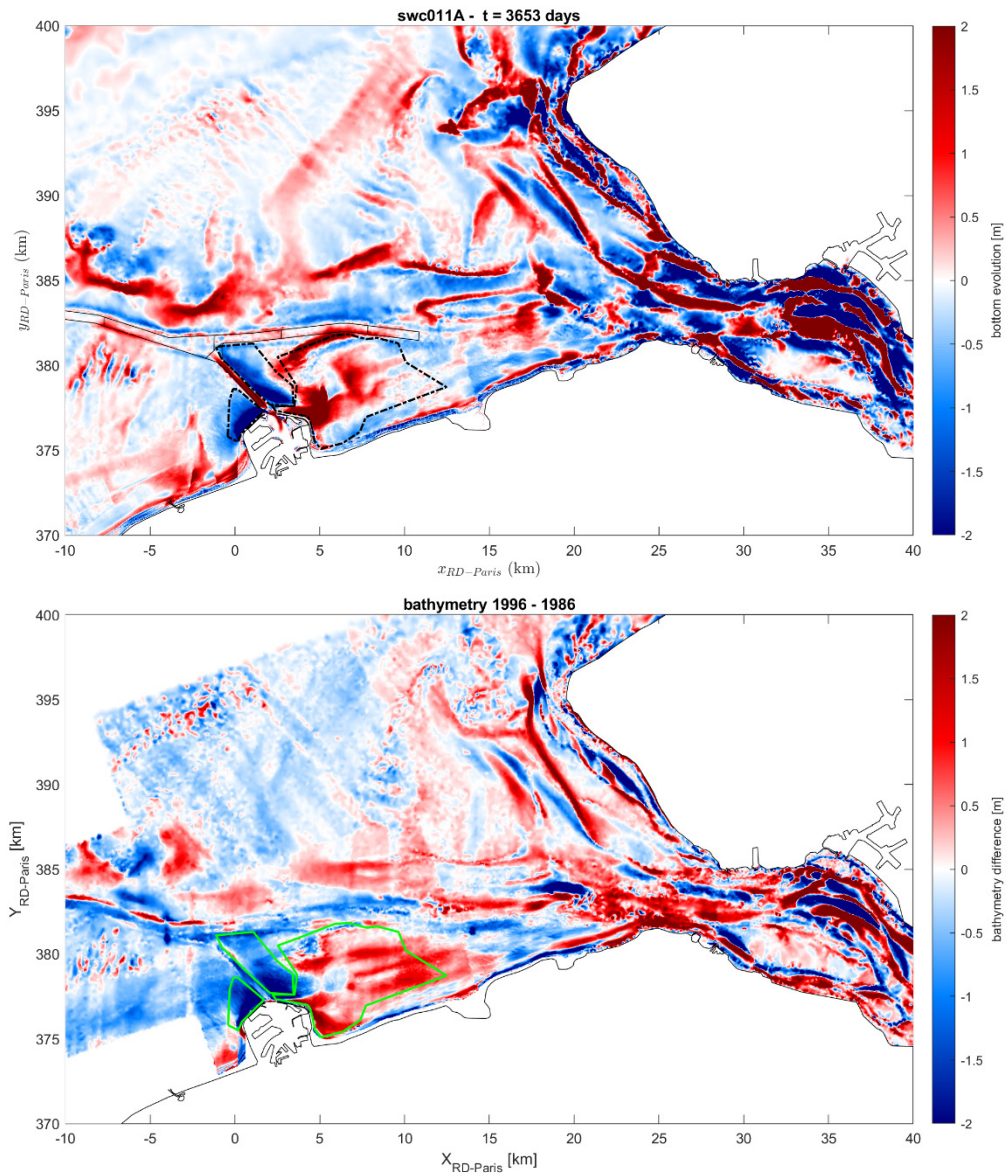
Figure 102 – Bed level change [m] obtained by use of Bijker's formula and RT137 (top figure) and measured bed level change (bottom figure) after a simulation period of 10 years; Sand volume change is calculated in the depicted polygons.

Table 25 gives the measured and the modelled sediment volume changes inside the polygons depicted in Figure 102 for the period 1986-1996. The modelled volumes come from simulations with Bijker's formula and two different representative tides, i.e. RT153 and RT137. It is found that RT137 is more active than RT153, giving larger eroded volumes in front of Zeebrugge breakwaters and stronger accumulation at Paardenmarkt. Compared to the measured volumes, RT137 performs better in the estimation of eroded volume at the eastern breakwater, but overestimates the accumulated volume at Paardenmarkt. It is reminded that RT137 is the tide that scores highest in the representation of the mean sediment transport at this area. Careful observation of the sed/ero patterns of Figure 101 (bottom) and Figure 102 (top), formed close to the eastern breakwater of Zeebrugge, indicates that RT137 drives these patterns eastwards relatively faster than RT153. This is a desired behavior if we take into account the corresponding measured patterns of Figure 102 (bottom).

Table 25 – Sediment volume changes inside the polygons of Figure 102 for the period 1986-1996 (10 morphological years). Comparison between the measurements and the results of Bijker's formula considering two representative tides (RT153 & RT137).

Area (polygon)	Volume change 1986-1996 [x10^6 m^3]		
	Modelled RT153	Modelled RT137	Measured
Eastern Breakwater	-6.4	-8.0	-9.0
Western Breakwater	-6.8	-8.3	-7.4
Paardenmarkt	+16.4	+19.5	+14.5

5.1.7 On the role of BAW smoothing and selection of advection scheme (SUPG) for stability and to supress spurious wiggles

BAW smoothing

In order to smoothen out instabilities of the sea bottom during the morphological simulation (especially close to non-erodible areas) the BAW (Bundesanstalt für Wasserbau) institute has updated the subroutine '*bedload_solvs_fe.f*' that solves the Exner equation (continuity of sediment mass) implementing a filtering procedure of the bed level. This development prevents from the continuous growth of spurious numerical spikes of the bottom level by reversing the local direction of sediment transport. The additional computational cost of BAW smoothing is negligible.

The updated solver of the Exner equation was utilized in an one year morphological simulation considering wave and current forcing and model settings identical to a run without the implementation of BAW smoothing. Hardly noticeable differences can be observed in Figure 103, which depicts the sed/ero patterns after one year, between the run without bottom smoothing (top plot) and the run in which the BAW smoothing is activated (bottom plot). A closer look would reveal the smoothening of some spikes observed close to the coastline, around the non-erodible groynes, and at the west breakwater of Zeebrugge harbor (also non-erodible structure). Therefore the utilization of the smoothing algorithm is advised for long term morphological modelling with the model.
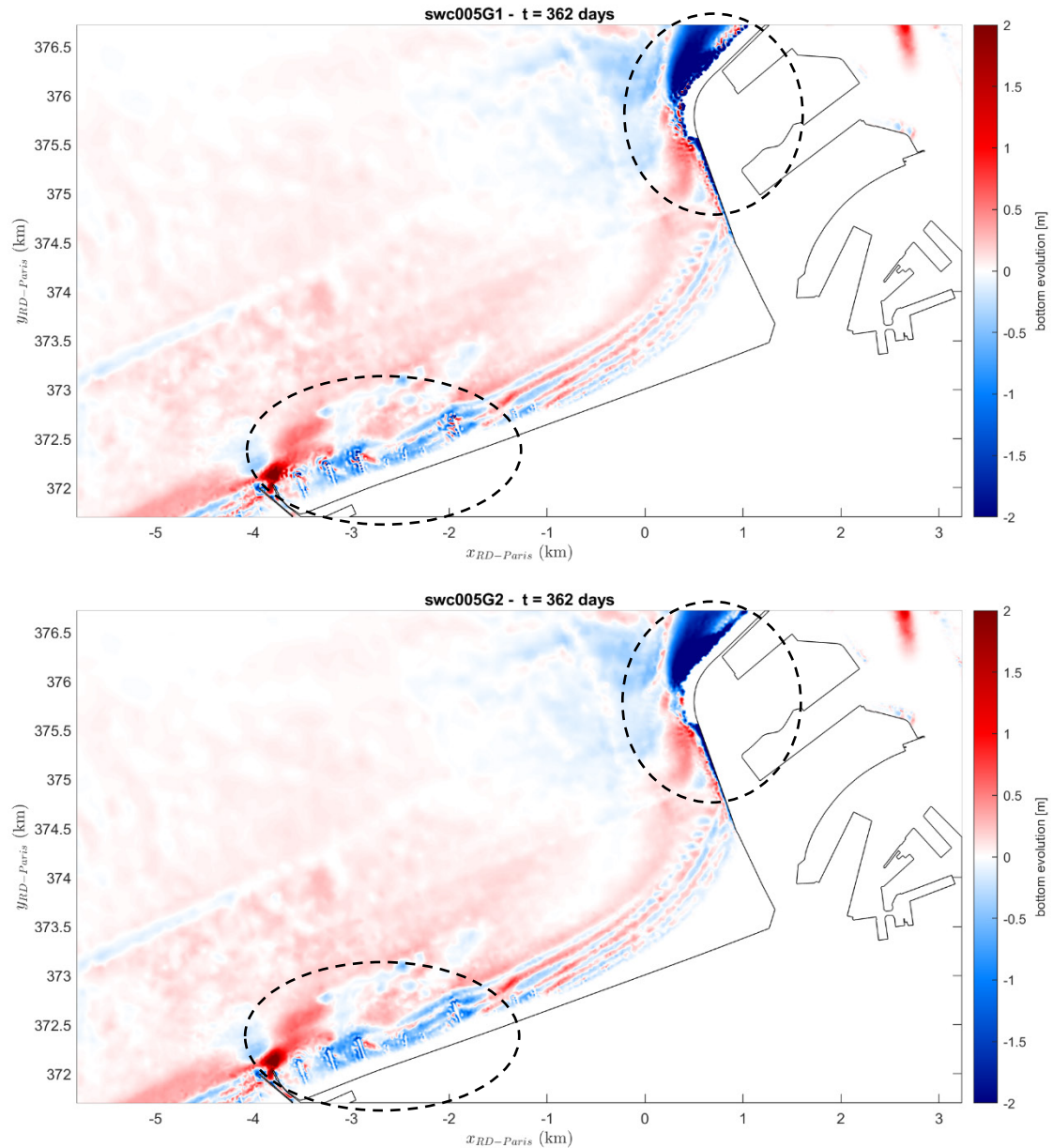
Figure 103 – Bed level change [m] obtained after about one year by use of the SVR formula; [top] Bottom smoothing is OFF, [bottom] Bottom smoothing is ON. [RT153, wave+current case, morfac=10]

SUPG scheme

The SUPG method (Streamline Upwind Petrov-Galerkin) is a numerical stabilization technique being used in the advection step for each of the considered valiables (velocity, water depth, tracers, turbulence). In TELEMAC the user must fix the type of upwind scheme required with the keyword SUPG OPTION which is a table of 4 integers relating, in order, to the velocities, depth, tracer and k-Epsilon model. As for the water depth, the SUPG treatment is mathematically not far from adding a diffusion or from smoothing the depth and it has a powerful effect on stability.

The possible values are the following:

- 0: No upwind scheme,
- 1: Upwind scheme with the classic SUPG method, i.e. upwind scheme = 1,
- 2: Upwind scheme with the modified SUPG method, i.e. upwinding equal to the Courant number.

In many TELEMAC applications the suggested SUPG OPTION values for velocity and water depth are 2;0, respectively. These values were adopted in the basic settings of the reference runs of Scaldis-Coast. However, due to the fact that spurious wiggles were appearing during the morphological evolution, especially at areas of steep slopes at the seabed (e.g. Pas van Zand channel and Flemish Banks), the upwinding was applied also for the water depth. It was found that when setting SUPG OPTION=0;1, (no upwinding for velocity and classic upwinding for depth) the wiggles were smoothened out. The latter SUPG OPTION values were adopted as default for Scaldis-Coast simulations, since they lead to more realistic long-term evolution of the seabed (even though more diffusive). Besides, in the manual it is recommended to use option 1 (which can be considered as more "universal") if the Courant number cannot be calculated accurately.
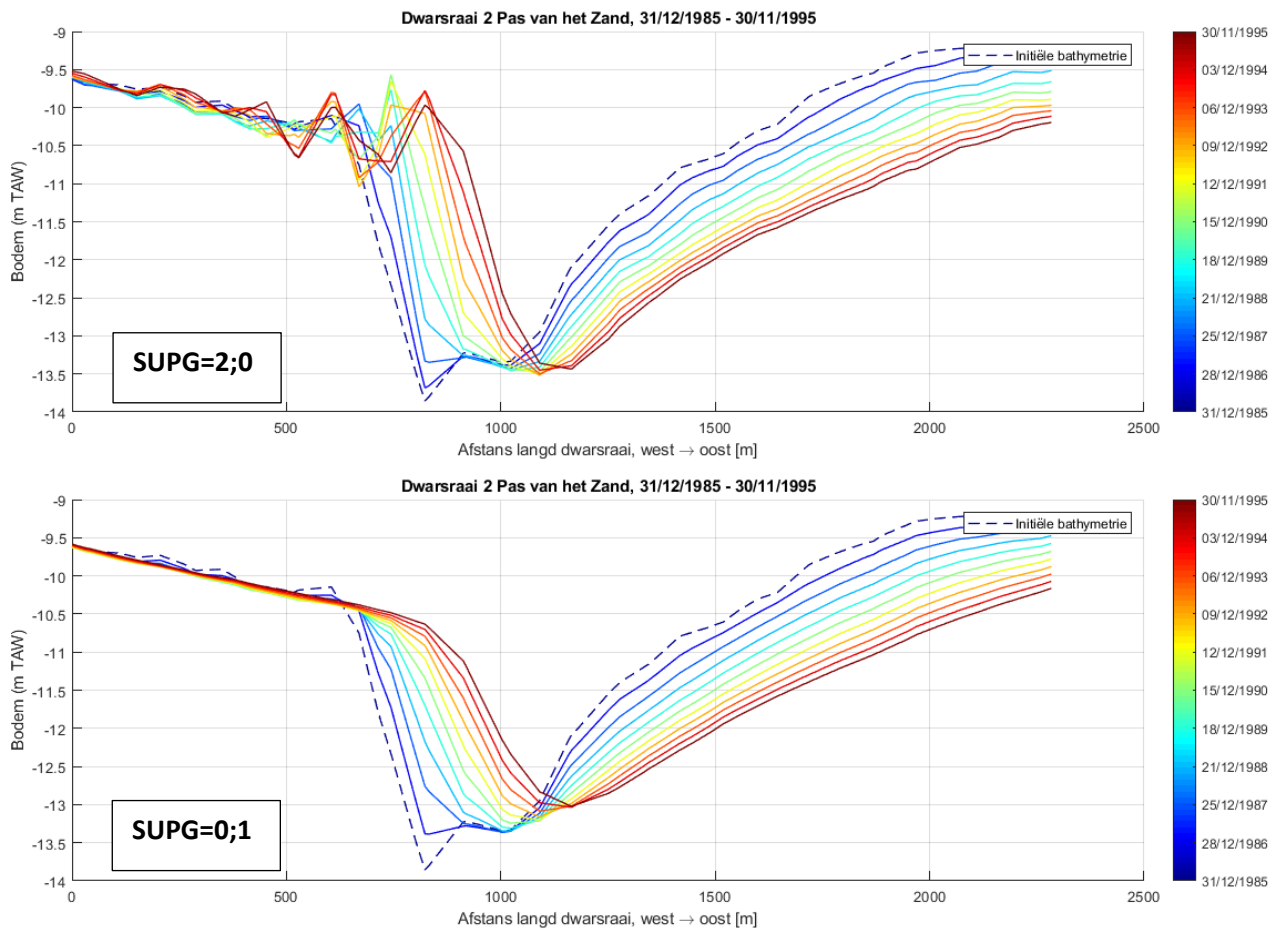
Figure 104 – 10-year bed level evolution [m] at a cross section in the middle of the Pas van Zand channel [top] SUPG=2;0, [bottom] SUPG=0;1. [Bijker formula, RT137, pure current case, morfac=10, No-dredging]

5.1.8   Conclusions

The performance of our morphodynamic model was evaluated by means of a long-term morphological hindcast exercise related to a major human intervention at the Belgian coast, i.e. the expansion of Zeebrugge port in the year 1986. The initial bathymetry of the model was based on a compilation of historical bathymetric maps around the year 1986, when the expansion of the port of Zeebrugge was completed. Qualitative comparison of the predicted sedimentation/erosion patterns at the area around the port against the measured ones, developed in a time span of 10 to 30 years, verified the good performance of the model. Specifically:

- The erosion pattern at the entrance of port of Zeebrugge (pit) is more or less captured by the model.
- Strong sedimentation at Paardenmarkt (and the surroundings) is numerically predicted by the model even though the pattern presents some differences compared to the measured ones
- The model seems to be incapable of reproducing the accumulation of sediment at Bay of Heist. This discrepancy is mainly attributed to differences in the sediment composition, which in reality contains a large fraction of mud.

Along with the reference morphological simulation, in which pure tidal forcing was considered, a series of numerical experiments were conducted in order to investigate the sensitivity of the results to different physical parameters:

- Sediment transport formula: Along with the reference formula (Engelund & Hansen), which accounts for steady currents, formulas that can account for coupled wave- and current-induced transport, i.e. those of Soulsby- Van Rijn (1997), Van Rijn (2007) and Bijker (1992) were also tested. The first two formulas tend to substantially overestimate the magnitude of the morphological patterns at deeper areas. The Bijker's formula, however, presents many similarities with the formula of Engelund & Hansen, but is also capable of reproducing the morphological patterns close to the coastline when the wave effects are taken into account.
- Representative tide: It was found that the representative tides influence on the patterns at the area around the port is rather limited. On the other hand, it seems to affect substantially the formation of the sed/ero patterns and therefore the morphological evolution of the Flemish banks.
- Sediment grain size: The consideration of a spatially-varying d_{50} distribution indicated that the local reduction of the grain size results into faster (eastward) movement of the sed/ero patterns around Zeebrugge. At the mouth of Western Scheldt, the morphological patterns were found to be relatively weaker for the case of varying d_{50} due to the increase of the local grain size of sediment. Furthermore, the relatively coarser sediment at the area of the Flemish Banks is in favour of their morphological stabilization.
- Wave action: In general, the shape of the wave + current induced sed/ero patterns developing at the broader area east of Zeebrugge are similar to those of the pure current case, however, the magnitude of the first is larger than that of the second. Major differences between the two simulations can be observed along and very close to the coastline. Additionally the accumulation of sand at Bay of Heist, even though it is not accurately captured by the model, is now more evident.

The performance of the model was improved by employing numerical stabilization techniques in order to smooth out spurious wiggles at the vicinity of steep bed slopes and close to non-erodible structures (groynes – breakwaters).

5.2   Dredging volumes

NESTOR is a module within the TELEMAC-MASCARET suite that combined with the SISYPHE module can apply data from dredging operations in the calculation of bed morphology. The duration of dredging activity, the volume of sediment removed and the size of the dredged area can be defined.

The capabilities of NESTOR combined with SISYPHE have been utilised in this section. In order to account for dredging processes, the dredging and dumping sites can be introduced by polygons and for each polygon dredging actions must be defined. The type of action can be dig by time or by criterion. In this model dig by criterion is the most appropriate. Within NESTOR, the following variables for each dredging activity need to be defined:

- *TimeRepeat*: the dredging takes place every certain amount of (morphodynamic) time, which is defined in this variable.
- *CritDepth*: critical depth is the bottom depth that when it is exceeded, NESTOR performs dredging and removes material from the particular dredging site. It has to be mentioned that NESTOR can take action only every *TimeRepeat*. This variable is the closest term to the maintenance depth.
- *DigDepth*: is the maximum depth that NESTOR will reach in a particular dredging activity. The difference between *DigDepth* and *CritDepth* is what is known as overdepth.

The NESTOR module will check from the selected starting time instant, with the selected frequency, the depth of the dredging zone. If the critical depth is exceeded, the module starts deepening the zone. The critical depths are equal to the maintenance depths we want to apply based on the documented data. An overdepth value equal to 0.50 m has been considered.

The documented data for the dredging activities refer to years starting from 1 April of each year and ending to 31 March of the following year (Vroom & Schijverhof, 2015). Each dredging activity will be referred from this point as *Action* for direct reference to the NESTOR keyword. The Actions include two major fields:

- Dredging in the offshore region of Zeebrugge port
- Dredging in the Western Scheldt area

The following sections will provide further information of all the actions that have been included in the Scaldis-Coast model.

5.2.1   Dredging in the region of Zeebrugge port and Western Scheldt

The Actions that take place in the offshore region of Zeebrugge port are given in the memo of Vroom & Schijverhof (2015) and include maintenance and capital dredging. The dredging sites are shown in Figure 105 and include:
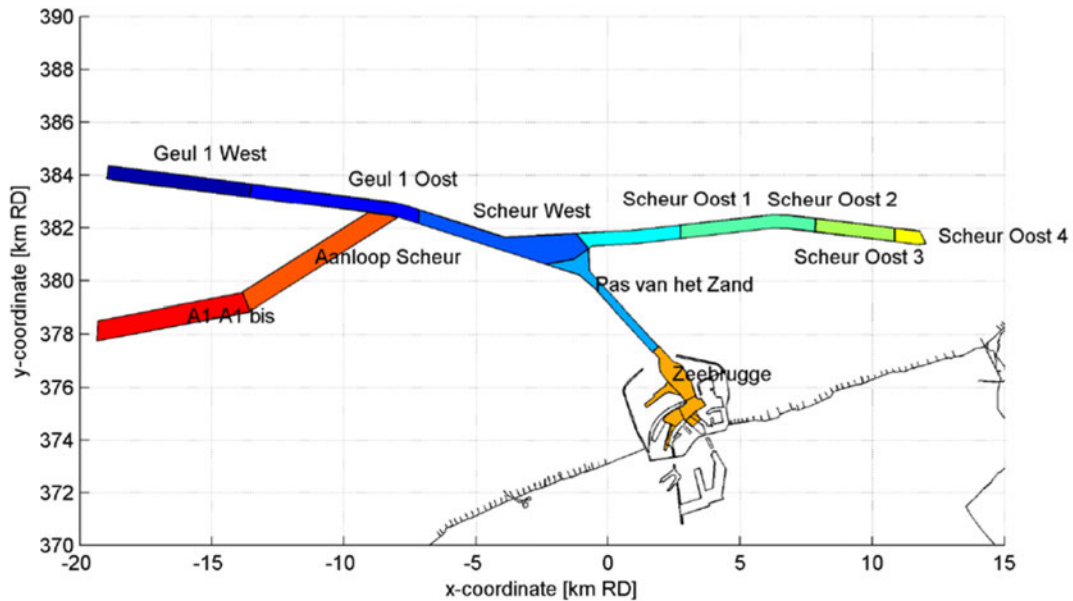
Figure 105 – Location of the dredging zones offshore of Zeebrugge port. Dredging sites *A1 – A1 bis* and *Aanloop Scheur* are not included in Scaldis-Coast.

- *Geul 1 West*
- *Geul 1 Oost*
- *Scheur West*
- *Scheur Oost 1*
- *Scheur Oost 2*
- *Scheur Oost 3*
- *Scheur Oost 4*
- *Pas van het Zand*
- *Zeebrugge haven (OuterPort + Voorhaven)*

The dredging sites *A1 – A1 bis* and *Aanloop Scheur* have not been included in Scaldis-Coast model due to the fact that they have been considered as secondary. In practice these sites don't require maintenance dredging. The dredging sites within Zeebrugge port include the *OuterPort* (Centraal Deel Nieuwe Buitenhaven, CDNB) and the *Voorhaven*, shown in Figure 106, which together are forming the Zeebrugge port as stated in the dredging actions in Table 26. Due to the fact that the material dredged from the CDNB and Voorhaven is mainly silt material, no dredging action is defined for this part of the model. It must be pointed out that within *OuterPort* shown in Figure 106, the port's entrance is included. This is an area where strong sedimentation is taking place. This area is not part of the *OuterPort* in later version of the model.
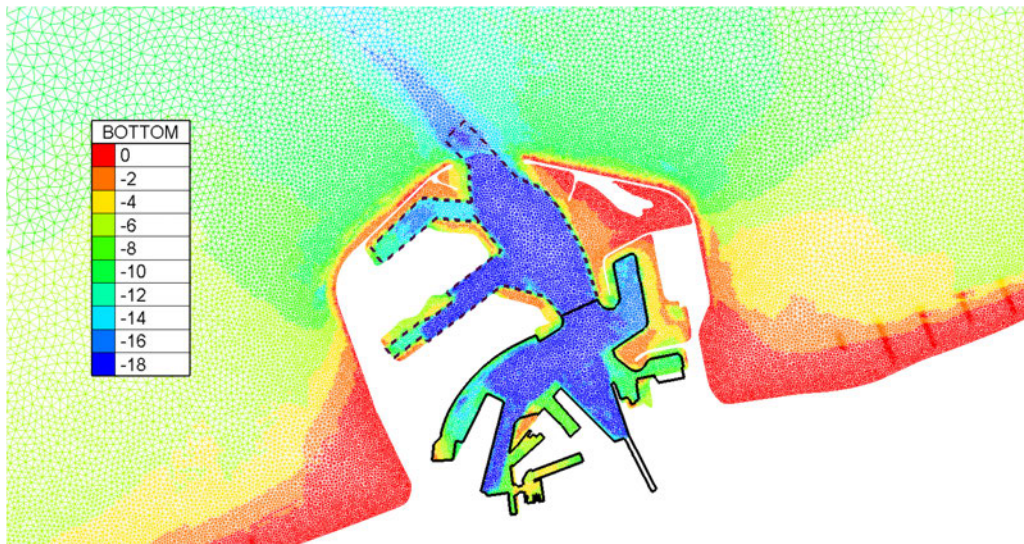
Figure 106 – Location of the dredging zones within Zeebrugge port including *OuterPort* site (dashed line) and *Voorhaven* (solid line).
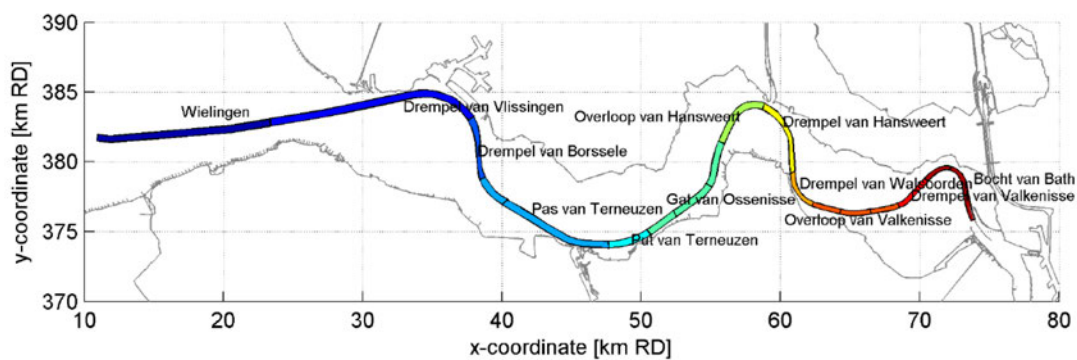
Figure 107 – Location of the dredging zones in the Western Scheldt region.

In addition, Figure 107 depicts all the dredging sites along the Western Scheldt region. The west side of *Wielingen* site is connected with *Scheur Oost 4* (see Figure 105). The dredging sites are:

- *Wielingen*
- *Drempel van Vlissingen (sill of Flushing)*
- *Drempel (sill) van Borssele*
- *Pas van Terneuzen*
- *Put van Terneuzen*
- *Gat van Ossenisse*
- *Overloop van Hansweert*
- *Drempel van Hansweert*
- *Drempel van Walsoorden*
- *Overloop van Valkenisse*
- *Drempel van Valkenisse*
- *Bocht van Bath*

Based on the available data shown in the work of Vroom & Schijverhof (2015), *Wielingen* has a particular maintenance depth. However, based on the reported dredged volumes, no amount of material has been dredged on *Wielingen* and thus, no dredging action has been considered in the model. The maintenance dredging depths in Western Scheldt are common for all the above dredging sites. Nevertheless, as for instance no dredging volume is reported at *Drempel van Vlissingen* till 1999, we consider that no dredging activity takes place before this year. This way it is easier to identify the areas where a sediment transport model in SISYPHE combined with NESTOR is overpredicting accretion of sediment, which would have increased the total of dredged volume per site.

Table 26 – Critical depths per dredging zone. Source: Chantal Martens, MOW Vlaanderen. The vertical reference level is TAW. Values in red are not mentioned in (Vroom & Schijverhof, 2015).

	Pas van het Zand	Scheur West	Geul 1 Oost	Geul 1 West	Scheur Oost 1	Scheur Oost 2	Scheur Oost 3	Scheur Oost 4	Wie-lingen	Zee-brugge haven	Western Scheldt
	TAW										
1984-1986	12.19	12.19	-	-	-	-	-	-	-	-	12.02
1986-1988	12.69	12.69	-	-	-	-	-	-	-	-	12.02
1988-1989	13.69	14.49	-	-	14.19	13.99	13.89	13.69	-	-	12.02
1989-1990	13.89	14.49	-	-	14.19	13.99	13.89	13.69	-	-	12.02
1990-1992	13.99	14.49	-	-	14.19	13.99	13.89	13.69	-	-	12.02
1992-1993	13.99	14.49	-	-	14.19	13.99	13.89	13.69	-	13.69	12.02
1993-1997	13.99	14.49	-	-	14.19	13.99	13.89	13.69	-	-	12.02
1997-1998	13.99	14.49	-	-	14.19	13.99	13.89	13.69	-	-	13.67
1998-1999	13.99	15.69	15.79	16.09	14.19	13.99	13.89	13.69	-	-	13.67
1999-2000	13.99	15.69	15.79	16.09	15.49	15.39	15.39	15.29	15.19	-	13.67
2000-2005	15.39	15.69	15.79	16.09	15.49	15.39	15.39	15.29	-	-	13.67
2005-2006	15.99	16.39	16.39	16.37	15.69	15.59	15.59	15.49	15.11	15.23	13.67
2006-2008	15.99	16.39	16.39	16.37	15.69	15.59	15.59	15.49	15.11	-	13.67
2008-2009	15.99	16.39	16.39	16.37	15.69	15.59	15.59	15.49	15.11	15.69	13.67
2009-2013	15.99	16.39	16.39	16.37	15.69	15.59	15.59	15.49	15.11	15.69	14.72
2013-2014	16.03	16.43	16.43	16.43	15.73	15.63	15.63	15.63	15.13	15.69	14.72

5.2.2   Dumping sites

The material dredged from the sites mentioned in the previous section has been moved to the so called dumping sites. Those sites for the Zeebrugge port are indicated in Figure 108 and the average percentage (%) of dredged material distributed is indicated in Table 26. It must be mentioned that only *S1*, *S2* and *W2* sites have been considered in Scaldis-Coast model. The site S3 and R4 are older disposal sites which are no longer in use. Zeebrugge East (ZBO) is mainly used for dredging material from the maintenance of the port area. This is mainly muddy material which is not included in the model. The red polygon in Figure 108 was a temporary disposal are only used for the widening of the Wielingen.
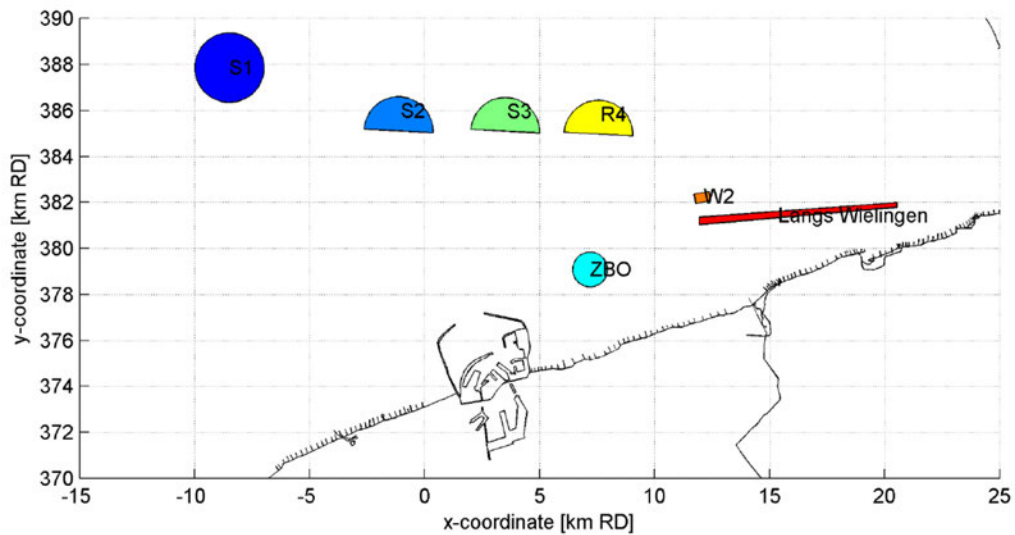
Figure 108 – Location of the dumping zones around Zeebrugge port. Only sites *S1* and *S2* have been used for Scaldis-Coast model.

Table 27 – Averaged percentage of maintenance dredged material (TDM) per dredging site to respective dumping sites based on Vroom & Schijverhof (2015).

		Disposal site		
		ZBO	S1	S2
Dredging site	Voorhaven	72%	14%	14%
	OuterPort	50%	35%	15%
	Pas van het Zand		70%	30%
	Scheur West		85%	15%
	Scheur Oost		81%	19%

Concerning the dumping sites for Western Scheldt, there are two configurations, one shown in upper Figure 109 from 1985-2009 and another one in lower Figure 109 from 2010-2014. Fully detailed information for the dumping information are extensively provided in Vroom & Schijverhof (2015) and this information has been used for Scaldis-Coast model.
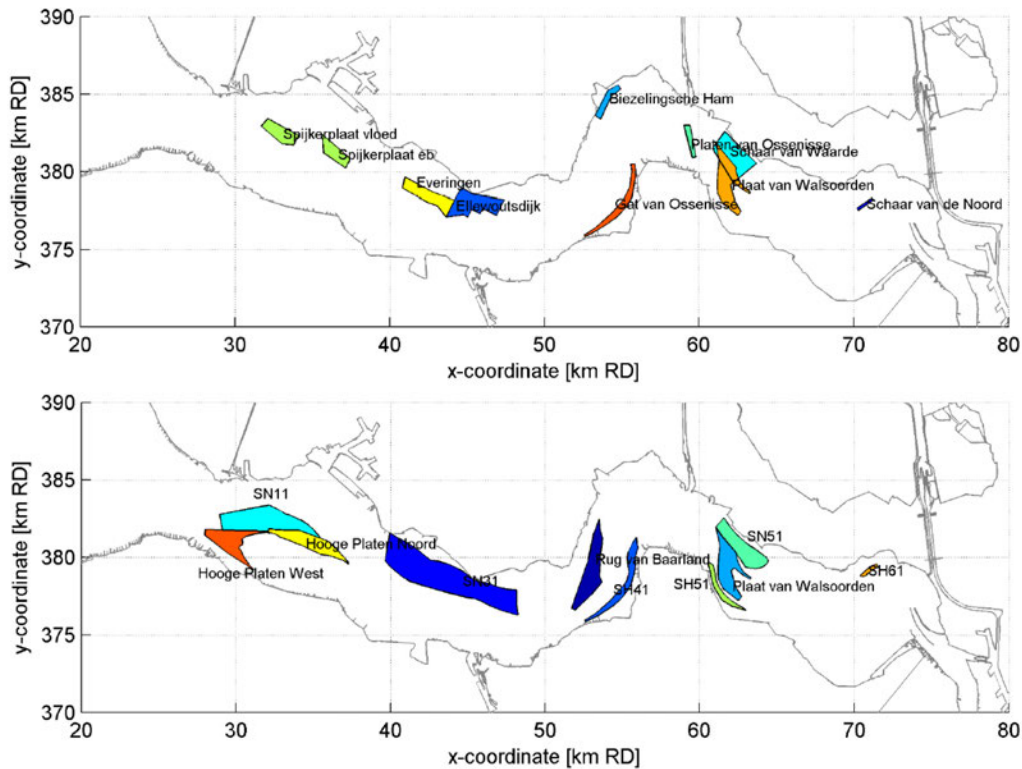
Figure 109 – Location of the dumping zones along the Western Scheldt from 1985 to 2009 (up) and from 2010 to 2014 (down).

5.2.3 Application of dredging/dumping using NESTOR in Scaldis-Coast model

In this section, the results of the simulations of Scaldis-Coast model conducted by coupling TELEMAC2D with SISYPHE/NESTOR and in some cases also with TOMAWAC will be discussed. The computed volumes from the numerical model for different sediment transport models will be compared with the available field measurements.

5.2.4 Model set-up

For the investigation of the effect of different sediment transport models the new grid [D2chWS] based on the base grid [D2] was used so that the grid point is aligned with the dredging polygons (adapted to prevent elements to be partially inside and partially outside the dredging zone. This allows the dredged volumes to be computed more accurately. The dredging sites to which the mesh is aligned are *Wielingen, Drempel van Vlissingen* named from this point onwards as *Rede van Vlissingen en Honte, Drempel (Sill) van Borssele, Pas van Terneuzen, Put van Terneuzen, Gat van Ossenisse, Overloop van Hansweert, Drempel van Hansweert, Drempel van Walsoorden, Overloop van Valkenisse, Drempel van Valkenisse* and *Bocht van Bath*. The mesh in the vicinity of the dredging site *Drempel (Sill) van Borssele*, indicated by the closed polygon, in Western Scheldt region, is shown in Figure 110. It can be observed that all the triangles within the dredging site/polygon are fully included inside and that there are minimum 5 vertices along the width of the dredging site.
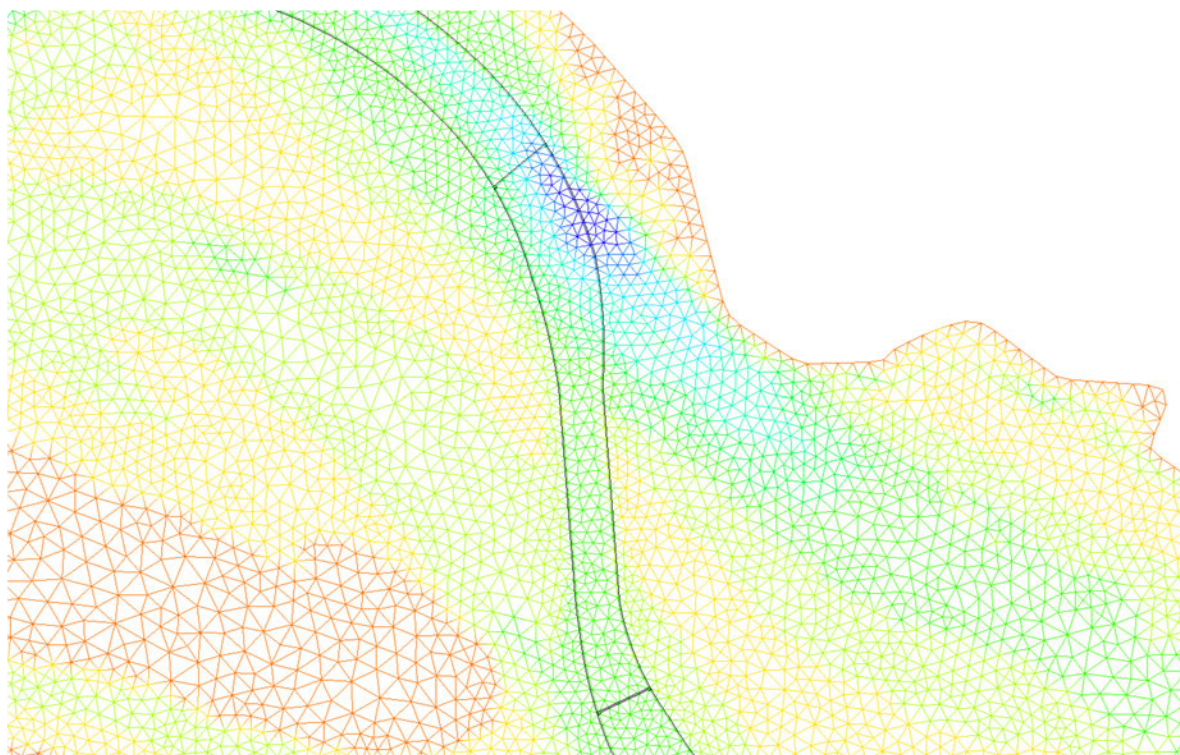
Figure 110 – Mesh detail for the adapted mesh to the Western Scheldt dredging sites (*Drempel (Sill) van Borssele* site region).

The simulations consist of two sets of simulations:

1. Ten years hindcasting simulations starting from 01/01/1986, one year hydrodynamics with morphodynamic amplification factor equal to 10) referred to as hindcasting 1986-1996 and
2. one set of computations starting from 01/01/2014 and lasting for 2 years (morphodynamic factor equal to 1), referred to as hindcasting 2014-2015.

As NESTOR module is coupled with SISYPHE, the morphological factor applied to SISYPHE is also affecting the NESTOR. Thus, all the considered dredging activities indicated in NESTOR denote morphodynamic time.

Notice from Table 26 that the hindcast simulations both include maintenance dredging and capital dredging with the deepening of *Pas van het Zand* and *Scheur* in 1988. It must be pointed out that based on Table 26, a maintenance depth is kept for instance at Western Scheldt at 12.02 m from 1984-1997. Nevertheless, based on the work by Vroom & Schijverhof (2015), no dredging takes place for instance in Put van Terneuzen before 1992. Thus, we also consider that dredging starts in year 1992 instead of 1984. This way, we can directly identify regions where the sediment transport models are predicting higher deposition of sediment. By using this approach we do not count additional dredged material computed by the sediment transport model that would have been added in the total dredged volume for each dredging site.

The modelled dredging volumes are validated against the reported dredging volumes. Since the model only includes sand fractions whilst the real dredged material includes both sand and muddy material, only the sand fraction of the dredged material is compared to the modelled volumes. In the simulations of 2014-2015 the first year is considered as a morphological spin-up period. Only the dredged volumes of the second year are compared with the annual maintenance dredging volumes.

Based on the preliminary findings, the repetition frequency of the dredging activities (1, 2 or 3 months) does not make a difference in the total computed dredged volumes. Therefore, for the present set of simulations only a repetition frequency of 1 month is considered.

Hard layers

The hard layers refer to a defined bathymetry over which there is no further material available to be eroded/dredged and transported. This bathymetric level is underneath the actual bathymetry and this concept is used so that the sediment transport model stops being active when it erodes the seabed intensely and reaches this level.
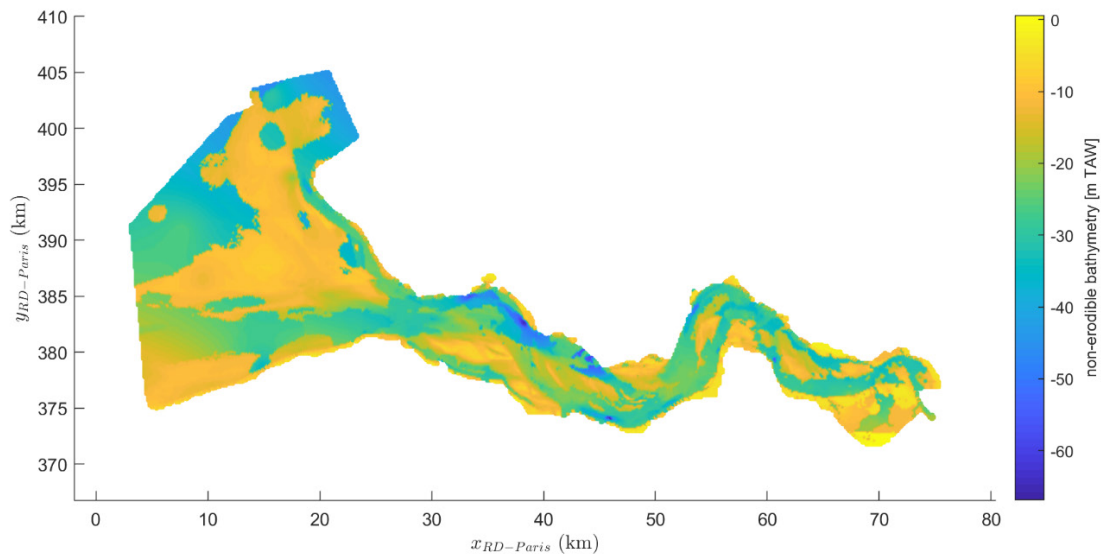
Figure 111 – Non-erodible bathymetry as indicated by (Dam, 2012) based on bathymetries from 1960 to 2011.
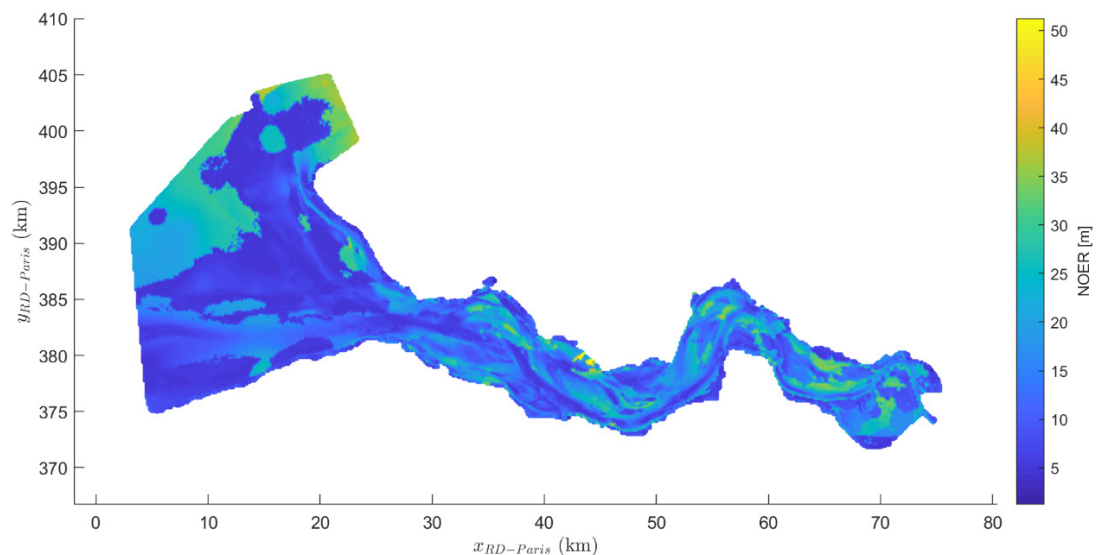
Figure 112 – Thickness of the erodible bed (variable NOER) based on the difference of the non-erodible map in Figure 111 and the bathymetry used for the hindcasting simulations.

In the Western Scheldt area the non-erodible bathymetry is shown in Figure 111 based on the work by Dam (2012). The non-erodible map (resolution 20m x 20m) was determined by examining bathymetries from 1960 up to 2011. The difference of the bathymetry used for the hindcasting simulations and the non-erodible map gives the thickness of the erodible material introduced into TELEMAC as variable NOER (Figure 112).

In addition, the region outside of Zeebrugge port and the positions of the groynes have also been considered as fully non-erodible, as it can be seen in Figure 113. The variable NOER within TELEMAC2D indicates the depth that can be deformed by SISYPHE. Thus, NOER=0 around Zeebrugge indicates no available depth to be deformed and no bed evolution is allowed in Zeebrugge breakwaters.
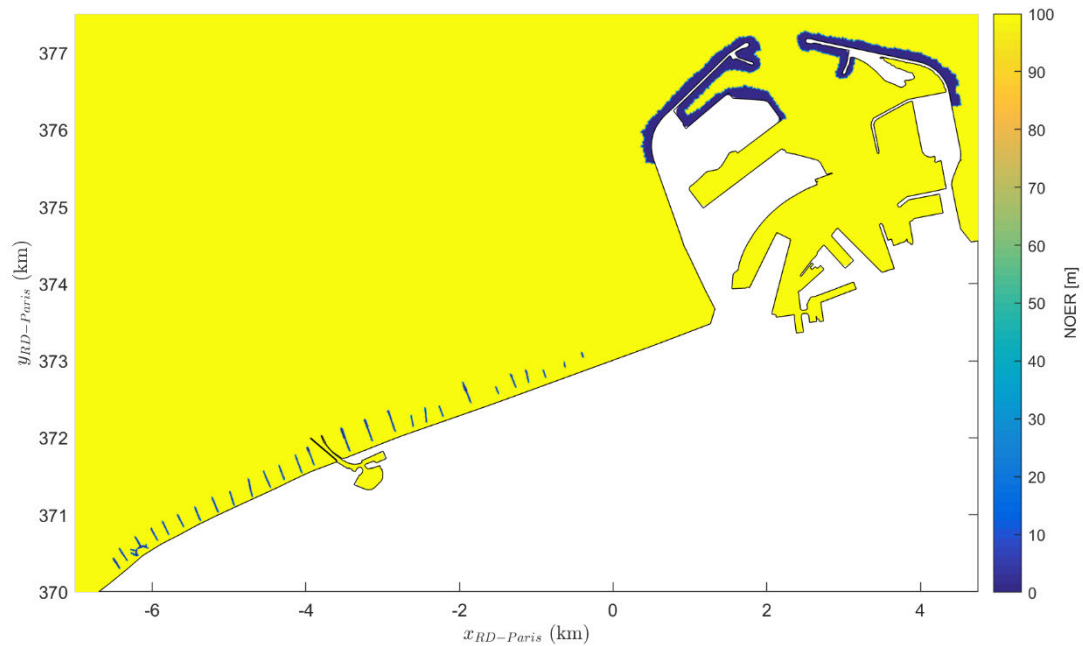
Figure 113 – Snapshot of the areas considered as non-erodible (NOER=0) including the breakwaters of Zeebrugge port and the groynes in the vicinity of Blankenberge.

Common considerations for the simulated sets

For both hindcasting simulations:

- Modified grid D2chWS aligned with the dredging polygons for the Western Scheldt fairway.
- The dredging activities from year 1984 up to year 2014 are shown in section 5.2.1 and 5.2.2 where the critical/target depths in TAW vertical reference level. For simulations that start from 2014 it is consider that the target depths reported in that table for years 2013-2014 remain the same.
- Dredging activities are repeated on a monthly basis. In preliminary investigations
- The overdepth (difference between critical depth and dig depth) is considered equal to 0.50 m.
- The sediment transport models examined in this chapter are Bijker (with beta parameter equal to b=5.5 for d_{50}=250 µm, default value is 2), Engelund & Hansen, Soulsby – Van Rijn and Van Rijn (2007) formulas. The beta parameter for Bijker's formula has been calibrated for different sediment diameters and for d_{50} equal to 250 µm, beta takes values between 5.5 and 5 (as considered in section 5.1.6).

For the hindcasting 1986-1996 simulations:

- The initial bathymetry is the one of the year 1986, see also the previous section for the composition of the initial bathymetry.
- The simulations are conducted for hydrodynamics and morphodynamics without wave effects.
- The simulations are conducted using representative tide number RT137, which is the most representative for all the examined sediment transport models in terms of accurate representation of sediment transport rates in the area of Zeebrugge and Western Scheldt, see also Table 20 on page 71. Hydrodynamic duration of the simulations is 360 representative tidal cycles.
- A morphodynamic acceleration factor equal to 10 is applied for the sediment transport model so the morphodynamic simulation lasts from 1986 to 1995 (MORFAC = 10).
- The results concerning morphodynamics and computed dredged volumes are gathered for the total of the morphodynamic simulation period 1986-1995 and compared with available records of dredged volumes for the same period.
- For all the simulations, the previously described hard layers have been considered for more realistic morphodynamic simulations.

For the hindcasting 2014-2015 simulations:

- The bathymetry consists of various bathymetric sets for the domain of interest between years 2004 and 2016. Bathymetric data for Western Scheldt have been delivered by RWS for year 2015, whereas the bathymetric data for the coastal zone have been collected by airborne Lidar sensors in 2015, and has a very high resolution 1m x 1m. Belgian Continental Shelf (BCP) data comes from MDK coastal division, and was collected by different measurement campaigns from 2004 to 2016.
- The simulations are conducted for hydrodynamics and morphodynamics. Some of the simulations take into account the wave effects.
- The simulations are performed using the brute force data i.e. the real tide for hydrodynamics, wind and wave input for the year 2014 and the data are repeated for the second year of simulation.
- A morphodynamic factor equal to 1 is applied for the sediment transport model and the results concerning morphodynamics and computed dredged volumes are gathered only for the second simulated year and they are compared for the available records of the year 2014.

The dredged volumes within the simulations are compared with the measured volumes reported in the memo by Vroom & Schijverhof (2015). In this memo, all the dredged volumes of the sites offshore from Zeebrugge port (*Geul, Scheur, Pas van het Zand*) are reported in ton dry material (TDM) and the volumes have been converted in m^3 based on the provided conversion 1 m^3 = 0.94 TDS for porosity equal to 0.4. By assuming a more compact sand with porosity equal to 0.3, the conversion becomes 1 m3 = 1.26 TDM. Since for the dredging sites the material is a sand silt mixture, the sand fraction has been considered equal to 33.3% for *Pas van het Zand* and 53.2% for *Scheur West* according to the report by Vroom *et al* (2016). Thus for the reported measurements in the offshore Zeebrugge region the measured volumes correspond to m^3 of sand for porosity equal to 0.3. In the memo by Vroom & Schijverhof (2015), the volumes on the Western Scheldt dredging sites (*Rede van Vlissingen en Honte, Drempel (Sill) van Borssele, Pas van Terneuzen, Put van Terneuzen*) refer to in situ volumes (m^3) and they consist almost exclusively of sand.

5.2.5   Hindcasting 1986-1996 simulation results

Table 28 – Simulated cases for hindcasting 1986 - 1996 with different considered sediment transport models.

Run name	Sediment transport model	GRID
hrun04	Bijker	D2chWS
hrun05	Soulsby – Van Rijn (SVR)	D2chWS
hrun05-D2	Soulsby – Van Rijn (SVR)	D2
hrun30	Engelund & Hansen (EH-30)	D2chWS
hrun71	Van Rijn 2007 (VR07)	D2chWS

Based on the considerations mentioned above, a set of simulations has been conducted for hindcasting for different sediment transport models. In addition, we examine the effect of the imposition of hard layers on the erosion/deposition patterns. The hard layers are allowing erosion to happen up to specific depth over which the bed underneath is considered not anymore erodible. The hard layers are applied based on the work of Dam (2012).

The simulations are listed in Table 28 and the results came from coupling TELEMAC2D with SISYPHE and NESTOR. For comparison purposes we also include a simulation using Soulsby – Van Rijn (SVR) model with the original grid (i.e. not aligned with the dredging polygons: mesh [D2]). The first results reported concern the erosion/deposition patterns. As expected the most active model is the one of Soulsby – Van Rijn (Figure 115) followed closely by Van Rijn 2007 (Figure 117). Engelund & Hansen (Figure 116) and Bijker (Figure 114) models demonstrate lower but probably more realistic activity in erosion/deposition patterns, see also Section 5.1.3.
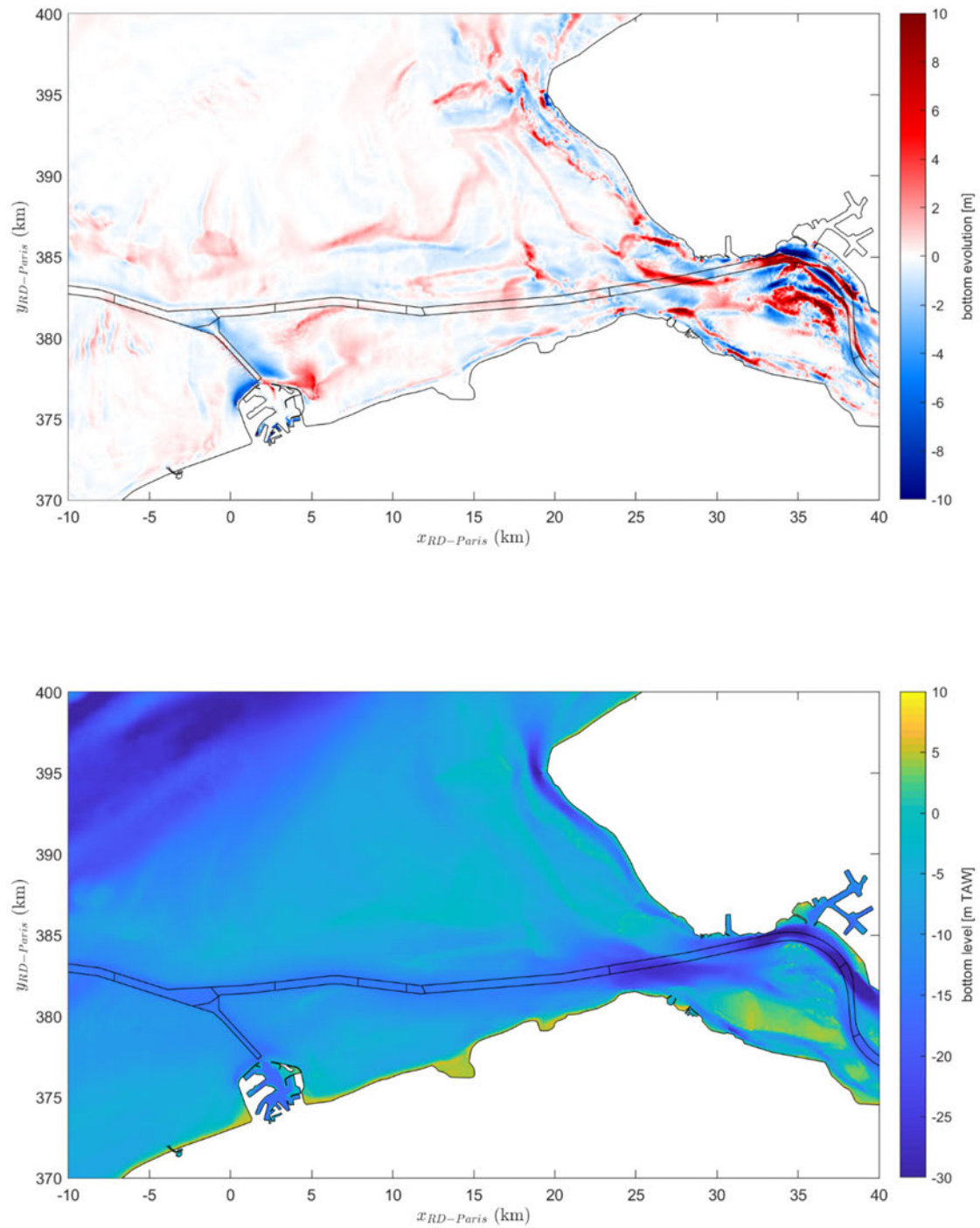
Figure 114 – (Upper figure) Contour plot of erosion/deposition patterns and (lower figure) contour plot of bathymetry, after 10 years morphodynamic time in Scaldis-Coast model. Sediment transport model by Bijker (hrun04).
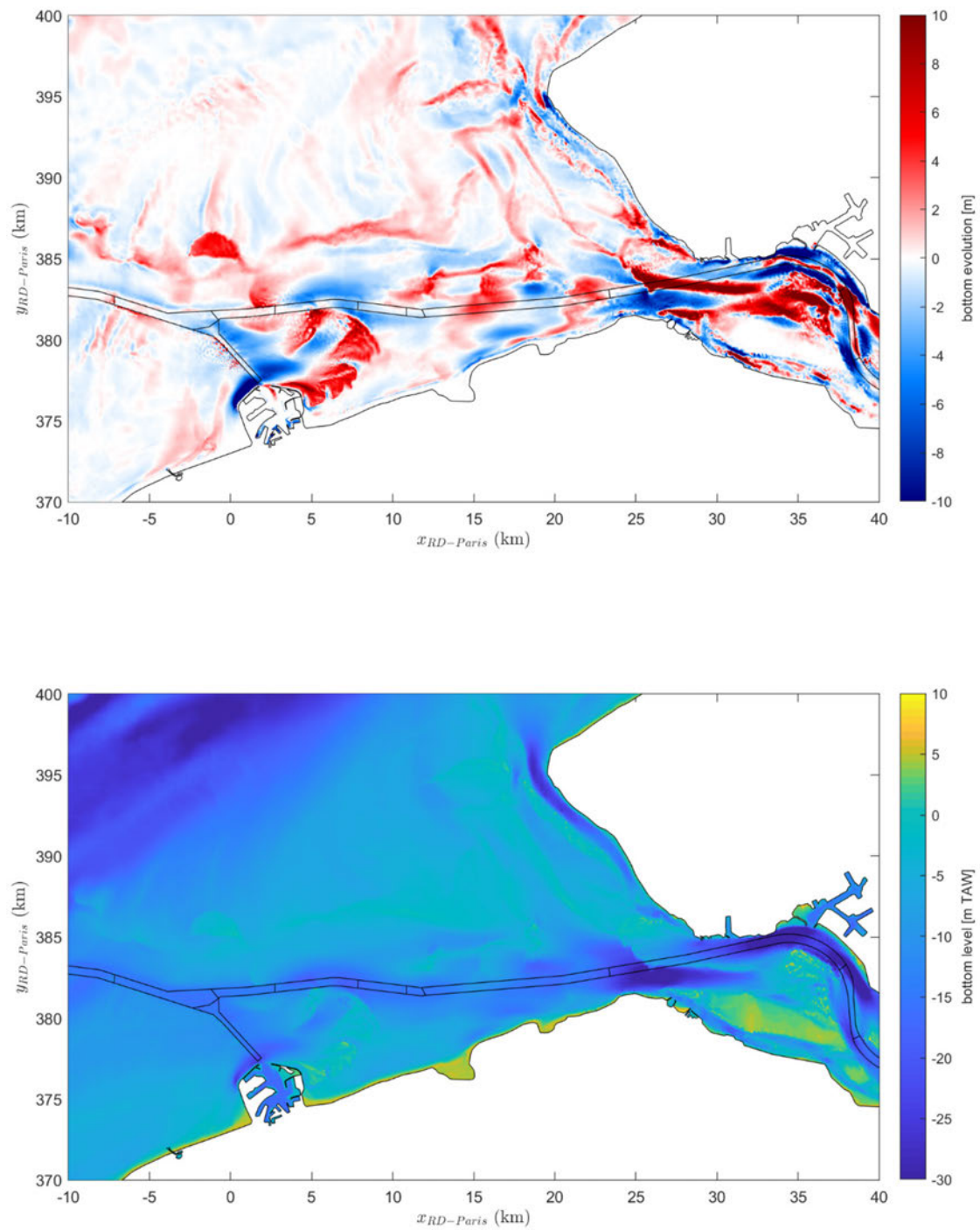
Figure 115 – (Upper figure) Contour plot of erosion/deposition patterns and (lower figure) contour plot of bathymetry, after 10 years morphodynamic time in Scaldis-Coast model. Sediment transport model by Soulsby – Van Rijn (hrun05).
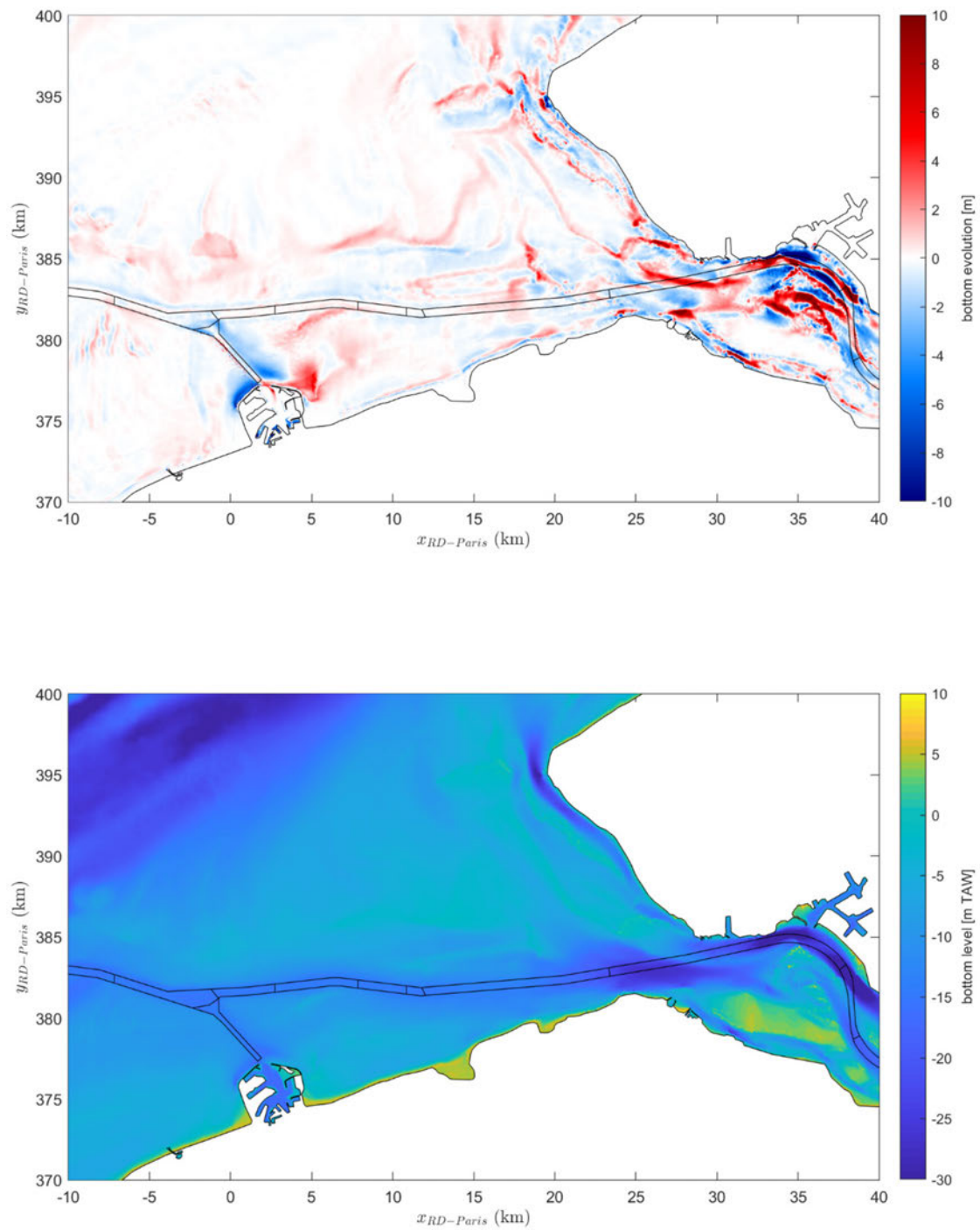
Figure 116 – (Upper figure) Contour plot of erosion/deposition patterns and (lower figure) contour plot of bathymetry, after 10 years morphodynamic time in Scaldis-Coast model. Sediment transport model by Engelund & Hansen (hrun30).
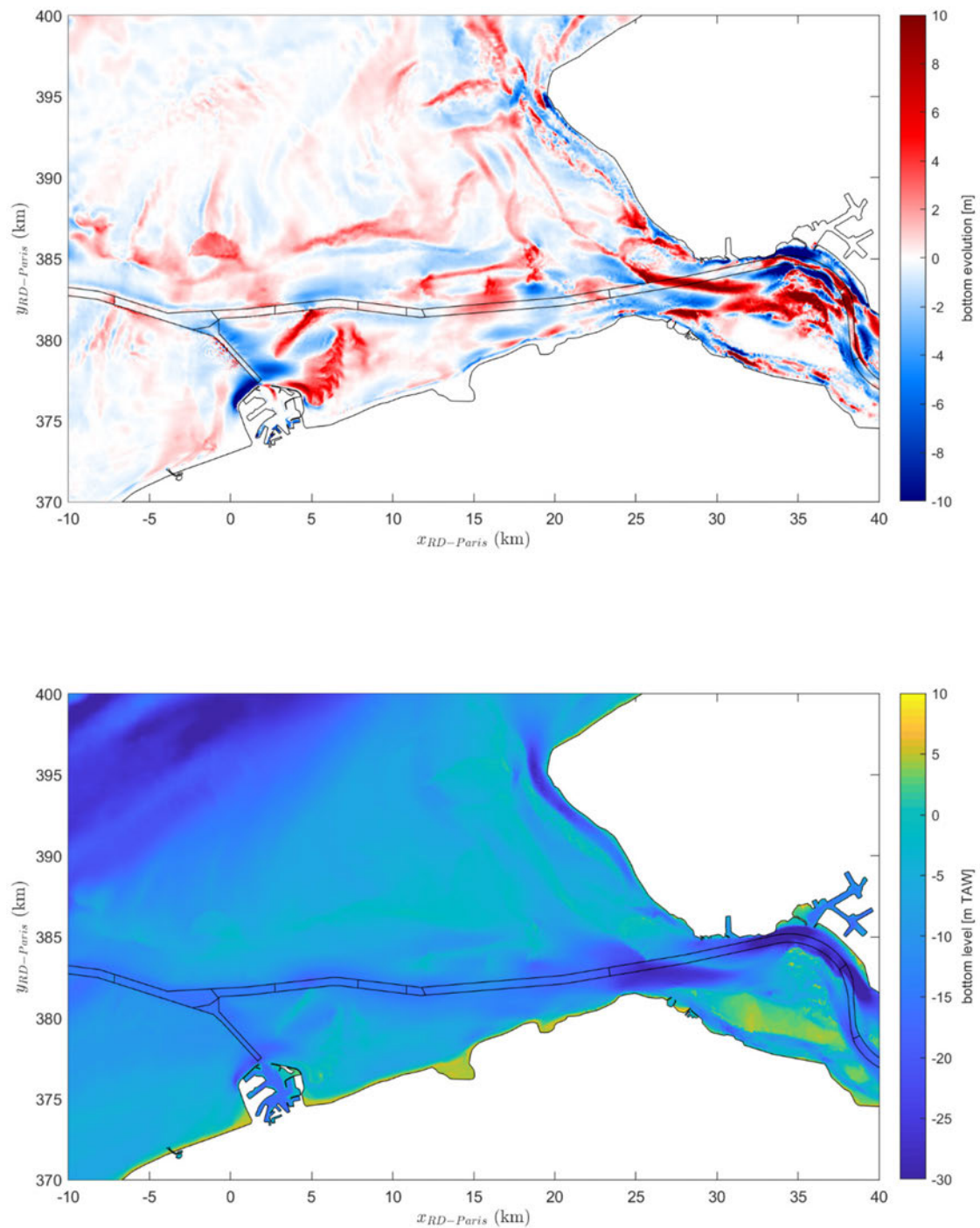
Figure 117 – (Upper figure) Contour plot of erosion/deposition patterns and (lower figure) contour plot of bathymetry, after 10 years morphodynamic time in Scaldis-Coast model. Sediment transport model by Van Rijn (2007) (hrun71).

Furthermore, the major focus of this investigation is to compare the computed dredged volumes against the available recorded volumes between 1986-1995. In Table 29 and Figure 118 we demonstrate the results for the dredging sites with non-zero dredged volumes in the outer Zeebrugge region and in the Western Scheldt from the entrance to *Put van Terneuzen*, which are found within the model's area of interest.

Table 29 – Dredged volumes in the different dredging sites for the hindcasting simulations with different sediment transport formula.

Run name	hrun04 (Bijker)	hrun05 (SVR)	hrun05-D2 (SVR)	hrun30 (EH-30)	hrun71 (VR07)	Measured Data
Scheur	3.27	17.57	9.16	3.32	10.77	27.49 (22.99-33.35)
Pas van het Zand	8.24	16.56	13.15	8.25	14.49	17.77 (14.66-28.42)
Drempel van Borssele	1.38	7.06	8.73	1.75	6.14	6.29 (3.93-7.86)
Put van Terneuzen	0.00	4.19	2.84	0.01	2.36	0.77

It can be seen that Soulsby - Van Rijn model has the best performance in predicting the dredged volumes especially in *Pas van het Zand* and *Drempel van Borssele*, even though it underestimates *Scheur* and overestimates *Put van Terneuzen*. Van Rijn 2007 model also performs in an acceptable manner, whereas the rest of the models appear to severely underestimate the dredged volumes. It must also be highlighted the different volumes computed by run hrun05-D2 with the original grid D2 to the Western Scheldt dredging sites. The differences between the dredged volumes in those two runs indicate the importance of the mesh to be aligned with the dredging sites in order to achieve a more realistic computation of the volumes that have been removed by NESTOR and have more accurate morphodynamic simulation results.
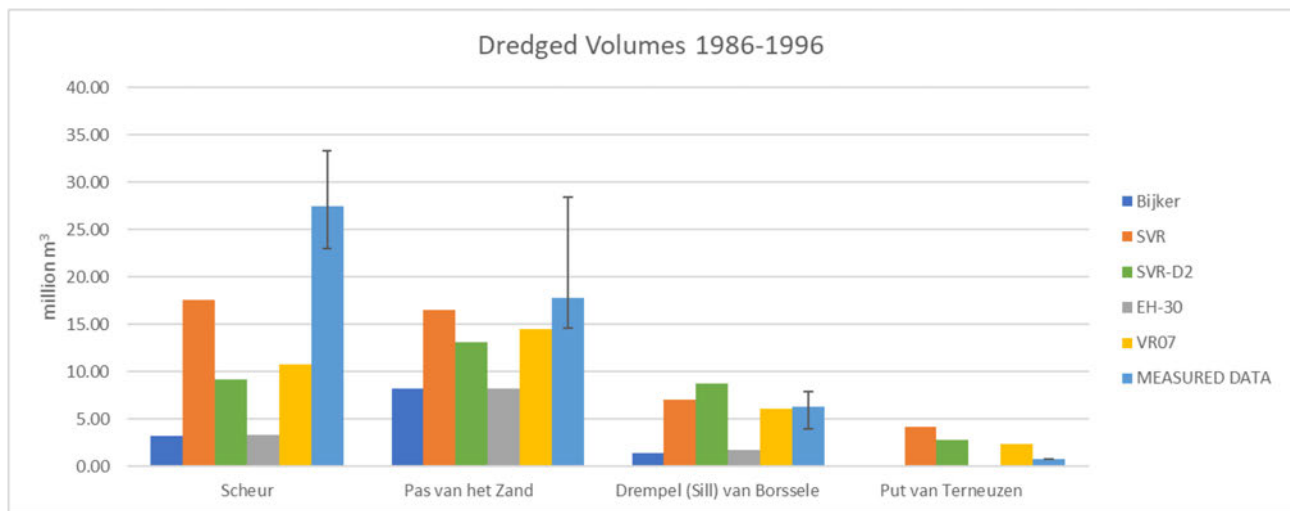
Figure 118 – Dredged volumes in the different dredging sites for the hindcasting simulations with different sediment transport formula.

In addition, Figure 119 and Figure 120 demonstrate the temporal evolution of dredging process for the sites *Pas van het Zand* and *Drempel (Sill) van Borssele* for Soulsby – Van Rijn (SVR) model. It can be observed that in the case of *Pas van het Zand*, there is a relatively constant volume of material removed from the site and only a jump exists at the beginning of the year 1988, that corresponds to the capital dredging with an increase in target depth (Table 26). Notice that for converting the reported dredging tons dry material to in situ sand volumes, the same assumption on sand content is used for both the maintenance as the capital dredging.

When deepening a channel, the original bed material is dredged which can be different from settled sediment that needs to be removed by maintenance dredging. On the other hand, *Drempel (Sill) van Borssele* is demonstrating an almost linear cumulative volume behaviour since the target depth is not changing and every month a somewhat steady volume is being dredged.
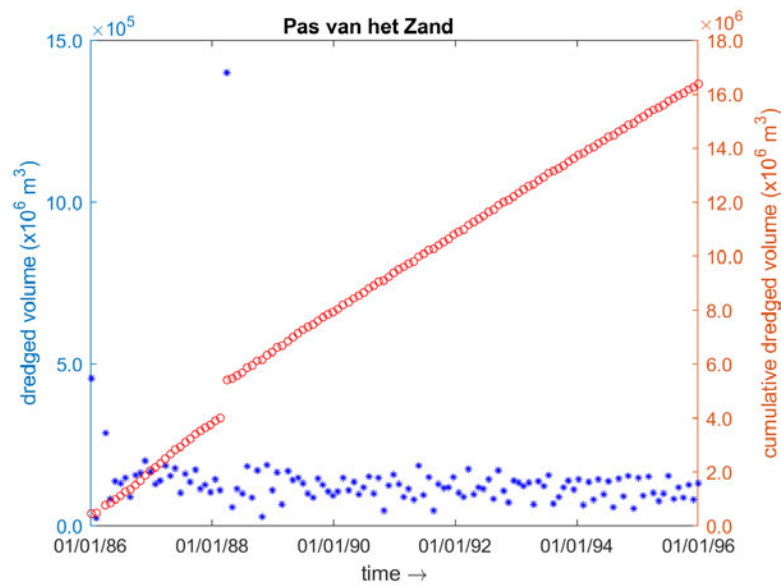
Figure 119 – Timeseries and cumulative timeseries of the dredged volume in the site *Pas van het Zand* (hrun05).
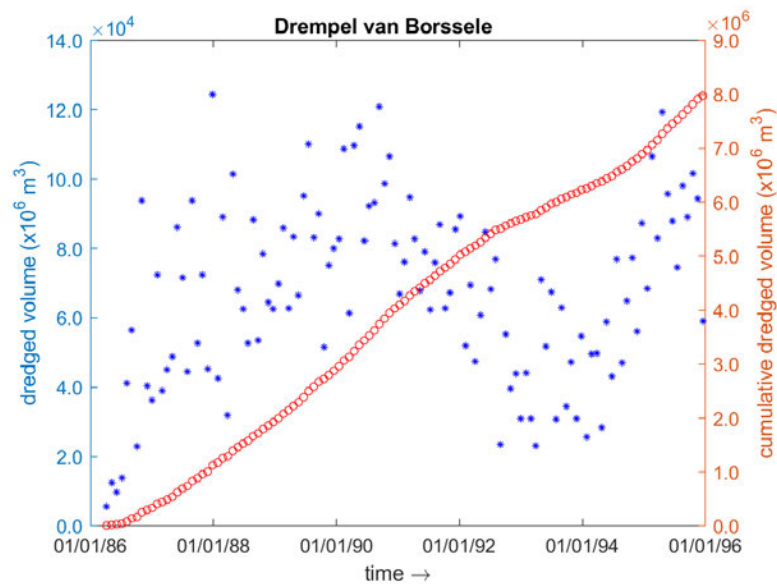
Figure 120 – Timeseries and cumulative timeseries of the dredged volume in the site *Drempel (Sill) van Borssele* (hrun05).

In addition, in order to extract more information on the results, various bed evolution sections have been plotted as indicated in Figure 121 along the navigational channel, including *Rede van Vlissingen en Honte*, *Drempel (Sill) van Borssele*, *Pas van Terneuzen* and *Put van Terneuzen*. Four additional sections have been plotted perpendicularly to the navigational channel. The orientation of the section along the navigational channel is from *Rede van Vlissingen en Honte* (left) to *Put van Terneuzen* (right) and for the perpendicular sections direction is from the right to the left bank.
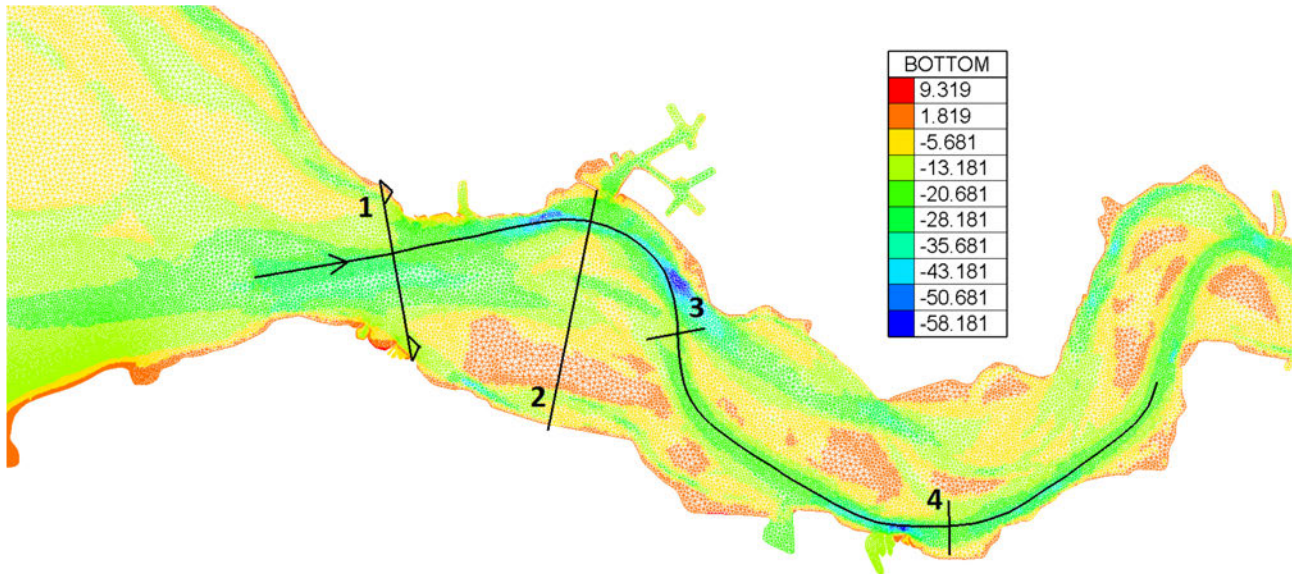
Figure 121 – Location of transects for the bed evolution within Wester Scheldt area.

Firstly, the measured information on the bathymetries from year 1986 to the year 1996 are provided along the aforementioned sections in Figure 122-Figure 126. It can be observed that from one year to the next, there are no intense differences, except for transect number two where the dynamic behaviour of the *Spijkerplaat* and *Schaar van de Spijkerplaat* becomes clearly visible. However, there are not exact information about the date/time of each year that the data have been monitored in relation to the dredging activities that took place.

In the same figures (Figure 122-Figure 126) the resulting bed evolution sections are shown, for sediment transport model by Bijker (hrun04). Significant downstream migration and deposition patterns can be observed at *Rede van Vlissingen en Honte* whereas in reality the sill is relatively stable (Figure 122). Also upward Terneuzen the bed is more active that can be observed in the bathymetric surveys. In the middle of *Drempel (Sill) van Borssele* can be observed an area that dredging is performed as the target depth between -12.02 m and -12.52 m is maintained. Around ~35-37 km, it can be observed that intense erosion have taken place which has reached the non-erodible bathymetry indicated by the dashed line. The bed levels that exceed the horizontal line of -12.02 m indicate that the model locally more active and predicts higher sediment deposition that what has happened in reality.

Figure 123 to Figure 126 show the bed evolution perpendicularly to the navigational channel for sediment transport model by Bijker (hrun04). Section 1 shows no intense erosion/deposition pattern, whereas section 2 indicates substantial erosion in the vicinity of the navigational channel (≈0.5-1.5 km of the section) evolving towards the north. In all perpendicular sections it appears that the minimum dredging depth is maintained between -12.02 m and -12.52 m.
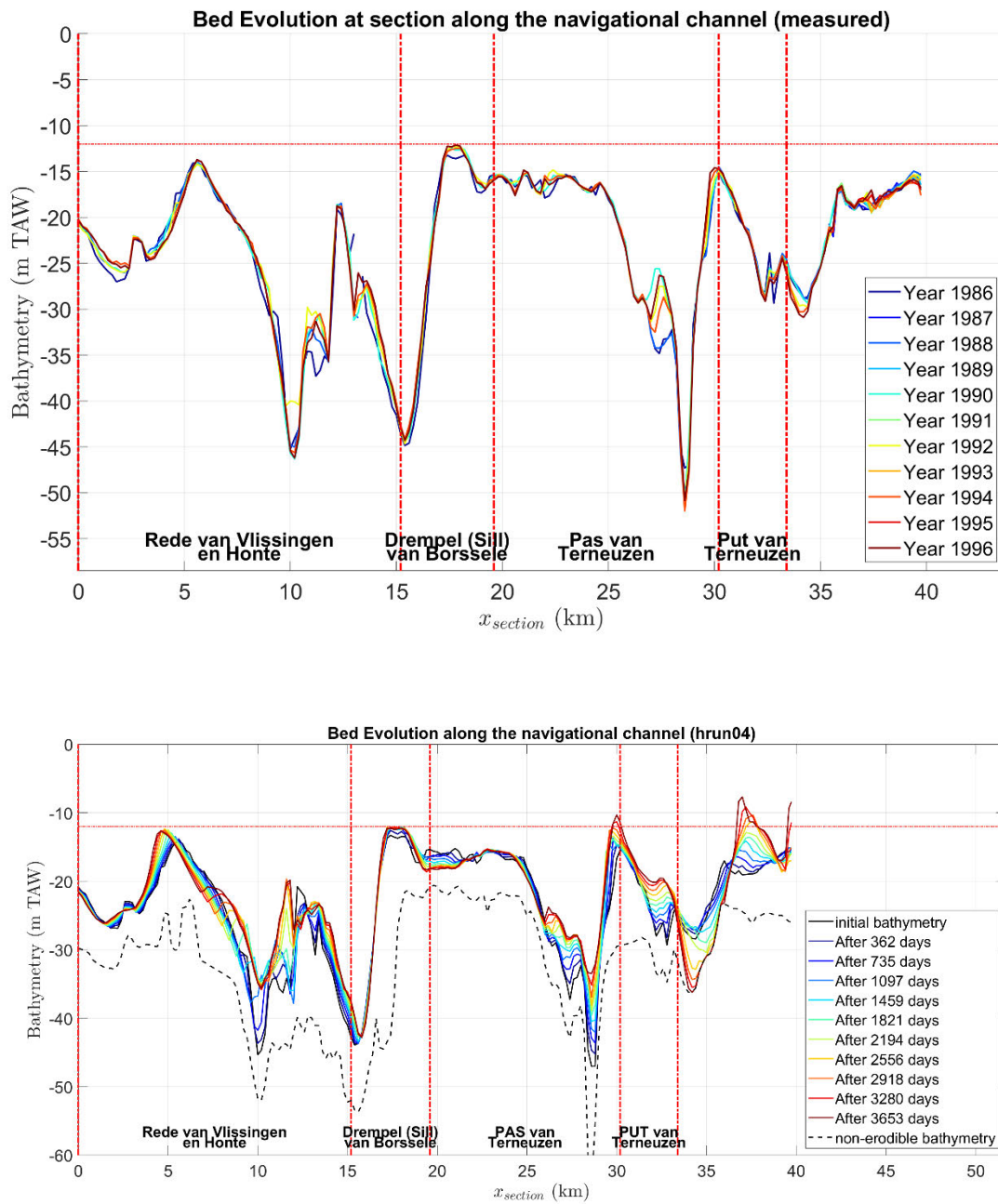
Figure 122 – Bed evolution on section along the navigational channel, upper figure: measured data, lower figure: Sediment transport model by Bijker (hrun04). Horizontal line corresponds to maintenance depth and vertical lines correspond to the boundaries of the dredging sites.
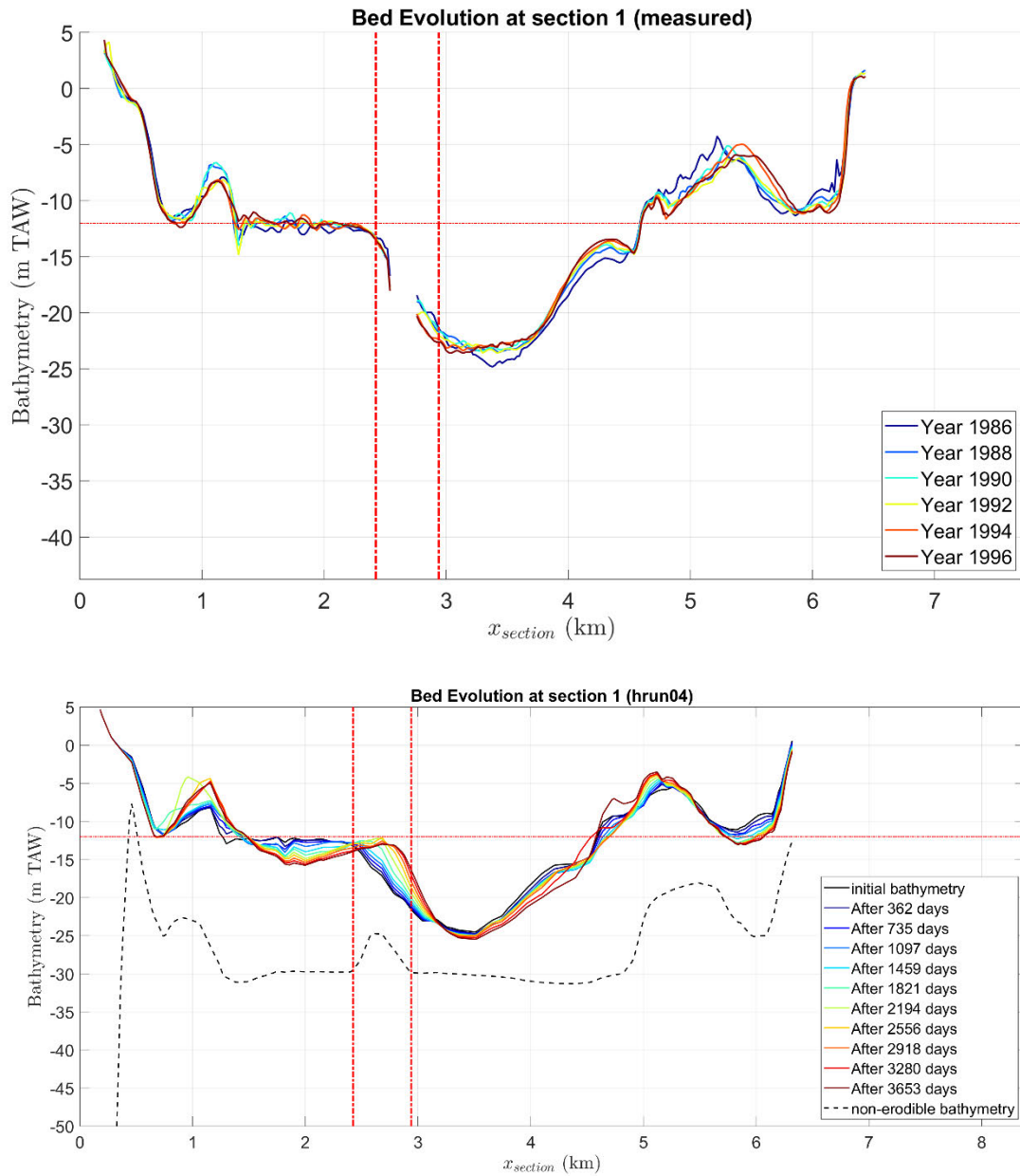
Figure 123 – Bed evolution on transect 1, upper figure: measured data, lower figure: Sediment transport model by Bijker (hrun04). Horizontal line corresponds to maintenance depth and vertical lines correspond to the boundaries of the dredging site.
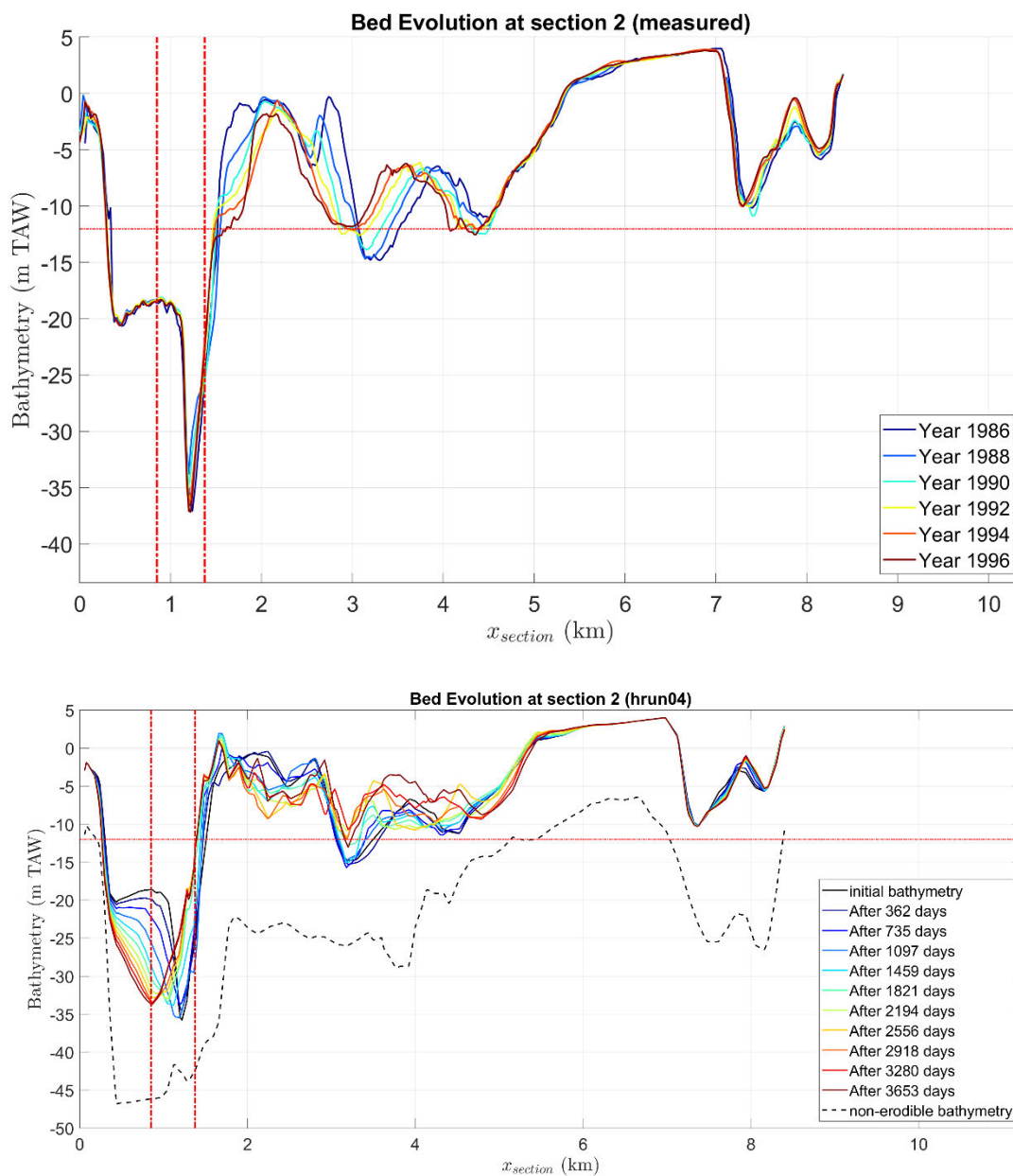
Figure 124 – Bed evolution on transect 2, upper figure: measured data, lower figure: Sediment transport model by Bijker (hrun04). Horizontal line corresponds to maintenance depth and vertical lines correspond to the boundaries of the dredging site.
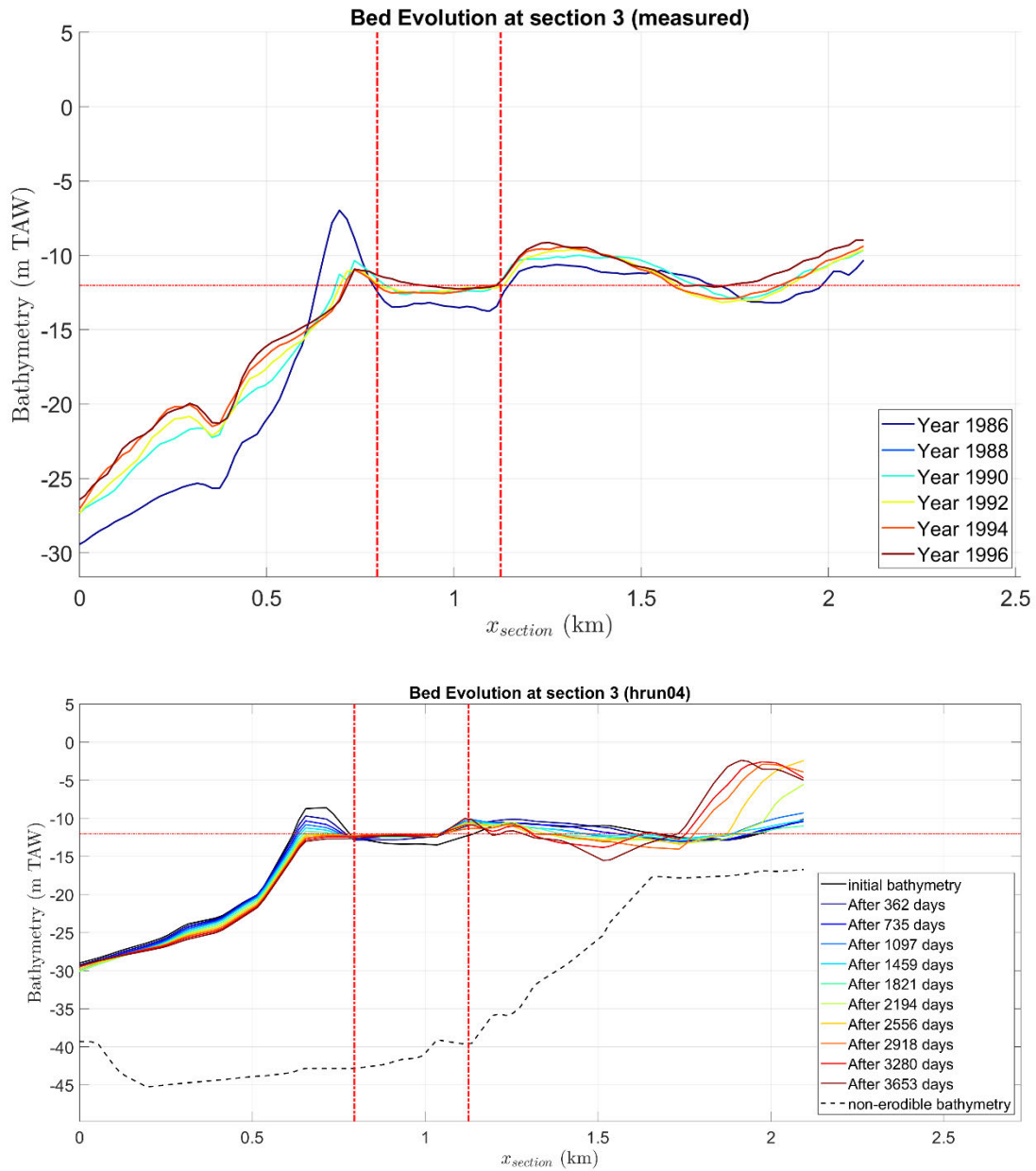
Figure 125 – Bed evolution on transect 3, upper figure: measured data, lower figure: Sediment transport model by Bijker (hrun04). Horizontal line corresponds to maintenance depth and vertical lines correspond to the boundaries of the dredging site.
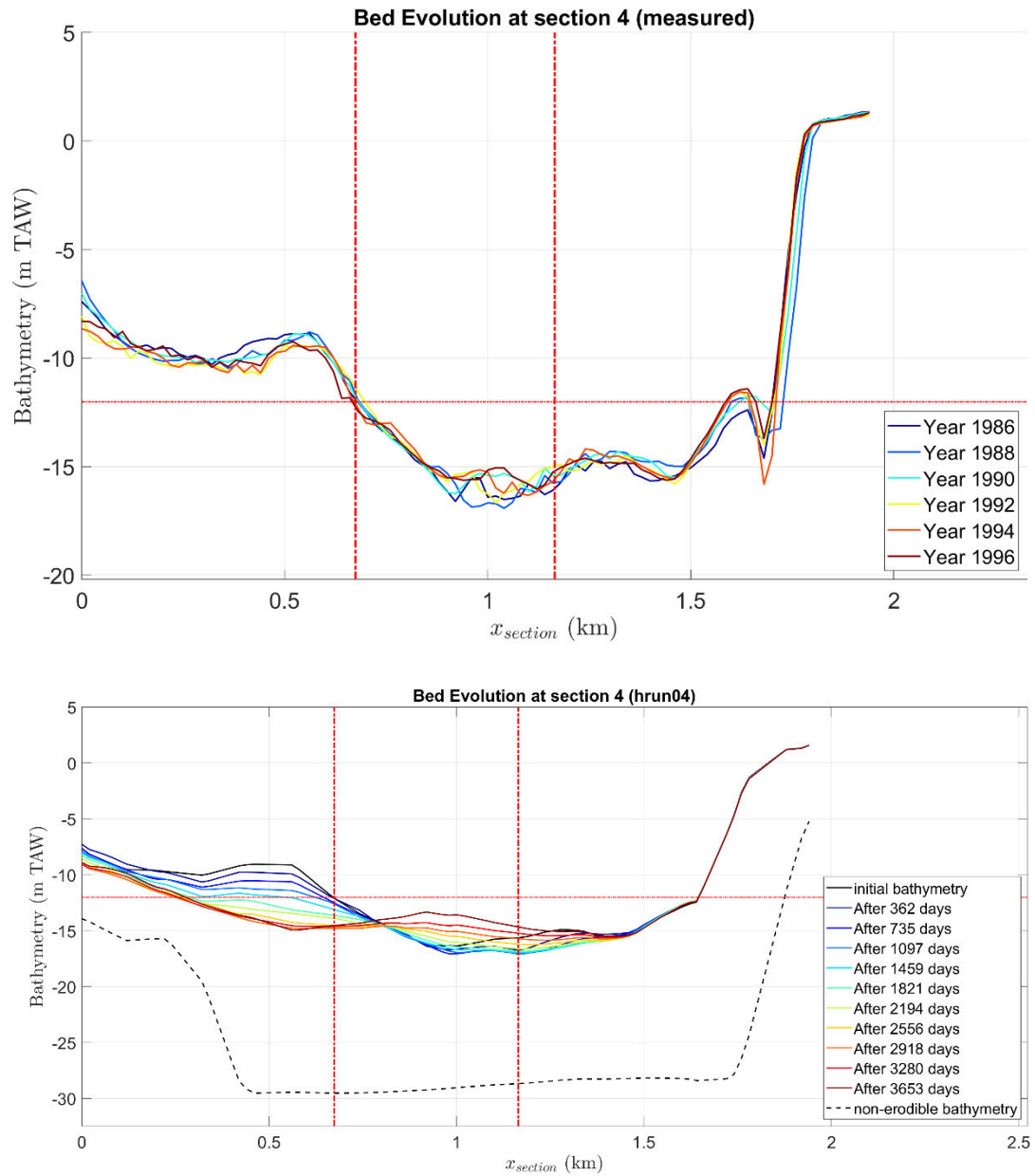
Figure 126 – Bed evolution on section 4, upper figure: measured data, lower figure: Sediment transport model by Bijker (hrun04). Horizontal line corresponds to maintenance depth and vertical lines correspond to the boundaries of the dredging site.
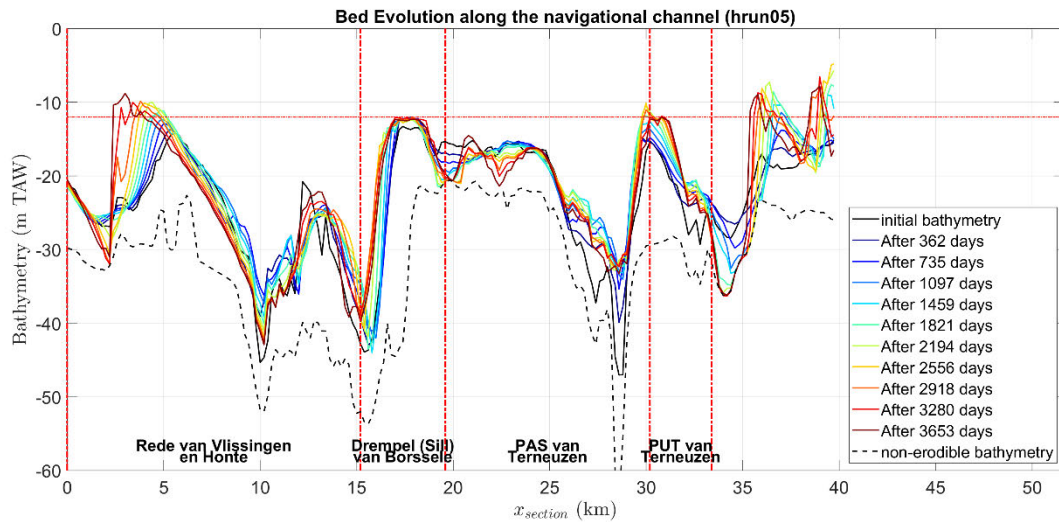
Figure 127 – Bed evolution on section along the navigational channel. Sediment transport model by Soulsby - VanRijn (hrun05). Horizontal line corresponds to maintenance depth and vertical lines correspond to the boundaries of the dredging site.

Figure 127 shows the bed evolution along the navigational channel for sediment transport model by Soulsby – Van Rijn (hrun05). It demonstrates the most intense activity among the sediment transport formulas examined as it can be seen from the erosion/deposition patterns. The deposition pattern around ≈3-5 km indicates the ebb dominance of the flow in Western Scheldt mouth. The intense deposition of sediment in that region indicates that the sediment transport model is locally more active. The bed level exceeds the maintenance depth of -12.02 m which is not what has happened in reality based on the measured data. Moreover, dredging processes are active not only in the middle of *Sill van Borssele* but also in the beginning of *Put van Terneuzen* sites.

5.2.6 Hindcasting 2014-2015 simulation results

In this set of simulation, a short term hydrodynamic and morphodynamic investigation is conducted for the most recent years 2014-2015 and results concerning sediment transport patterns and dredged volumes are compared against the available field measurements.

The wave effect on the erosion/deposition patterns and also the imposition of hard layers is examined in this set of simulations. The full set of the simulated cases is shown in Table 30.

Table 30 – Simulated cases for hindcasting 2014-2015 with different considered sediment transport models, waves effect, hard layer imposition and morphological factor (MOFAC).

Run name	Sediment transport model	Wave effect	Hard layers
nrun04	Bijker	NO	NO
nrun05	Soulsby – Van Rijn (SVR)	NO	NO
nrun05a	Soulsby – Van Rijn (SVR)	YES	NO
nrun05b	Soulsby – Van Rijn (SVR)	NO	YES
nrun30	Engelund & Hansen (EH-30)	NO	NO
nrun71	Van Rijn 2007 (VR07)	NO	NO
nrun71a	Van Rijn 2007 (VR07)	YES	NO
nrun71b	Van Rijn 2007 (VR07)	NO	YES
nrun71c	Van Rijn 2007 (VR07)	YES	YES

Effect of sediment transport formula

In this section the results for the simulated cases nrun04, nrun05, nrun30 and nrun71 are discussed in terms of erosion/deposition patterns and the dredged volumes are compared against the available field data.

The erosion/deposition patterns demonstrate once more the intense sedimentation caused by Soulsby – Van Rijn and Van Rijn (2007) models not only in the Western Scheldt region but also in the Blankenberge region where after the 2 years simulation, the deposited material in the dumping site has already started moving to the east. It has also to be mentioned that the relatively high deposition on the dumping sites S1 and S2 (see Figure 108) is mainly attributed to the fact that the initial bathymetry in the dredging sites is not exactly equal to the maintenance depths defined with the dredging actions shown in Table 26.
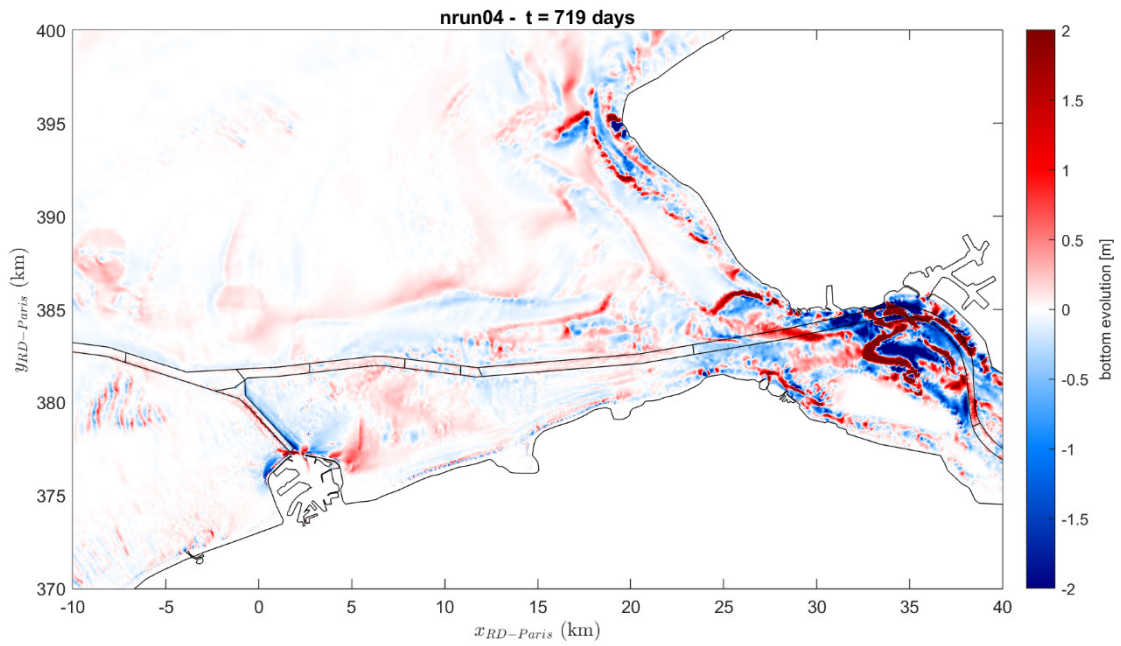
Figure 128 – Contour plot of erosion/deposition patterns after 2 years (2014-2016) morphodynamic time in Scaldis-Coast model. Sediment transport model by Bijker for case nrun04.
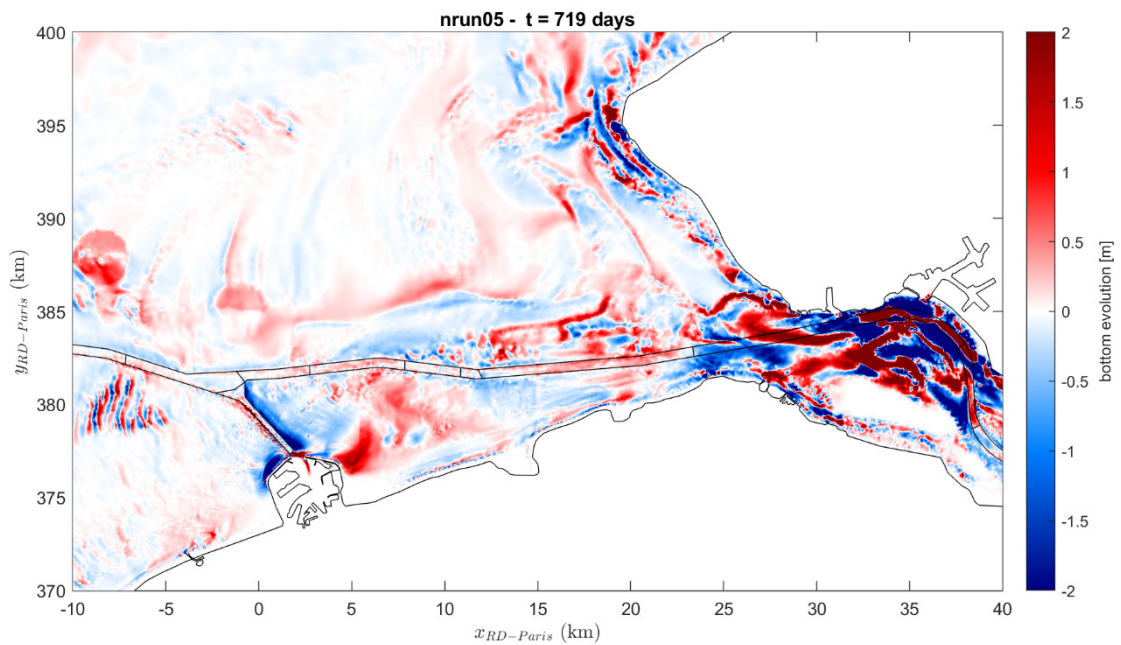
Figure 129 – Contour plot of erosion/deposition patterns after 2 years (2014-2016) morphodynamic time in Scaldis-Coast model. Sediment transport model by Soulsby – Van Rijn for case nrun05.
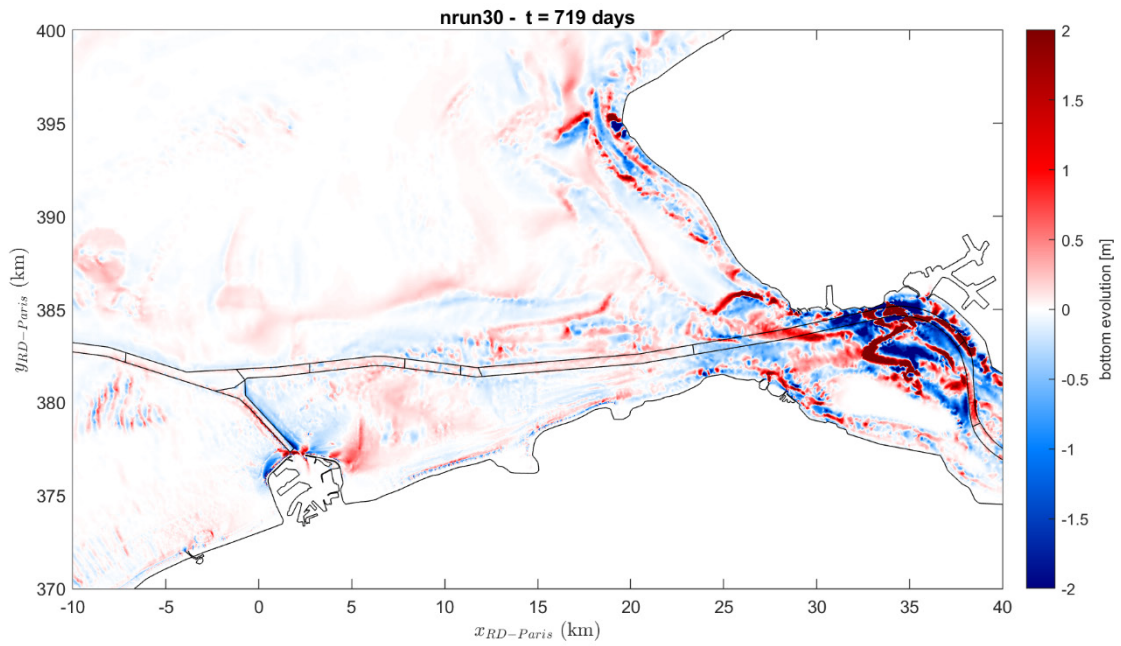
Figure 130 – Contour plot of erosion/deposition patterns after 2 years (2014-2016) morphodynamic time in Scaldis-Coast model. Sediment transport model by Engelund & Hansen for case nrun30.
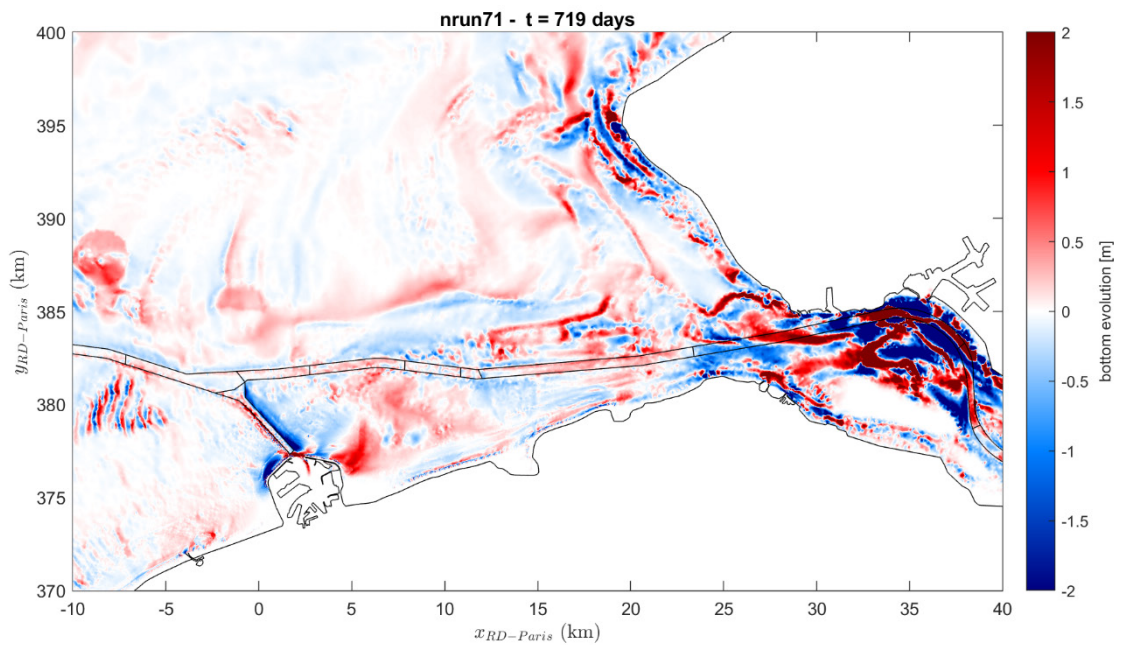
Figure 131 – Contour plot of erosion/deposition patterns after 2 years (2014-2016) morphodynamic time in Scaldis-Coast model. Sediment transport model by Van Rijn (2007) for case nrun71.

Figure 132 indicates the total dredged volume computed by summing up all the dredging activities that took place the second year of the simulation, as first year was omitted for warm up purposes. The measured volumes indicate that *Sill van Borssele* is the site with the highest amount of dredged volume. It can be seen that in total measured and computed volumes are closest for Soulsby – Van Rijn and Van Rijn (2007) models. Engelund & Hansen and Bijker models significantly underestimate the dredged volumes once again.
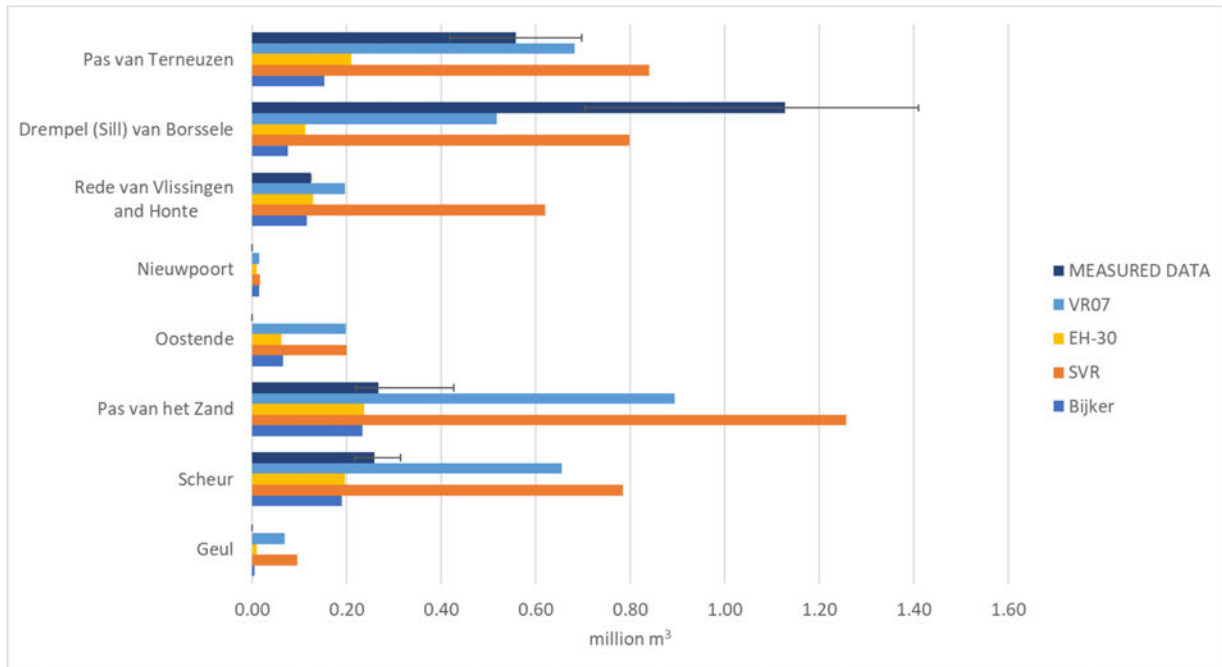
Figure 132 – Bar plot for the total dredged volumes for the major dredging sites, accounting only for the second year of the total 2 simulated years (2014-2016) for different sediment transport models.

A quite high value of dredged volume for site *Rede van Vlissingen en Honte* can be observed for Soulsby – Van Rijn model (nrun05) in Figure 132, significantly higher than the prediction by the other sediment transport models and the measured volumes. This can be explained by Figure 129 where an intense deposition area is observed in the entrance of Western Scheldt approximately in the middle of the dredging site and develops from southeast to the northwest. If we take a closer look in Figure 133 for the section along the navigational channel for simulation nrun05, it can be seen that dredging activity takes place at ≈5-6 km for maintaining the target depth of 14.72 m and this dredged region has a length of ≈1 km. This compared to Figure 134 showing the bed evolution along the navigational channel for Van Rijn (2007) model (nrun71) which is the next more intense sediment transport model, it can be seen that the same region is much less extensive. This explains the difference in the computed dredged volumes observed in Figure 132 for *Rede van Vlissingen en Honte*. The extended dredging activity in *Sill van Borssele* justifies the high computed dredged volumes which are substantially smaller compared to the measured volumes though.
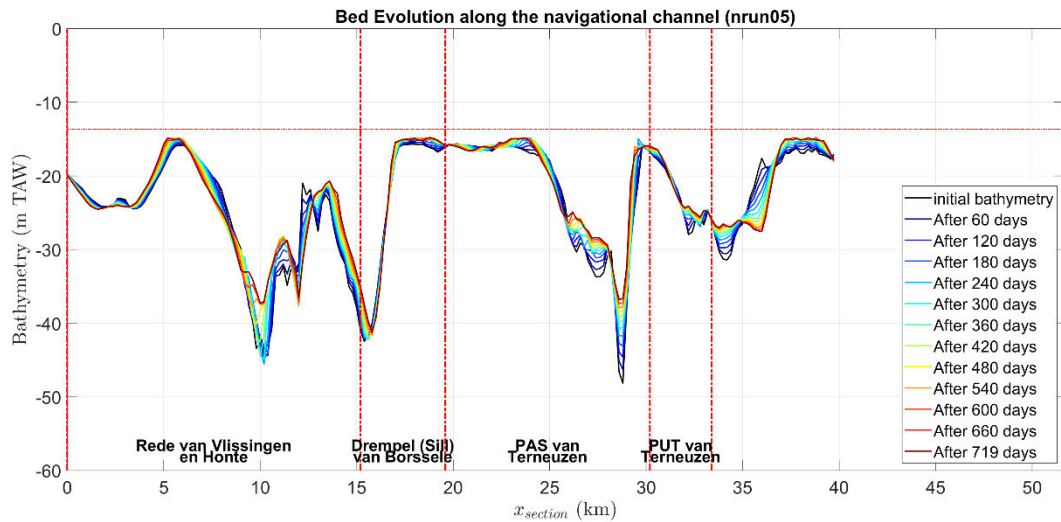
Figure 133 – Bed evolution on section along the navigational channel. Sediment transport model by Soulsby - VanRijn (nrun05).
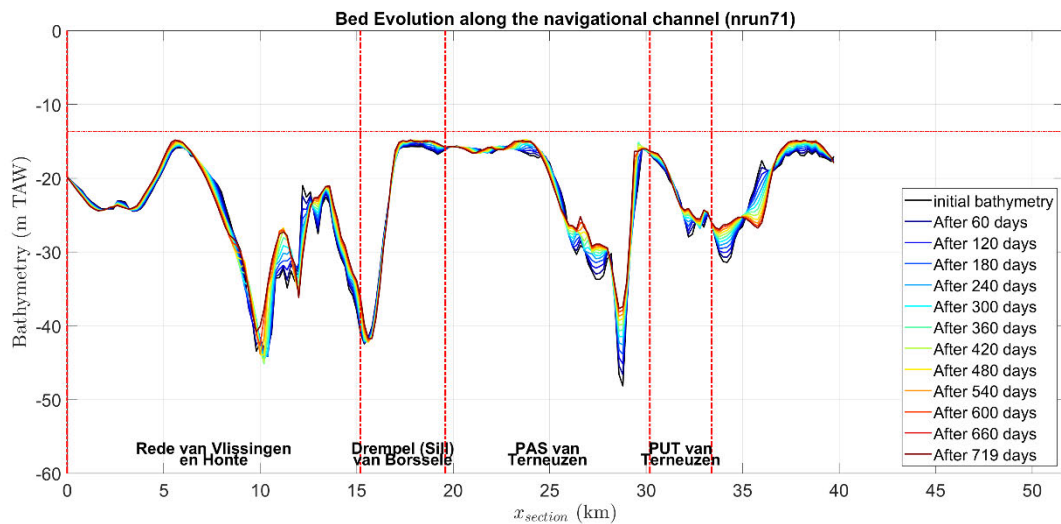
Figure 134 – Bed evolution on section along the navigational channel. Sediment transport model by Van Rijn (2007) (nrun71).

Figure 135 and Figure 136 show the timeseries and cumulative timeseries of dredged volumes for the sites *Pas van het Zand* and *Drempel (Sill) van Borssele* for Soulsby – Van Rijn (SVR) model. Within the examined second year of the simulation they demonstrate a non-uniform temporal variation of dredged volumes. However, the computed values demonstrate the closest agreement with the measured values shown in Figure 132.
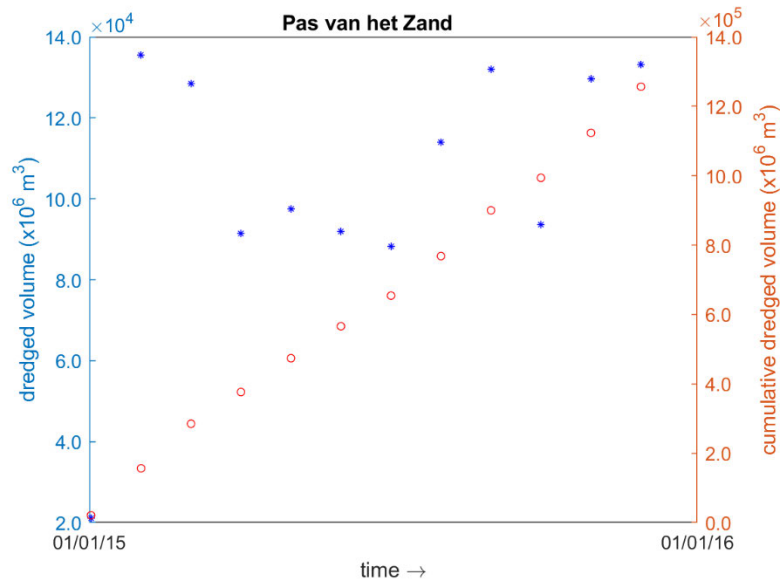
Figure 135 – Timeseries and cumulative timeseries of the dredged volume in the site *Pas van het Zand* (nrun05).
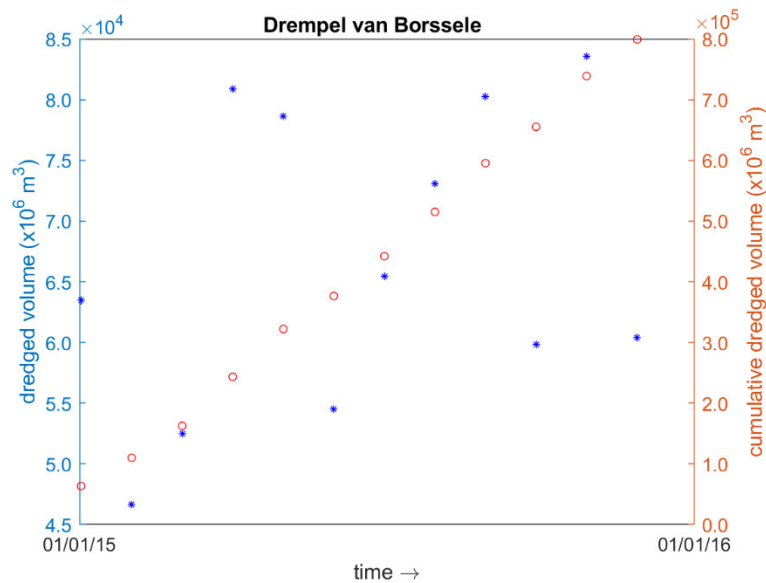
Figure 136 – Timeseries and cumulative timeseries of the dredged volume in the site *Drempel (Sill) van Borssele* (nrun05).

It has to be mentioned that for the computations nrun04, nrun05, nrun30 and nrun71 the required computation time for 2 years simulation accounting for hydrodynamics, sediment transport and dredging was equal to 12.5 hours.

Effect of waves

In this subsection we compare the dredged volumes for the second year of the simulation for the two models (Soulsby – Van Rijn and Van Rijn (2007)) that gave the closest estimation of the dredged volumes when accounting only for the hydrodynamic input. At this point we demonstrate the results of nrun05a and nrun71a taking into account also the wave action. The coupling between TELEMAC2D and TOMAWAC has been achieved using the TEL2TOM functionality presented in sections 2.2.3 and 2.2.4.

The erosion/deposition patterns shown in Figure 137 and Figure 138, indicate a relatively more active coastal zone due to wave-driven currents along with relatively more intense patterns offshore from Western Scheldt mouth. However, the shape of those patterns is retained with consideration of waves or without, which indicates that the wave effect in the region is minor. The wave effect can be observed also on the dredged volumes shown in Figure 139 where simulations with wave consideration result in higher dredged volumes up to an average percentage of 15% higher than simulations without waves. Soulsby – Van Rijn and Van Rijn (2007) are still performing the best with consideration of waves, compared to the field measurements.

It has to be mentioned that for the computations nrun05a and nrun71a that waves are taken into account via coupling with TOMAWAC, the required simulation time is equal to 5 days which is 9.6 times more time consuming than the simulations of the previous subsection.
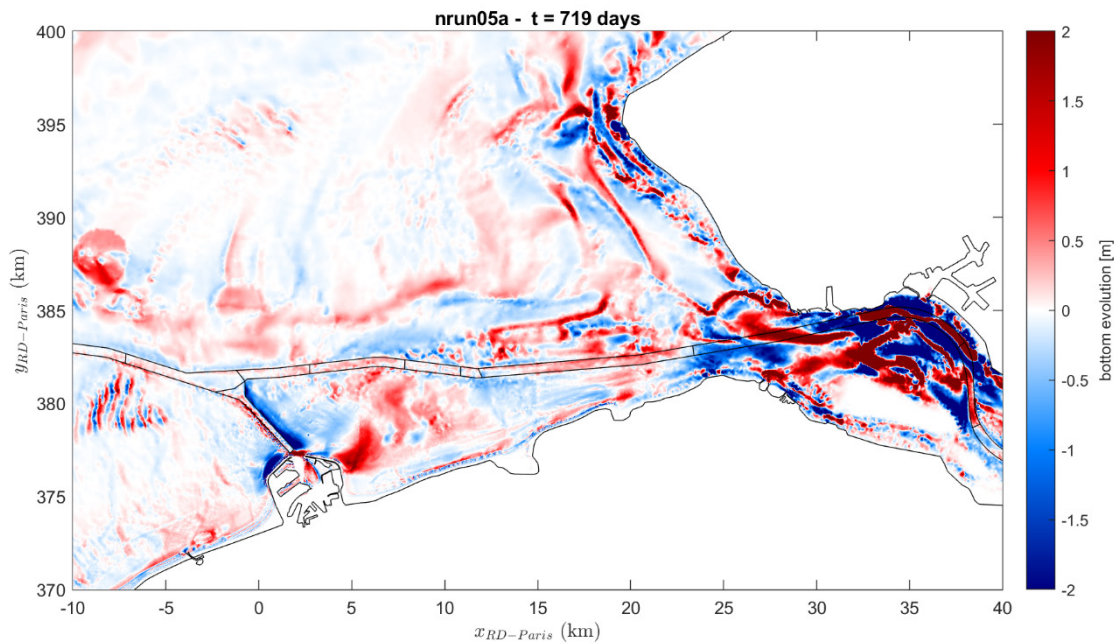
Figure 137 – Contour plot of erosion/deposition patterns after 2 years (2014-2016) morphodynamic time in Scaldis-Coast model. Sediment transport model by Soulsby – Van Rijn with wave effect for case nrun05a.
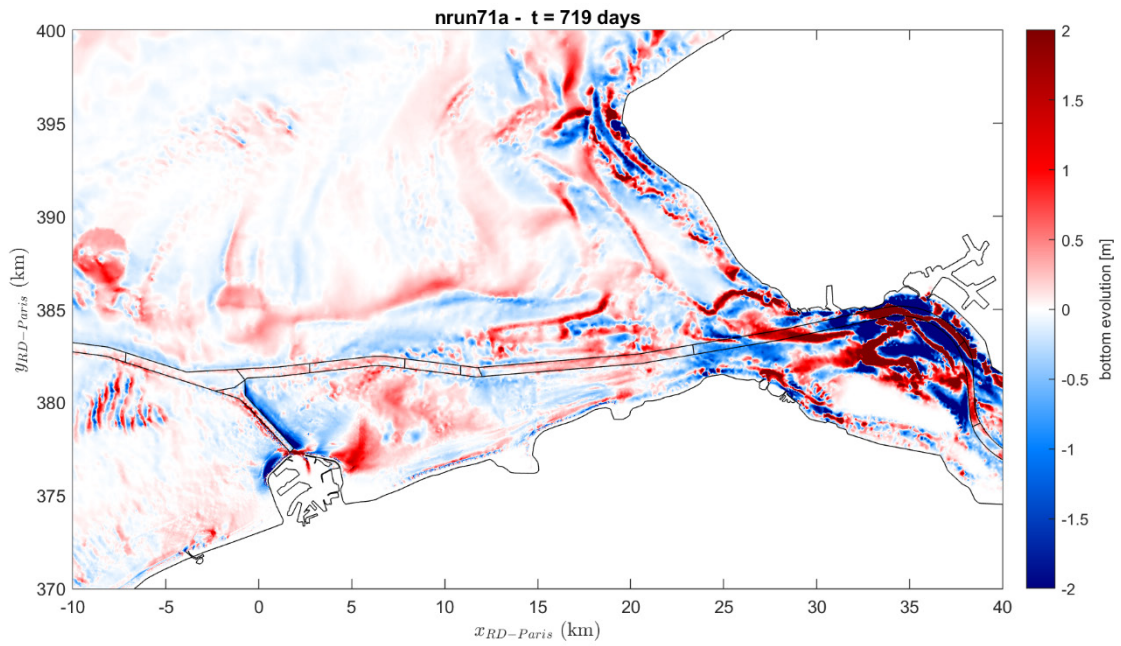
Figure 138 – Contour plot of erosion/deposition patterns after 2 years (2014-2016) morphodynamic time in Scaldis-Coast model. Sediment transport model by Van Rijn (2007) with wave effect for case nrun71a.
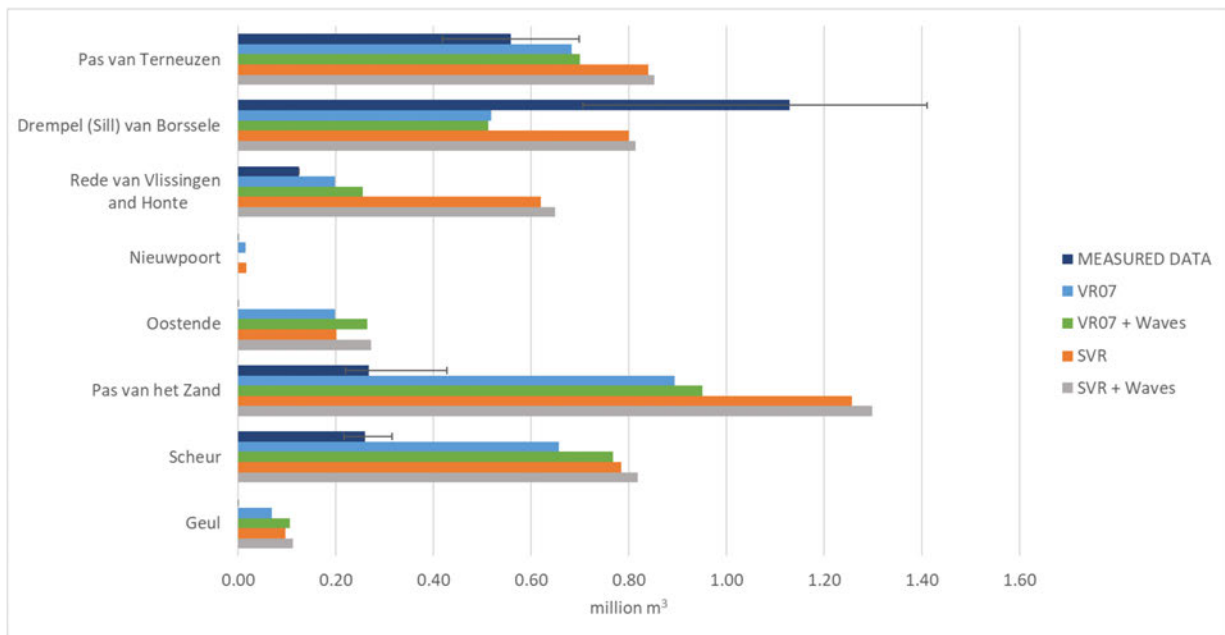
Figure 139 – Bar plot for the total dredged volumes for the major dredging sites, accounting only for the second year of the total 2 simulated years (2014-2016) for different sediment transport models and consideration of wave effect.

Effect of Hard Layers consideration

Nevertheless, one of the known information is that not all regions in the domain of interest allow for unlimited erosion depths. Thus, there are areas with specific erosion capacity which in the Western Scheldt region have been identified by comparison of bathymetries between years 1960 and 2011, as previously discussed. Those hard layers have been implemented through the variable NOER within the TELEMAC2D geometry selafin file. The results of test cases nrun05b and nrun71b, coming from cases nrun05 and nrun71, respectively, and include the hard layers.

The erosion/deposition patterns do not demonstrate any significant visual differences with those of runs nrun05 and nrun71 shown in Figure 129 and Figure 130. This result is reflected also in the dredged volumes within those two cases which result in volumes that differ by maximum 1% from the computed dredged volumes on test cases without hard layers.

For the above reasons we have considered an additional case nrun71c which is once more the same as nrun71 with the addition of hard layers and wave action consideration. However, the differences between this case and the cases simulated with Van Rijn (2007) model (nrun71, nrun71a and nrun71b) did not demonstrate significant differences concerning the erosion/deposition patterns and difference in the computed dredged volumes is ±1% compared with the previous cases.

This outcome is expected in the sense that a simulation up to 2 years will most possible not result in erosion at such an extent that the non-erodible bed will be reached, regardless of the choice of sediment transport model. The bed evolution in section along the navigational channel for run nrun71c can be seen in Figure 140.
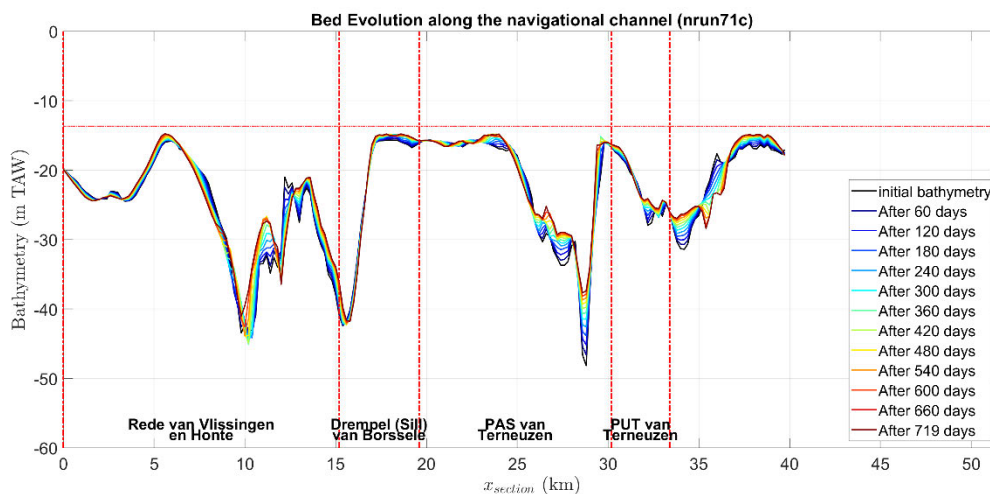
Figure 140 – Bed evolution on section along the navigational channel. Sediment transport model by Van Rijn (2007) (nrun71c).

5.2.7 Conclusions

Based on the simulations performed in this chapter we can conclude the following:

- The mesh was locally adapted to meet the dredging polygons, this improves the accuracy of the dredging volumes.
- The effect of waves is minor with respect to computing accurately the dredged volumes since the computed values are ≈15% higher than without wave consideration. The effect is slightly higher for the coastal fairways than for the channels in the Western Scheldt, still for the coastal channels it is rather limited.

- Consideration of a non-erodible bathymetry is important in performing long term morphodynamic simulations especially in cases of very active sediment transport models (Soulsby – Van Rijn, Van Rijn (2007)).
- Overal the model is underestimating the dredging volumes. This is both on the long term (10 year hindcast) as for a short run of one year with brute force tidal, wave and wind coditions, representing the current dredging strategy. Although Enguland & Hansen en Bijker are shown to predict the morphological more reliable in general, the predicted dredging volumes are most underestimated. On the other hand dredging volumes by Soulsbe & Van Rijn and Van Rijn 2007 seems to be more in line with the reported dredging volumes - at least for Pas van het Zand, Scheur and Terneuzen, less for Vlissingen (overestimating) and Borssele (still underestimating) – but they are considered to be morphologically unrealistically active in the overhaul part of the domain.
- At the moment it is not yet understood why the model is performing poorly in predicting dredging volumes.

5.3 Validation of the longshore transport: Wenduine and Blankenge cases

Longshore sediment transport created by waves and currents plays a considerable role in the long-term morphological behaviour of the Belgian coast. Because of the longshore sediment transport, the area around Wenduine encounters structural erosion and the nourishment in this area is subjected to a limited lifecycle, while the harbour of Blankenberge experiences strong sedimentation in its entrance channel requiring frequent dredging. These two issues provide suitable hindcast cases to validate long-shore driven beach morphology of this model.

The table below summarizes the simulations which are applied to validation of the longshore transport.

Table 31 – Summary of the simulations for validation of the longshore transport

runID	Mesh	TOM2TEL	MorFac	Transport formula	Grain size	Tidal force
HSW015b	D2[1]	NO	1	Soulsby-van Rijn	250µm	Brute
HSW071	G01	NO	1	Soulsby-van Rijn	250µm	Brute
HSW101_06a	D4	YES	1	Bijker	200µm, 500µm	Brute
HSW101_06b	D4	NO	1	Bijker	200µm, 500µm	Brute
HSW101_07a	G01	NO	1	Bijker	200µm, 500µm	Brute

---

[1] In this version of the model, the submerged dam of Blankenberge was modelled as a closed dam, which is incorrect for the situation at that time. The submerged dam will be replaced by a full dam in 2025.

5.3.1 Wenduine

This morphological model was run with brute force wave and wind conditions in combination with the representative tidal forcing during the period between the June 1st, 2014, and to the June 1st, 2015 (HSW015b, SVR). The modelled bed evolution was validated with net volume change in the closed pink box along the coast (Figure 141 and Figure 142). The period is characterised by strong erosion of the recently nourished Wenduine foreshore and beach nourishment. The representative tide was adopted here, because the aim of the testcase is to validate the model for long term longshore processes. However, brute force wave wind conditions are used because of the moment of running this testcase, there was still ambiguity with respect to the method of the wave schematization, see Section 4. Recall the in the end the annual net longshore transport of the selected representative year is close to the June 2014 – June 2015 period, (Section 4.4).

Figure 141 displays the modelled morphological change over 1 year. The observed morphological change was calculated based on the difference between lidar and foreshore surveys of spring 2014 and spring 2015 (Figure 142). Both the model and the measurement display strong erosion in front of Wenduine, as the initial bathymetry (spring 2014) includes a recent nourishment executed in February-March 2014. The observed erosion volume within the pink box reaches 145 830 m^3 which is very closely represented by the model: 146 600 m^3. However, the location of the erosion is slightly different in the model. The modelled erosion takes place more offshore than the observed one. In this 2D model, cross-shore processes are not implemented yet (see later Section 7.1), thus on- and offshore transport due to stokes drift and undertow do not exist (L.C van Rijn *et al.*, 2003; Walstra *et al.*, 2012). This could be considered as a major interpretation for the different location of the erosion between the measurement and model. Also, the use of a representative tide instead of a full tidal spring-neap tidal cycle can have an impact on this, i.e. the absence of high-water spring and storm tides.

In addition to the erosion, the model shows strong sedimentation in the Blankenberge access channel. The observations do not display this, due to the maintenance dredging works that were executed throughout year 2014-2015, which were not yet implemented in the model at the time of this test case, see also next section. Another visible difference could be found in both sides of the Blankenberge access channel. The measurement exhibits significant sedimentation on the dry beaches east and west of the marina access channel, but the model does not. This difference is due to the fact that some of the sand dredged at the Blankenberge access channel is deposited at these locations as a temporary storage of sand reserves for beach maintenance.
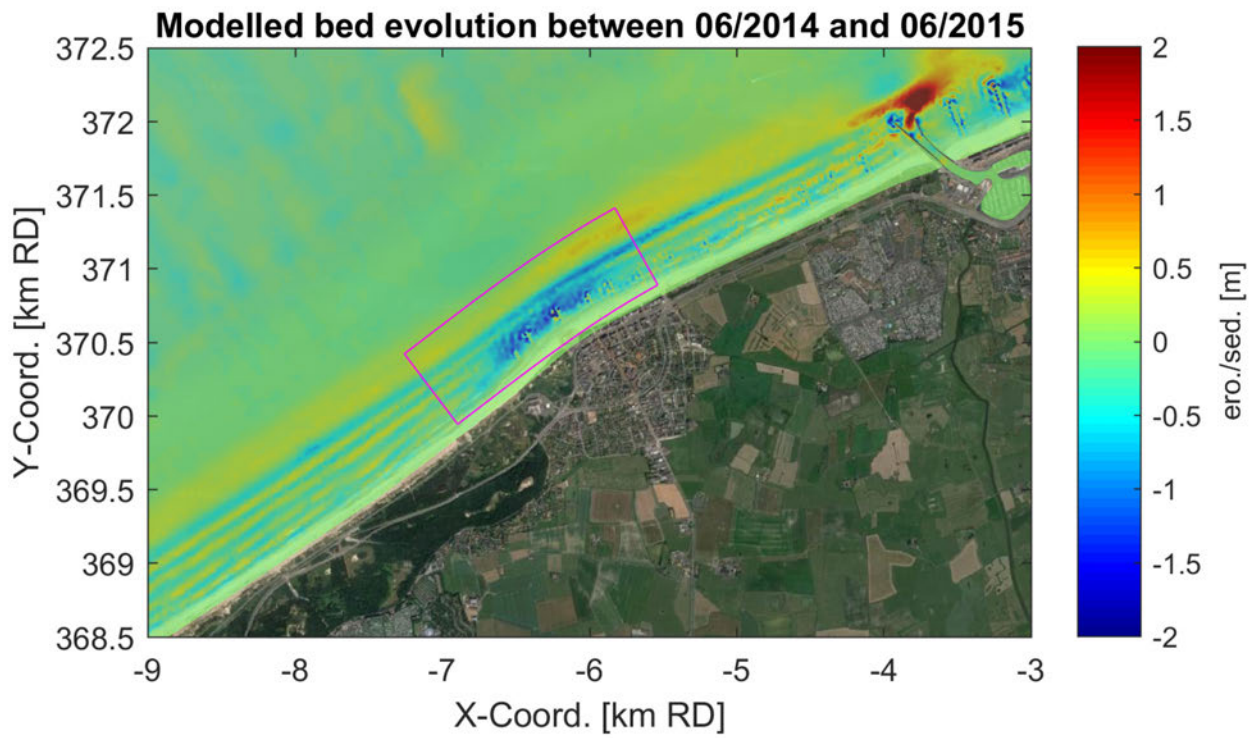
Figure 141 – Modelled 1-year morphological change at Wenduine (HSW015b, SVR).
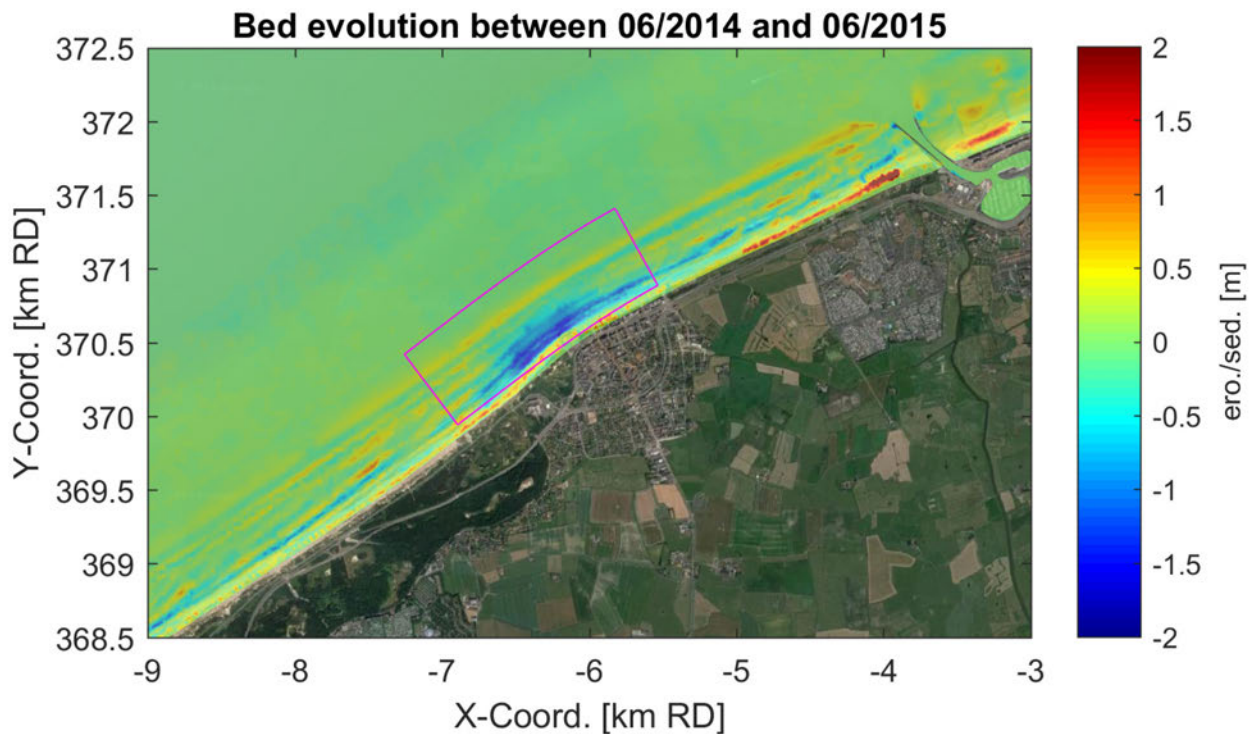
Figure 142 – Observed 1-year morphological change at Wenduine.

5.3.2   Blankenberge

Annual sedimentation rates

The model HSW071 has been run with brute forces of the previously selected representative year, a sedimentation/erosion map around the port of Blankenberge is plot (Figure 144). A detail of the grid at the Blankenberge marina access channel is shown in Figure 143. This is the standard grid of the model. The grid is slightly refined around the structures and the channel. However, inside the channel the grid is limited to maximum four cells in the width of the channel.

From the comparison between Figure 144 and Figure 145, it could be found that the sedimentation pattern is similar in general, although the sedimentation in front of the channel entrance (zone A) is underestimated by the model. The sum of sedimentation in Zone A, B and D reaches 165 000 m³/year according to the estimation of dredging volumes over the past 30 years (1980-2010) (Teurlinx *et al.*, 2009), while the modelled sedimentation achieves 169 000 m³/year within the dashed polygon (Figure 144). The sedimentation in Zone C is mainly caused by aeolian transport which is not considered in the morphology model.
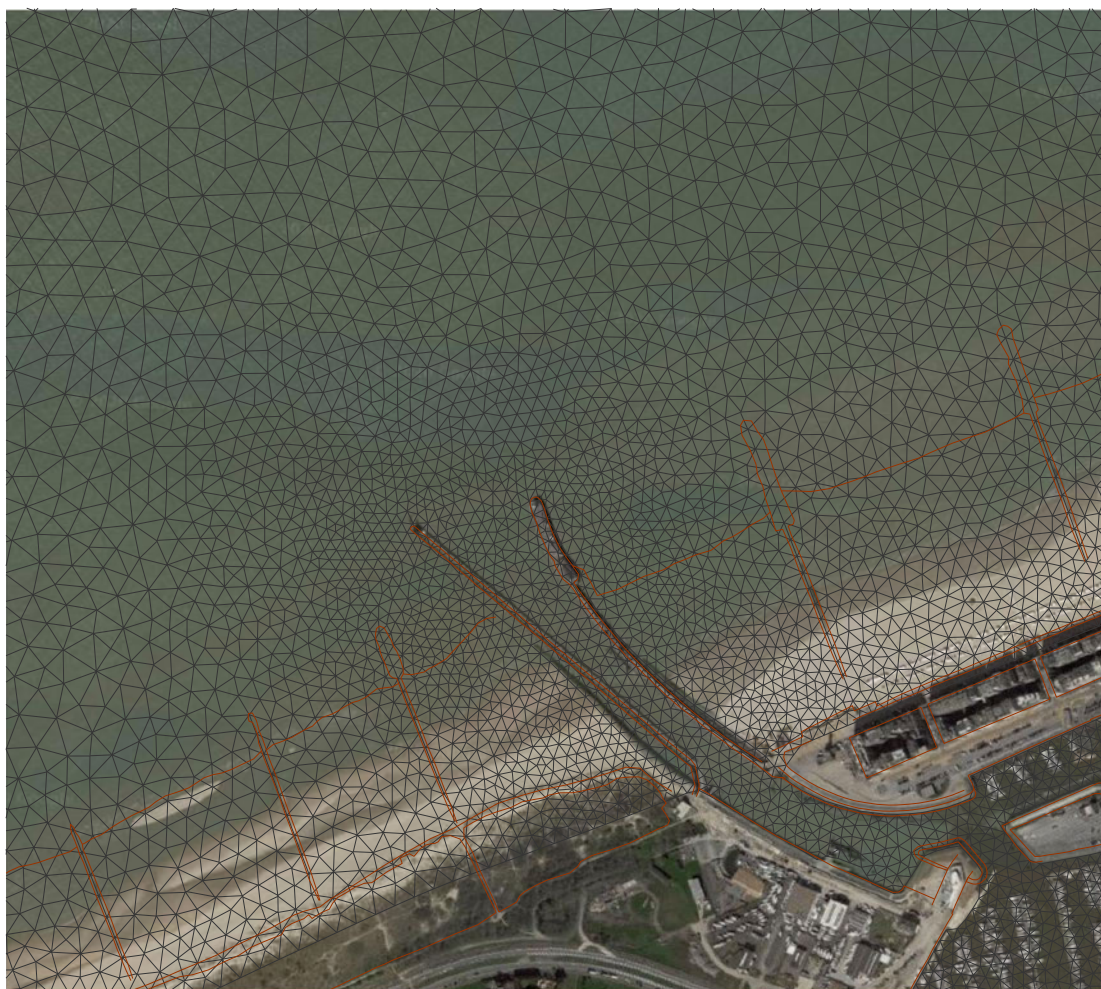
Figure 143 – Detail of the grid at the Blankenberge marina acces channel (HSW071)
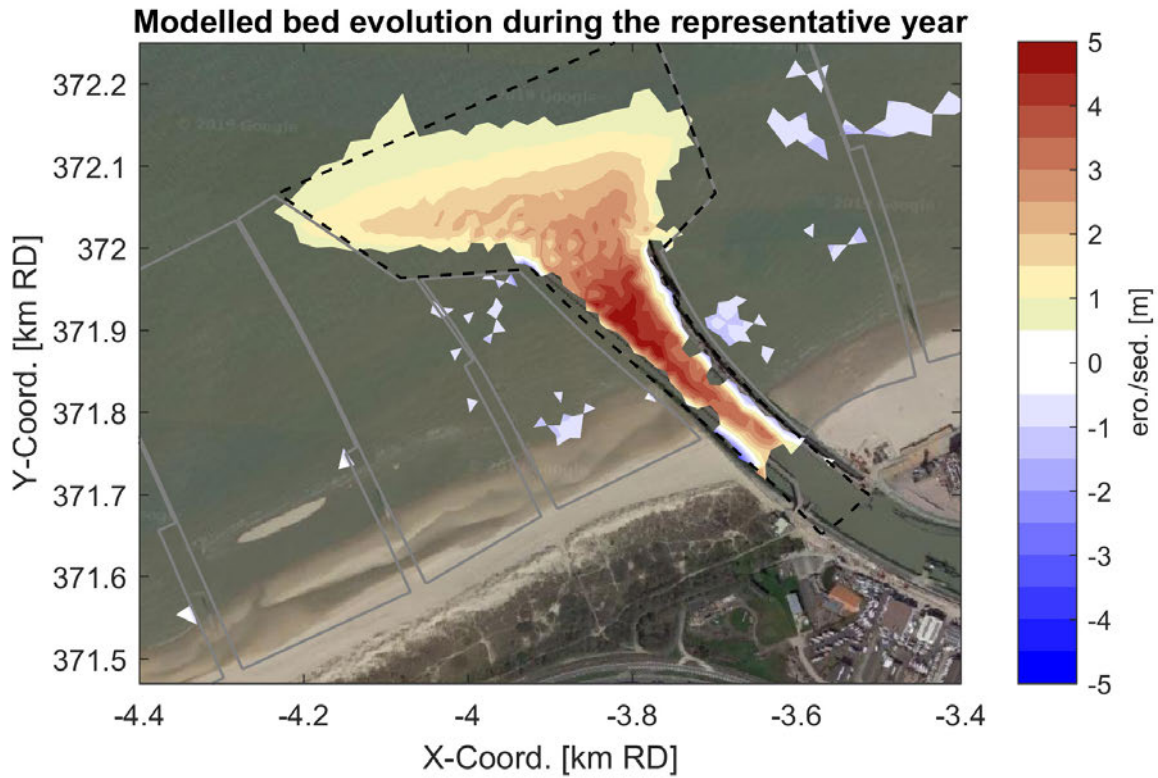
Figure 144 – Modelled annual sedimentation in the entrance channel for the port of Blankenberge (HSW071 SVR).
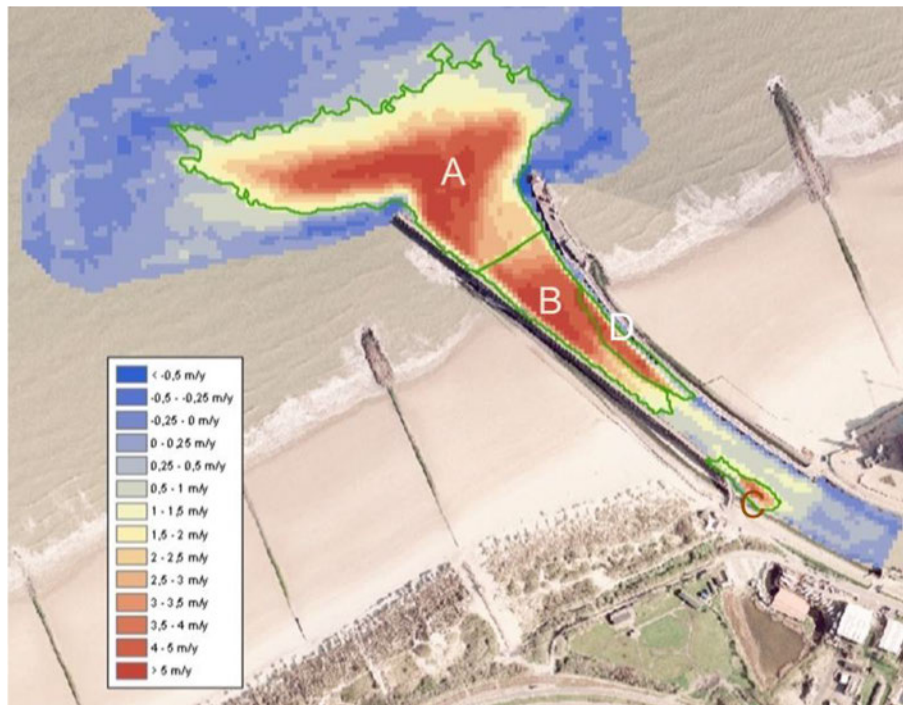
Figure 145 – Estimated annual sedimentation in the entrance channel for the port of Blankenberge based on the bathymetric surveys (Teurlinx *et al.*, 2009).

Ciara storm February 2020

In addition to the comparison of the annual sedimentation, such a one-year simulation and previous study also suggest that individual storm events can cause strong sedimentation in the port of Blankenberge, Figure 146 and Figure 147. The storm Ciara which took place in February 2020, provides another good case to further validate the morphology model. For the preparation of the regular dredging works planned at the end of the winter the marina intrance and forshore was surveyed on February 6th, this is only three days before the storm. Shortly after the storm, February 14th, the survey was repeated, see Figure 148. Together with the hydrodynamic and meteorologic measurements of *Meetnet Vlaamse Banken*, this forms a valuable dataset for model validation.

The morphology model is driven by hydrodynamic boundary conditions from the regional ZUNO model (Maximova *et al.*, 2016), wave and wind boundaries from the measurement station Westhinder which is deployed by Afdeling KUST.

The hydrodynamic validation of the storm was carried out at 6 stations (4 for water level, 2 for currents), and their location is shown in Figure 149. The station Westhinder is situated at the offshore boudary of the model. The comparison of wate level at Westhinder shows a fairly good agreement between the model and measurement, which indicates reliability of the regional ZUNO model (Figure 150). The water level at the other 3 stations is also reproduced quite well by the model. The storm surge is observed to reach around 5.5 m TAW. The measurement station of Blankenberge is located in the marina. Such a small-scale infrastucture may have a strong local effect on the hydrodynamics. The modelled water level at Blankenberge shows a slightly larger error than that at the other stations.

Moreover, the current velocity was validated against the measurement at 2 stations Bol Van Heist and Scheur Wielingen, and their location could be also found in Figure 149. The model is capable of capturing periodic variation of tidal currents (Figure 151). The velocity magnitude at Bol Van Heist is visibly underestimated by the model. The underestimation has been reported in many previous studies (Dujardin *et al.*, 2010; G. K. Kolokythas *et al.*, 2018a; Van den Eynde *et al.*, 2007; Wang *et al.*, 2015), and is considered to be associated with the installing location of the measurement station, where local bathymetric effects may play a significant role in the local flow. In the second half day of 9 February, the monitoring instrument at Bol Van Heist might not work properly, because the sampled data appears to be very suspicious during this period.

Figure 146 – Areal photograph of the sedimentation in the channel after storm Ciara
(© Koninklijk Belgisch Instituut voor Natuurwetenschappen (KBIN))

Figure 147 – Sedimentation Blankenberge channel, day after storm Ciara (source:
https://www.vrt.be/vrtnws/nl/2020/02/13/jachthaven-blankenberge-moeilijk-bereikbaar-na-storm-ciara/)
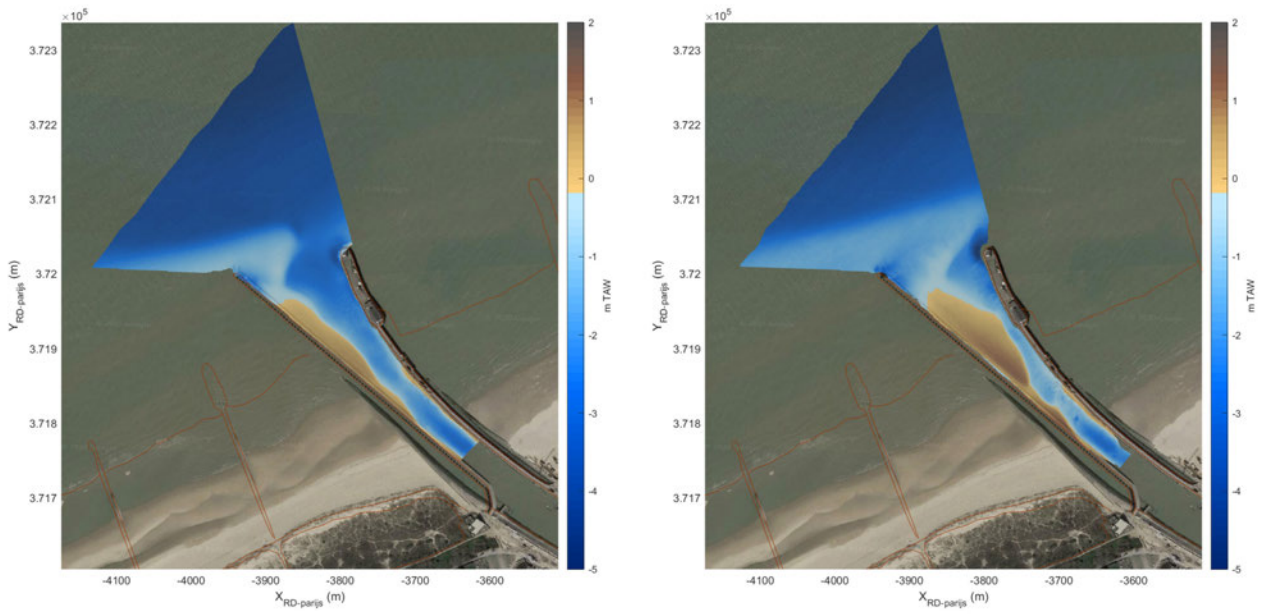
Figure 148 – Pre- and post-storm bathymetric surveys (left: February 6th, 2020; right: February 14th, 2020), depth in mTAW)

Figure 149 – Locations of the water level and current velocity measurement stations.
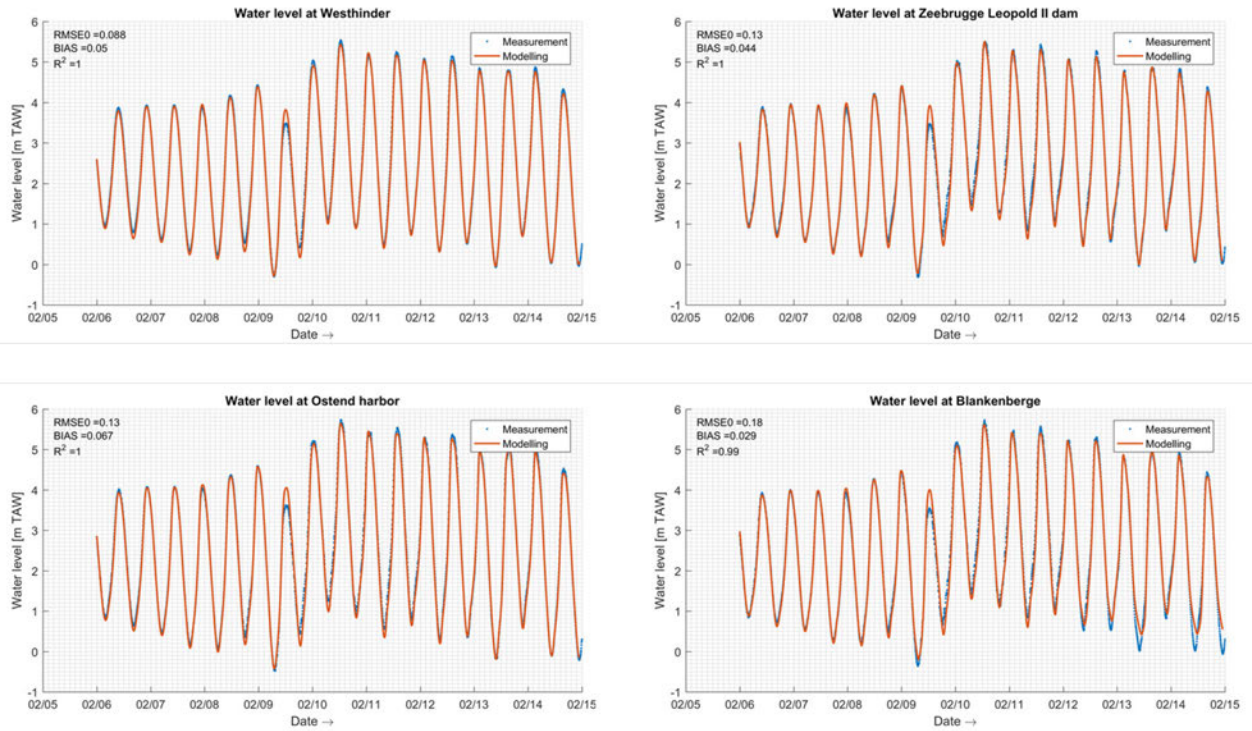
Figure 150 – Comparison of water level between the observed data and modelled results at measurement stations.
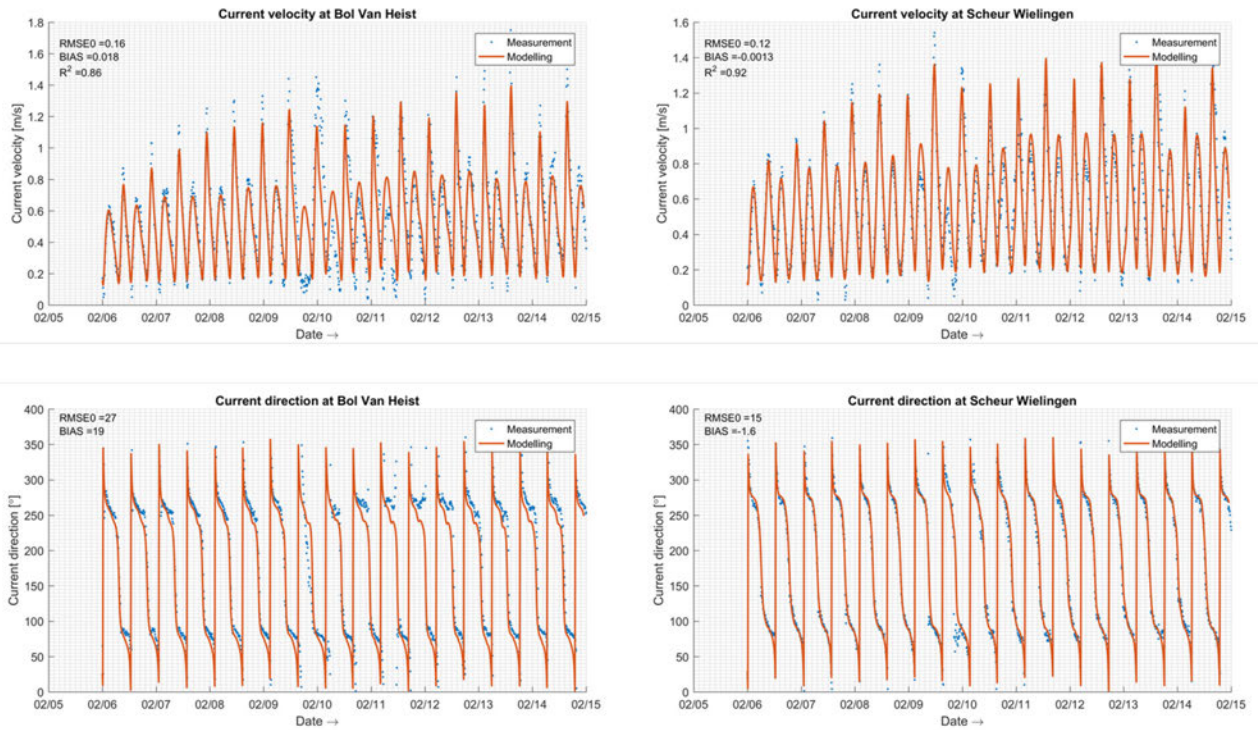
Figure 151 – Comparison of current velocity and direction between the observed data
and modelled results at measurement stations.

In addition to the validation of the hydrodynamic model, the wave model was validated based on comparison of significant wave height between measurement and model at 3 stations A2, Oostende and Zwin (Figure 152). The wave boundary and wind input of the wave model are both from the data collected at the station Westhinder. The comparison at the other 3 stations shows a reasonably good agreement between the measurement and model (Figure 153). The model appears to slightly overestimate the significant wave height. The overestimation could be attributed to the space-uniform wind field which is determined by the wind data collected at the offshore station Westhinder.

Bathymetric surveys for the port of Blankenberge were carried out on 6 and 14 February 2020 respectively, which are before and after the storm. The bed evolution during the storm could be calculated from the two bathymetric surveys (Figure 154).

The similar spit-shaped sedimentation has been also reproduced by the morphology model for the storm (Figure 155). Because the simulation period for the storm is normally not very long, the morphology model could be also applied without TOM2TEL (identical meshes for both TELEMAC and TOWAMAC models), or with refined grids around the area of interest. It could be observed that the simulations with and without TOM2TEL gave quite similar results (Figure 155 and Figure 156). Another simulation has been performed with refined grids (G01 mesh) around the channel of the port, and the modelled spit-shaped sedimentation appears to be even closer to the observed one (Figure 157). A further quantitative comparison is performed in Table 31. Both the observed net and gross sedimentation volumes are underestimated by all the three simulations. The D4 mesh without TOM2TEL gives 41 800 m^3 and 41 200 m^3 for the total gross and net sedimentation volumes respectively, which are the closest to the measured ones 47 700 m^3 43 600 m^3, although the modelled and measured sedimentations in the separate zones "Voorplein" and "Geul" are apparently different. This considerable difference might be associated with the bathymetric data applied to the model, because outside the black dash polygons the bathymetric data is from the survey undertaken in early 2019, almost one year before the storm.

It could be concluded that the morphology model is able to correctly simulate both the annual and storm-induced sedimentation volumes although the sedimentation pattern in not totally in agreement with the measured pattern.

Figure 152 – Locations of the wave measurement stations.
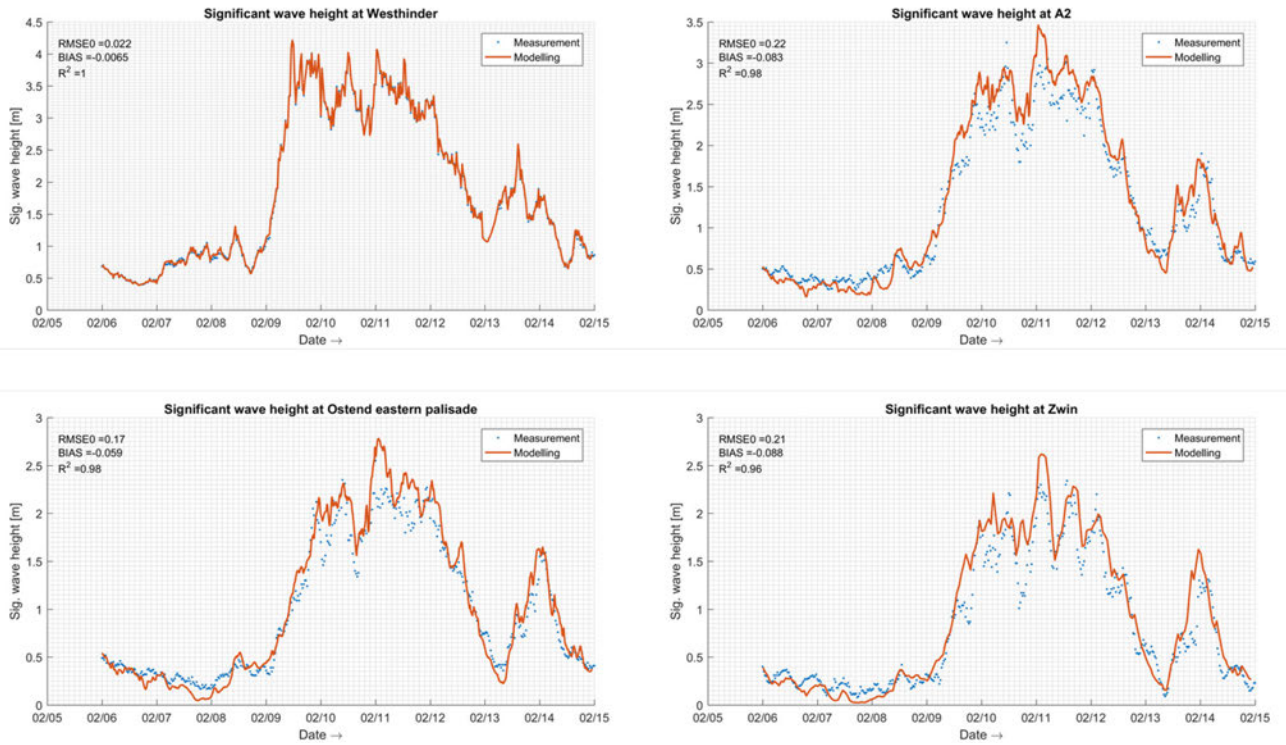
Figure 153 – Comparison of significant wave height between the observed data and modelled results at measurement stations.
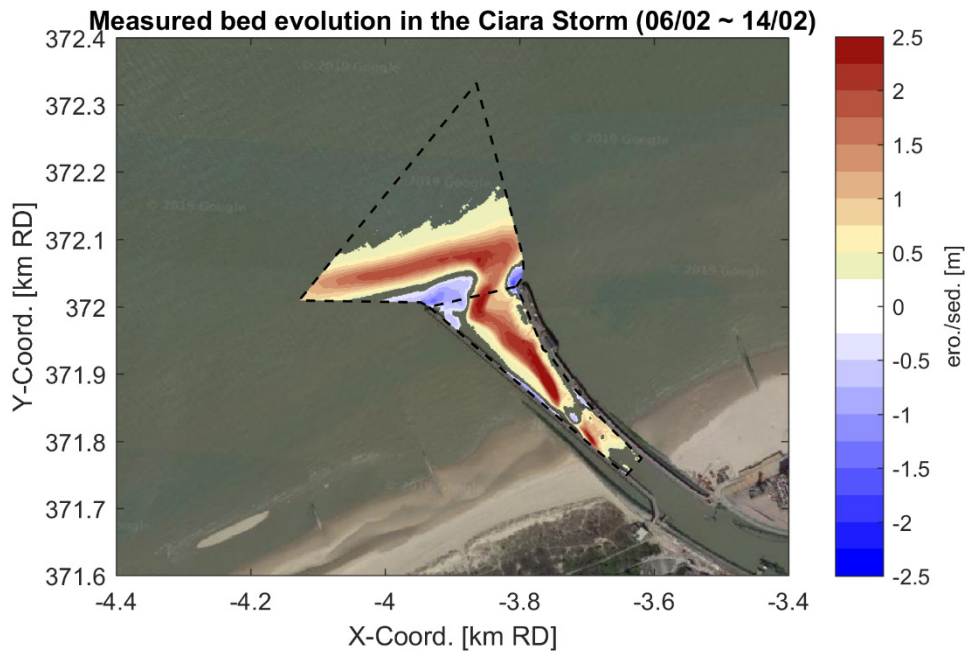
Figure 154 – Observed sedimentation in the entrance channel for the port of Blankenberge during the Ciara Storm.
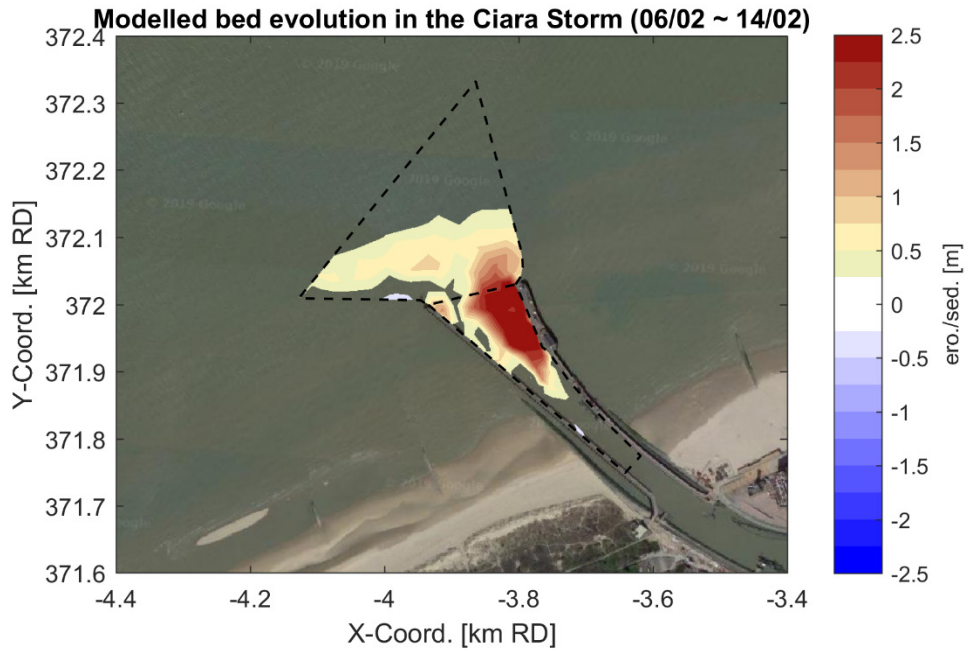
Figure 155 – Modelled sedimentation (with TOM2TEL, D4 mesh, Bijker, HSW101_06a) in the entrance channel for the port of Blankenberge during the Ciara Storm.
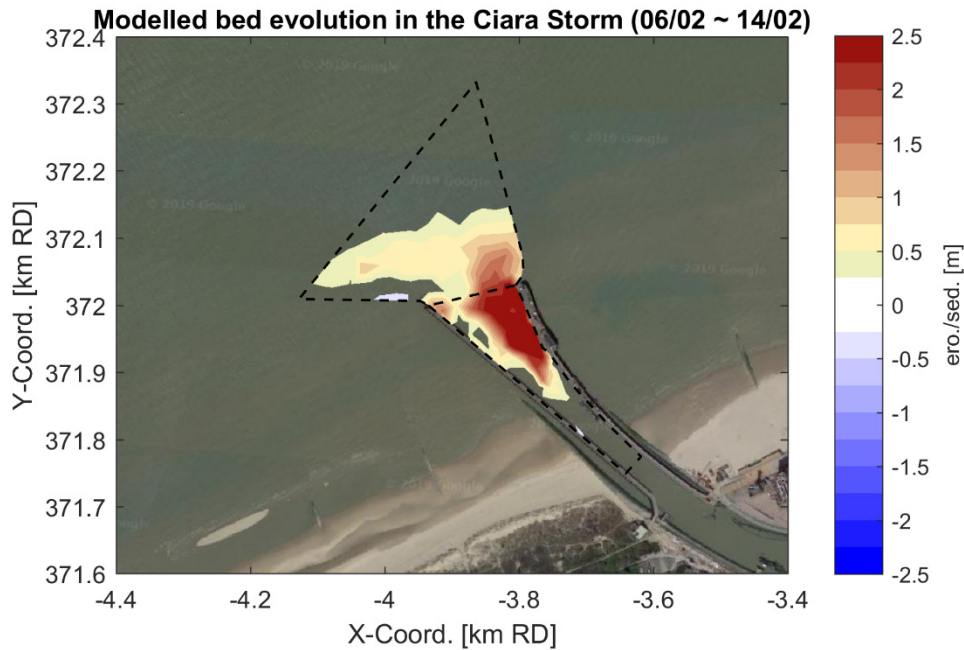
Figure 156 – Modelled sedimentation (without TOM2TEL, D4 mesh, Bijker, HSW101_06b) in the entrance channel for the port of Blankenberge during the Ciara Storm.
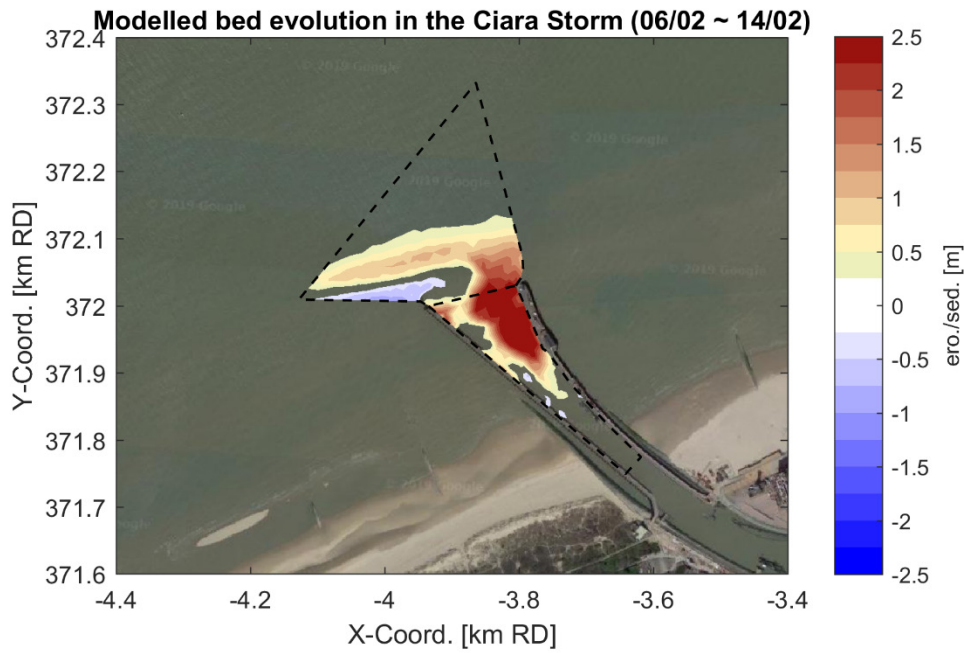
Figure 157 – Modelled sedimentation (without TOM2TEL, G01 mesh, Bijker, HSW101_07a) in the entrance channel for the port of Blankenberge during the Ciara Storm.

Table 31 – Sedimentation volumes in the port of Blankenberge during the Ciara storm.

	Voorplein (m³)		Geul (m³)		Total (m³)	
	Net	Gross	Net	Gross	Net	Gross
Observed	27 100	29 800	16 500	17 900	43 600	47 700
Modelled with TOM2TEL, D4 Mesh	18 500	18 800	20 800	21 000	39 300	39 800
Modelled without TOM2TEL, D4 Mesh	19 600	20 000	21 600	21 800	41 200	41 800
Modelled without TOM2TEL, G01 Mesh	17 300	19 400	21 000	21 400	38 300	40 800

5.3.3   Conclusions

The three testcases show that the model is capable of representing alongshore driven morphological evolution of the beach and foreshore. Both on the long term, e.g. beach erosion Wenduine and annual siltation of the Bankenberge entrance channel, as on the short term: sudden siltation of the channel during a storm event. Notice that for this validation cases the original grid of the model is used. Although the high resolution in the nearshore area, still in the zones of interest the grid is still relatievely coarse, e.g. the channel is limited to four cells. For specific studies, one could consider refining the grid even more in the zone of interest. This might improve the results even more.

5.4   Parallel efficiency testing

The scalability of the utilized software package (coupled flow, wave, morphology modules), i.e. its ability to present substantially decreasing computational times with increasing number of utilized number of CPUs (cores), is investigated in this section. The testing included a set of 10 identical morphodynamic simulations of short duration, which were performed on the BrEniac cluster of KU Leuven University by use of different number of CPUs. Specifically, the skylake nodes (Xeon Gold 6132@2.6 GHz, 28 cores each) were employed for the testing. Note that the TEL2TOM functionality was activated in this series of runs. The parallelization efficiency of the code was performed by use of the two following metrics:

- Speedup index (S_p), which is defined as the ratio between the computational time (wall-clock time) of the baseline run and the computational time of a parallel run with larger number of cores.
- Efficiency (α_p), which is defined as the ratio between the Speedup and the normalized number of the cores (S_p/n_{cpu}) [normalized number of cores, $n_{cpu} = n_{irun}/n_{baseline}$]

The calculation of the aforementioned metrics is clarified in the following Table:

Table 32 – Basic parameters in parallel efficiency evaluation.

Number of nodes	Total number of cores	Wall clock time (s)	Speedup (w.r.t. baseline)	Efficiency
$A_{baseline}$	$B_{baseline}$	$C_{baseline}$	1	1
A1	B1	C1	$C_{baseline}/C1$	$(B_{baseline}*C_{baseline})/(B1*C1)$
A2	B2	C2	$C_{baseline}/C2$	$(B_{baseline}*C_{baseline})/(B2*C2)$
Baseline = minimal configuration with which the computational task can be carried out. *Wall clock time = difference between start/end of the computational task, including any I/O operations*				

The results of the scalability testing are summarized in Table 33. The efficiency of the code versus the number of cores, is given in Figure 158.

Table 33 – Speedup & Efficiency of the Scaldis-Coast model on the BrEniac cluster of KU Leuven University. Test no. 6 (in bold) corresponds to the optimal simulation.

# test	Number of nodes	Total number of cores	Wall clock time (s)	Speedup (w.r.t. baseline)	Efficiency
1	1	7	35895	1.00	1.00
2	1	14	20425	1.76	0.88
3	1	28	9177	3.91	0.98
4	2	56	4627	7.76	0.97
5	3	84	3448	10.41	0.87
6	**4**	**112**	**2902**	**12.37**	**0.77**
7	5	140	2941	12.21	0.61
8	6	168	2375	15.11	0.63
9	7	196	2191	16.38	0.59
10	8	224	2065	17.38	0.54
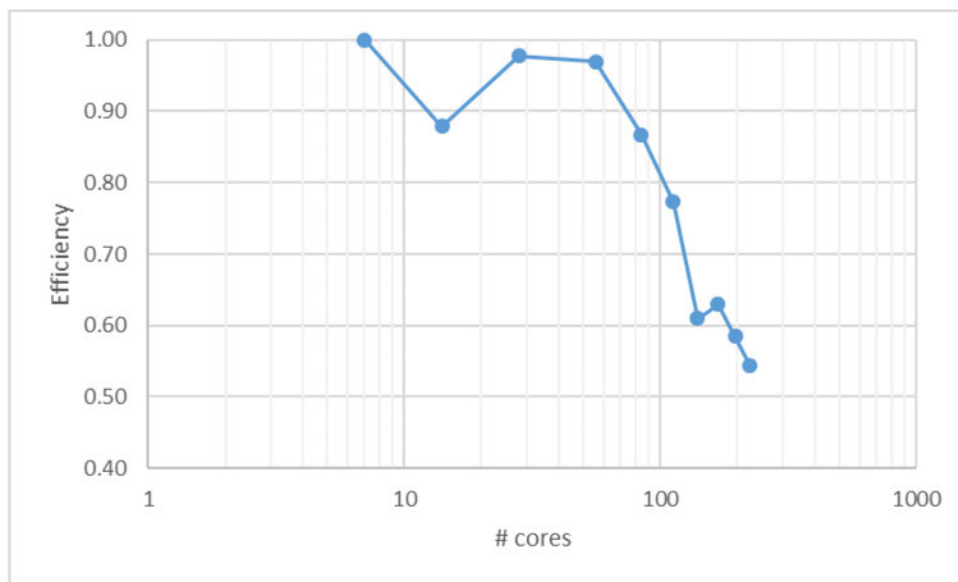
Figure 158 – Efficiency (α_p) of the code versus the number of cores utilized for the parallel test runs.

Analyzing the results it is observed that the Efficiency of the code decreases substantially when the number of cores becomes larger than 112 cores. Since it is generally suggested (by HPC experts) that the efficiency should remain over 70%, the optimal number of cores when Scaldis-Coast simulations are performed on the BrEniac cluster is 112. Simulations with larger number of cores are not always discouraged, especially when there is restriction on the desired wall-clock time of a simulation.

6   Scenario: Sea level rise

6.1   Introduction

The sea level rise effect on the sediment transport at the Belgian coast and at the mouth of Western Scheldt, is investigated in this chapter. Numerical simulations -hydrodynamic and sediment transport- are performed by means of the Scaldis-Coast model, considering the scenario of future sea level rise SLR=300 cm along with the Reference scenario (current situation). The specific SLR scenario has been proposed in the framework of the Complex Project Coastal Vision (*Complex Project Kustvisie,* CPK) as the worst-case scenario for sea level rise by the year 2100, considering as reference the year 2014. The boundary conditions for Scaldis-Coast are derived from a CSM-ZUNO model run with the increased water level superimposed on the CSM continental shelf boundaries.

In the following section the basic elements of the model set-up are given. Then the results of the tidal and harmonic analysis for the expected variation in the amplitude and the tidal phase, the harmonic constituents and the sediment transport results focusing at the coastal area and the Western Scheldt mouth, are presented.

Important to notice here is that for the 2100 run the current bathymetry of the coast and Western Scheldt is maintained. It is a source of uncertainty that is unknow how the bed will evolve the next decades under the pressure of climate change, sea level rise and anthropogenic interferences. The validity of the model results with respect to the sediment transport rates and tidal harmonics in the estuary depends on capability of the estuary to grow with sea level rise.

6.2   Model set-up

6.2.1   Investigated scenarios

In the following table, the investigated scenarios and their identifiers are presented.

Table 34 – Description of investigated scenarios.

Scenario	ID	Run ID	Sea level rise [cm]
Reference	T0	SLR000	0
Moderate	SLR300	SLR001	300

6.2.2   Basic settings

The SLR impact on the tidal characteristics and the hydrodynamics is investigated by executing simulations with TELEMAC-2D model. The settings of the hydrodynamic model are identical to those presented in Section 3.2.1 of the present report (see Table 18 on page 63), with the exception that the wind forcing is not considered now. The effect of waves are not taken into account.

For the SLR impact on the sediment transport, coupled simulations of TELEMAC-2D with SISYPHE are performed. The coupling of the two modules takes place at every time-step of the computation (COUPLING PERIOD FOR SISYPHE=1), or in other words, the hydrodynamic and the morphodynamic time-steps are identical. The sediment transport formula utilized in this exercise is the one proposed by Soulsby and Van Rijn (SvR).

6.2.3   Simulation period

The standalone hydrodynamic model computes water levels and flow velocities for the period from 04/08/2014 to 24/08/2014. The basic tidal analysis is performed during the spring-neap period from 08/08/2014 to 24/08/2014.

For the coupled hydrodynamic-sediment transport simulations, the simulation period covers almost the whole year 2014 (from 06/01/2014 to 31/12/2014) in order to calculate the yearly mean sediment transport and to extract the representative tide for the SLR scenario.

6.2.4   Offshore boundary conditions

The hydrodynamic model is forced by time-series of the water level and velocities (of time-step equal to 10 minutes), which resulted after running the Continental Shelf Model (DCSMv5) and the nested ZUNOv3 (ZUidelijke NOordzee - Southern North Sea) model for the period from 01/01/2014 to 31/12/2014, considering absence of wind (harmonic run), for the current situation as well as the considered SLR scenario.

A correction of the harmonic components is calculated based on the comparison of the M2, M4, S2 phases of the ZUNO (reference) results and measurements for the year 2014 at the station Vlakte van de Raan (see Table 19). After decomposition and correction, the water level signal is re-synthesized in order an unbiased time series to be applied at the boundary of Scaldis-Coast model. Note that for the year 2014 there was a small correction of the zero harmonic (Z0) component equal to -1.9 cm.

Table 35 – Correction of harmonic components of water level variation for the year 2014 applied to the Reference & the SLR runs.

Harmonic component	Correction
Phase M2	+5°
Phase M4	-6°
Phase S2	+8°

6.2.5   Computational time

A typical standalone hydrodynamic simulation of one spring-neap tidal cycle takes around 1.5 hours on 32 CPUs. A typical coupled simulation (TELEMAC-2D / SISYPHE) of one year takes around 36 hours on 32 CPUs. Taking into account the above computational times (and also the fact that there occur 2 spring-neap cycles per month) it can be said that the cost of SISYPHE is rather small, almost negligible.

6.3   Tidal analysis

The basic tidal analysis is performed for the period from 08/08/2014 to 24/08/2014, which includes both neap and spring tidal cycles, in order to investigate the influence of the sea level rise on the basic tidal characteristics. The results of the analysis refer to selected locations at the coast and the Scheldt estuary, where continuous measurements are also conducted (see Figure 159). Note that a detailed analysis of the SLR impact on the tidal characteristics is beyond the scope of the present study. A detailed investigation of the effect of different SLR scenarios on the tidal characteristics of the southern North Sea and the Scheldt estuary can be found in Chu *et al.* (2020).
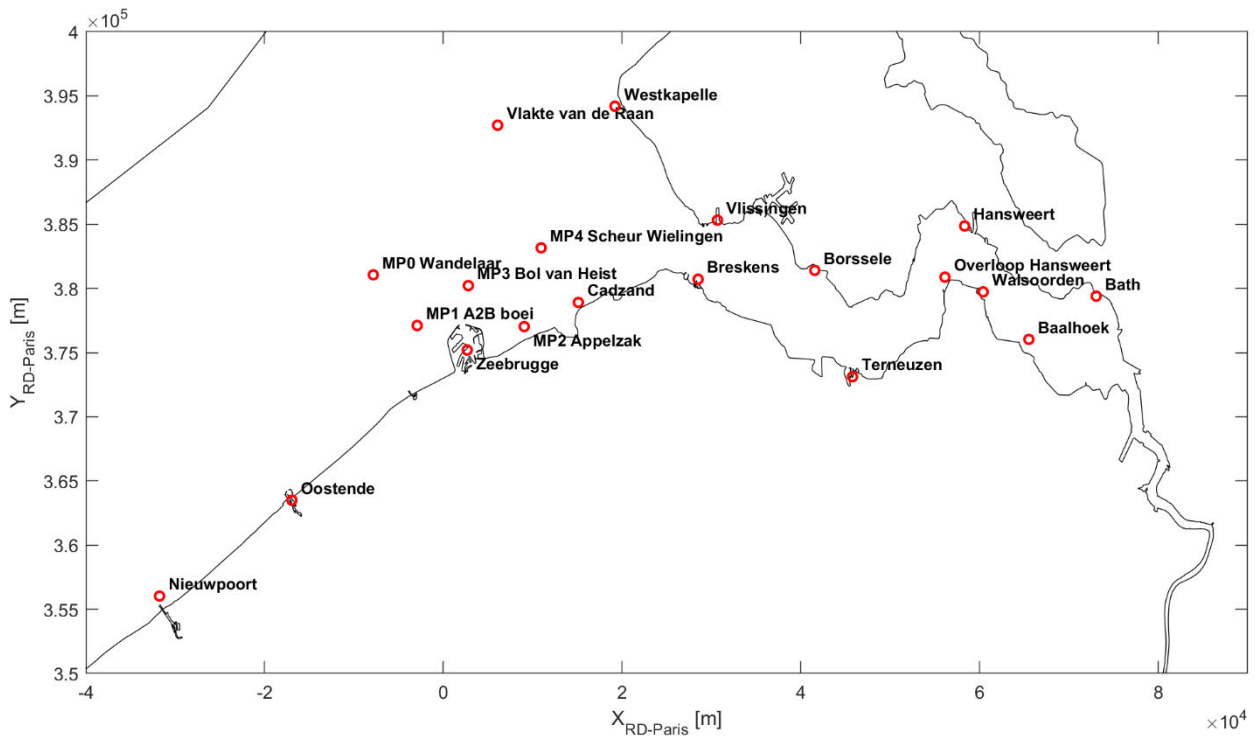
Figure 159 – Locations of the water level measurement stations used in the tidal analysis.

6.3.1   Basic tidal analysis

The bias in the complete water level time-series between the SLR300 scenario and the Reference scenario, presented in Figure 160, indicates the successful response of the model to the imposition of the offshore boundary conditions for each of the sea level rise scenarios. In other words the difference between the mean sea level of the sea level rise scenarios and the Reference scenario almost coincides with the imposed sea level rise at all locations.
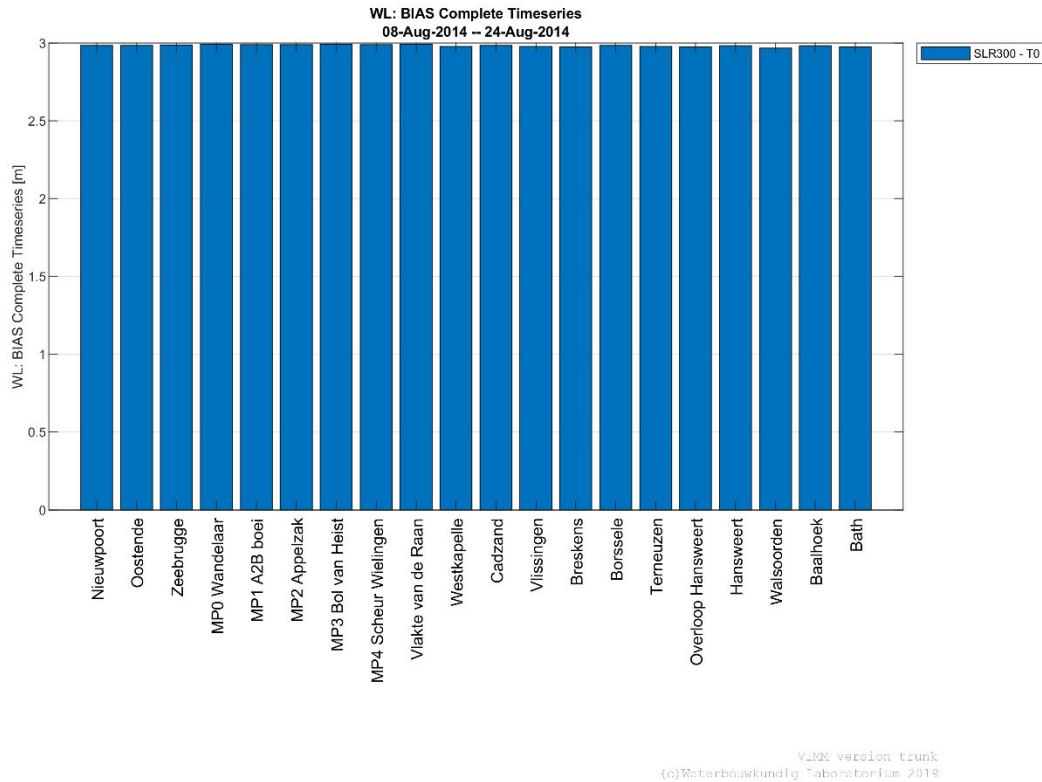
Figure 160 – Bias in the complete water level time-series between the SLR300 scenario and the Reference scenario.

In Figure 161 and Figure 162 the bias in the time of occurrence of high (HW) and low water (LW) levels between the SLR300 and the Reference scenario, are shown, respectively. The most obvious indication of the two figures is that the sea level rise leads to acceleration of the tidal wave, since both HW and LW levels present a backward shift in time for the considered scenario at each location, i.e. about 25 and 35 minutes at the coast and the Western Scheldt, respectively. This means that, a general trend of increasing time shift as the tidal wave approaches and enters the Western Scheldt is observed.

The acceleration of the tidal wave with SLR can be roughly explained by the wave theory for shallow waters, according to which the celerity of the tidal wave, defined as $C = (gh)^{1/2}$ -where g is the gravitational acceleration and h is the water depth- increases with increasing water depth.
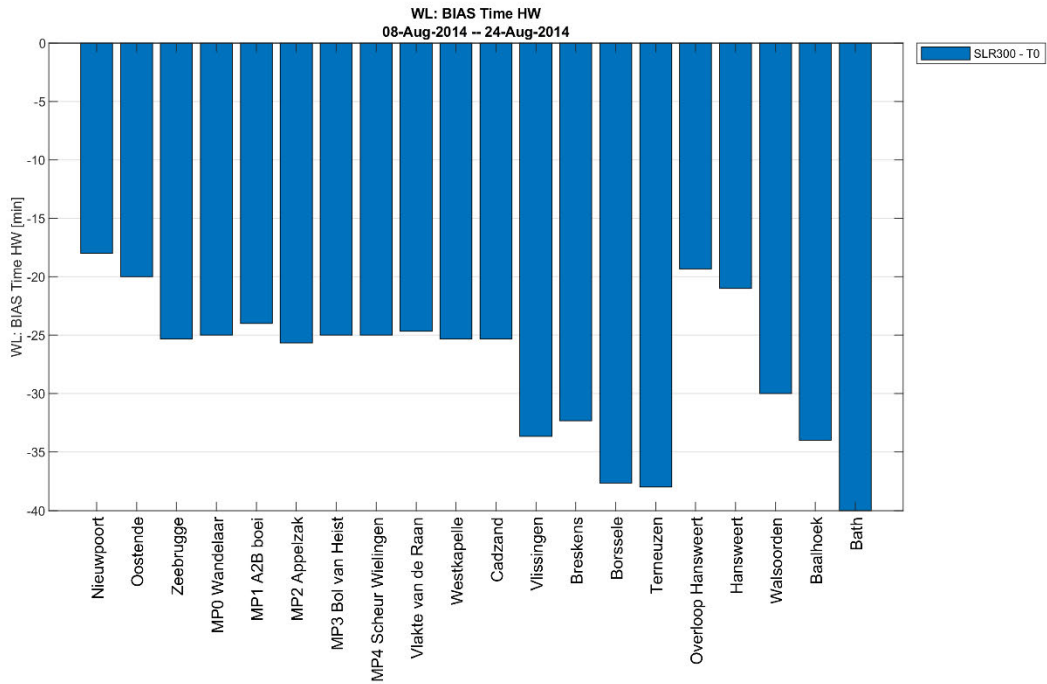
Figure 161 – Bias in the time of high water levels between the SLR300 scenario and the Reference scenario.
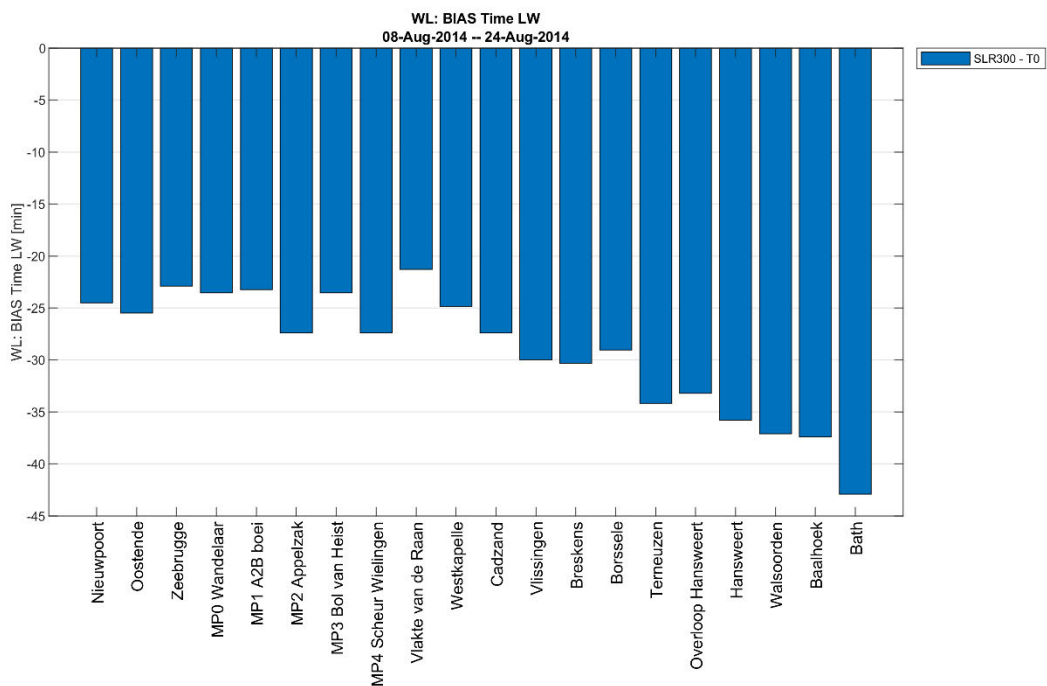
Figure 162 – Bias in the time of low water levels between the SLR300 scenario and the Reference scenario.

The bias in the HW and LW levels between the SLR300 scenario and the Reference scenario at the selected observation points, are shown, respectively, in Figure 163 and Figure 164. It is found that for all the scenarios, the biases in HW levels at the coastal stations are about 11 cm higher than the mean sea level (MSL) increase.

The latter can be considered equal to the bias in the complete water level time series (see Figure 160). On the other hand, biases in LW levels at the coast are about 14 cm lower than the MSL increase. This is an indication that the sea level rise leads to increase of the tidal range (≈25 cm averaged at the coast). At the observation points in the Western Scheldt exhibit in general a bit higher HW levels (+15 cm) and a bit lower LW levels (-16 cm) compared to the coastal observation points. This means that the averaged tidal range increase is Western Scheldt is about 30 cm.
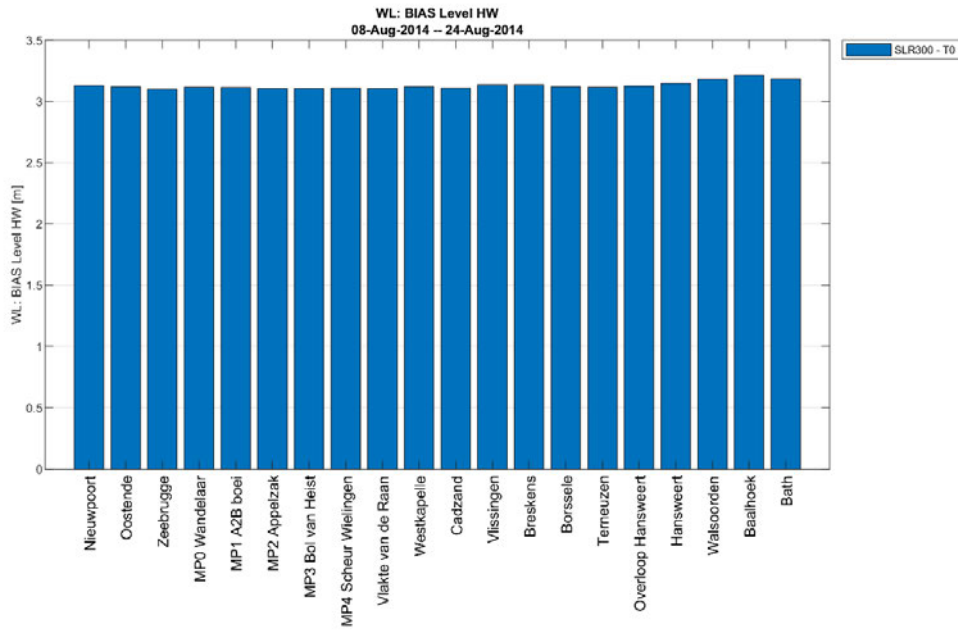
Figure 163 – Bias in the high water levels between the SLR300 scenario and the Reference scenario.
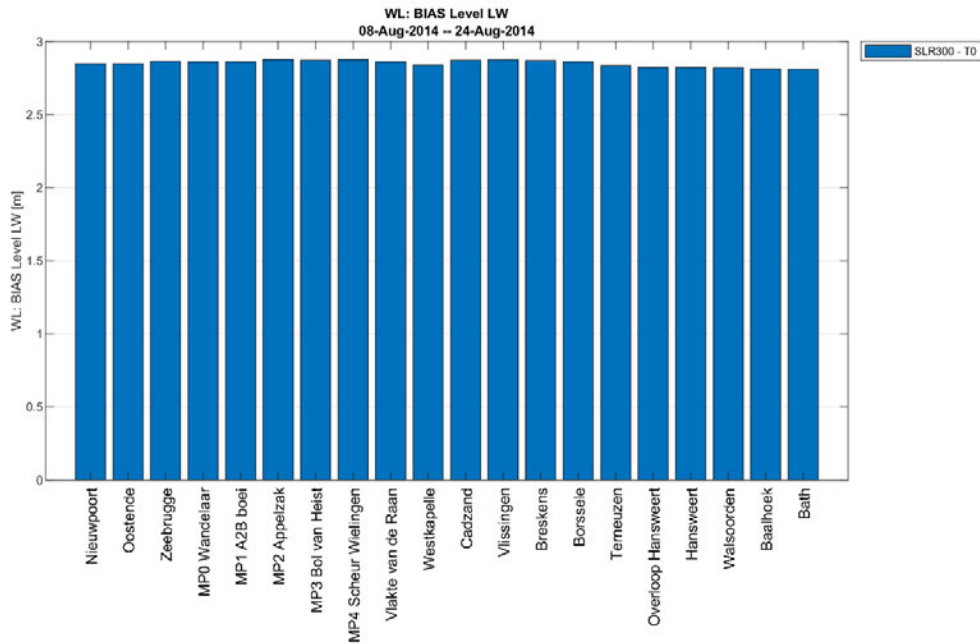
Figure 164 – Bias in the low water levels between the SLR300 scenario and the Reference scenario.

6.3.2 Basic harmonic analysis

The amplitude of the most important harmonic constituents of the tide, i.e. the M2, S2, M4 constituents, at the considered locations for the SLR300 and the Reference scenarios are shown respectively in Figure 165, Figure 166 and Figure 167. As expected, the M2 and S2 amplitudes increase with increasing sea level about 12 cm and 4 cm at the coastal stations on average, respectively, and about 16 cm and 6 cm at the stations in the Western Scheldt, respectively. This means that the M2, S2 amplitude increase is slightly enhanced as the tidal wave reaches the mouth and the upstream locations of the Western Scheldt. On the contrary, M4 amplitude generally decreases (1-2 cm) with increasing sea level rise, except for the stations downstream of Western Scheldt (Vlissingen to Terneuzen) where the amplitude increases 1-2 cm. The increase of M2 and S2 constituents is physically explained by the attenuation of the bottom roughness due to the large increase of the water column (less energy losses). On the other hand, higher harmonics like M4 are partly generated by interaction with roughness, so reduced bottom roughness influence means less potential for generation of higher harmonics.
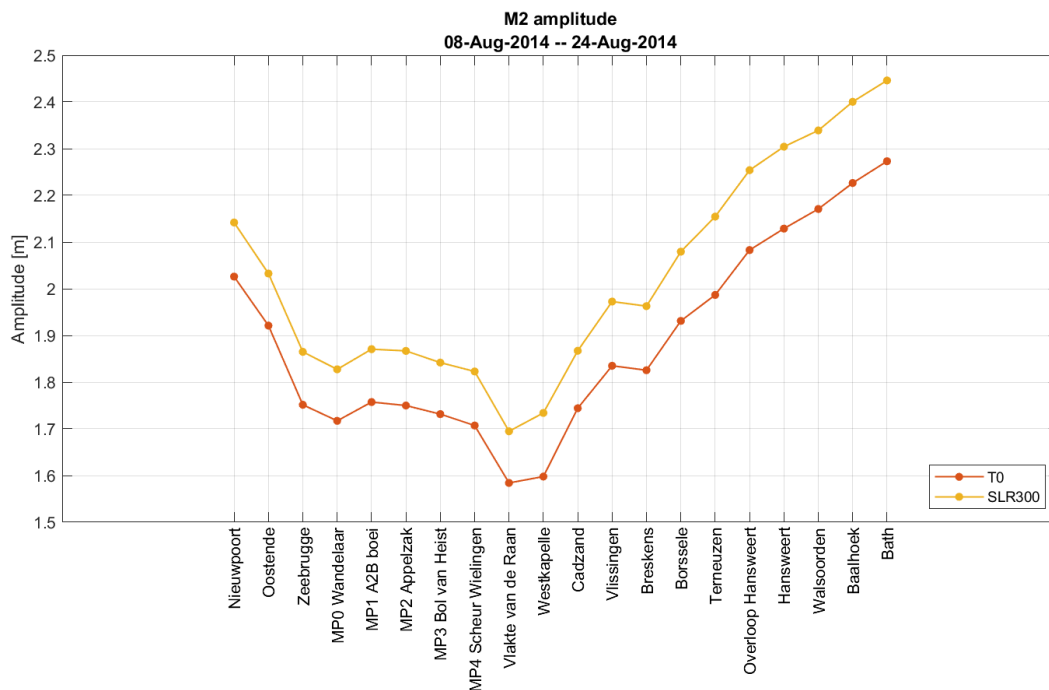
Figure 165 – Amplitude of the M2 tidal constituent at the considered locations for the SLR300 and the Reference scenarios.
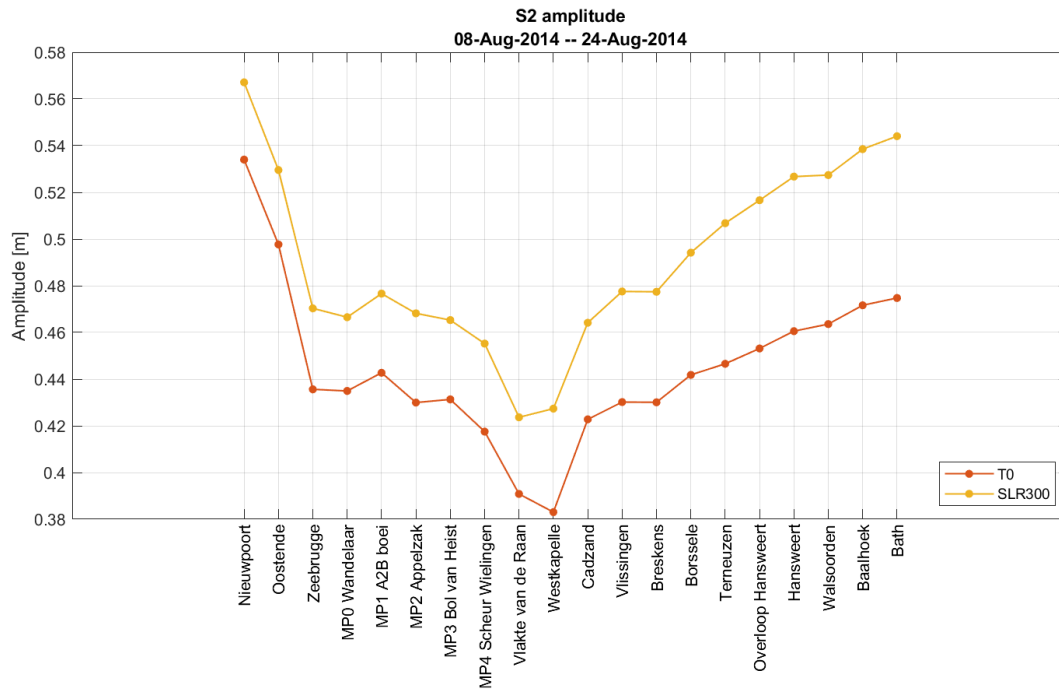
Figure 166 – Amplitude of the S2 tidal constituent at the considered locations for the SLR300 and the Reference scenarios.
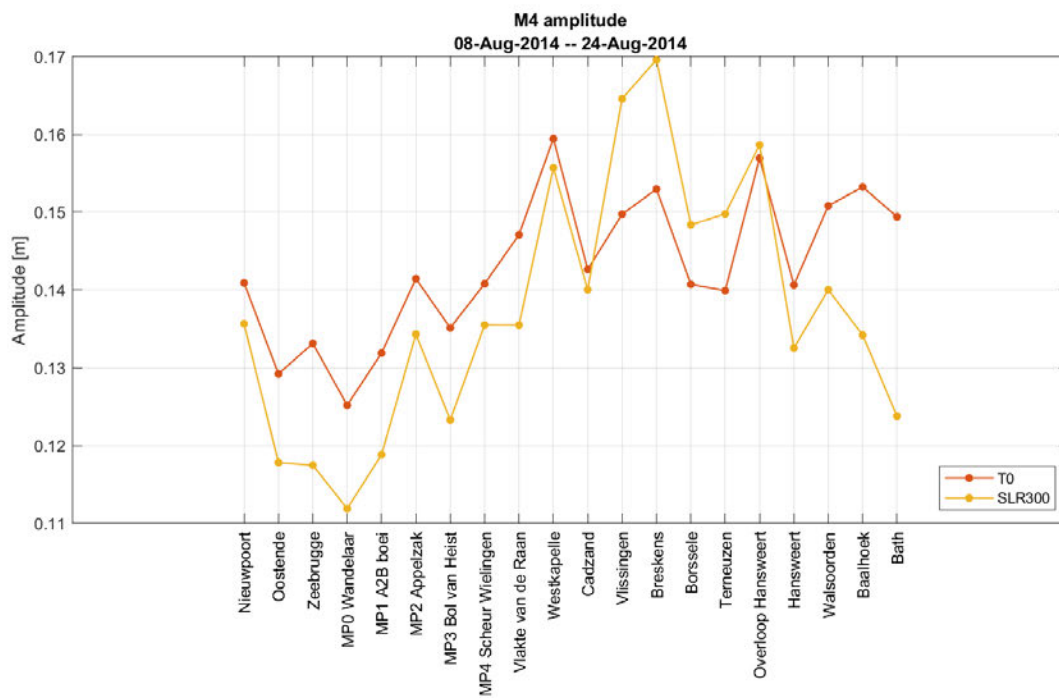
Figure 167 – Amplitude of the M4 tidal constituent at the considered locations for the SLR300 and the Reference scenarios.

The phase of the M2, S2, M4 constituents, at the considered locations for the investigated scenarios are shown respectively in Figure 168, Figure 169 and Figure 170. In general the phase of the considered constituents decreases with increasing sea level rise (tidal wave acceleration) or in other words the phase shift increases with increasing sea level rise. The phase shift for the considered constituents increases more as the tidal wave reaches the mouth and the upstream locations of the Western Scheldt, i.e. 5° difference on average between the coastal stations and those in the Western Scheldt. The physical explanation of this behavior is that higher water column means faster propagation of the tidal wave (C = $(gh)^{0.5}$), both for the rotating Kelvin wave in the Southern North Sea and for the progressive part of the tidal wave in the estuary.
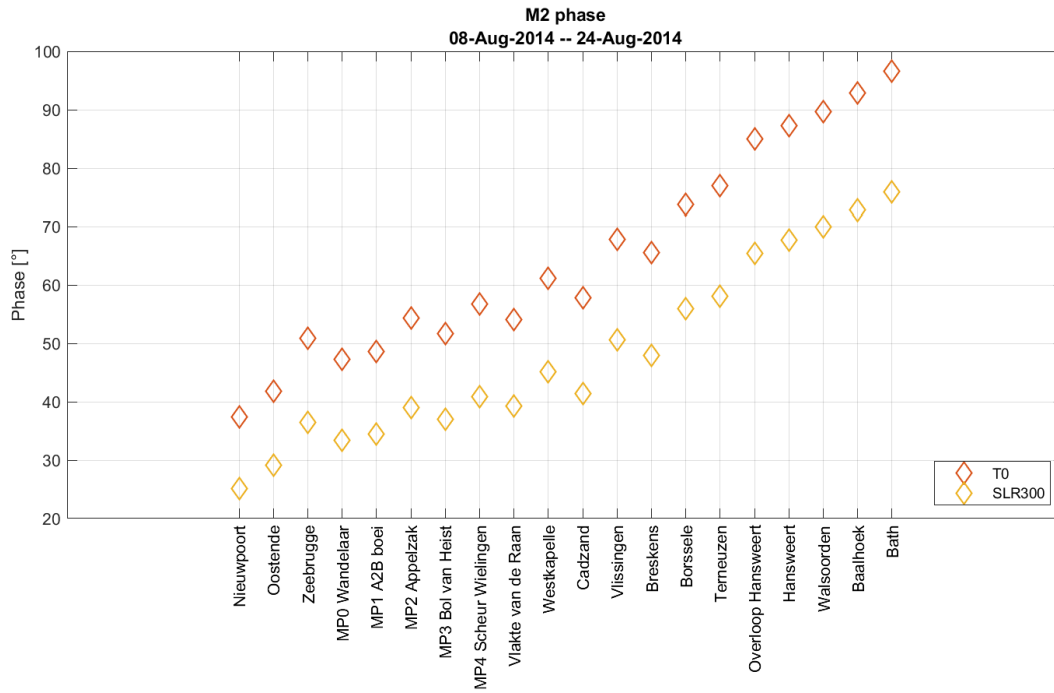
Figure 168 – Phase of the M2 tidal constituent at the considered locations for the SLR300 and the Reference scenarios.
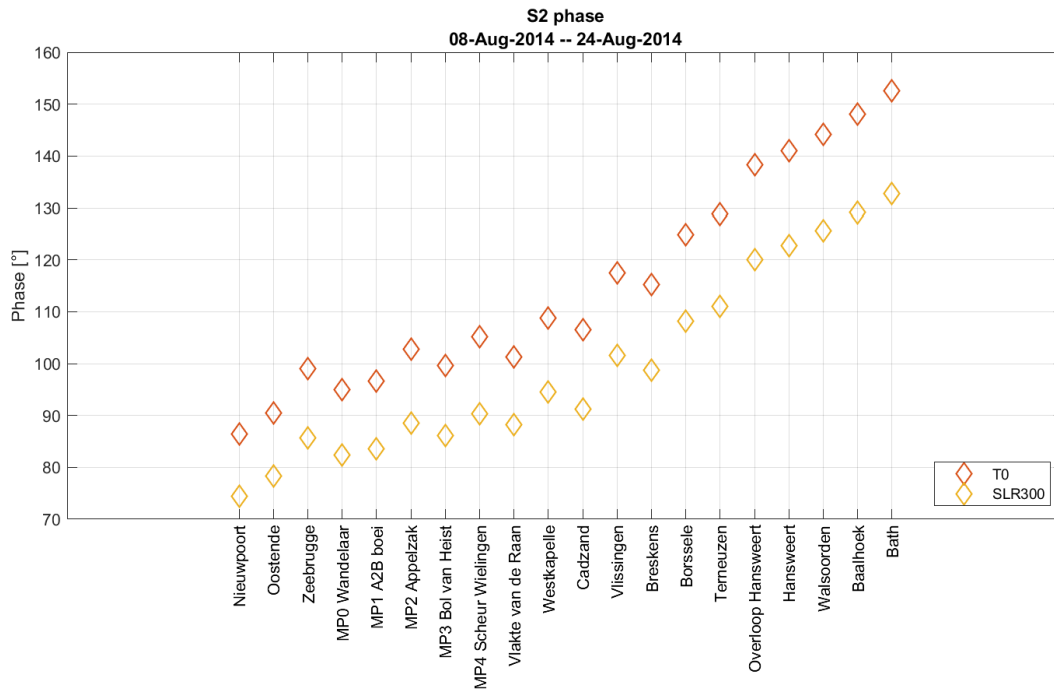
Figure 169 – Phase of the S2 tidal constituent at the considered locations for the SLR300 and the Reference scenarios.
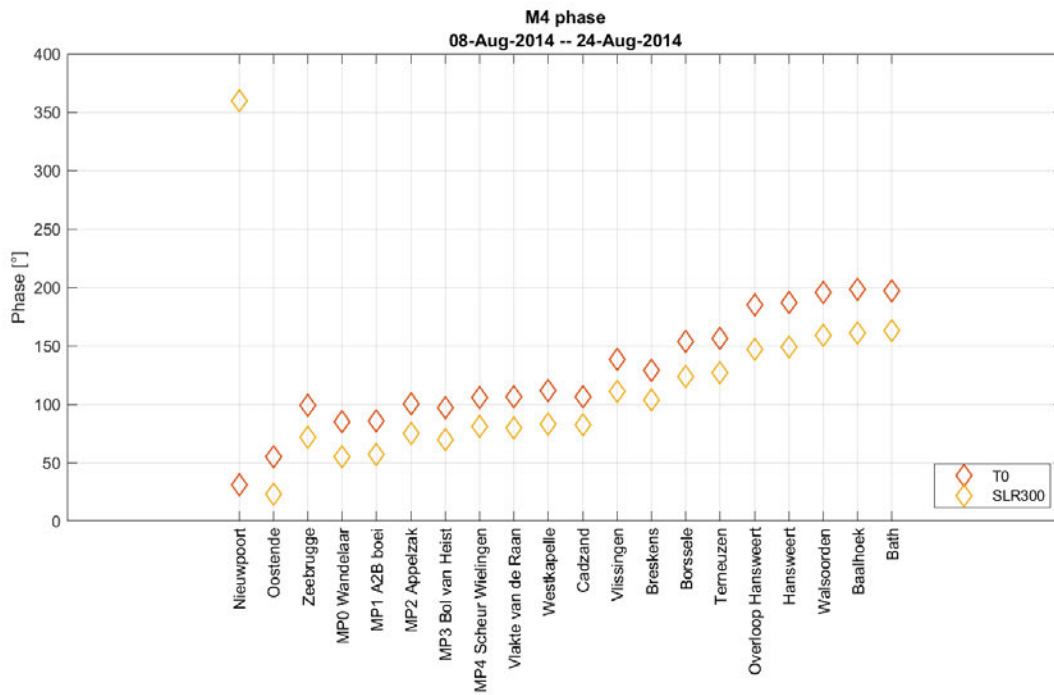
Figure 170 – Phase of the M4 tidal constituent at the considered locations for the SLR300 and the Reference scenarios.

6.4   Sea level rise impact on sediment transport

The mean (yearly-averaged) sediment transport rate (magnitude) for the Reference (slr000) and the sea level rise (slr001) scenarios, and the difference between the two of them (slr001-slr000), are shown in Figure 171 and Figure 172, respectively. In Figure 171, it is shown that for both scenarios the highest rates appear at the area between Zeebrugge harbor and Vlissingen. Specifically, rates around 5×10^{-5} m^2/s and 20×10^{-5} m^2/s are observed in front of Zeebrugge breakwaters and at Vlissingen, respectively, for the Reference scenario. For the SLR300 scenario the aforementioned rate for Zeebrugge is somewhat smaller, while the rates at Vlissingen reach values up to 35 m^2/s. High transport rates are also observed at the area of Blankenberge-Wenduine, at Ostend and at the region of the Flemish banks (around 10^{-5} m^2/s).

In general the most noticeable differences between the two maps of Figure 171 are observed at the area between the Zeebrugge harbor and at the mouth of Western Scheldt, i.e. where the highest rates appear. This is confirmed in Figure 172, where it is shown that the sea level rise leads to reduction of the transport rates in the area east of Zeebrugge (max reduction -2×10^{-5} m^2/s) and around the navigation channels of Scheur and Wielingen (-10^{-5} m^2/s), and to increase of maximum transport rates at the mouth of Western Scheldt and specifically at the area of Vlissingen (up to $+15 \times 10^{-5}$ m^2/s) and at Westkapelle (up to $+7 \times 10^{-5}$ m^2/s). A reduction of the magnitude of transport rate (up to -5×10^{-5} m^2/s) at the area of Vlissingen is also observed.
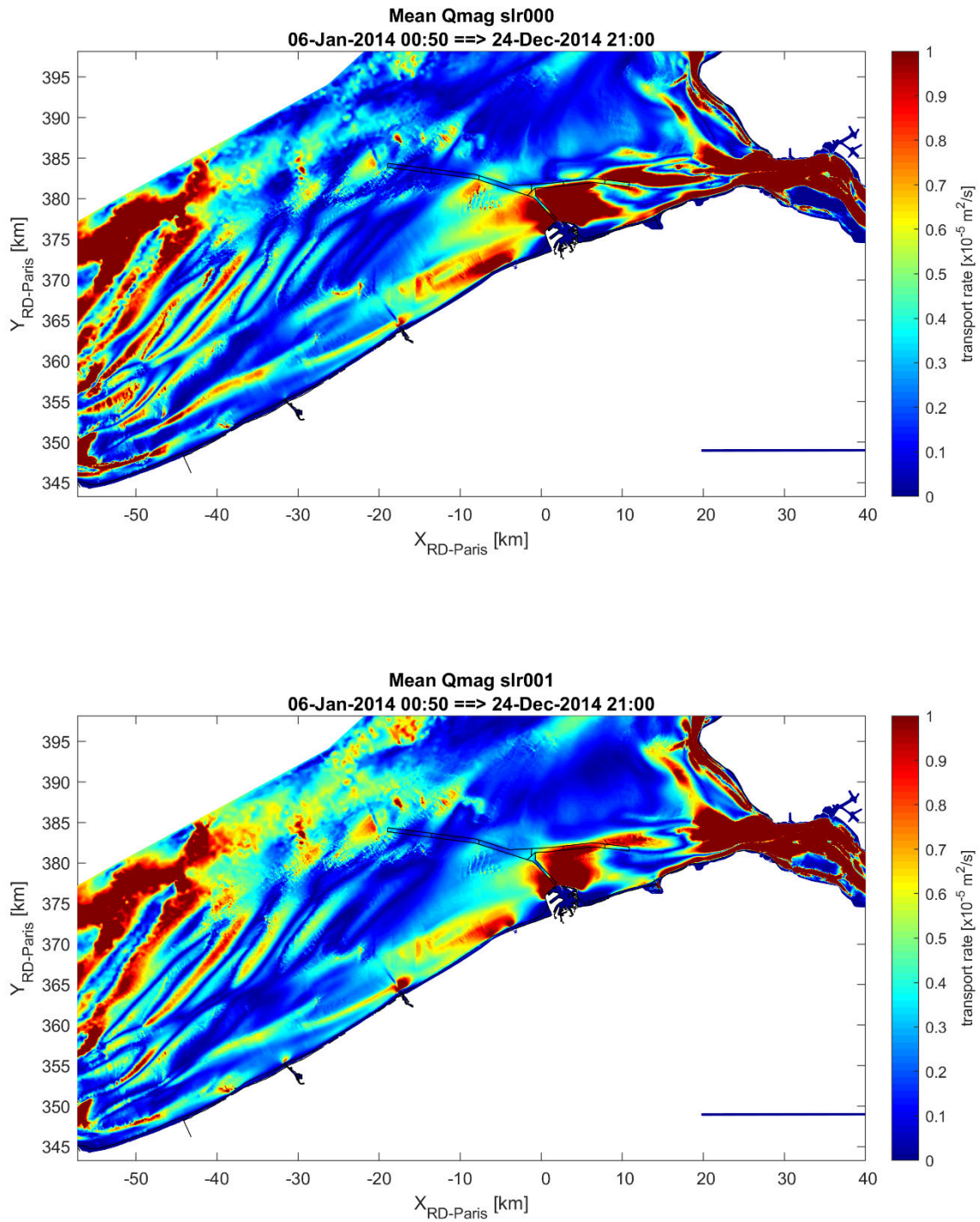
Figure 171 – Mean (yearly-averaged) sediment transport rate (magnitude, x10^{-5} m^2/s) for the Reference (slr000) and the SLR300 (slr001) scenarios.

Absolute difference in mean sediment transport slr001 - slr000
06-Jan-2014 00:50 ==> 25-Dec-2014 00:00
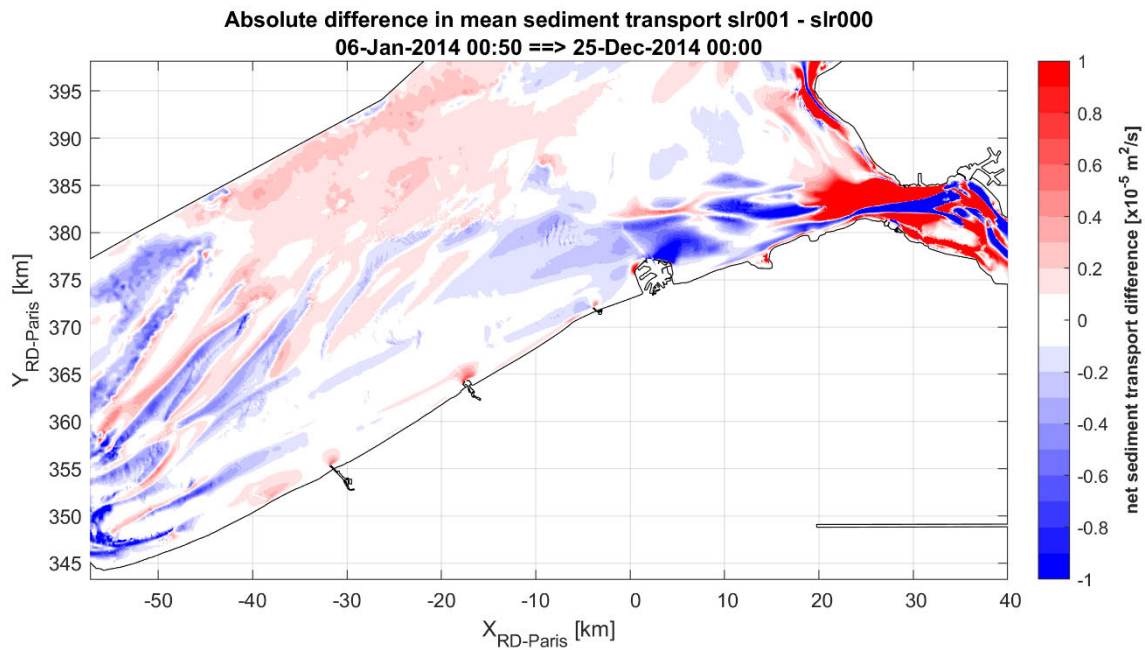
Figure 172 – Difference in mean (yearly-averaged) sediment transport rate (magnitude, x10^{-5} m^2/s) for the Reference (slr000) and scenarios between the SLR300 (slr001) and the Reference scenario.

The alternating patterns at the area of Vlissingen (shown in Figure 172) for the difference in transport rates are related to the direction of the sediment transport as shown in Figure 173, where, apart from the magnitude contours, the sediment transport direction through vectors at the area between Zeebrugge harbor and Vlissingen is provided . Comparing the two panels of Figure 173, it can be observed that the ebb-dominated sediment transport at Vlissingen (westward vectors) is substantially enhanced with sea level rise, while the flood-dominated one (eastward vectors) is less extended across the Western Scheldt mouth. It is also worth to mention that the sediment transport at the Bank of Zoutelande (close to Westkapelle) directed towards the mouth is substantially increased.

6.5   Conclusions

In this chapter the impact of seal level rise (SLR) on the sediment transport at the Belgian coast and at the mouth of Western Scheldt, was investigated. Numerical simulations -hydrodynamic and sediment transport- were performed with the Scaldis-Coast model, considering an extreme scenario of future sea level rise SLR=300 cm along with the Reference scenario (current situation

The model runs show that the increased sea level rise causes increase of the tidal range at the investigated area of the Belgian and Dutch coast (~8% of the SLR) and in the Western Scheldt (~10% of the SLR). Changes in the tidal amplitude are accompanied by changes in the tidal phase, i.e. the tidal wave is accelerated about 25 min at the coast on 35 min in the Western Scheldt.

As for the effect of SLR on the sediment transport rates, the most noticeable differences compared to the Reference scenario were observed at the area between the Zeebrugge harbor and at the mouth of Western Scheldt, i.e. where the highest rates appear. The sea level rise leads to reduction of the transport rates in the area east of Zeebrugge and around the navigation channels of Scheur and Wielingen, and to increase of the maximum transport rates at the mouth of Western Scheldt and specifically at the area of Vlissingen.
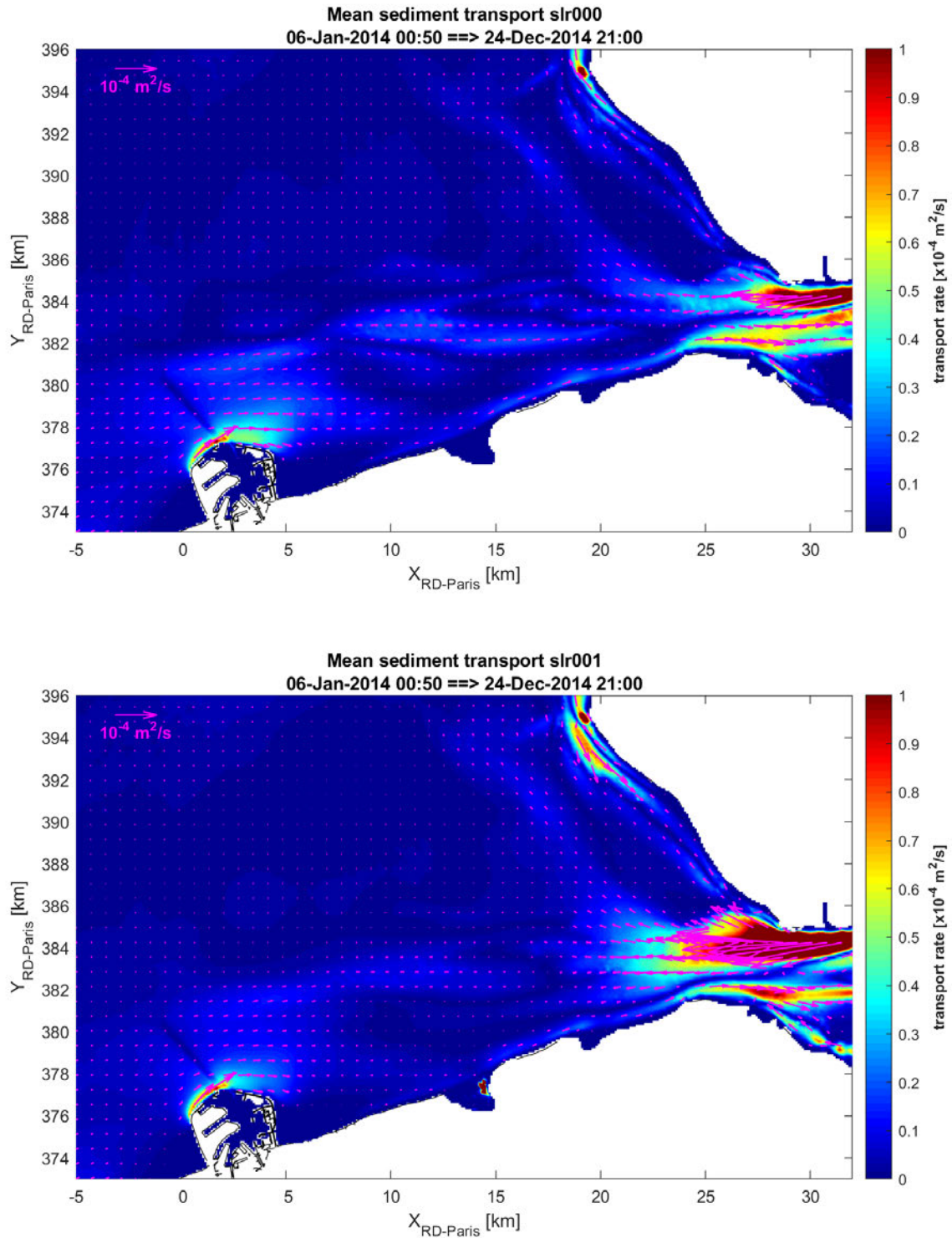
Figure 173 – Mean (yearly-averaged) sediment transport rate (magnitude, x10^{-4} m^2/s) contours and vector field for the Reference (slr000) and the SLR300 (slr001) scenarios at the area between Zeebrugge and Vlissingen.

7 New developments

7.1 Cross-shore processes

Cross-shore processes are playing an important role in the beach erosion under storm conditions, both also on the long term in the natural cross-shore natural feeding of the beach under calm conditions. These processes are in general difficult to model in large scale coastal models. Different physical processes contribute to the onshore and offshore transport of sediment. These processes are not yet implemented in the TELEMAC-MASCARET software suite. In this section new features with respect to some of the principal cross-shore transport processes are proposed. They are implemented in GAIA, however so far, they are not yet fully validated for the Belgian coast. These are preliminary results.

7.1.1 General features

The GAIA modification for taking into account the cross-shore sediment transport processes include modification of the depth averaged flow velocities that will be used for computation of suspended sediment transport using the advection-diffusion equation:

$$\frac{\partial hC}{\partial t} + \frac{\partial hU^E C}{\partial x} + \frac{\partial hV^E C}{\partial y} = \frac{\partial}{\partial x}\left(h\varepsilon_s \frac{\partial C}{\partial x}\right) + \frac{\partial}{\partial y}\left(h\varepsilon_s \frac{\partial C}{\partial y}\right) + E - D$$

where C is the depth-averaged concentration, h is the water depth, ε_s is the eddy viscosity, and E and D are the non-cohesive erosion and deposition, respectively.

The additional velocity components accounting for cross-shore transport are based on formulations as implemented in XBeach [9] and they are explained in detail in the following sections. This is achieved within the newly added subroutine GAIA_CROSS_SHORE.

In our approach, the generalized Lagrangian mean velocities U^L, V^L are given as:

$$U^L = U^E + U^s \ , \qquad V^L = V^E + V^s$$

where U^E, V^E are the Eulerian velocities and U^s, V^s are the velocities due to Stokes drift. The sediment transport needs to be calculated using the Eulerian velocity in the advection-diffusion equation. However, the velocities calculated by TELEMAC2D are the Lagrangian velocities U^L, V^L. Therefore, one can take the effect of Stokes drift and the return current generated by the Stokes drift into account using:

$$U^E = U^L - U^s \ , \qquad V^E = V^L - V^s$$

In case we have waves moving towards the coast in a stationary situation, we have U^L=0 (no net flow of water towards the coast, and therefore U^E=-U^s, showing that the return current (U^E) is opposite to the Stokes drift (Groeneweg, 1999).

The depth averaged flow velocities used for accounting for cross-shore sediment transport have the form of:

$$U^{tot} = U^L + sin\theta(U_{NL} - U_{ST}) \ , \qquad V^{tot} = V^L + cos\theta(U_{NL} - U_{ST})$$

The terms in these equations due to Stokes drift (U_{ST}, and wave non-linearity U_{NL}) are explained in the next sections. ϑ is the wave direction.

7.1.2 Stokes drift and Return flow

The Stokes drift occurs in the nearshore in the upper part of the water column (see Figure 174), because the motion of water particles do not demonstrate a perfectly circular track. as the horizontal orbital velocity increases with the distance from seabed (van Rijn & Walstra, 2003), leading to lower seaward velocities under the wave trough than the shoreward velocities under the wave crest.
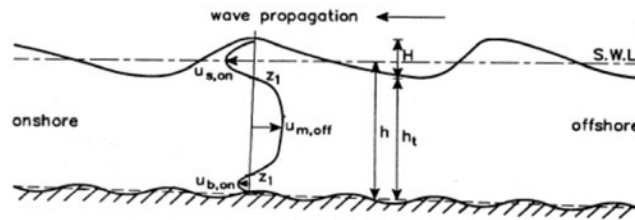
Figure 174 – Time averaged velocity profile (Longuet-Higgins, 1953) showing from top to bottom: Stokes drift, return flow and streaming.

This velocity difference has a magnitude of the order of 0.1 m/s in shallow water. The Stokes drift is taken into account by adding an extra velocity with magnitude U_{ST} and components U^s, V^s, based on the expression:

$$U_{ST} = {E_w}/{\rho h c}$$

$$U^s = U_{ST} \sin\theta \quad , \quad V^s = U_{ST} \cos\theta$$

where U^s and V^s are the velocity components due to the Stokes drift [16], E^w is the wave-group varying short wave energy computed by:

$$E^w = {\rho g H_s^2}/{16} \qquad (6)$$

The angle ϑ is the wave direction (TOMAWAC convention, i.e. 0 degrees for waves going to the North), ρ is the water density, c is the phase velocity, g is the gravitational acceleration and H_s is the significant wave height.

7.1.3 Wave non-linearity

The wave non-linearity consists of wave skewness and wave asymmetry.

The wave skewness (Sk) indicates that wave crests are higher and shorter in duration than the troughs. The shoreward velocity under the crest is higher than the seaward velocity under the wave trough (skewness). Even though the mean orbital velocity is zero, the resulting mean bed shear stress and sediment transport is directed onshore.

Wave asymmetry (As) refers to the higher acceleration of the wave front compared to the wave tail. Phase lag effects (asymmetry) between maximum velocity and flow reversal has effect on sediment stirring [6]. Finally, horizontal pressure gradients can result in plug flow, or loosening up of sediment blocks from the bed. This phenomenon is more intense for asymmetric waves (Foster *et al.*, 2006) resulting in onshore transport.

The contribution of wave non-linearity is calculated by means of an extra velocity with magnitude U_{NL} and components U^a, V^a:

$$U_{NL} = (f_{Sk}Sk - f_{As}As)u_{rms}$$
$$U^a = U_{NL}sin\theta \quad , \quad V^a = U_{NL}cos\theta$$

where f_{Sk} and f_{As} are calibration factors with values from 0 to 1.0 and a recommended value of 0.1, u_{rms} is the root-mean square velocity computed as:

$$u_{rms} = U_w\sqrt{2}$$

and U_w is the orbital velocity, calculated in TOMAWAC. Then, the skewness and asymmetry can be computed using the Boltzmann sigmoid through the expressions:

$$Sk = Bcos\psi \quad , \quad As = Bsin\psi$$
$$\psi = -90 + 90tanh(^{p_5}/_{Ur^{p_6}})$$
$$B = p_1 + {(p_2 - p_1)}\Big/{\left(1 + exp\frac{p_3 - logUr}{p_4}\right)}$$

where Ur is the Ursell number computed by:

$$Ur = {3}/_{4} \cdot \left[{0.5H_s k}\Big/{(kh)^3}\right]$$

and k is the wave number. $p_{1:6}$ are parametrization factors based on field observations [2]. In the present work we considered the mean values as:

$$p_1 = 0.000 , \quad p_2 = 0.875 , \quad p_3 = 0.471$$
$$p_4 = 0.297 , \quad p_5 = 0.815 , \quad p_6 = 0.672$$

Variables including local orbital velocity, significant wave height, water depth and wave direction are communicated directly from TOMAWAC, whereas the wave celerity is calculated form the wave period and the wave number, which is computed using the subroutine WNSCOU using the local water depth and the wave period from TOMAWAC.

7.1.4   Blankenberge

An application of Ciara storm has been conducted with the set-up presented in section 5.3.2, using the implemented the cross-shore transport processes. For comparison three different cases have been examined v8p1 and shown in Table 36. The simulations have been conducted using version v8p1 of TELEMAC-MASCARET suite.

Table 36 – Simulated cases for Ciara storm with different considered sediment transport models.

Run name	Bedload transport model	Suspended sediment transport model	cross-shore transport processes
C001	Soulsby – Van Rijn (SVR) [5]	-	NO
C002	-	Soulsby – Van Rijn (SVR) [4]	NO
C003	-	Soulsby – Van Rijn (SVR) [4]	YES

The case C001 is used to compare the version v8p1 and module GAIA with the case presented in section 5.3.2 using v7p3 and module SISYPHE. The case C001 is giving the same results with the post-storm erosion-deposition patterns as it can be observed in Figure 175. However, it must be highlighted that in TELEMAC2D v8p1, there is an option to have a wind influence varying with speed switched on by default (COEFFICIENT OF WIND INFLUENCE VARYING WITH SPEED). This option was not applied to v7p3 and thus, had to be switched off on the present cases because it has a significant effect in the erosion-deposition patterns. Case C001 shown in Figure 175 shows the same results with the previous case shown in Figure 154.
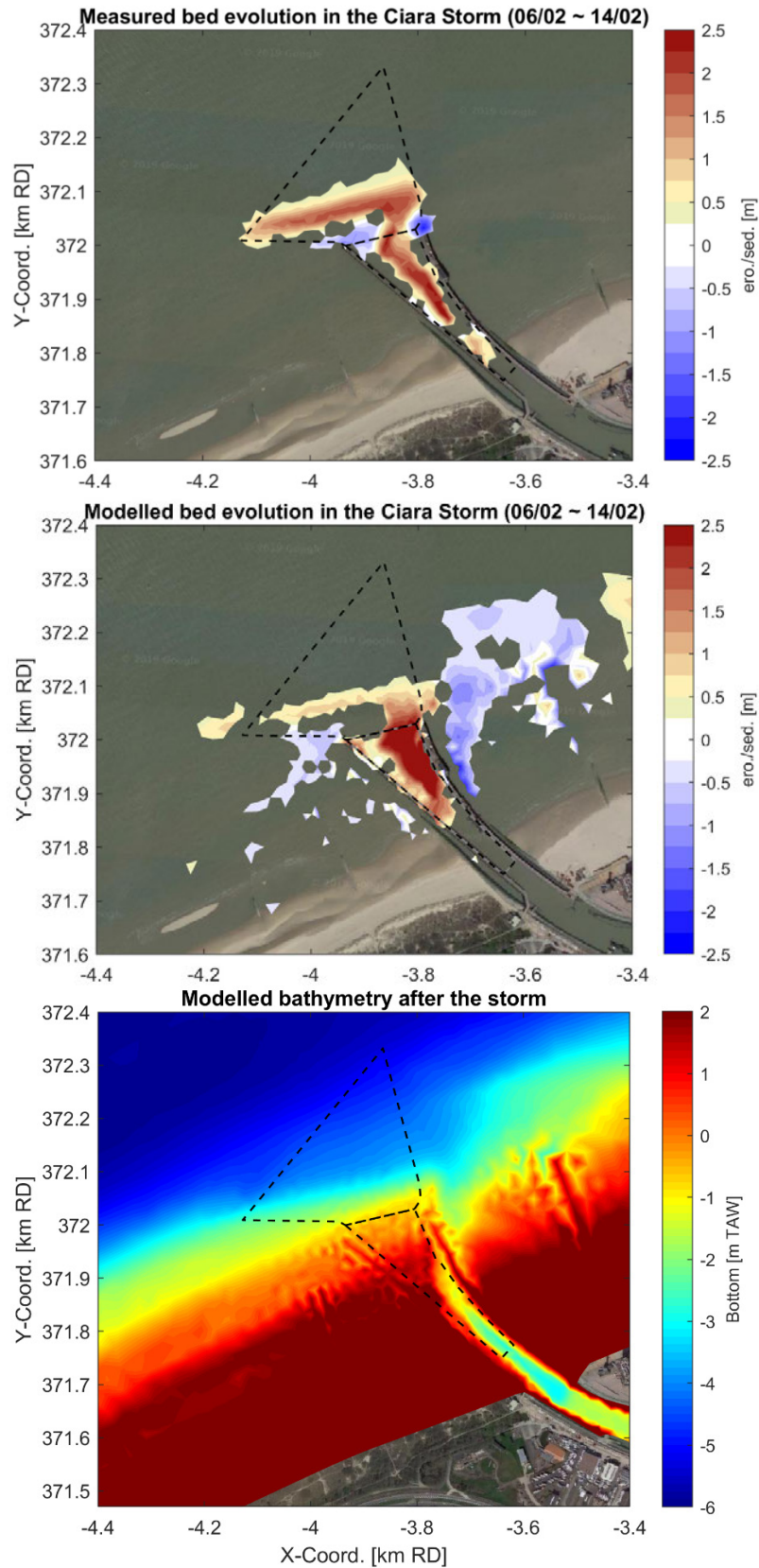
Figure 175 – Observed (top), modelled (middle) sedimentation and modelled final bathymetry (bottom) in the entrance channel for the port of Blankenberge during the Ciara Storm (case C001).

The case C002 considering suspended sediment transport with Soulsby – Van Rijn (SVR) [4] without cross-shore processes, result in milder erosion-deposition patterns as it can be observed in top Figure 176. The high deposition in the entrance of the port is still evident, but the measured deposition in zone "Voorplein" (offshore polygon) cannot be captured. On the other hand, consideration of cross-shore transport processes in case C003 indicate that the measured bar in zone "Voorplein" can be also observed in the simulation results, even though the bar for case C003 is found relatively closer to the port entrance (see Figure 177).
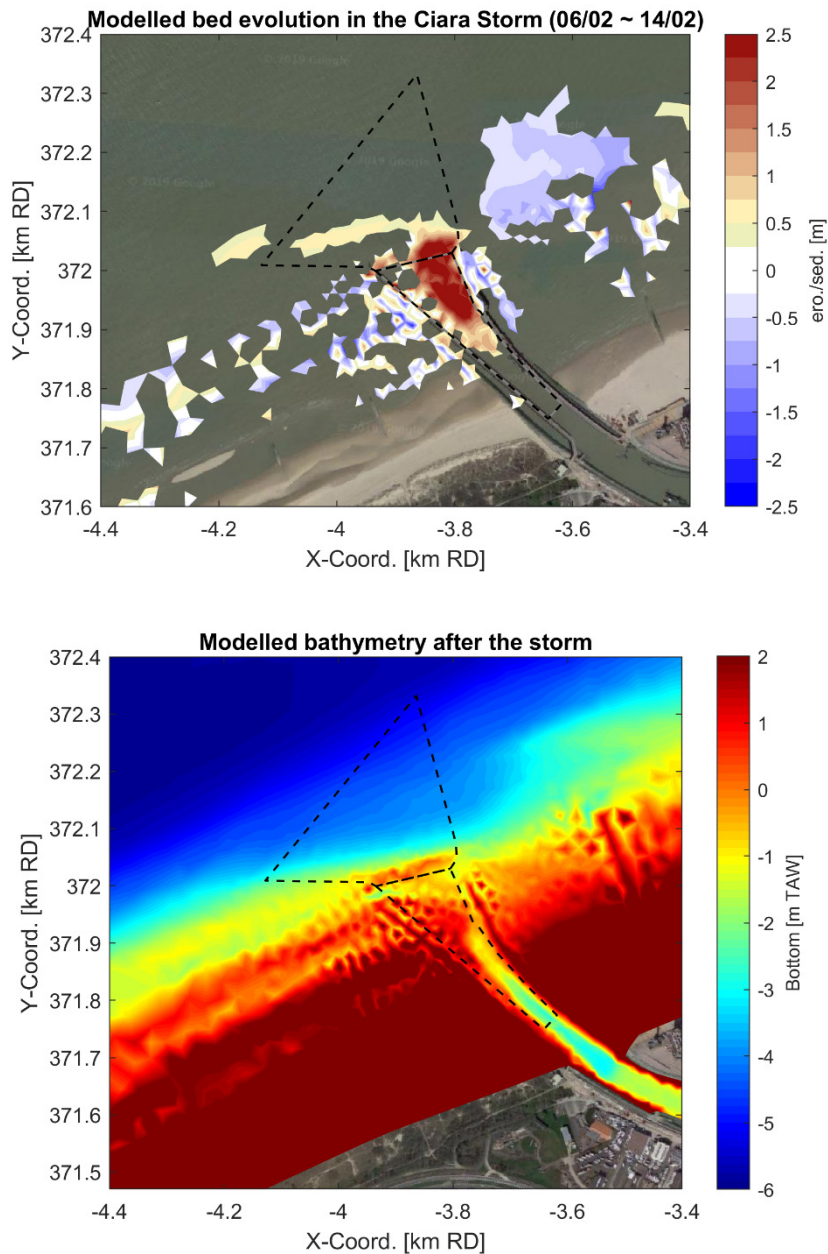
Figure 176 – Modelled sedimentation (top) and final bathymetry (bottom) in the entrance channel for the port of Blankenberge during the Ciara Storm for case C002 with suspended sediment without cross-shore transport.
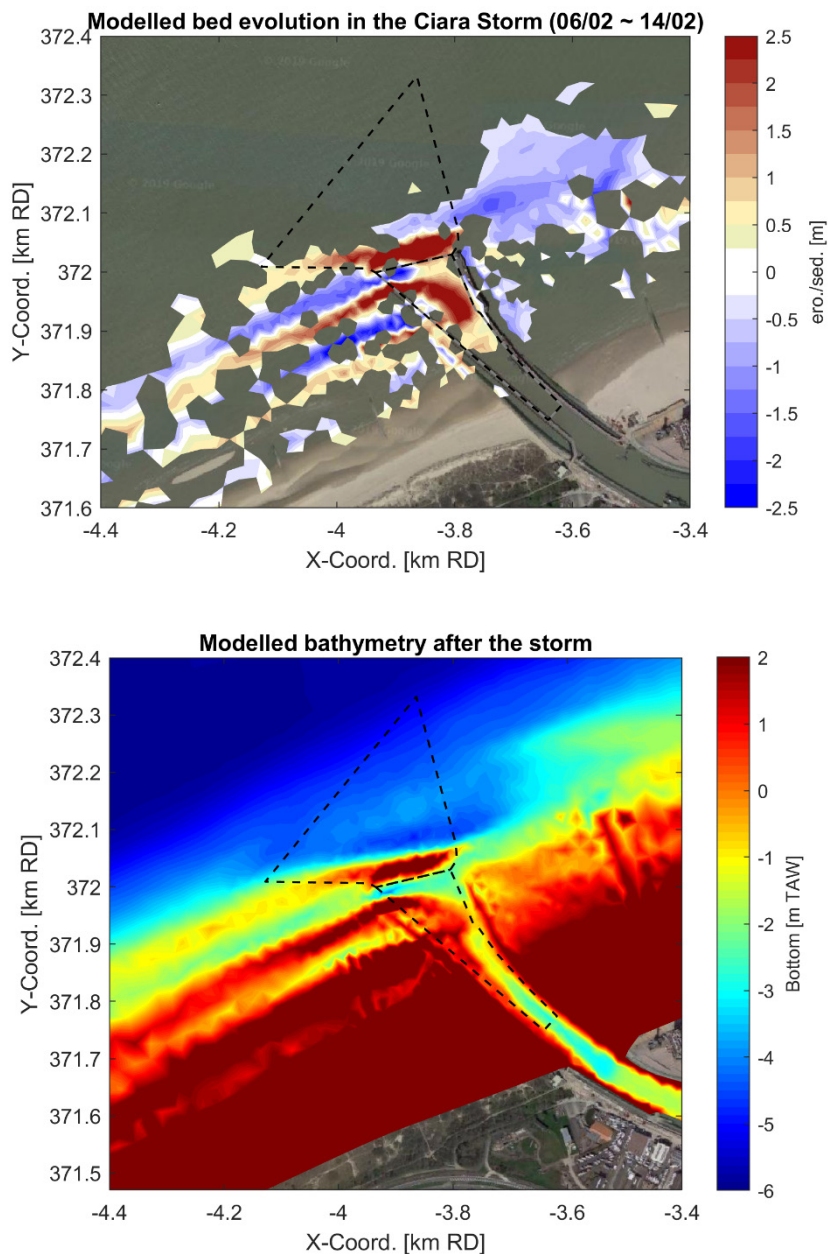
Figure 177 – Modelled sedimentation (top) and final bathymetry (bottom) in the entrance channel for the port of Blankenberge during the Ciara Storm for case C003 with suspended sediment with cross-shore transport.

The differences between the three simulated cases can be also seen in the calculated modelled total gross and net sedimentations in Table 37. Case C001 shows that like in section 5.3.2 the net sedimentation reach 43 600 m³ and 41 700 m³. Case C002 considering suspended sediment transport without cross-shore processes results in 38 700 m³ and 38 000 m³ with similar erosion-deposition patterns like in case C001. Finally, case C003 with suspended sediment transport and cross-shore processes result in 45 400 m³ and 39 200 m³ which is close to the measured ones 47 500 m³ 43 800 m³ and result in close sedimentation patterns with the measured ones. It can be concluded that consideration of cross-shore transport processes results in improving the sedimentation patterns and the computed volumes.

Table 37 – Sedimentation volumes in the port of Blankenberge during the Ciara storm (cases C001, C002 and C003).

	Voorplein (m^3)		Geul (m^3)		Total (m^3)	
	Net	Gross	Net	Gross	Net	Gross
Modelled C001	13 000	14 700	28 700	28 900	41 700	43 600
Modelled C002	14 300	14 800	23 700	23 900	38 000	38 700
Modelled C003	21 900	26 200	17 300	19 100	39 200	45 400
Observed	27 100	29 700	16 700	17 800	43 800	47 500

7.2 Sand-mud interaction

7.2.1 Introduction

The Belgian coastal zone, in the vicinity around Zeebrugge, is characterized by a local turbidity zone and high contents of mud in the bottom. So far most morphological models for the Belgian coast are limited to sand transport only. However, it is expected that the mud content will have an impact on the morphology. Also, dredging sediments from maintenance dredging dumped at the assigned deposit sites, consist of a mixture of sand and mud: sediment from the maintenance of the shipping lanes Pas-van-het-Zand and Scheur contain between 40 and 60% of mud. The mud-content has an effect on the stability of the dumped sediments and the evolution of the bottom at and near the deposit sites. Therefore, the aim of this study is to incorporate cohesive sediments in the attempt to improve the morphodynamic model for the Belgian coast, making it capable of coping with mixed sediment transport. It is important to emphasize that the detailed modelling of the cohesive sediment dynamics is beyond the scope of the present study.

To achieve this objective, the new sediment transport module of TELEMAC suite, also known as GAIA, will be utilized. According to the GAIA User Manual (2019), GAIA is based on the historical sediment transport module SISYPHE, where a large number of improvements, corrections and optimizations have been implemented. Thanks to its unified framework, GAIA efficiently manages different sediment classes, sand-mud mixtures, etc. for both 2D and 3D cases.

In the present memo, a deep insight in the mixed sediment transport parameters considered in GAIA is conducted through the well-known 10-year hindcast exercise (1986-1996) by Scaldis-Coast model. The early results of this application showed that apart from the model parameters that can be adjusted in the calibration stage, modifications in the formulation (for the mixture) are needed in order to acquire reasonable results. The effect of these adjustments and modifications is presented mainly through the comparison of the modelled and the measured sedimentation-erosion patterns at the area between Zeebrugge port and the Western Scheldt mouth.

7.2.2   Model set-up

In the beginning, pure current simulations were considered for the hindcast exercise, i.e. coupled TELEMAC-2D and GAIA simulations. The most important settings of both modules are summarized in Table 18. The coupling of the hydro- and morphodynamic modules initiates after a warming-up of the hydrodynamic module for a short simulation period of two diurnal tidal cycles, so that a fully developed flow field occupies the computational domain.

Table 38 – Main settings of the morphodynamic Scaldis-Coast model.

	Parameter	Value
TELEMAC-2D	Time step	10 s
	Initial conditions	developed flow field after warming-up of 2 diurnal tidal cycles
	Version of TELEMAC	TELEMAC V8P1 (Goblinshark)
	Wind	Off
	Bed Roughness formula	Manning varying roughness distribution (n=0.022 at coast)
	Option for treatment of tidal flats	1: equations solved everywhere with correction on tidal flats
	Treatment of negative depths	1: smoothing
	Horizontal turbulence model	4: Smagorinski
	Scheme for advection of velocities	1: method of characteristics
	Scheme for advection of depth	5: conservative scheme
GAIA	Bed load transport formula	7: Van Rijn (1984); 4: Bijker (1992); 71: Van Rijn (2007); 5: Soulsby & Van Rijn (1997)
	Suspension transport formula (sands)	All available are tested
	Equilibrium inflow concentration	Yes
	Scheme for advection of tracers	1: method of characteristics
	Morphological Factor on Bed Evo.	10
	Sediment density (sand & mud)	2650 kg/m^3
	Median sand grain diameter (D_{50})	200µm, 250µm & spatially varying (2 classes: 200µm -500µm)
	Median mud grain diameter (D_{50})	60 µm
	Settling velocity	Sand: Calculated by GAIA; Mud: 0.001 m/s
	Number of layers for init. stratification	2
	Active layer thickness	0.1 m (0.01 x MOFAC)
	Mud concentration	Layer 1: 100-200 mg/l; Layer 2: 400 mg/l
	Critical erosion shear stress (mud)	Layer 1: 0.5-0.7 N/m^2; Layer 2: 1.0 N/m^2
	Partheniades constant	10^{-3} kg/m^2/s
	Formula for slope effect	1: Koch & Flokstra (1981) / BETA = 1.3

A schematized tidal forcing consisting of 350 successive representative tides RT137, i.e. 362 days (about 1 year), was applied in the hydrodynamic module. Implementing of MOFAC equal to 10 leads to a morphological simulation of about 10 years (1986-1996).

The basic source for the mud content estimation in the seabed of the Belgian coast is the high-resolution data (250 m x 250 m) of Figure 96, which was reported in the thematic maps of MAREBASSE project (Van Lancker *et al.*, 2007), and it is only limited within the Belgian Continental Shelf (BCS). For the rest of the coastal part of the Scaldis-Coast domain, lower-resolution data (1x1 nautical mile) from the NOAH project available by Helmholtz-Zentrum Geesthacht (HZG) (Bockelmann *et al.*, 2018) were used (Figure 179). The percentage of mud in the seabed sediment over the model's domain, after the compilation of the two databases, is shown in Figure 180.
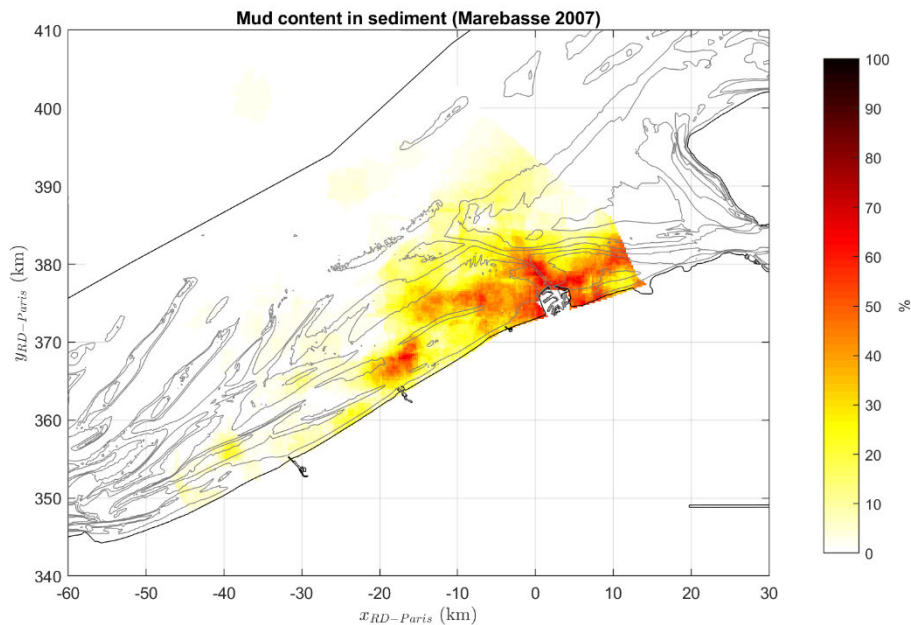
Figure 178 – Mud content (%) distribution within the Belgian Continental shelf as reported in Van Lancker et al. (2007).
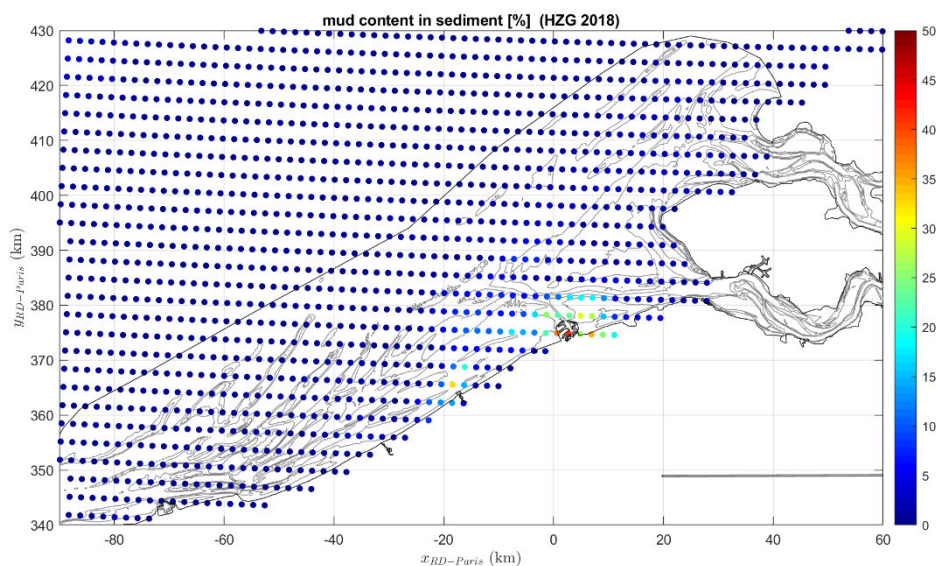
Figure 179 – Mud content (%) distribution at the southern North Sea region as reported in Bockelmann et al. (2018).
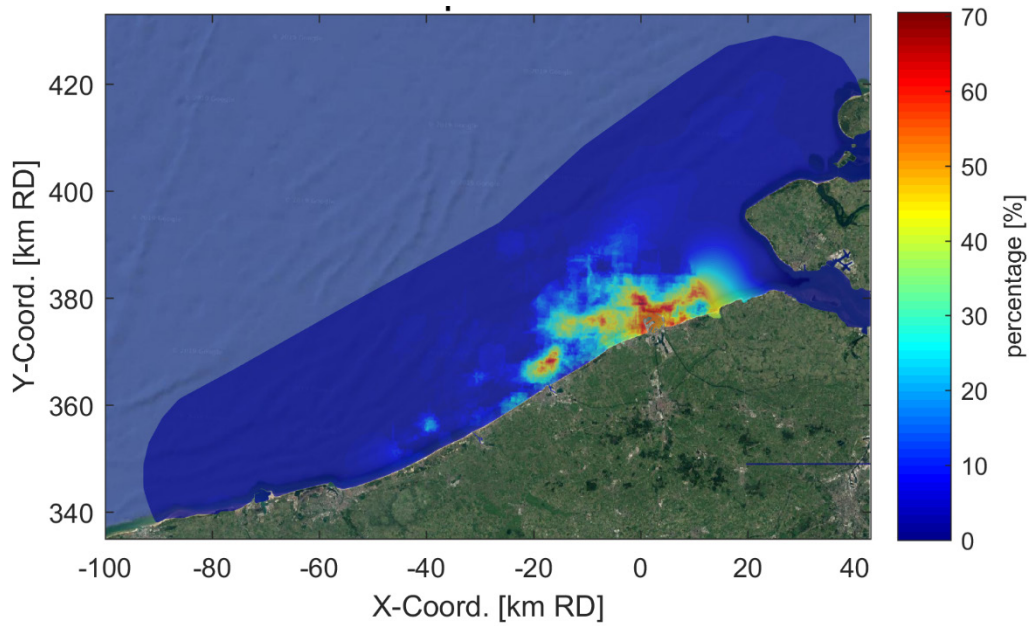
Figure 180 – Mud content distribution over Scaldis-Coast domain.

7.2.3 Improvements for mixed sediment in GAIA

The modifications in GAIA's source code are related to the main parameters that determine the erosion of seabed mixtures. Namely, these are: (a) the critical erosion shear stress and (b) the erosion rate of the mixture.

Default formulation for erosion of mixtures

In GAIA, a single erosion rate for the mixture is computed in the surface (active) layer, based on a single critical shear stress for the mixture.

The critical shear stress is computed by default in the following way:

- critical shear stress for a mass cohesive sediment fraction of the mixture below 30% is equal to the critical shear stress for non-cohesive sediment alone:

$$\overline{\tau_{ce_j}} = \tau_{ce_j}^1 \qquad (index\ 1\ denotes\ sand\ fraction;\ j\ is\ the\ layer\ number) \tag{1}$$

- critical shear stress for a mass cohesive sediment fraction of the mixture above 50% is equal to the critical shear stress for cohesive sediment alone:

$$\overline{\tau_{ce_j}} = \tau_{ce_j}^2 \qquad (index\ 2\ denotes\ mud\ fraction;\ j\ is\ the\ layer\ number) \tag{2}$$

- critical shear stress for a mass cohesive sediment fraction of the mixture between 30% and 50% is interpolated from the two cases above:

$$\overline{\tau_{ce_j}} = \tau_{ce_j}^1 + \frac{\left(f_{2j}-0.30\right)\left(\tau_{ce_j}^2 - \tau_{ce_j}^1\right)}{(0.50-0.30)} \tag{3}$$

where $f_{2j} = M_{sj}^2/(M_{sj}^1 + M_{sj}^2)$ is the mass ratio of mud in the mixture for each layer.

Erosion rate is computed in the following way:

- erosion rate for a mass cohesive sediment fraction of the mixture below 30% is equal to the erosion rate for non-cohesive sediment alone:

$$\bar{E}_J = E_j^1 = w_{s1} C_{eq} \tag{4}$$

where w_{s1} is the settling velocity of sand, and C_{eq} is the equilibrium near-bed concentration.

- erosion rate for a mass cohesive sediment fraction of the mixture above 50% is equal to the erosion rate for cohesive sediment alone:

$$\bar{E}_J = E_j^2 = \begin{cases} M\left[\left(\dfrac{\tau_b}{\tau_{ce_J}}\right) - 1\right] & if\ \tau_b > \overline{\tau_{ce_J}} \\ 0 & otherwise \end{cases} \tag{5}$$

where M the Krone-Partheniades erosion law constant [kg/m^2/s] and τ_b is the instantaneous skin friction.

- erosion rate for a mass cohesive sediment fraction of the mixture between 30% and 50% is interpolated from the two cases above:

$$\bar{E}_J = E_j^1 + \frac{\left(f_{2_j} - 0.30\right)\left(E_j^2 - E_j^1\right)}{(0.50 - 0.30)} \tag{6}$$

The total erosion rate is then distributed among non-cohesive sediment and cohesive sediment according to their respective fraction in the mixture.

Modifications in formulation

A better understanding of how the erosion of mixtures works in GAIA, can be acquired through a simple test case of a steady flow over a bed of mixed sediment. The parameters needed to calculate the erosion rate of the mixture for this test case, are shown in the following table:

Table 39 – Main parameters of the test case of an erosive steady flow.

Parameter	Value
Skin friction τ_b	2 N/m^2 [input]
Median sand grain diameter D$_{50}$	250 µm [input]
Critical shear stress of sand τ_{cr}	0.18 N/m^2 (calculated by formula in GAIA)
Settling velocity of sand w_{s1}	0.035 m/s (calculated by formula in GAIA)
Near-bed concentration C_{eq} (van Rijn)	18.4 mg/l (sandy bottom - f_{2j} < 0.3)
Critical erosion shear stress of mud τ_{ce}	0.5 N/m^2 [input]
Partheniades constant M	10^{-3} kg/m^2/s [input]
Erosion rate for sandy bed (f_{2j} < 0.3)	0.64 kg/m^2/s
Erosion rate for muddy bed (f_{2j} > 0.5)	0.003 kg/m^2/s

In Figure 181, the variation of the erosion rate of the mixture, $\bar{E}$, versus the mass ratio of mud in the mixture, f_{2j}, is depicted by the orange line. The yellow and the green lines correspond to the erosion rates of the sand fraction and the mud fraction, respectively, which are calculated as $\overline{E_{sand}} = \bar{E}(1 - f_{2j})$ and $\overline{E_{mud}} = \bar{E} f_{2j}$.
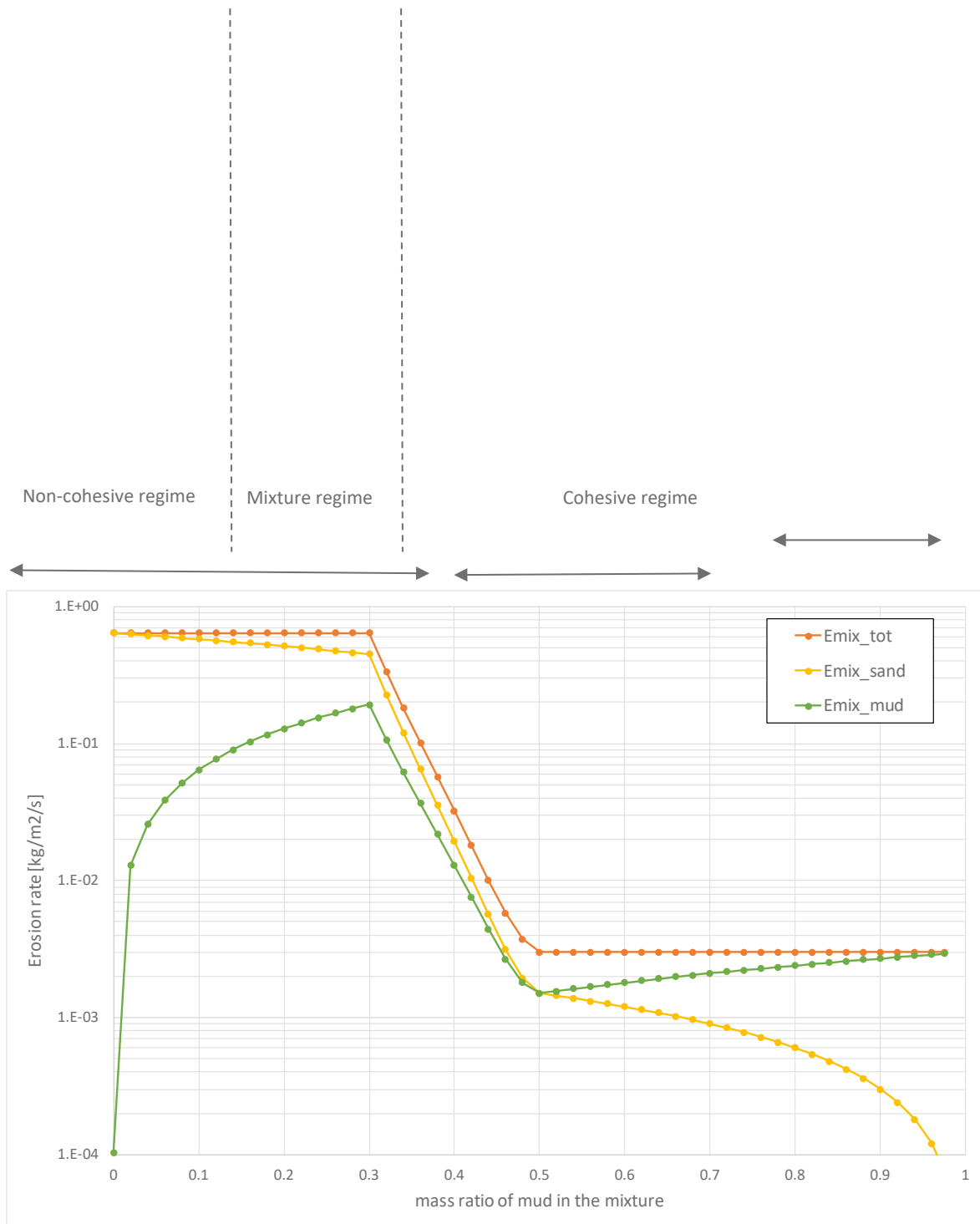
Figure 181 – Erosion rates (default GAIA formulation) versus mass ratio of the mud, for the test case of the steady flow (Table 39).

The erosion rate of mud (green line) increases unnaturally for 0.5 > f_{2j} > 0.3 (mixture regime), dominated by the linear interpolation (between the erosion rates of the two fractions) expressed by Eq. 6. In GAIA the advection-diffusion equation is solved separately for each class of sediment, not representing ideally the physical erosion of mixtures, therefore such high mud erosion rates would trigger exaggerated erosion/suspension of the mud fraction. Practically, such a variation of the mud erosion rate would cause abrupt transportation of the total mud fraction from erosive to accretive areas.

A first attempt to improve this unnatural behavior, without completely changing the formulation of GAIA for mixed erosion rates, is presented in this section. The main idea was to implement calibration coefficients on the existing model. The selection of the coefficients was mainly based on trial and error.

First a calibration coefficient C_1 could be applied on $\overline{E_{sand}}$ and $\overline{E_{mud}}$, within the mixture regime, while the total erosion rate of the mixture, $\bar{E}$, remains unchanged:

$$C_1 = \left[\frac{\left(f_{2_j} - 0.30 \right)}{(0.50 - 0.30)} \right]^n \qquad \text{(selected n=2)} \qquad (7)$$

The erosion rate for each class is now calculated as $\overline{E_{mud}} = \bar{E} C_1 f_{2j}$ and $\overline{E_{sand}} = \bar{E}\left(1 - C_1 f_{2j}\right)$.

Note that $C_1 = 1$ for $f_{2j} > 0.5$ (cohesive regime) and $C_1 = 0$ for $f_{2j} < 0.3$ (non-cohesive regime). The latter statement indicates that mud is not any more allowed to go in suspension under the assumption that it is trapped in the pores between the sand grains which dominate in the bed composition. Mud presenting in the mixture can be still entrained in suspension through bedload transport of non-cohesive sediment. However, this elimination of direct mud erosion can be reconsidered (it is open for improvement).

Additionally, two more calibration coefficients could be applied in the default erosion model, i.e. one applied on the critical erosion shear stress of the mixture $\overline{\tau_{ce_j}}$, and another one on the total erosion rate of the mixture $\bar{E}$. The coefficients are introduced in Eq. 3 and Eq. 6 (mixture regime only), respectively in the following manner:

$$\overline{\tau_{ce_j}} = \tau^1_{ce_j} + \left[\frac{\left(f_{2_j} - 0.30 \right)}{(0.50 - 0.30)} \right]^{n_\tau} \left(\tau^2_{ce_j} - \tau^1_{ce_j} \right) \qquad (8)$$

$$\bar{E}_J = E_j^1 + \left[\frac{\left(f_{2_j} - 0.30 \right)}{(0.50 - 0.30)} \right]^{n_e} \left(E_j^2 - E_j^1 \right) \qquad (9)$$

The selected values are $n_\tau = n_e = 0.5$.

The effect of the aforementioned calibration coefficients on the erosion rates within the mixture regime can be seen in Figure 182. The erosion rate of the mixture $\bar{E}$ (orange line), affected by the coefficients n_e and n_τ, presents now hyperbolic growth as we move to the non-cohesive regime ($f_{2j} = 0.3$). The mud erosion rate $\overline{E_{mud}}$ (green line) is affected additionally by coefficient C_1, hyperbolically decreasing to zero as the mud ratio approaches the lower critical value of mud fraction (0.3). On the other hand, the sand erosion rate $\overline{E_{sand}}$ (yellow line) very quickly becomes dominant in the mixture, coinciding with the curve of $\bar{E}$.

Another adjustment in the source code of GAIA is performed, with respect to the bedload transport initiation. By default, bedload transport is computed only if mass cohesive sediment fraction in the active layer is lower than 30%. This threshold is increased by 10% (to 33%) so that bedload transport can be initiated for mixtures that contain a bit more mud than the default percentage. This adjustment is coupled with the implementation of the coefficient C_1, which practically eliminates mud erosion for mud ratios a bit larger than 30%, preventing (unnaturally) bedload from initiation. Larger values (than 10%) of increase can also be tested as a calibration parameter.
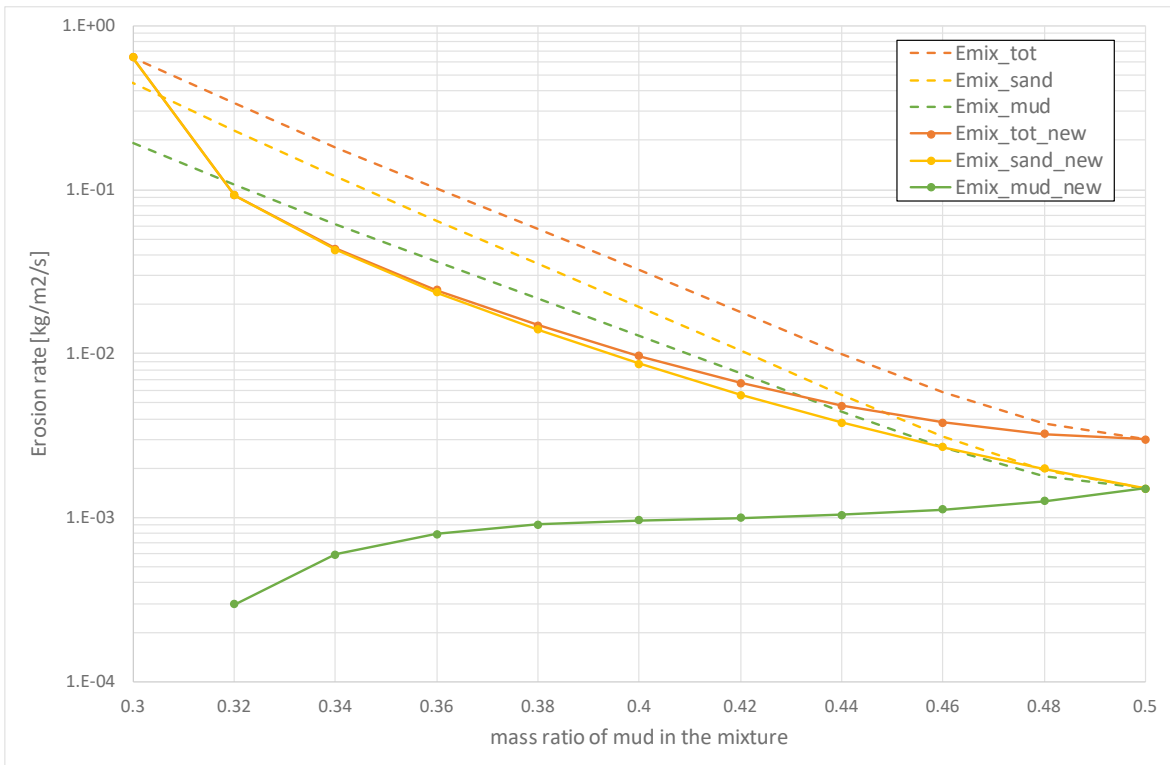
Figure 182 – Calibrated versus default erosion rates in function with mass ratio of the mud (mixture regime only), for the test case of the steady flow.

The interventions in the default formulation for erosion of mixtures are then tested in a pure-current Scaldis-Coast application of limited simulation period (6 diurnal tidal cycles). In this application the following GAIA parameters are used:

Table 40 – Main GAIA parameters of the test Scaldis-Coast application.

Parameter	Value
Bed load transport formula	7: Van Rijn (1984)
Suspension transport formula (sands)	3: Van Rijn (1984)
Median sand grain diameter (D_{50})	250μm
Morphological Factor on Bed Evo.	1
Number of layers for init. stratification	1
Active layer thickness	0.01 m (0.01 x MOFAC)
Mud concentration	100 g/l
Critical erosion shear stress (mud)	0.5 N/m^2
Partheniades constant	10^{-3} kg/m^2/s

The bed level change at the vicinity of Zeebrugge port at the end of the simulation period for both simulations with the default and the calibrated erosion formulation, is shown in Figure 101. Visual comparison of the two sub-figures is indicative of how effective is the calibration of the mixed erosion formulation. Obviously, the calibrated simulation leads to more realistic sedimentation erosion patterns compared to the simulation with the default settings, which predicts exaggerated erosion of sediment at the areas of large mud content (see also Figure 180). It is reminded that the calibrated mud erosion rate is the main factor for moderating the highly erosive behavior at the specific areas. As for the realistic prediction of the magnitude of the patterns, the calibration exercise will be continued in the following section, where the long-term hindcast exercise is examined.
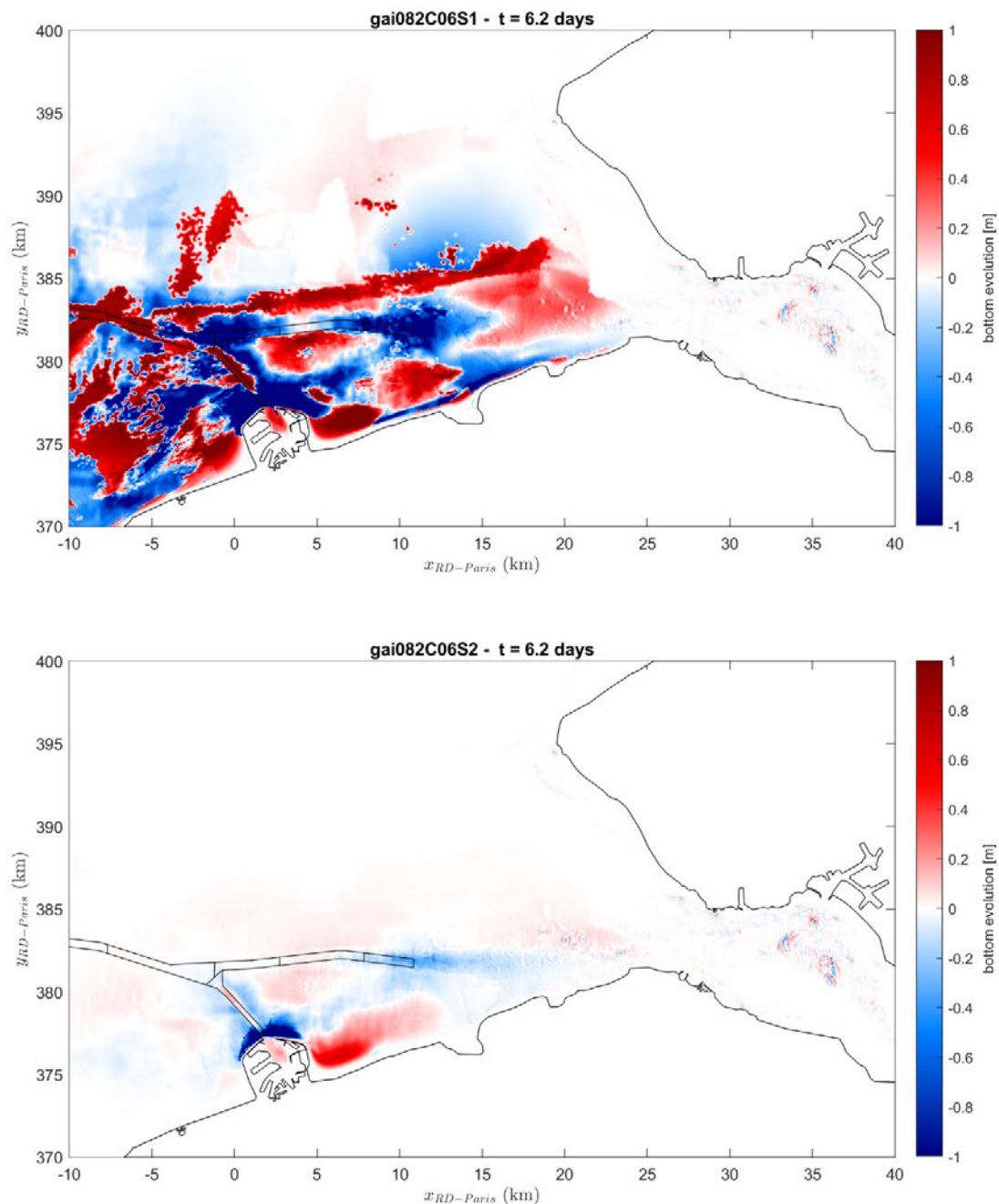
Figure 183 – Bed level change [m] for the pure-current case in Scaldis-Coast after a simulation period of about 6 days; (top) default formulation for erosion of mixtures, (bottom) calibrated formulation for erosion of mixtures.

7.2.4   Hindcast application

The starting point of the simulation period of this exercise coincides with the completion of the extension of the port of Zeebrugge (construction of breakwaters), which affected substantially the morphological equilibrium of the surrounding area. The hindcast application has been investigated previously by means of Scaldis-Coast model considering non-cohesive sediment (sand) transport only (Kolokythas *et al.*, 2019a). Even though the results were satisfactory, improvement of performance was suggested in restricted areas of the domain, like the area of Bay of Heist, where underestimated sedimentation was numerically predicted. It is believed that the composition of transported sediment material is of high importance for the sediment dynamics at the specific location. Hence, this exercise is repeated here considering mixed sediment (mud-sand) transport.

In the following sections, sensitivity tests of various physical parameters (like median grain size) and transport formulations are conducted aiming to improve the performance of the model in hindcast sedimentation-erosion patterns and sediment volume transfer at the area of interest.

Reference simulation

The major GAIA parameters of the reference mud-sand simulation are shown in the following Table 41. The bed-load formula selected is the Bijker's one coupled with D_{50} = 200 μm, for consistency with the calibrated non-cohesive model. The formula of Van Rijn is retained for the calculation of the near-bed equilibrium concentration.

Table 41 – Main GAIA parameters of the test Scaldis-Coast application.

Parameter	Value
Bed load transport formula	4: Bijker (1992)
Suspension transport formula (sands)	3: Van Rijn (1984)
Median sand grain diameter (D_{50})	200μm
Morphological Factor on Bed Evo.	10
Number of layers for init. stratification	2
Active layer thickness	0.1 m (0.01 x MOFAC)
Mud concentration	Layer 1: 200 g/l; Layer 2: 400 g/l
Critical erosion shear stress (mud)	Layer 1: 0.7 N/m^2; Layer 2: 1.0 N/m^2
Partheniades constant	10^{-3} kg/m^2/s

In Figure 184, the bed level change at the vicinity of Zeebrugge port and the mouth of Western Scheldt at the end of the simulation period for the reference simulation, is shown (top panel). The results of a simulation neglecting the presence of mud in the computational domain (mud content = 0%) are depicted in the bottom panel of Figure 184 for better illustration of the mud impact on the sediment transport through comparison. As expected, the differences between the two simulations are restricted at the areas where mud is present (see Figure 180). The most striking effect on the mud-sand mixture consideration is observed at the area of Bay of Heist (east of Zeebrugge port), where significant accretion of sediment occurs. It seems that the mixed-sediment transport prevents sediment from piling at the east side of the eastern breakwater (see bottom panel), helping in the 'smoother' distribution of it at Bay of Heist and at Paardenmarkt areas.

Additionally, the erosion patterns in front of the port breakwaters (along Pas van het Zand channel) present smoother distribution for the reference simulation. Sedimentation at the area of Vlaakte van de Raan seems to be slightly more enhanced for the reference simulation.
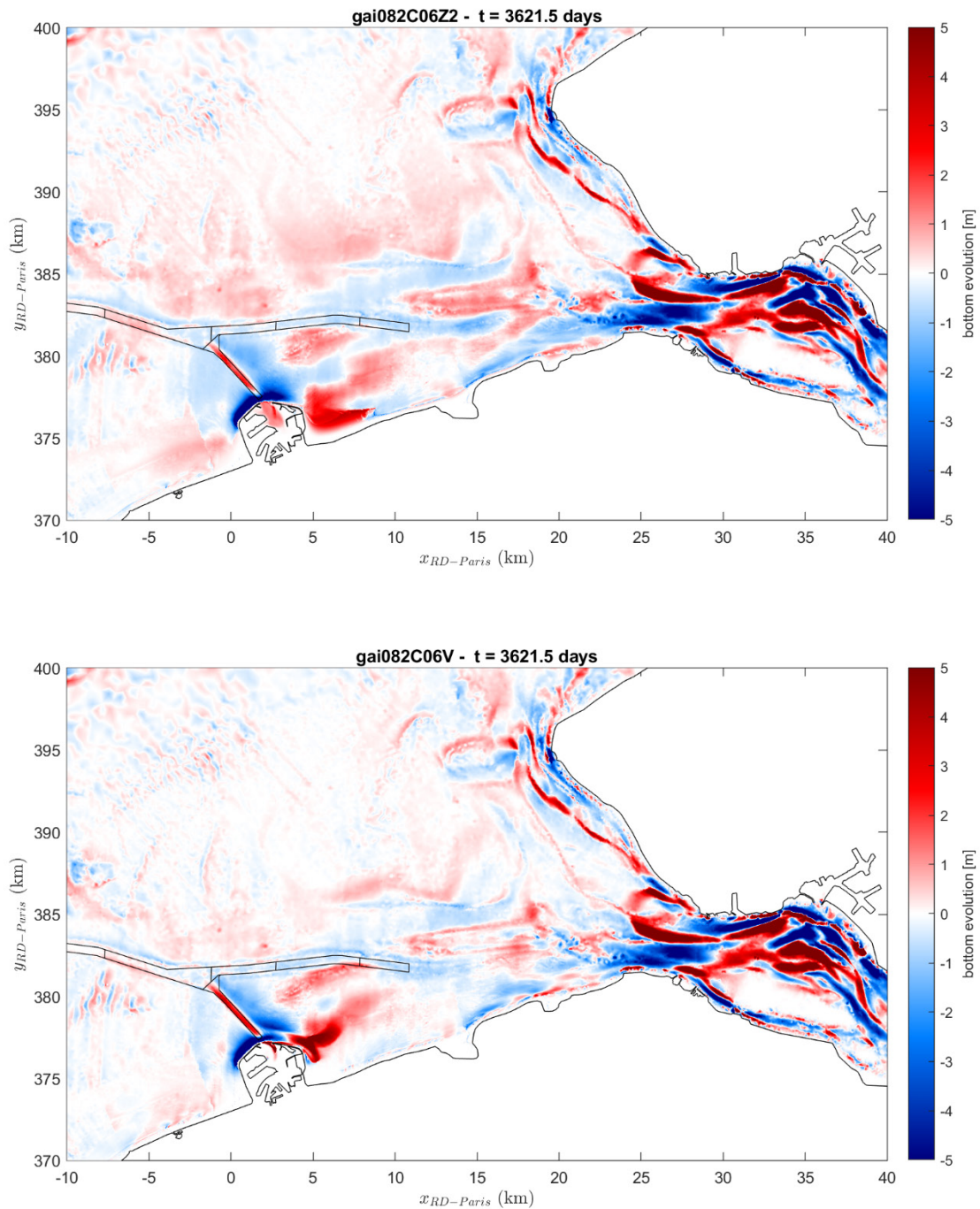
Figure 184 – Bed level change [m] obtained after a simulation period of 10 years; (top) reference simulation: sand-mud ratio based on map of Figure 180, (bottom) mud content = 0% (non-cohesive sediment transport).

Sediment transport formula

In this section, different sediment transport formulas, i.e. bed-load formulas and near-bed equilibrium concentration (or else suspension) formulas, available in GAIA are tested. First, the results for the sedimentation- erosion patterns at the end of the simulation period for the bed-load/suspension formulas of Van Rijn (VR) and of Soulsby and Van Rijn (SvR), are presented in Figure 185.
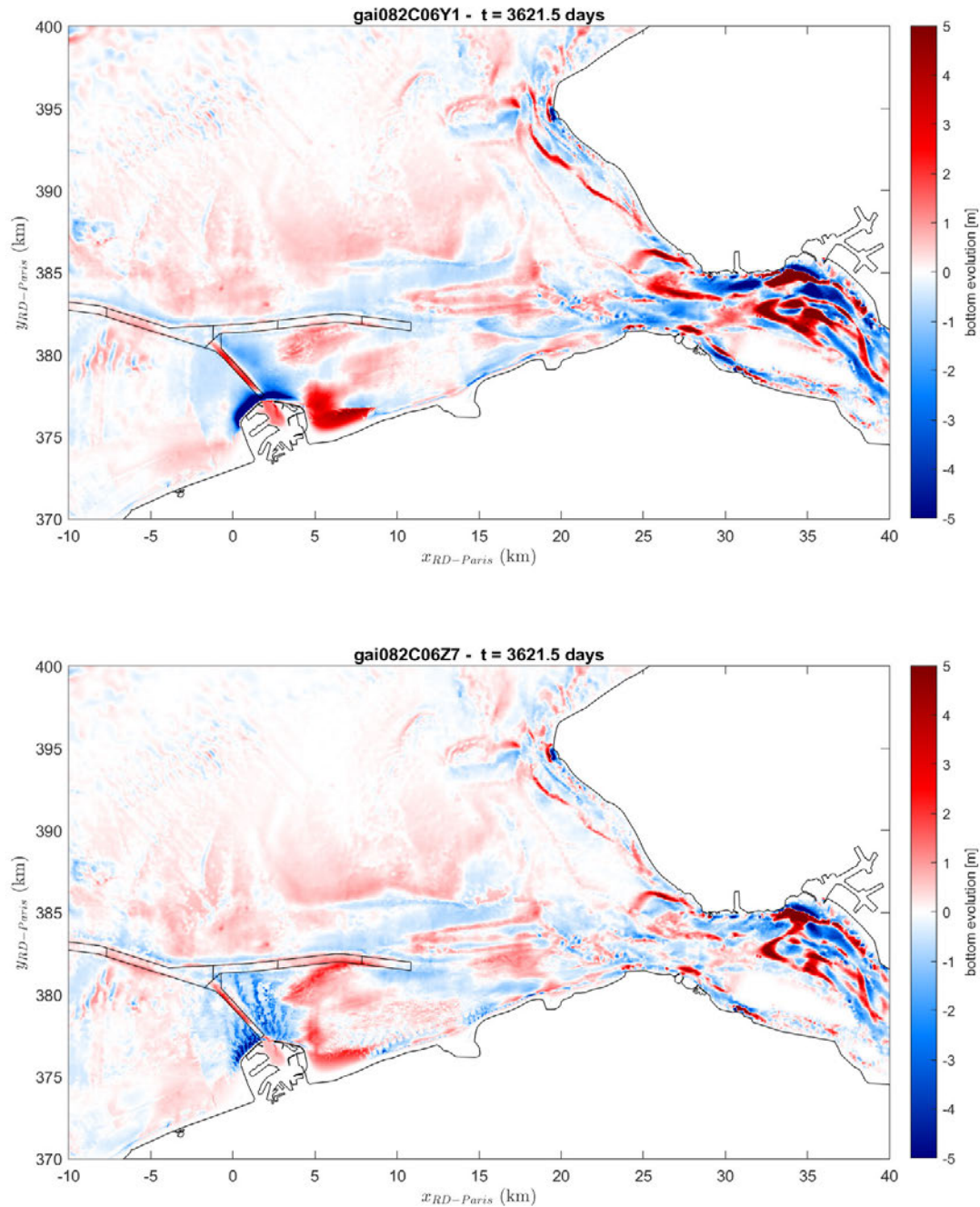
Figure 185 – Bed level change [m] obtained by use of different sediment transport formulas (bed-load and suspension) after a simulation period of 10 years; (top) Van Rijn 2007 [71] + Van Rijn 1984 [3], (bottom) Soulsby and Van Rijn [5] + Soulsby and Van Rijn [4].

Note that the median grain diameter for these formulas is $D_{50} = 250$ μm. It is found that both formulas present similar sed/ero patterns between them, but also compared to the Bijker's one (Figure 184), even though remarkable differences can be spotted. VR formula results into less strong sed/ero patterns compared to the ones of Bijker's, fact that can be partially attributed to the coarser sand grain diameter. The piling of sediment next to the eastern breakwater is also more intense for the case of the VR formula. As for the SvR formula sed/ero patterns, those are even less intense compared to the other two formulas. Remarkable is the wiggly surface of the erosion pattern in front of the port breakwaters, along the Pas van het Zand channel. This behavior is possibly related to the threshold for the initiation of bed-load transport in case of mixed sediment and needs to be further investigated.
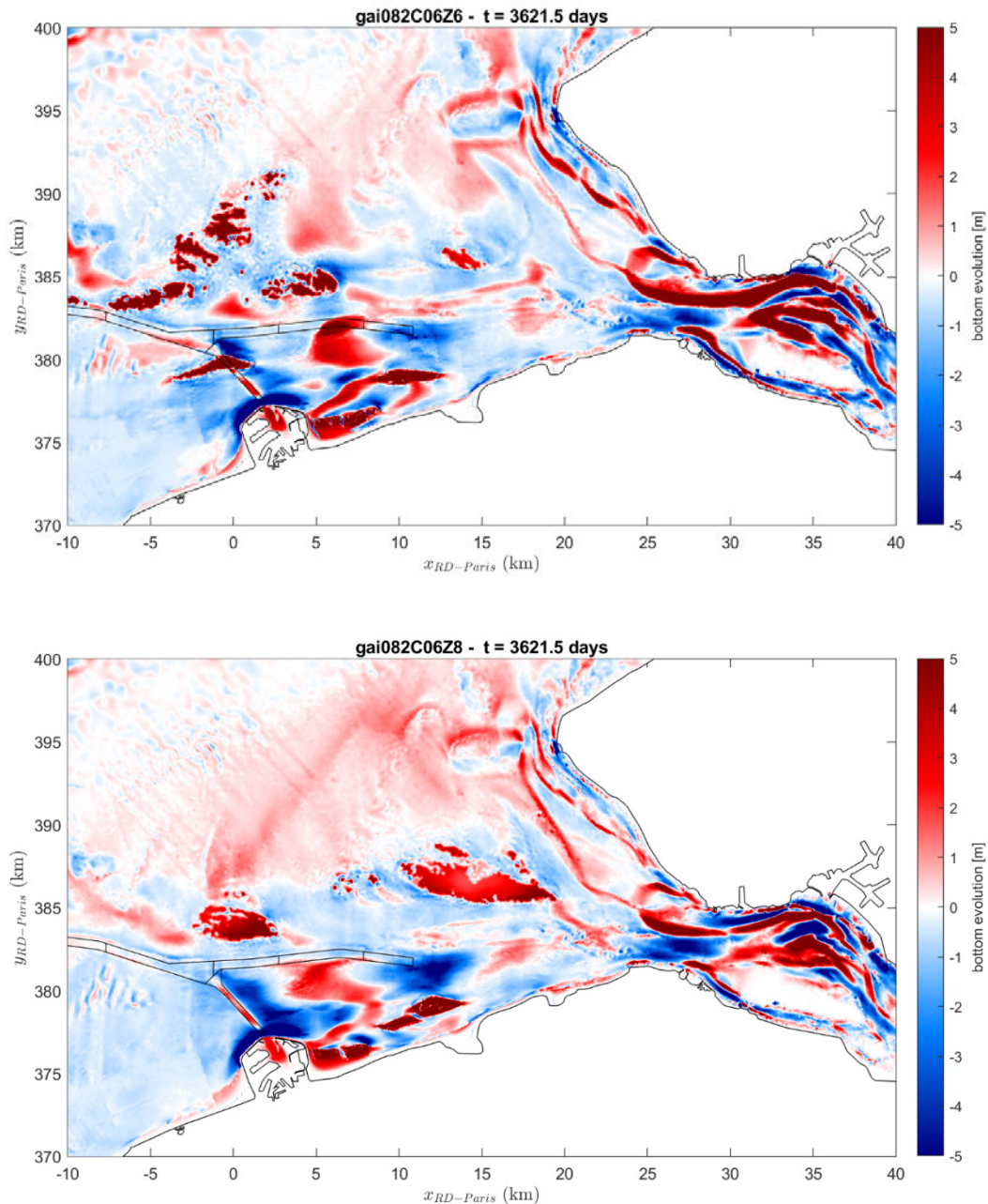
Figure 186 – Bed level change [m] obtained by use of different suspension transport formulas after a simulation period of 10 years ; (top) Bijker's formula [2], (bottom) Zyserman & Fredsoe formula [1]. Bed-load formula for both simulations = Bijker [4].

Next, the effect of coupling different near-bed equilibrium concentration (or else suspension) formulas with the (preferred) bed-load formula of Bijker is presented in Figure 186. The bed level change in the end of the simulation period is given for the suspension formula of Bijker (top panel) and of Zyserman & Fredsoe. In general, both formulas exhibit high intensity leading into patterns that differ in shape and in magnitude compared to those of the reference run (Figure 184). Obviously, extra calibration is needed before the utilization of a suspension formula other than the one of Van Rijn, coupled with the bed-load formula of Bijker.

Varying D_{50} & Hard layers

In the reference run a unique value for the median gain diameter of sand (D_{50}) is utilized all over the computational domain of Scaldis-Coast model. Besides, the total thickness of the movable (erodible) bed layers has been given a large value (= 100 m), i.e. practically there is no restriction on sediment availability. In this section, the implementation of a spatially varying D_{50} distribution coupled with a spatially varying thickness of the erodible bed, both based on available maps, takes place. The spatially varying D_{50} map comes from the compilation of the the high-resolution data reported in the thematic maps of MAREBASSE project (Van Lancker *et al.*, 2007) and the map of the northwest European Continental Shelf sedimentary environment (R. Wilson *et al.*, 2017). The erodible bed thickness map is mainly based on the work by Dam (2012), who examined bathymetries at the Western Scheldt (including the mouth) from 1960 up to 2011. Detailed presentation of the aforementioned databases is given in Kolokythas *et al.* (2020) in sections 5.3 and 4.2, respectively.

The spatially-varying d_{50} transport calculation in the Scaldis-Coast model, is achieved through the concept of equivalent sediment transport is implemented. The concept employed in GAIA (as it was in SISYPHE) is to calculate the transport rate of material with specific d_{50} by summing the transport rates of two sediment classes, one of minimum D_{50} (=200 μm) and one of maximum D_{50} (= 500 μm). Then, the percentage (availability) of each of the two selected classes in every grid node is calculated, so that their total transport rate is identical to the transport rate of the real D_{50} value. Detailed presentation of the implementation of the varying-D_{50} sediment transport is given in section 5.3 in Kolokythas *et al.* (2020). As input for the model, the availability map of one of the two classes has to be given. For the case of Bijker's formula the availability map is shown in Figure 99.

The thickness of the erodible bed is introduced in the model through the same variable used for the introduction of the non-erodible structures (groynes, dams, breakwaters). The map utilized for the tests of the present memo is given in Figure 188. Note that the data of Dam (2012) has been manually extrapolated in order to cover the surrounding area of the port of Zeebrugge.
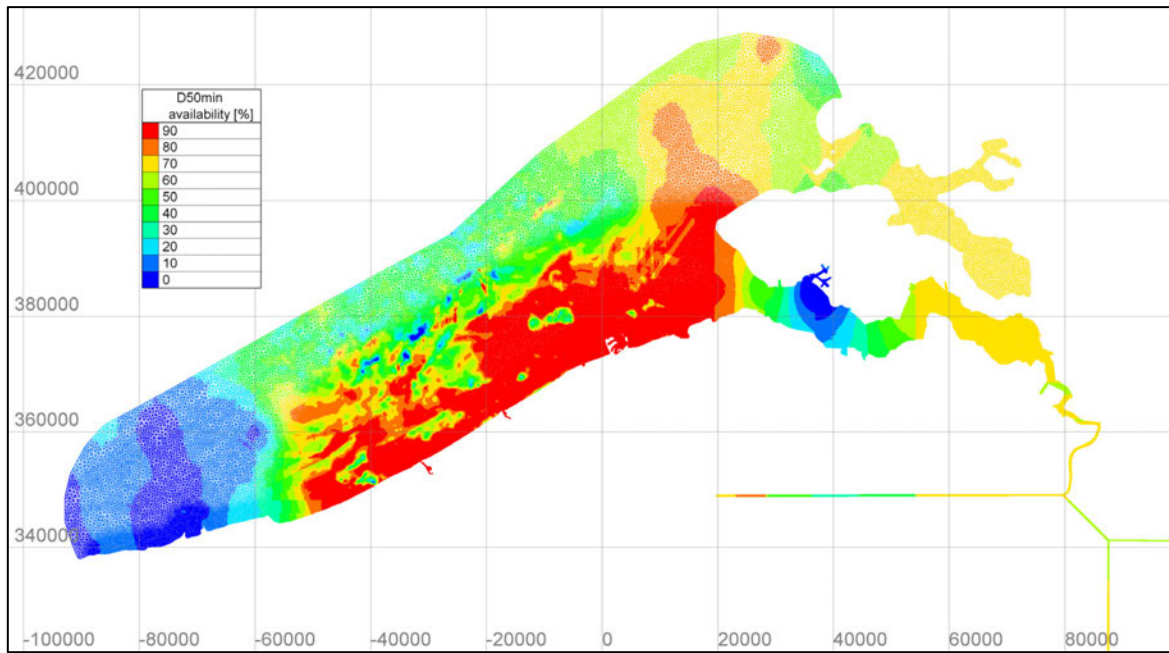
Figure 187 – Percentage of fine sand (dmin = 200 µm) in the sediment mixture of two classes (200 & 500 µm) over the Scaldis-Coast domain, based on the available sediment maps and the Bijker's formulation.
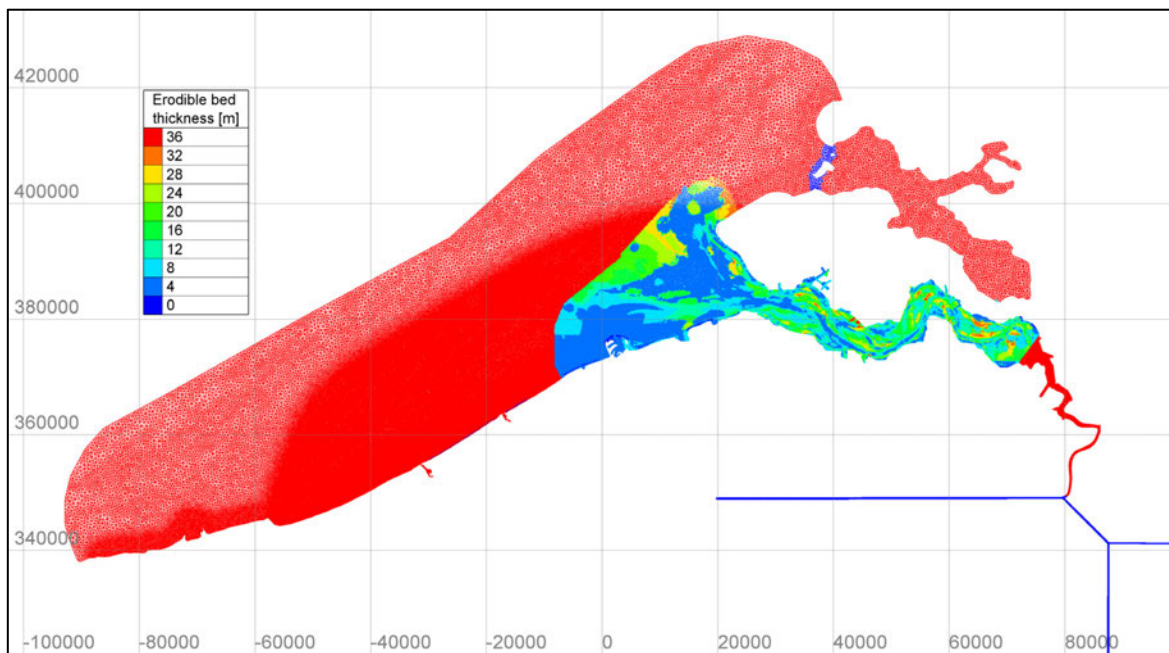
Figure 188 – Erodible bed thickness [m] over the the Scaldis-Coast domain, based on the available map of Dam (2012) and the locations of the non-erodible structures. The original data has been extrapolated to include the surroundings of Zeebrugge port.

Before presenting the results of the simulations with varying D_{50} of sand and limited erodible thickness, the bed level change and the predicted volume changes in selected polygons around Zeebrugge port, at the end of the simulation period (after 10 years), are shown in Figure 189 for the reference run. The bottom level difference between historical bathymetries 1986 & 1996, which gives the measured volume changes in the same polygons is shown in Figure 190. Note that the outline of the three polygons (ZB west, ZB east & Paardenmarkt) is based on the shape of the measured sed/ero patterns as shown in Figure 190. It is found that the reference run leads into accurate prediction for the volume change at Paardenmarkt, however it seems to overestimate the accretion of sediment at the Bay of Heist and underestimate the sedimentation at Paardenmarkt. In addition, the model overestimates the erosion by about 10% and 20% at the west and the east polygon in front of Zeebrugge port, respectively, however the shape of both erosion patterns is very well predicted. Not implementing dredging at Pas van het Zand and dumping with the Paardenmarkt polygon is a fact to be taken into account while assessing the numerical results.

Figure 189 – Bed level change [m] and volume change [m3] in selected polygons around the port of Zeebrugge, obtained after a simulation period of 10 years for the reference simulation.
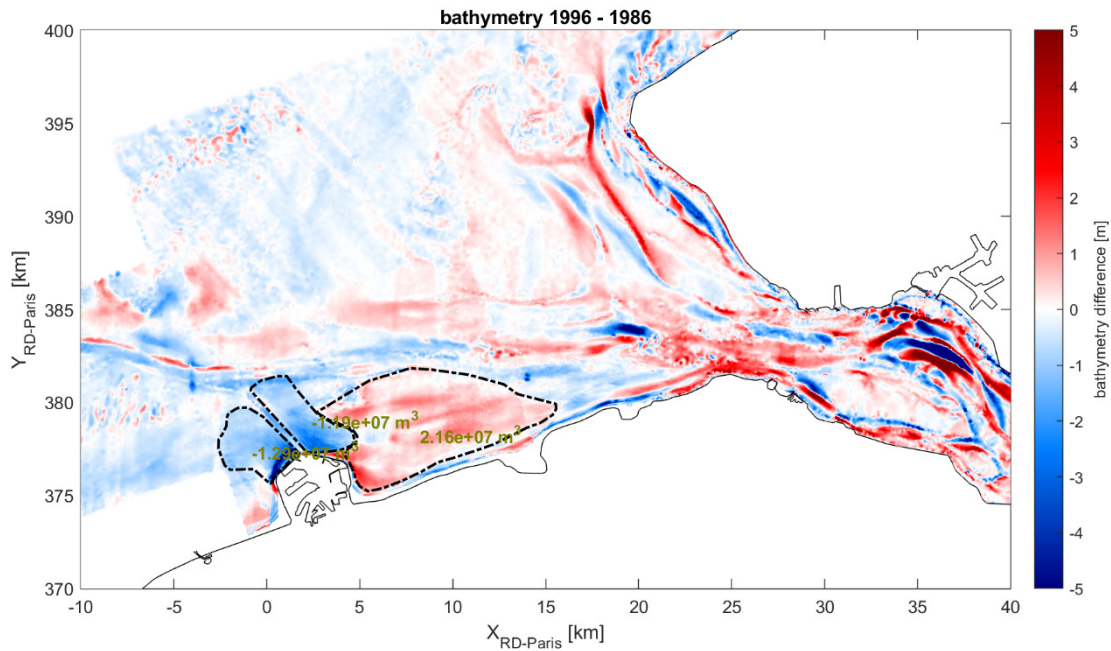
Figure 190 – Bottom level difference between historical bathymetries 1986 & 1996. Measured volume change in erosive and accretive polygons around port of Zeebrugge is also depicted.

In Figure 191, the bed level change and the volume changes at the selected polygons around Zeebrugge port are presented for a simulation with varying erodible bed thickness – based on the map of Figure 188 – (top panel) and a simulation with varying D_{50} of sand (see Figure 187) and varying erodible bed thickness (bottom panel). The rest settings for both simulations are identical to the reference run. Obviously, for the case of limited erodible thickness, the results are very similar to those of the reference run. Noticeable reduction (≈20%) can be found in the eroded volume at the west-breakwater polygon, bringing the prediction closer to the measured value. A small reduction of the accreted volume at Paardenmarkt is also observed.

Figure 191 – Bed level change [m] and volume change [m3] in selected polygons around the port of Zeebrugge, obtained after 10 years; (top) uniform D50 (= 200 µm) + varying erodible bed thickness, (bottom) varying D50 + varying erodible bed thickness.

Larger differences are observed when comparing the bottom panel of Figure 191 (varying D_{50} + varying erodible bed thickness) to the reference run. These differences are mainly located at the area of Paardenmarkt, where the predicted volume change is now reduced by about 30% also meaning an underestimation of the same order of magnitude when compared to the measured one. This behavior, apart from the reduced sedimentation at Bay of Heist (which is desired), is mainly attributed to the local variation of the d_{50} (clusters of coarse sediment), southeast of the Scheur channel, which enhances the erosion at the northeast boundary of the Paardenmarkt polygon (which is unwanted).

Under the assumption that the clusters of coarser sediment appeared a long time after the port expansion, these are replaced by fine sediment and then the simulation (gai082C06Z4) is repeated. As shown in Figure 193, the volume change in the polygon of Paardenmarkt is now substantially increased, reaching a value very close to the measured one. Other positive effects of incorporating varying D_{50} is the enhancement of the sedimentation pattern at Paardenmarkt, and the reduction of the sed/ero magnitude at the mouth of the Western Scheldt. Practically no differences are observed at the erosion polygons in front of Zeebrugge, as the D_{50} values are equal to 200 µm.
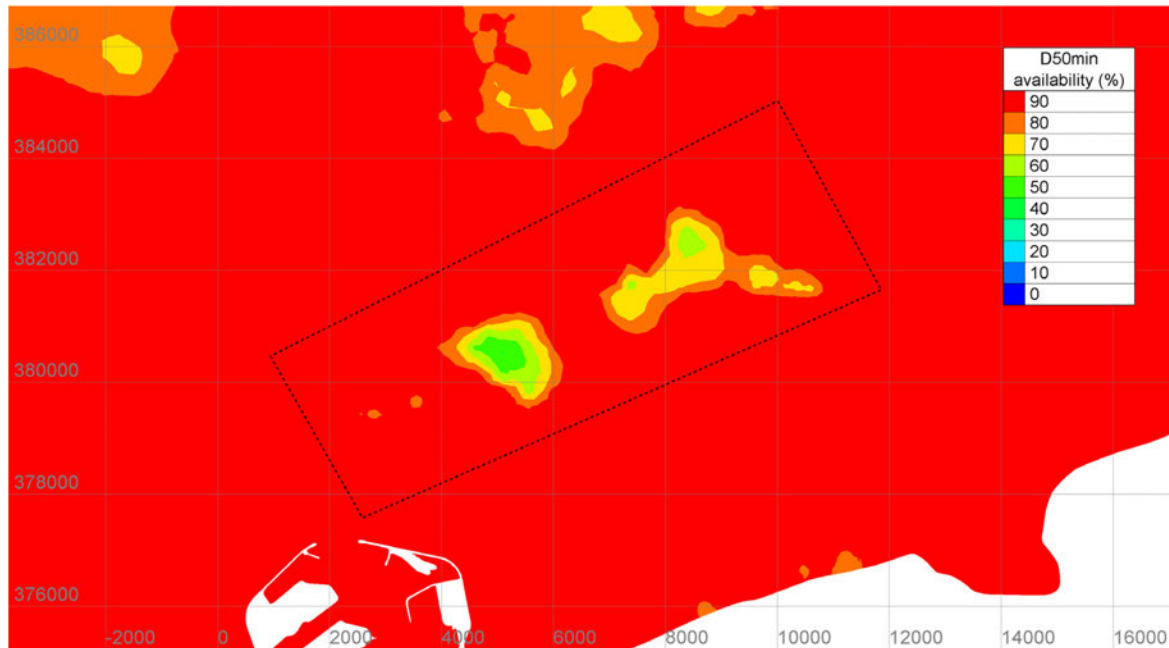
Figure 192 – Percentage of fine sand (dmin = 200 µm) in the sediment mixture of two classes (200 & 500 µm) at the area of Paardenmarkt. The clusters of coarser sediment in the polygon are replaced by fine sediment (d50 = 200 µm).
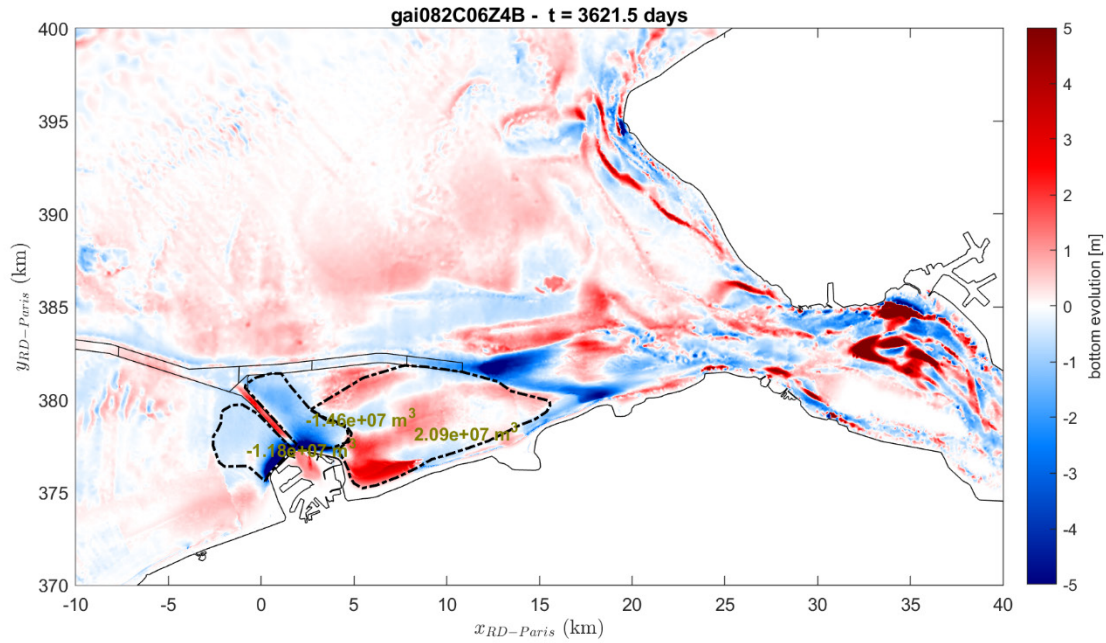
Figure 193 – Bed level change [m] and volume change [m3] in selected polygons around the port of Zeebrugge, obtained after 10 years; after removing the coarse sediment clusters at the north of Paardenmarkt.

Dredging

Coupling of Nestor with mud transport is not yet realized in GAIA.

Wave + current induced transport

Next, the hindcast exercise is repeated taking into account wave- and current-induced sediment transport, by activating the TOMAWAC module. The settings of the calibrated TOMAWAC module, presented in chapter 4 of progress report by Kolokythas *et al.* (2018), are utilized in this exercise. Additionally, the TEL2TOM functionality is employed in order to efficiently reduce the computational time. The grid description is given in section 6.3 of progress report by Kolokythas *et al.* (2019b).

For the wave and wind forcing of the model, the simplified conditions that result from the wave/wind input reduction of the one year data (2014-2015), presented in chapter 2 of progress report by Kolokythas *et al.* (2019b), are utilized. The aforementioned conditions, which are presented in 4.4.3, are imposed in a 'structured' formation, constructed in a realistic manner, taking into to account the seasonality of the wave conditions (calm conditions in summer – stormy conditions in winter).

Table 42 – Wave and wind conditions after input reduction of one-year data (June 2014- June 2015) used for the schematized forcing of the Scaldis-Coast model. H_{m0}: significant wave height; T_p: peak wave period; Dir: wave/wind direction (Nautical); U_{wi}: wind speed.

Condition No.	H_{m0} [m]	T_p [s]	Dir [°]	U_{wi} [m/s]	Occur. Ratio [%]
1	0.67	5.65	26	5.37	29.66
2	0.84	5.01	312	6.54	18.69
3	1.32	6.02	24	8.10	7.91
4	2.05	5.99	306	12.25	3.24
5	3.26	7.13	307	16.83	1.08
6	3.09	7.38	225	17.07	1.19
7	2.87	7.14	238	16.76	1.40
8	2.28	6.62	224	14.07	2.41
9	2.16	7.03	21	11.46	2.38
10	2.04	6.31	238	13.57	3.15
11	1.03	4.48	213	8.89	13.53
12	0.95	4.77	241	8.15	15.36

In Figure 194, the bed level change and the volume changes at the selected polygons around Zeebrugge port are presented for the wave + current simulation with varying D_{50} and varying erodible bed thickness, for direct comparison against gai082C06Z4B run (see Figure 193,) which does not include the effect of waves. In general, the wave action enhances the sediment transport at the shallower areas (close to the beach) compared to the pure current case. With regard to the shape of the sed/ero patterns, noticeable differences can be spotted along the Knokke-Heist beach, where material is now accumulated in a relatively narrower zone close tote beach (Bay of Heist), while erosion and sedimentation at Knokke and at the Zwin, respectively, are now more pronounced and look more similar to the measure ones (see Figure 190). The predicted volume change at the Paardenmarkt is decreased compared to the pure current case. It is conjectured that the action of the waves coming from the north, contributes in the deceleration of the eastward movement of the sedimentation pattern at the Paardenmarkt area. In the meantime, wave action "pushes" more intensively the transferred material from the port breakwaters towards the beach (that's why the accretion zone at Bay of Heist becomes narrower). The erosion volume at the west breakwater is now found relatively increased, while the one of the eastern breakwater remains more or less stable. Other differences at the sed/ero patterns can be found at the area of Westkapelle, where the sedimentation stripes are now more intense, while smaller differences are observed at the area of Vlakte van de Raan, where the patterns turn to be smoother compared to the pure current run.
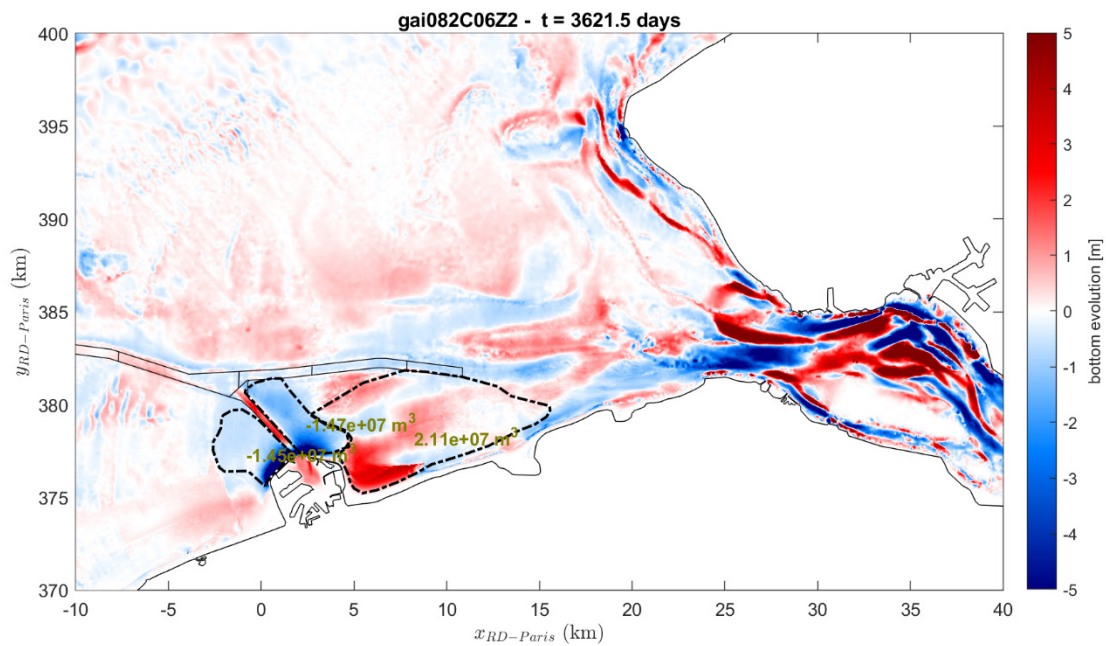
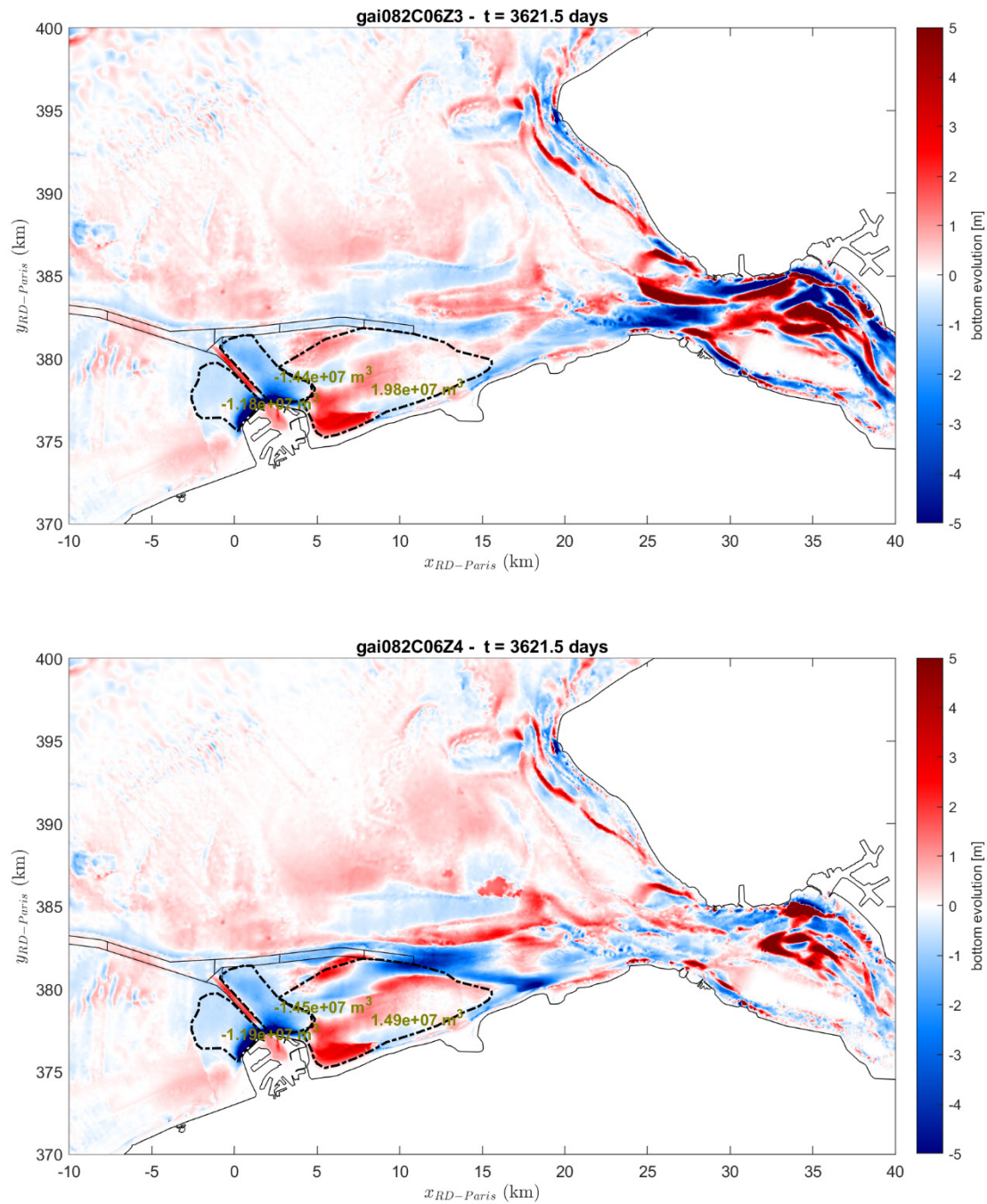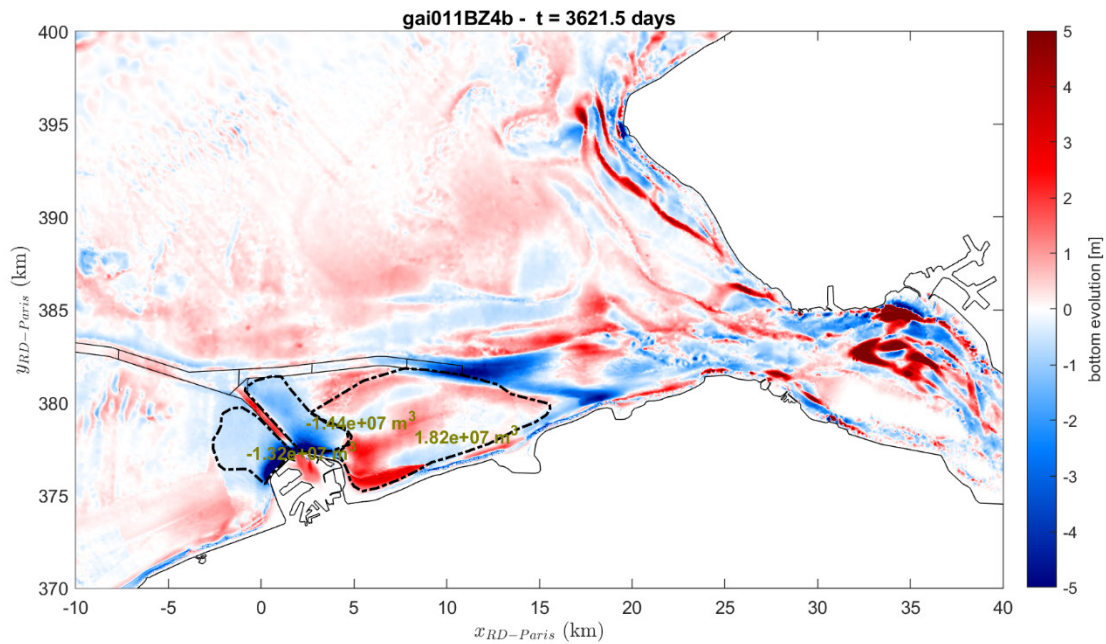Figure 194 – Bed level change [m] and volume change [m3] in selected polygons around the port of Zeebrugge, obtained after 10 years; for the wave + current case, with varying D50 and varying erodible bed thickness.

7.2.5   Conclusions

The default formulation for mixed-sediment transport in GAIA cannot be directly implemented for the purposes of Scaldis-Coast model. This is because the erosion rate of mud increases unnaturally within the mixture regime (mud ratio between 50% to 30%) as the mud content decreases, triggering exaggerated erosion/suspension of the mud fraction and consequently abrupt transportation of the total mud fraction from erosive to accretive areas. In this memo, a first attempt to improve this unnatural behavior, without completely changing the formulation of GAIA for mixed erosion rates, is presented. The main idea was to implement calibration coefficients on the existing model mainly based on trial and error method.

The effect of the modifications in the mixed sediment formulation of GAIA is investigated through the well-known 10-year hindcast exercise (1986-1996), which focuses on the morphodynamic changes of the western Belgian coast after the expansion of port of Zeebrugge. Comparison between modelled and the measured sedimentation-erosion patterns at the area between Zeebrugge port and the Western Scheldt mouth and also volume changes at the area in the vicinity of the port verify the good performance of the calibrated model. The main improvement in the model's performance by considering mixed sediment transport, is the capturing of sediment accretion at the Bay of Heist and also the generally improved representation of sedimentation and erosion patterns at Paardenmarkt and in front of the port, respectively.

8 Scaldis-CoastScaldis-CoastScaldis-CoastConclusions and Recommendations

8.1 Advised model settings and performance

The tables below give an overview of the model settings that have been demonstrated to have the best overall performance. The Bijker formulation in combination with the proper calibration factor and grain size distribution is a good compromise to represent both the tidally driven offshore morphologic dynamics and the wave driven nearshore dynamics. It was found that for the offshore dynamics the Engelund & Hansen formulation also performs well, although Engelund & Hansen does not take wave effects on the sediment transport into account. For the beach dynamics Van Rijn 2007 perform comparable to Bijker, but the tidally dynamics in the offshore are considered the be to active.

Thanks to the new development of the TEL2TOM coupling module, a coarser mesh for the wave transformation model can be applied without compromising on the accuracy. This can reduce the computational time by a factor two. With a morphological amplification factor ten (MORFAC = 10), a ten years morphodynamic simulation, i.e. one-year hydrodynamics based on the representative tide and the representative year for wind and wave forcing, takes around 3 to 3.5 days of computational time on 100 computation cores. The computation time and parallelization efficiency depends on the hardware architecture and compiler, but in general it was found that parallelization scales well up to 100 cores.

Recently, a half year time series of representative wave and wind conditions has been defined as well. Although in the report for most test cases morfac 10 was selected, latest results reveal that with the half year representative wave and wind time series, a morfac 20 is verified. This reduces the computational cost with another factor 2 which makes the model super-efficient with respect to computational cost for long term morphodynamics.

Table 43 – Setting of the Hydrodynamic model

Physical processes	Bottom shear stress, Coriolis, tide, wind and wave-current interactions
Boundary conditions	Representative tide: RT137
Bottom roughness	Manning (Variable roughness coefficient between 0.014 and 0.04)
Wind	Off
Turbulence	Smagorinsky (C_s=0.1)
Advection scheme	SUPG(0;1)
Free surface gradient compatibility	0.9
HD-time	1 year (705 tidal cycles + 2 days of warmup period)
Timestep	10 s
Matrix solver	GMRES
Mass lumping H	1.0
Wetting-drying scheme	1

Table 44 – Settings of the wave model

Physical processes	Wave propagation, current-wave interaction (2-way coupling), refraction, wind induced wave setup, dissipation by whitecapping, bottom shear and depth induced wave breaking, non)linear wave-interactions
Non-linear frequency transfers	Quadruplets (DIA)
Linear wave growth	Yann
Whitecapping	Van de Westhuysen
Depth-induced wave breaking	Battjes-Jansen
Number of directions	36 (Dθ=10 degrees)
Number of frequencies	24 (min =0.05Hz)
Timestep	120 s
Coupling	TEL2TOM (different grid resolutions for wave and hydrodynamic model. To speed up the model, the resolution of the wave model is about the half of the HD model, parts of the Western and Eastern Scheldt are removed from the wave model)
Current-wave interaction	Transport in frequency domain ignored
Boundary conditions	Westhinder measured times series (*Meetnet Vlaamse Banken*) For morphological long term modelling with MORFAC 20: Half year representative period of wave and wind conditions: 7/11/2013 – 6/5/2020

Table 45 – Setting of the sediment transport model

Sediment transport equation	Bijker (calibration parameter b=2)
D50	Spatially varying (200 to 500 µm)
Morfac	20
Morphologic time	10 years (353 tidal cycles, morfac 20)
Slope effect	Koch en Flokstra (β=1,3)
Secondary Flows	Off
Dredging and dumping	Nestor: dredging activity on maintaining critical depths Pas van het Zand, Scheur, Wielingen and Western Scheldt navigation channel

8.2   Assumptions and limitations of the model

8.2.1   Hydrodynamic model

The hydrodynamic model is 2D. It is expected that in the coastal zone effects of 3D are limited, except for cross-shore processes which are not considered yet in the current model suite. For the long-term estimation of the coastal resilience against climate change, it is expected that cross shore processes play an important role. Also, on the short term these processes play a role, e.g. beach recovery after a severe storm. It is known that these processes are difficult to model in large scale coastal models. Within the CREST project, strong efforts have been done in building a 3D highly accurate CFD model to investigate in detail the complex physics that are driving these cross-shore transport mechanisms. It is expected that from these so-called *numerical wave flume* experiments new parametrizations will be derived that can be implemented in large scale coastal models.

Salinity is not considered. It is expected that salinity gradients are low in the coastal zone and do not play an important role.

8.2.2   Wave model

There is no diffraction in the model. Diffraction is important for local effects and inside ports. Wave-driven currents are only driven by radiation stresses. Stokes drift is not modelled. This means that the model misses cross-shore processes. The implementation of cross-shore processes is currently under investigation. The main transport process along the Belgian coast is the longshore transport from west to east. However, cross-shore processes do play a role during storm events and the long-term natural feeding of the beach during periods of mild wave conditions. Notice however, that the latter are difficult to calibrate because lack of direct and accurate measurements of these processes in situ.

8.2.3   Morphology

Only sand fractions are modelled. No sand-mud interaction or less erosive clay layers are modelled. Mainly in the vicinity of Zeebrugge clay layers are present (Holocene Clay). The extension of the model to sand-mud is under investigation.

As mentioned before, at the moment the model is missing cross-shore processes, i.e. Stokes drift and cross-shore transport due to wave asymmetry.

Only sediment transport in the water is modelled, no aeolian transport nor dune formation is modelled.

The model tends to underestimate the dredging volumes in the main channels especially with Engelund & Hansen and Bijker transport formulas. Soulsby – Van Rijn and Van Rijn 2007 give better dredging volumes, however their overall behaviour with respect to tidally driven bed dynamics is considered as overactive. At the moment is unclear why Bijker tends to underestimate dredging volumes. The modelled dredging activities should be treated cautiously.

8.3   Further developments and improvements

A first attempt on implementing cross-shore processes has been taken. The GAIA module of the TELEMAC-MASCARET software suite has been extended with formulations for Stokes drift and wave asymmetry. It requires further validation and calibration before it can be reliable applied in large scale coastal models like the Scaldis-Coast model.

The formulations for Stokes drift and wave asymmetry induced sediment transport are based on suspended sediment formulations, using a modified velocity field in the advection diffusion equation to parametrize this effects. This implies that the overall sediment transport must be calculated using a an advection-diffusion approach, which in TELEMAC is currently only used for calculating the suspended load, and not for the bed load. Therefore, implementing the cross-shore processes will require extra calibration and validation not only in the nearshore, but for the whole domain.

Also, on the combined modelling of sand-mud mixtures, the first steps have been taken. However, so far, no reliable parameter setting and formulation applicable for the Scaldis-Coast model was defined. The Zeebrugge environment is characterised by high mud contents in the bottom. The mud content might have an effect on the sand transport as well, although it is not yet fully understood. Flanders Hydraulic Research is involved in the Dutch MUSA[2] project which is a consortium of different research institutes, universities and private partners doing fundamental research in the sand-mud interaction and morphology.

---

[2] Joined Reseach Project within the framework of the TKI-program (*Topconsortium voor Kennis en Inovatie*)

References

Bailard, J.A. (1981). An energetics total load sediment transport model for a plane sloping beach. *J. Geophys. Res. Ocean. 86*(*C11*): 10938--10954

Bijker, E.W. (1992). Mechanics of sediment transport by the combination of waves and current. *Des. Reliab. Coast. Struct. 23rd Int. Conf. Coast. Eng.*: 147–174. doi:uuid:4574aaa1-9246-4981-8305-c3a932e4ce03

Bockelmann, F.-D.; Puls, W.; Kleeberg, U.; Müller, D.; Emeis, K.-C. (2018). Mapping mud content and median grain-size of North Sea sediments – A geostatistical approach. *Mar. Geol. 397*: 60–71. doi:https://doi.org/10.1016/j.margeo.2017.11.003

Breugem, W.A.; Fonias, E.; Wang, L.; Bolle, A.; Kolokythas, G.; De Maerschalck, B. (2018). Neumann boundaries in TELEMAC 2D and their application to wave current interaction., *in*: (2018). *XXVth TELEMAC-MASCARET User Conference (in publication)*: Norwich (UK)

Breugem, W.A.; Fonias, E.; Wang, L.; Bolle, A.; Kolokythas, G.; De Maerschalck, B. (2019). TEL2TOM: coupling TELEMAC2D and TOMAWAC on arbitrary meshes, *in*: (2019). *XXVIth Telemac-Mascaret User Conference, 15-17 October, Toulouse: proceedings*

Chu, K.; Vanlede, J.; Decrop, B.; Mostaert, F. (2020). Validation of North Sea models: sub report 1. Validation and sensitivity analysis. Version 3.. *FHR reports*, 19_058_1. Flanders Hydraulics Research: Antwerp

Dam, G. (2012). Update niet erodeerbare lagen kartering Westerschelde [Onderwerp]

Dan, S.; Levy, Y.; Vereecken, H.; Verwaest, T.; Mostaert, F. (2017). Measuring campaigns of hydrodynamics and sand dynamics in Blankenberge: sub report 4. Data report 2012 and 2013. Version 2.. *FHR reports*, 00_064_3. Flanders Hydraulics Research: Antwerp. Available at: http://documentatiecentrum.watlab.be/owa/imis.php?module=ref&refid=285823

De Maerschalck, B.; Verwilligen, J.; Plancke, Y.; Verwaest, T.; Mostaert, F. (2017). Kabeltracé Borssele: advies kruising vaarwegen. Versie 5.0. *WL Rapporten*, 16_121_1. Waterbouwkundig Laboratorium: Antwerpen

Dujardin, A.; Van den Eynde, D.; Vanlede, J.; Ozer, J.; Delgado, R.; Mostaert, F. (2010). BOREAS - Belgian Ocean Energy Assessment: A comparison of numerical tidal models of the Belgian part of the North Sea. *WL Rapporten*, 814_03. Flanders Hydraulics Research: Antwerp

Engelund, F.; Hansen, E. (1967). A monograph on sediment transport in alluvial streams. TEKNISKFORLAG Skelbrekgade 4 Copenhagen V, Denmark: Technical University of Denmark 0stervoldgade 10, Copenhagen K.

Flather, R.A. (1976). Results from a storm surge prediction model of the north-west European continental shelf for April, November and December, 1973. *24*. Institute of Oceanographic Sciences

Foster, D.L.; Bowen, A.J.; Holman, R.A.; Natoo, P. (2006). Field evidence of pressure gradient induced incipient motion. *J. Geophys. Res. 111*(*C05004*)

Groeneweg, J. (1999). Wave-current interactions in a generalized Lagrangian mean formulation. Delft University of Technology

Koch, F.G.; Flokstra, C. (1981). Bed level computations for curved alluvial channels, *in*: (1981). *XIXth Congress of the International Association for Hydraulic Research*: New Delhi, India

Kolokythas, G.; De Maerschalck, B.; Wang, L.; Fonias, E.; Breugem, W.A. (2019). Scaldis-Coast: An Integrated Numerical Model for the Simulation of the Belgian Coast Morphodynamics, *in*: (2019). *Geophysical Research Abstracts (Vol. 21)*

Kolokythas, G.; Fonias, S.; Wang, L.; De Maerschalck, B.; Vanlede, J.; Mostaert, F. (2020). Modelling Belgian

Coastal zone and Scheldt mouth area: Sub report 11: Progress report 6 – Model developments: Grid optimization, Morphodynamics, Dredging/dumping subroutines, Wave conditions

Kolokythas, G.K.; Fonias, S.; Wang, L.; De Maerschalck, B.; Vanlede, J.; Mostaert, F. (2018a). Modelling Belgian Coastal zone and Scheldt mouth area: sub report 7. Progress report 3: Model developments: hydrodynamics, waves and idealized modelling. Version 4.. *FHR reports*, 15_068_7. Flanders Hydraulics Research: Antwerp

Kolokythas, G.K.; Fonias, S.; Wang, L.; De Maerschalck, B.; Vanlede, J.; Mostaert, F. (2019). Modelling Belgian Coastal zone and Scheldt mouth area: sub report 8. Progress report 4: Model developments: Waves, idealized modelling and morphodynamics. *FHR reports, 15_068_8*

Kolokythas, G.K.; Fonias, S.; Wang, L.; De Maerschalck, B.; Vanlede, J.; Mostaert, F. (2019). Modelling Belgian Coastal zone and Scheldt mouth area: sub report 9. Progress report 5: Model developments: Waves, idealized modelling and morphodynamics. *FHR reports, 15_068_9*

Kolokythas, G.K.; Wang, L.; Fonias, S.; De Maerschalck, B.; Vanlede, J.; Mostaert, F. (2018b). Modelling Belgian Coastal zone and Scheldt mouth area: sub report 6 – Progress report 2. Evaluation of numerical modelling tools and model developments. Version 3.. *FHR reports*, 15_068_6. Flanders Hydraulics Research: Antwerp

Latteux, B. (1995). Techniques for long-term morphological simulation under tidal action. *Mar. Geol. 126*(*1–4*): 129–141. doi:10.1016/0025-3227(95)00069-B

Longuet-Higgins, M.S. (1953). Mass transport in water waves. *Philos. Trans. R. Soc. Ser. A 245*(*3*): 535–581. doi:https://doi.org/10.1098/rsta.1953.0006

Maximova, T.; Vanlede, J.; Verwaest, T.; Mostaert, F. (2016). Vervolgonderzoek bevaarbaarheid Bovenzeeschelde: subreport 4 – Modelling Train CSM – ZUNO: validation 2013. *WL Rapporten*, 13_131. Waterbouwkundig Laboratorium: Antwerp

Montreuil, A.-L.; Dan, S.; Vereecken, H, B.; De Backer, E.; Verzhbitskiy, L.; Claeys, S.; Deschamps, M.; Mostaert, F. (2015). Alternative measures for beach nourishment maintenance: monitoring of a pilot experiment at Mariakerke: Measuring campaign October November 2015.: Anterp

Saberi, O.; Zenz, G. (2016). Numerical Investigation on 1D and 2D Embankment Dams Failure Due to Overtopping Flow. *Int. J. Hydraul. Eng. 5*(*1*): 9--18

Schramkowski, G.; Heredia Gomez, M.; Rauwoens, P.; van Oyen, T.; Monbaliu, J.; Komijani, H.; Breugem, A.; Delecluyse, K.; Chu, K.; Lee, B.J.; Vanlede, J.; Luyten, P.; Baetens, K.; Verwaest, T.; Mostaert, F. (2017). COHERENS: validation report. Version 3.. *FHR reports*, 00_147_1. Flanders Hydraulics: Antwerp. Available at: http://documentatiecentrum.watlab.be/owa/imis.php?module=ref&refid=289700

Soulsby, R. (1997). Dynamics of marine sands. H.R. Wallingford

Tassi, P.; Villaret, C. (2014). Sisyphe v6. 3 user's manual. *Rech. développement, Électricité Fr. Chatou*

Teurlincx, R., Van der Biest, K., Reyns, J., Verwaest, T., Mostaert, F., (2009). Haven van Blankenberge – Verminderen van de aanzanding van de havengeul en het voorplein: Eindrapport. Versie 2_0. WL Rapporten, 643_12. Waterbouwkundig Laboratorium: Antwerpen, België

Van den Eynde, D.; Kerckhof, F.; Francken, F.; Haelters, J.; Lauwaert, B. (2007). Ontwikkeling van de zandbank ter hoogte van Heist: Eindrapport: Brussels

Van Lancker, V.; Du Four, I.; Verfaillie, E.; Deleu, S.; Schelfaut, K.; Fettweis, M.; Van den Eynde, D.; Francken, F.; Monbaliu, J.; Giardino, A.; Portilla, J.; Lanckneus, J.; Moerkerke, G.; Degraer, S. (2007). Management, research and budgetting of aggregates in shelf seas related to end-users (Marebasse). *Final Report.*

van Rijn, L.; Walstra, D.J..; Grasmeijer, B.; Sutherland, J.; Pan, S.; Sierra, J.. (2003). The predictability of cross-shore bed evolution of sandy beaches at the time scale of storms and seasons using process-based Profile models. *Coast. Eng. 47*(*3*): 295–327. doi:10.1016/S0378-3839(02)00120-5

van Rijn, L.; Walstra, D. (2003). Modelling of sand transport in Delft3D

van Rijn, L.C.; Ruessink, B.G.; Grasmeijer, B.; van der Werf, J.; Ribberink, J. (2007). Wave-related transport and nearshore morphology, *in*: (2007). *Coastal Sediments '07*. pp.1--14

Vroom, J.; Schijverhof, R. (2015). Overzicht van menselijke ingrepen in de Westerschelde en haar mondingsgebied in de periode 1985-2014, 1210301-1-NaN-5. *1210301-001-ZKS-0005*. Deltares: Delft, The Netherlands

Vroom, J.; van Maren, B.; van der Werf, J.; van Rooijen, A. (2016). Zand-slib modellering voor het mondingsgebied van het Schelde-estuarium. Concept.

Walstra, D.J.R.; Reniers, A.J.H.M.; Ranasinghe, R.; Roelvink, J.A.; Ruessink, B.G. (2012). On bar growth and decay during interannual net offshore migration. *Coast. Eng. 60*(*1*): 190–200. doi:10.1016/j.coastaleng.2011.10.002

Wang, L.; Zimmermann, N.; Trouw, K.; De Maerschalck, B.; Delgado, R.; Verwaest, T.; Mostaert, F. (2015). Scientific support regarding hydrodynamics and sand transport in the coastal zone: calibration of a Long term morphological model of the Belgian shelf. *WL Rapporten*, 12_107. Flanders Hydraulics Research: Antwerp

Wilson, B.W. (1965). Numerical prediction of ocean waves in the North Atlantic for December, 1959. *Dtsch. Hydrogr. Zeitschrift 18*(*3*): 114–130

Wilson, R.; Heath, M.; Speirs, D.; Sabatino, A. (2017). Data for: 'A synthetic map of the northwest European Shelf sedimentary environment for applications in marine science'. doi:10.15129/1e27b806-1eae-494d-83b5-a5f4792c46fc

Zimmermann, N.; Wang, L.; Mathys, M.; Trouw, K.; Delgado, R.; Toro, F.; Verwaest, T.; Mostaert, F. (2012). Scientific support regarding hydrodynamics and sand transport in the coastal zone. Calibration of the Oostende-Knokke hydrodynamic and sediment transport model (OKNO), WL2012R744_30_17rev1_0: Antwerp, Belgium. 87 pp.

Appendix A.   Paper presented at the TELEMAC User Conference 2018 (TUC 2018)

Neumann boundaries in TELEMAC 2D and their application to wave-current interaction

WA Breugem[1], E Fonias[1,2], L Wang[1,2], A Bolle[1]

[1]International Marine and Dredging Consultants
Antwerp, Belgium
abr@imdc.be

G Kolokythas[2], B De Maerschalck[2]

[2]Flanders Hydraulics Research
Antwerp, Belgium

Abstract— In this paper, an implementation of the Neumann boundary conditions is presented in TELEMAC 2D. The application of these boundary conditions is shown in idealized test cases, in which a schematic representation of a coastal area is simulated. Examples are presented for cases with tidal flow, a wave-driven current (in which TELEMAC-2D is coupled to TOMAWAC), as well as for a combination of wave-driven currents and tidal flow.

Introduction

In the coastal zone, the flow patterns are determined by both tides and waves, leading to a complex interaction. In order to simulate these flow patterns well, Roelvink and Walstra [1] showed that it is advantageous to use the so-called Neumann boundary conditions for the lateral model boundaries. In these Neumann boundaries, the water level gradients are prescribed, rather than water levels or velocities, such that the flow can develop freely at the lateral boundaries and in this way, the flow parallel to the coast is not disturbed by the lateral boundaries.

In TELEMAC 2D, the main open boundary types are water level boundaries and velocity boundaries. Prescribing water level boundaries for the lateral boundary may lead to instabilities. Velocity boundaries can in principle be used. However, it can be difficult to know the velocities at the boundary in advance, because they are sensitive to the water depth at each location of the boundary. Further, in case of wave-current interaction, the velocity at the lateral boundary may be difficult to know as it also depends on the wave conditions. Therefore, it is advantageous to prescribe water level gradients (i.e. Neumann boundaries), because these are more easy to know in advance, they are almost constant over the boundary (and depend little on the water depth) and can incorporate the effect of wave conditions.

Therefore, an implementation of the Neumann boundary conditions is presented in this paper for TELEMAC 2D. The application of these boundary conditions is shown in idealized test cases, in which a schematic representation of a coastal area is simulated. Examples are presented for cases with tidal flow, a wave-driven current (in which TELEMAC-2D is coupled to TOMAWAC), as well as for combinations of wave-driven currents and tides.

Neumann boundary condition

Strategy

In order to use Neumann boundary conditions, the following strategy is used:

1. Water level gradient conditions are prescribed perpendicular to the boundary.
2. The water level gradients are converted to velocities normal at the boundaries.
3. In case the calculated velocities describe inflow, these velocities are applied at the boundary. Otherwise, an outflow boundary condition is used.

Derivation of the velocity perpendicular to the boundary

In order to derive the Neumann boundary condition, the depth averaged momentum equations are first written in a coordinate system aligned with the boundary (ζ,ξ), with ζ the direction perpendicular to the boundary (positive outward) and ξ the direction parallel to the boundary. Perpendicular to the boundary this gives:

$$\frac{\partial u_\zeta}{\partial t} + u_\zeta \frac{\partial u_\zeta}{\partial \zeta} + u_\xi \frac{\partial u_\xi}{\partial \zeta} = -g \frac{\partial \eta}{\partial \zeta} - \frac{c_f |u|}{H} u_\zeta + F_\zeta^{ext} + D \tag{1}$$

Here, u_ζ and u_ξ are the velocity components, perpendicular and parallel to the boundary, g is the acceleration due to gravity, η is the water level elevation, H the water depth, c_f a friction coefficient, F^{ext} the external forces (Coriolis force, atmospheric pressure gradient, waves and wind), and D is the diffusion term. Neglecting the advection and diffusion terms as the boundary and noting that the water level gradient is prescribed, the equation reduces to and ordinary differential equation:

$$\frac{du_\zeta}{dt} = -g \left(\frac{\partial \eta}{\partial \zeta}\right)^{ext} - \frac{c_f |u|}{H} u_\zeta + F_\zeta^{ext} \tag{2}$$

This equation is discretised with the semi-implicit theta scheme giving:

$$\frac{u_{n+1} - u_n}{\Delta t} = -g \left(\frac{\partial \eta}{\partial \zeta}\right)^{ext} - \frac{c_f |u|}{H} (\theta u_{n+1} + (1 - \theta)u_n) + F_\zeta^{ext} \tag{3}$$

, leading to:

$$u_{n+1} = \frac{1 + (1 - \theta)\frac{c_f |u|}{H}\Delta T}{1 + \theta \frac{c_f |u|}{H}\Delta T} u^n + \frac{\Delta T}{\left(1 + \theta \frac{c_f |u|}{H}\Delta T\right)} \left(F_\zeta^{ext} - g \left(\frac{\partial \eta}{\partial \zeta}\right)^{ext} \right) \tag{4}$$

In order to obtain a more stable behaviour during drying and flooding at the boundary (such may occur at a beach), thesecond term on the right hand side of equation 4 is multiplied with a drying flooding factor α, which is defined as:

$$\alpha = \max \left(\min \left(\frac{H}{H_{min}}, 1 \right), 0 \right) \tag{5}$$

, with H_{min} a threshold water depth, currently set to 0.5 m.

Velocity parallel to the boundary

A similar equation as equation 4 can be derived for the velocities parallel to the boundary. However, the water level gradient parallel to the boundary is not prescribed. Test were performed using this equation by estimating the water level gradient from the existing free surface gradient. However, these tests showed that the model became unstable. Hence the flow parallel to the boundary is currently neglected.

Implementation

The Neumann Boundary condition implementation consists of three parts:

- Routines to read the prescribed Neumann boundaries (`dedx.f` as well as changes in `bord.f`).
- A new subroutine (`neumann.f`), in which the velocities at the lateral boundary are calculated, which is called in `propag.f`, reusing the forces and bed friction terms that have already been calculated in this routine.
- A new subroutine `corr_outflow.f` called by `propag.f`, which is used in order to determine whether the flow at the boundary consist of inflow or outflow. In case of outflow the internal arrays LIMPRO and MASK are changed from a Dirichlet value to a Neumann value.

Parallelization was taken into account in the implementation and all the test described in this paper were performed in parallel.

User manual

In order to use the Neumann boundary conditions the user should set the following steps:

- Specify the boundary conditions for the Neumann boundaries as boundaries with prescribed velocity and free water level (5 6 6) in the CONLIM (`.cli`) file. Note that the implementation assumes smooth changes in the direction of the segments of the Neumann boundary. It is strongly recommended to apply only straight boundaries for the cross shore boundaries. Hence this should be taken into account when generating the mesh of the test case.
- Set the keyword TYPE OF BOUNDARY = 3 for the Neumann boundaries.
- Specify time series of the water level gradients for each Neumann boundary in the liquid boundary file, using the code DEDX followed by the number of the boundary. As an alternative, it is possible to program the routine `dedx.f` in order to provide the water level gradients. When doing so, care must be taken to the sign of the gradients, which is positive outward from the boundary. This means that typically, both cross shore boundaries will have a different sign.
- Additionally, it is needed to specify a water level on the offshore boundary. For typical tidal applications, this boundary need to change in space and time. In the applications, this is performed using some additional routines, which allow the specification of space and time varying water levels and velocities at the boundary using an ASCII input file. However, the authors consider that it is highly needed that space and time varying boundary conditions are standardized within TELEMAC

Application of neumann boundaries in a schematic coastal model

Model setup

The domain for the application of the Neumann boundary condition implementation is an idealized bathymetry of the Belgian coast west of Zeebrugge port (Figure 195).

Figure 195 ─ Bathymetric Section A-A for the schematized coastal model.

The bathymetry of the numerical domain considered has a constant slope of 1:50 from the coastline towards the offshore for a length of 1.1 km and the rest of the offshore bathymetry is flat at -17.33 m. The vertical levels reference is Mean Sea Level (MSL). A detail of the bathymetry formation is given by section A-A at Figure 196.
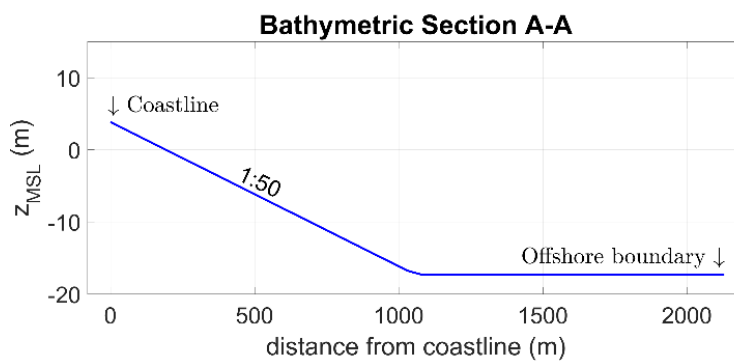

Figure 196 ─ Bathymetric Section A-A for the schematized coastal model

The numerical domain (see Figure 197) is discretized using a channel type mesh in the nearshore region with elements of 60 m long along the coastline and 20 m wide in the other direction. This has been chosen since the flow patterns are not expected to demonstrate variations in the longshore direction. In the rest of the domain (offshore) a triangular mesh is used with minimum element size equal to 60 m and expansion ratio of 7%.
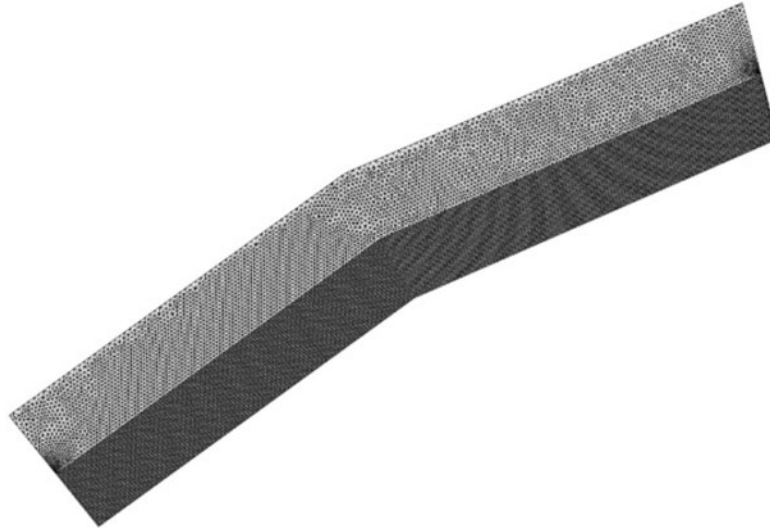

Figure 197 – Computational mesh forthe schematized coastal model

Concerning the boundary conditions of the numerical domain, two separate boundary conditions (.conlim) files are considered, one for TELEMAC 2D and one for TOMAWAC. In both the .conlim files the coastline side is considered as a solid boundary. For TELEMAC 2D the offshore boundary is an open boundary with prescribed water levels, whereas the lateral boundaries are open boundaries with prescribed UV velocities through which the Neumann boundaries will be imposed. For TOMAWAC, the side boundaries and offshore boundaries are considered as open boundaries with prescribed wave heights, wave periods and wave directions, which are then internally converted to a JONSWAP spectrum.

Model settings

Within the aforementioned numerical configuration, flows consisting of tide and/or wave action have been simulated.

The tidal flow is introduced by means of a sinusoidal free surface elevation in time and space using the expression:

$$\eta = \eta_o \, sin\left[2\pi\left(\frac{t}{T} - \frac{x}{L}\right)\right] \tag{6}$$

, where η_o=2 m is the tidal amplitude, T=12 hr is the tidal period and the tidal wavelength is $L = T\sqrt{gH_{max}} = 43200s \cdot \sqrt{9.81\,m/s^2 \cdot 17.33m} = 563241m$. The above free surface expression is applied along the offshore boundary of the numerical domain and the length x is equal to 0 on the east corner of the offshore domain and it increases along the offshore up to the maximum value of 13092 m on the west corner of the offshore domain. Those temporally variable values on the offshore nodes of the domain are included within the FORMATTED DATA FILE 1 required to assign the offshore boundary conditions in TELEMAC 2D.

For the implementation of Neumann boundary conditions a LIQUID BOUNDARIES FILE is required to assign the free surface spatial gradient $\partial\eta/\partial x$ according to:

$$\frac{\partial\eta}{\partial x} = -2\pi\frac{\eta_0}{L}\cos\left[2\pi\left(\frac{t}{T}-\frac{x}{L}\right)\right]\hat{n} \qquad (7)$$

, where $\hat{n}$ is the unit normal vector to the boundary, pointing outside of the numerical domain. This means that for the eastern boundary the value $\partial\eta/\partial x$ is assigned, whereas for the western boundary the value $-\partial\eta/\partial x$ is assigned. Finally, the OPTION FOR LIQUID BOUNDARIES has to be assigned with one value for each of the open boundaries. For the implementation of Neumann boundary conditions the value 3 must be assigned to the corresponding boundaries. For the numerical solution of TELEMAC 2D a constant time step of 10 s is considered.

For TOMAWAC boundary conditions, a constant wave attack from North is considered with a significant wave height H_s=2.0 m and a peak period T_p=6.32 s. TOMAWAC will be coupled with the TELEMAC 2D and a time step of 10 min is considered for the computation of the source terms and the advection timestep is equal to 1 min in TOMAWAC. Non-linear interactions between frequencies, white capping dissipation, depth induced breaking dissipation (NUMBER OF BREAKING TIME STEPS = 20) and triad interactions have also been considered along with stationary wind conditions from north with a velocity equal to 12.24 m/s.

TELEMAC 2D is used independently for the simulation of tidal flow, or coupled with TOMAWAC either for wave-driven currents. The total simulation time for each case was one week.

Results tidal flow

The simulation results for the tidal flow with TELEMAC 2D are presented in Figure 198. This figure shows contour plots of the velocity magnitude along with velocity vector fields throughout the last simulated tidal cycle every 1.5 hr. The velocity vectors are interpolated on a coastline adapted grid for clearer view. It can be observed that throughout the tidal cycle, the lateral boundaries using the newly implemented Neumann boundary conditions allow the tidal velocities to exit and/or enter the numerical domain smoothly. In addition, the formation of the boundary layer along the coastline and its temporal variation throughout the tidal cycle can be observed. At the snapshot at HW+1.5 hr the separation of the nearshore flow from the offshore flow can be observed as well, which is presumably because the change tin the flow velocity occurs later close to the coast, because of its lower water depth. This application indicates that the implementation of the Neumann boundary conditions works smoothly for simulating tidal flow.
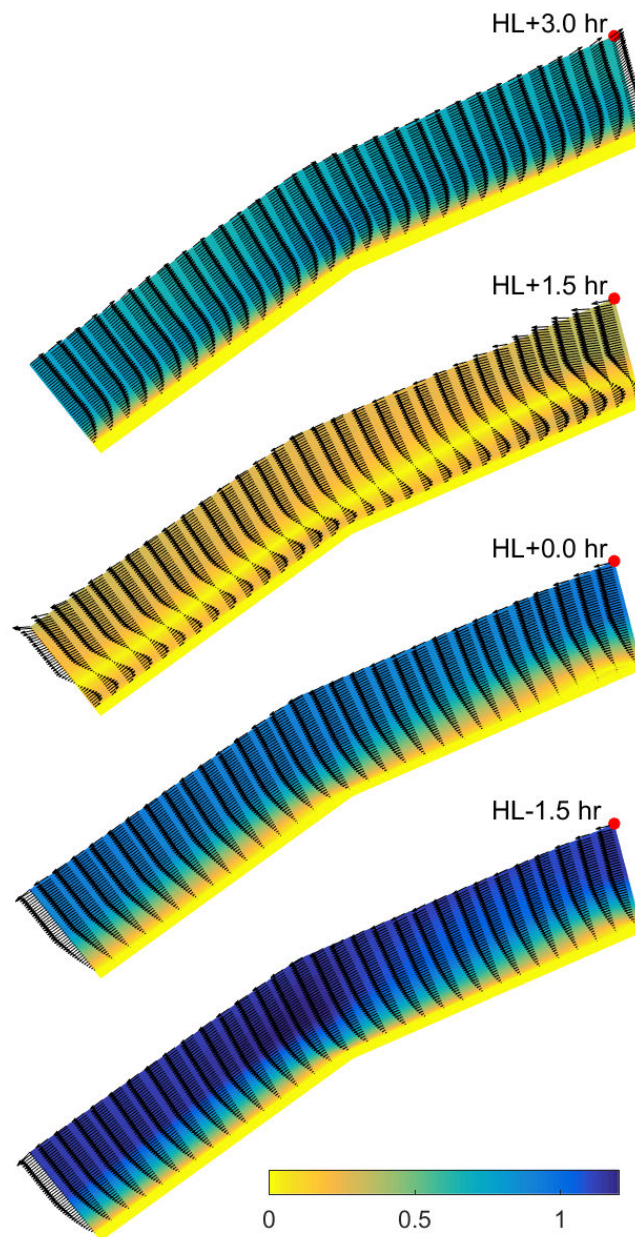

Figure 198 – Contour plots of velocity magnitude and velocity vector fields for tidal flow every 1.5 hours for half the tidal cycle.

Results for wave driven currents

In this section, the results of online coupling of TELEMAC 2D with TOMAWAC considering only wave action as described above, will be presented. The only difference with the above considerations is that the timeseries for Neumann conditions used here in the LIQUID BOUNDARIES FILE is equal to 0. The occurring velocity vectors and velocity magnitude contour plot are shown in Figure 199. The formation of the longshore current can clearly be observed. However, certain velocity disturbances are evident along the lateral boundaries. They are probably due to the applied wave boundary conditions in TOMAWAC. In TELEMAC 2D and TOMAWAC, the model domain must be the same, which means that the Neumann boundaries in TELEMAC 2D are calculated from the prescribed boundaries in TOMAWAC, rather than a calculated wave field. Hence, the changes in the wave field along the boundary (due to shoaling refraction and breaking) are not taken into account. This means that the velocity calculated at the boundary is not corresponding to the velocities in the inner domain, leading to disturbances. There may be another effect caused by neglecting the momentum balance perpendicular to the shore line. Nevertheless, the instabilities at the boundary are not affecting the current and the final solution in the inner part of the numerical domain.
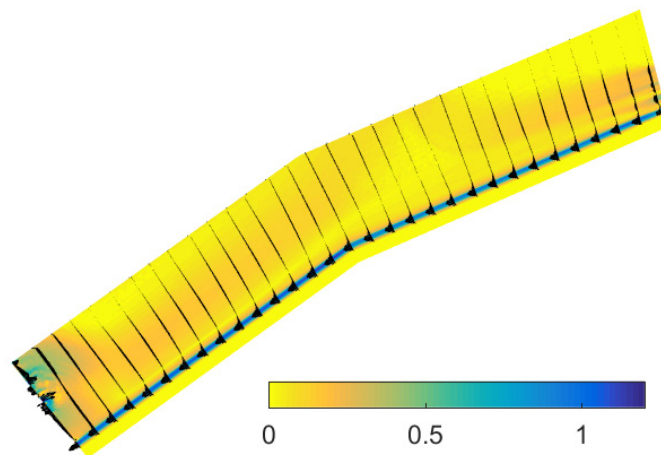

Figure 199 — Contour plots of velocity magnitude and velocity vector fields for wave driven currents.

Results for combined tides and wave driven currents

In the last simulated case, TELEMAC 2D and TOMAWAC are coupled to simulate the combined action of the tide and waves on this idealised coastal area. The values of the Neumann boundary conditions in this test case are determined using Equation 7, and the results are demonstrated in Figure 200. The longshore wave-driven current is evident throughout the whole tidal cycle, whereas a tidal flow pattern can be observed offshore. The flow separation is also observed here at 1.5 hr after high water, but the separation region is pushed more to the nearshore and the flow velocity magnitude in the nearshore zone is clearly reduced in comparison with the tidal case. Finally, slight disturbances in the flow field are observed at the lateral boundaries in the velocity profiles. This is again due to the fact that the wave field from the boundary in TOMAWAC is applied to calculate the velocity at the Neumann boundaries in TELEMAC 2D. However, even in this case, those disturbances do not seem to have a strong effect inner part of the computational domain.
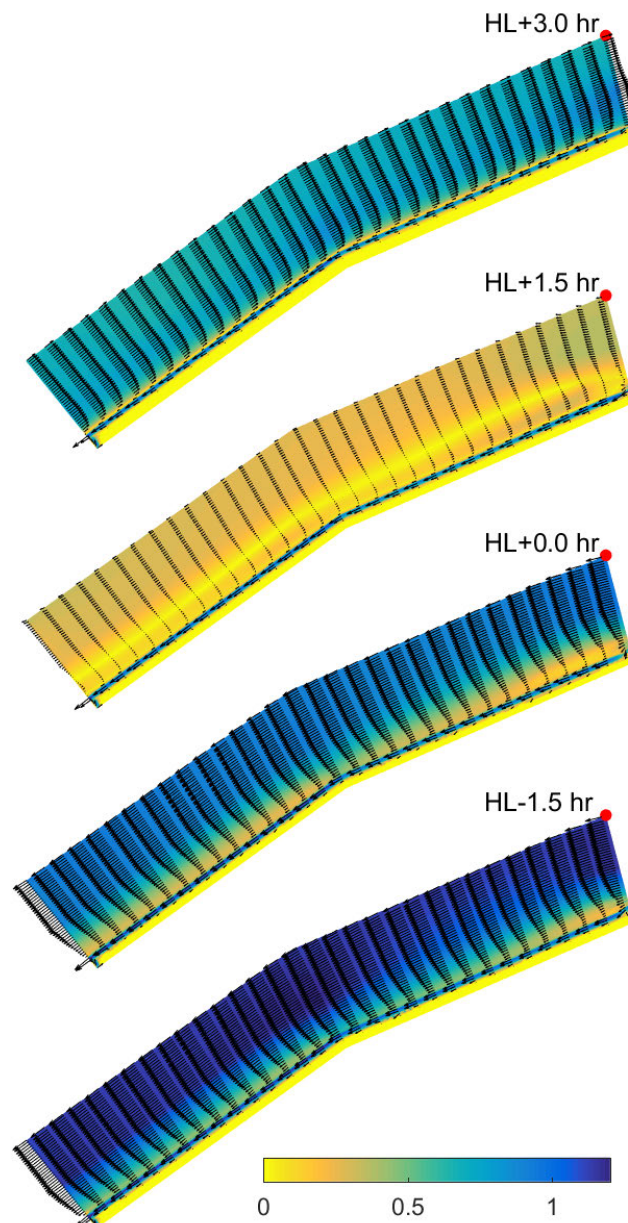

Figure 200 – Contour plots of velocity magnitude and velocity vector fields for combined tidal flow and wave driven currents every 1.5 hour for half a tidal cycle.

Future developments

The Neumann boundary conditions are shown to work well in tidal conditions and to show promising results in test cases where waves and currents are combined. The main deficiency in the latter test cases is because at the boundary, the wave field coming from TOMAWAC consist of a boundary condition, rather than a calculated wave field, leading to an overestimation of the wave field and hence inflow conditions that are too strong. There are two way to solve this:

- Implement Neumann boundaries conditions in TOMAWAC as well.
- Change the coupling between TELEMAC and TOMAWAC, such that both models can use different meshes, with a larger domain for TOMAWAC than for TELEMAC. In a two-way coupled simulation, the information that is send from TELEMAC to TELEMAC then needs to be determined by some sort of extrapolation.

It is considered that the latter approach offers many additional advantages (such as a large speed up by using coarser resolutions in TOMAWAC or by cutting off parts of bays of rivers with limited wave activities in TOMAWAC). Therefore, works is currently being performed in order to implement such a flexible coupling.

Additionally, it is considered to implement a modification to the OSU/TPXO routines, such that the water level gradients can directly be obtained from the tidal database.

Finally, it is considered to perform more testing with respect to the calculation of the velocities parallel to the boundary, as it is considered a substantial disadvantage that the flow needs to perpendicular to the boundary in the present implementation.

Because it is necessary to have space and time varying water levels at the offshore boundaries, it is highly recommended to standardize the different implantations that currently exist within the TELEMAC community, such that one standard file format can be used to prescribe space and time varying boundary conditions without any additional programming.

Conclusion

In this paper, the implementation of water level gradient boundary conditions for TELEMAC 2D is presented. This implementation is tested in three different test cases: a tidal flow, a wave-driven longshore current and a combination of both. The implementation is shown to give good results at the boundary for all these three test cases, although some additional work is still needed in order to improve the coupling between TELEMAC and TOMAWAC, in order to improve the results.

References

J.A Roelvink and D.-J. Walstra, "Keeping it simple by using complex models," Advances in Hydroscience and Engineering ,6 pp. 1-11, 2004.

Appendix B. Western Scheldt bed morphology sections for different sediment transport models
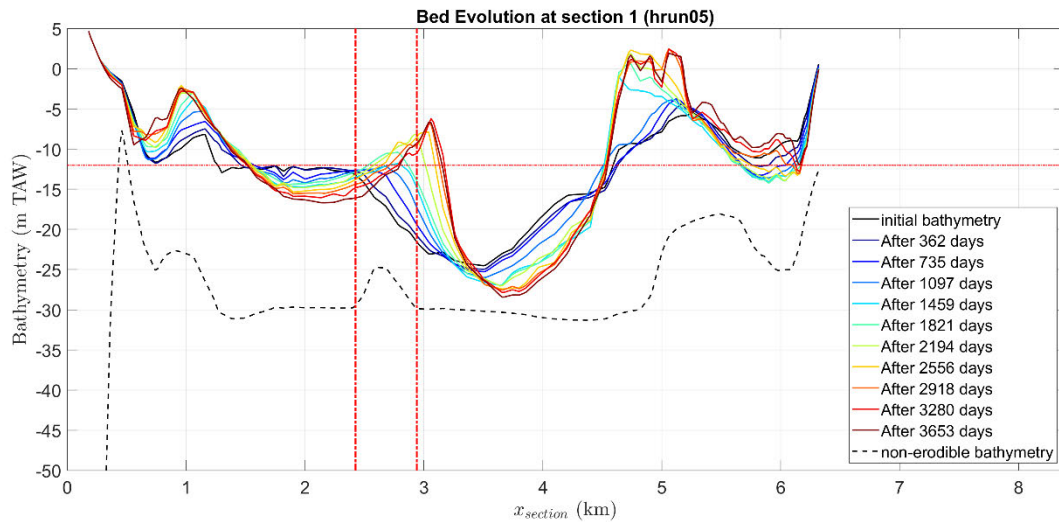
Hindcasting 1986-1996 simulation results

Figure 201 – Bed evolution on transect 1. Sediment transport model by Soulsby - VanRijn (hrun05). Horizontal line corresponds to maintenance depth and vertical lines correspond to the boundaries of the dredging site.
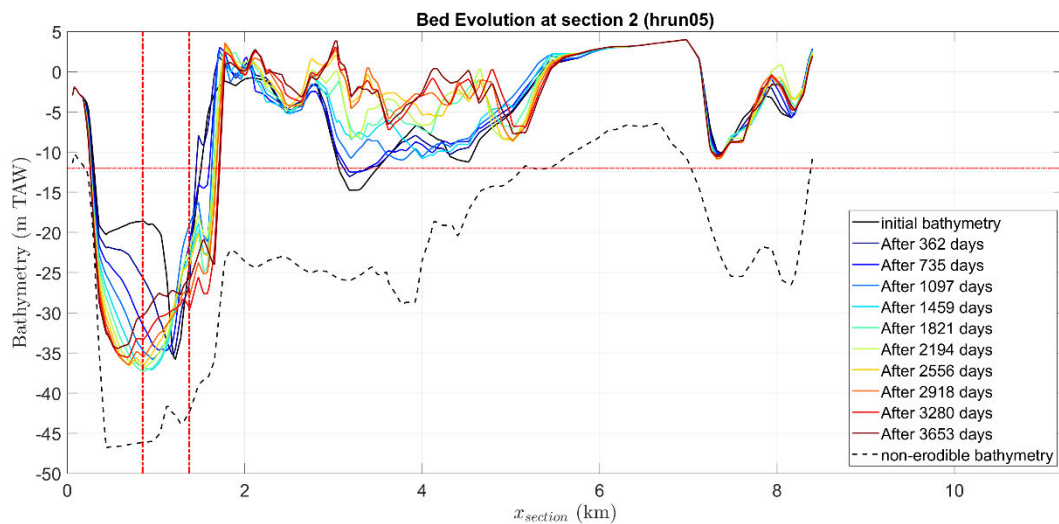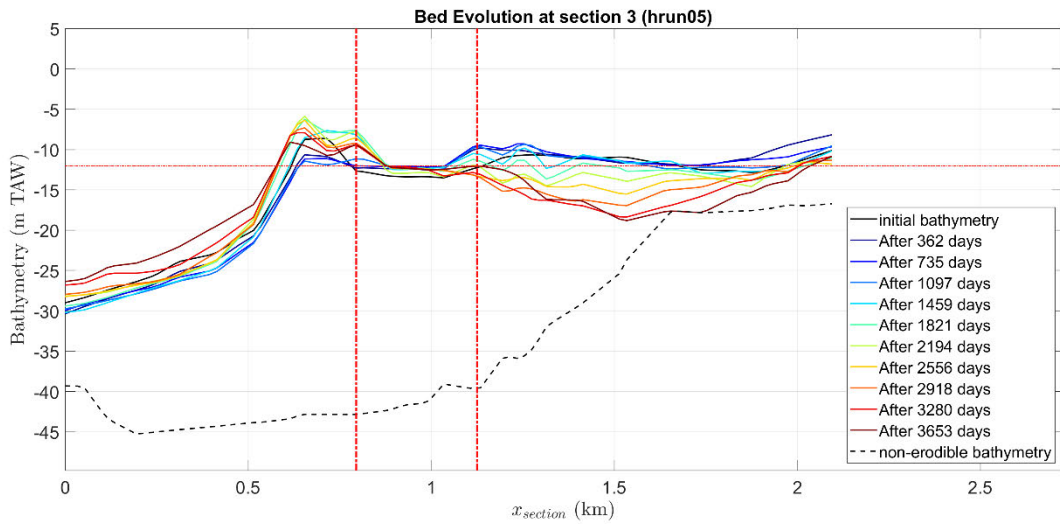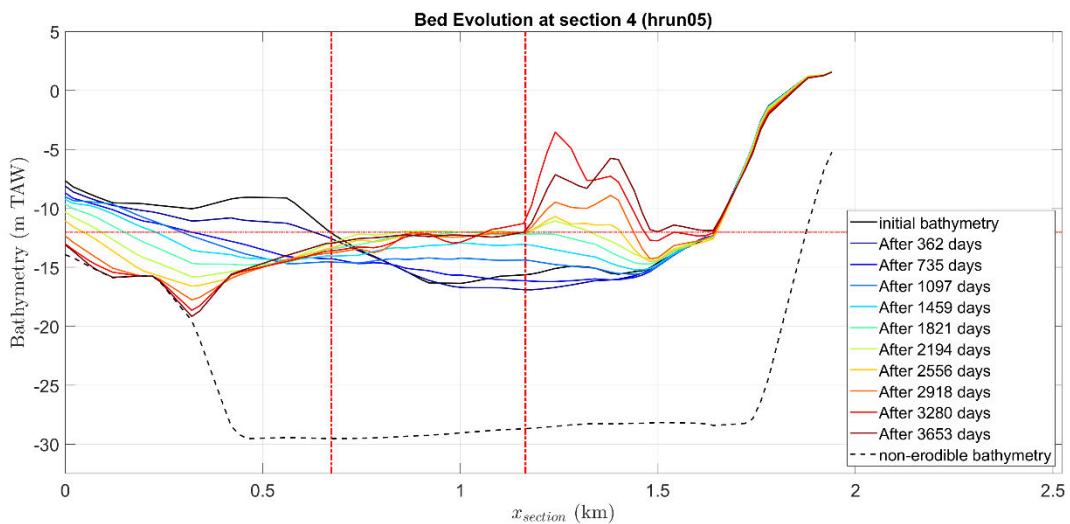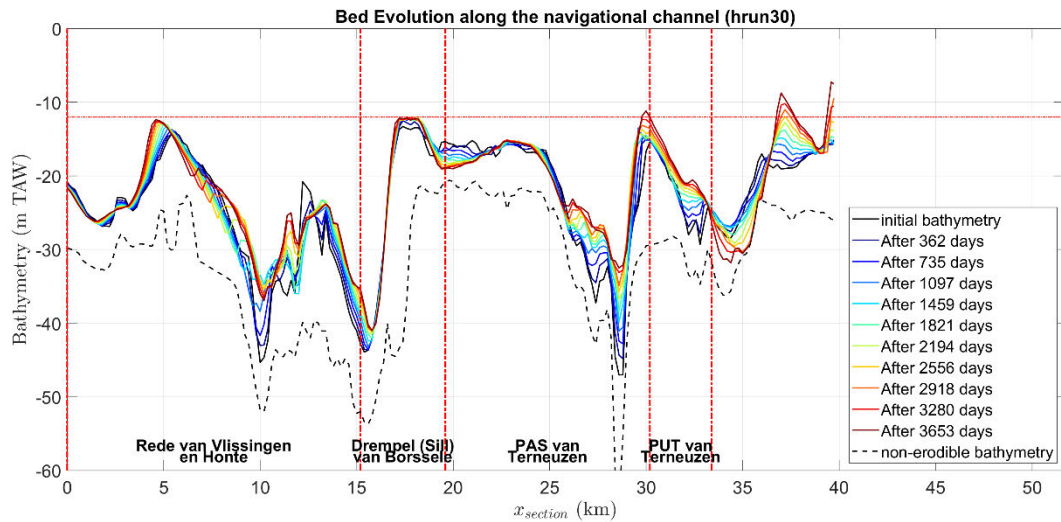

Figure 202 – Bed evolution on transect 2. Sediment transport model by Soulsby - VanRijn (hrun05). Horizontal line corresponds to maintenance depth and vertical lines correspond to the boundaries of the dredging site.
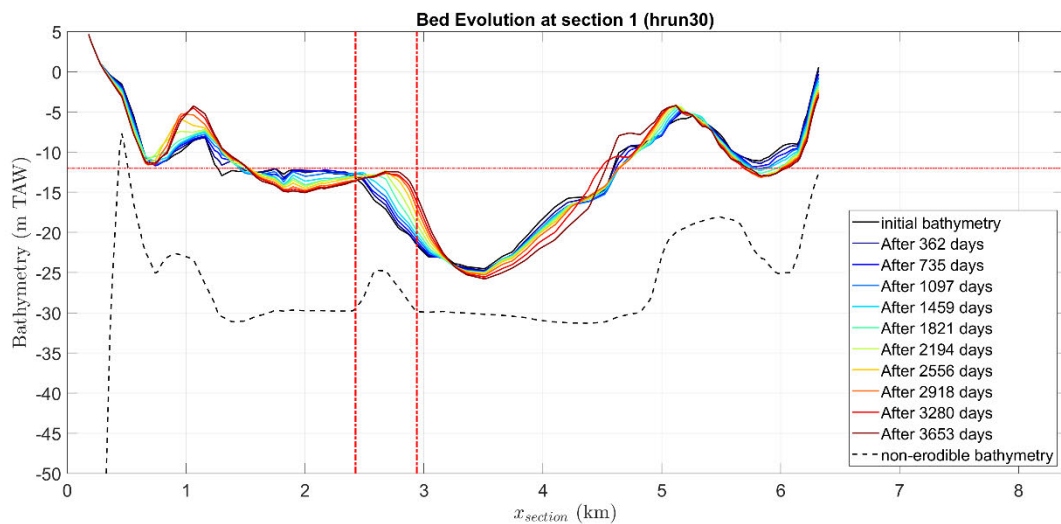
Figure 203 – Bed evolution on transect 3. Sediment transport model by Soulsby - VanRijn (hrun05). Horizontal line corresponds to maintenance depth and vertical lines correspond to the boundaries of the dredging site.

Figure 204 – Bed evolution on transect 4. Sediment transport model by Soulsby - VanRijn (hrun05). Horizontal line corresponds to maintenance depth and vertical lines correspond to the boundaries of the dredging site.

Figure 205 – Bed evolution on section along the navigational channel. Sediment transport model by Engelund & Hansen (hrun30). Horizontal line corresponds to maintenance depth and vertical lines correspond to the boundaries of the dredging site.
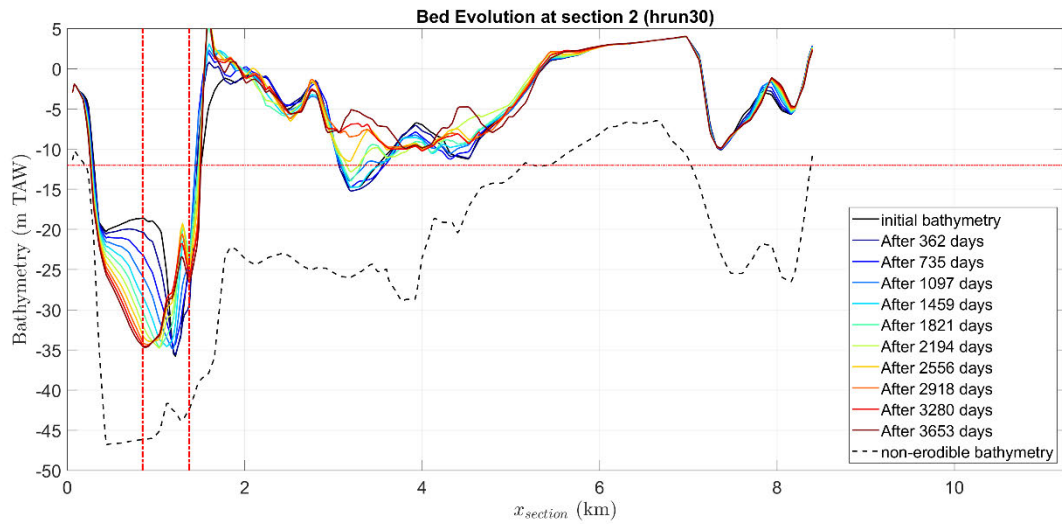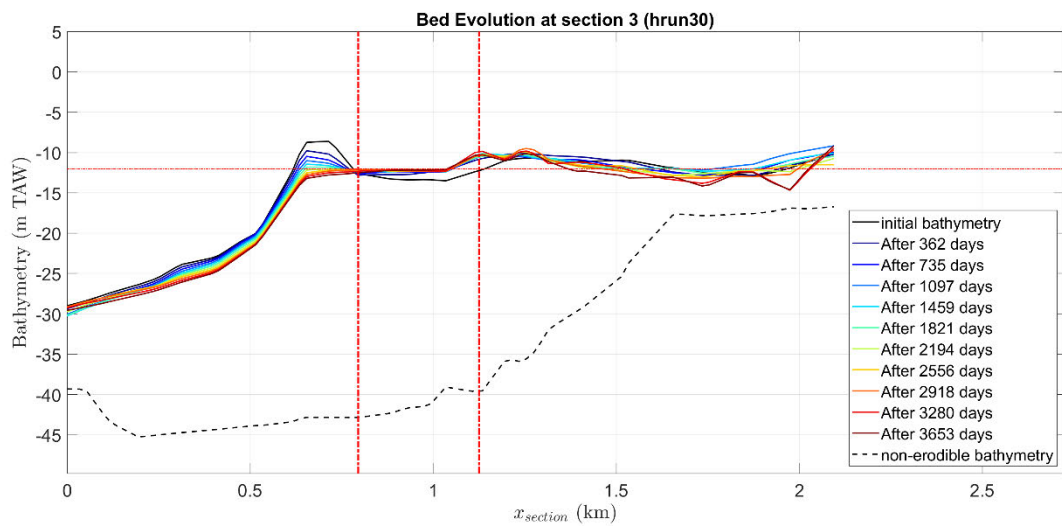

Figure 206 – Bed evolution on transect 1. Sediment transport model by Engelund & Hansen (hrun30). Horizontal line corresponds to maintenance depth and vertical lines correspond to the boundaries of the dredging site.
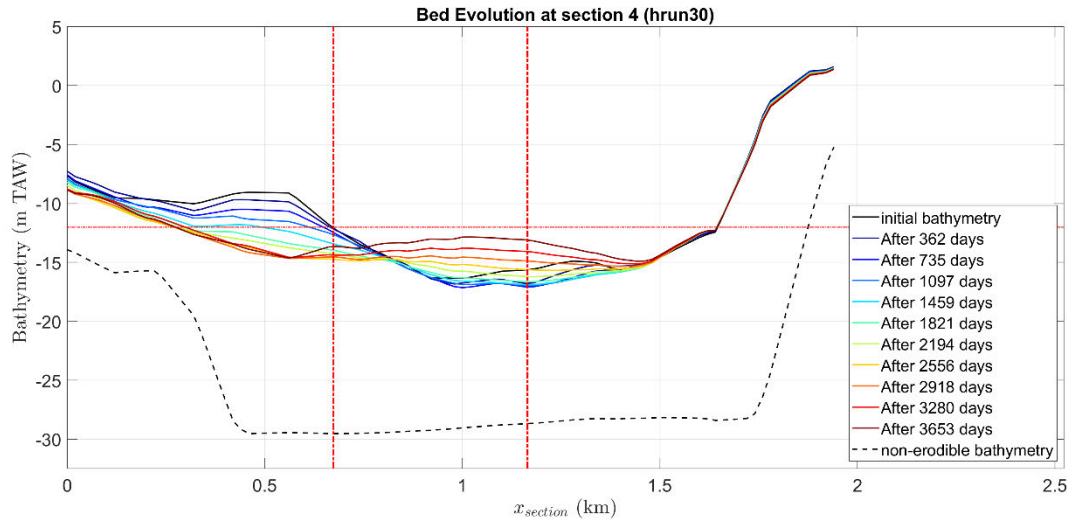
Figure 207 – Bed evolution on transect 2. Sediment transport model by Engelund & Hansen (hrun30). Horizontal line corresponds to maintenance depth and vertical lines correspond to the boundaries of the dredging site.

Figure 208 – Bed evolution on transect 3. Sediment transport model by Engelund & Hansen (hrun30). Horizontal line corresponds to maintenance depth and vertical lines correspond to the boundaries of the dredging site.

Figure 209 – Bed evolution on transect 4. Sediment transport model by Engelund & Hansen (hrun30). Horizontal line corresponds to maintenance depth and vertical lines correspond to the boundaries of the dredging site.
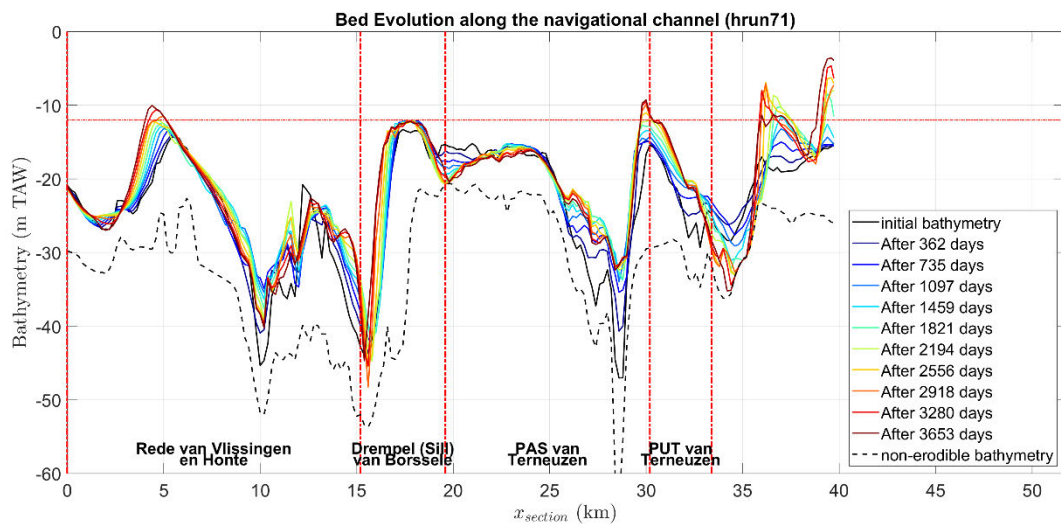

Figure 210 – Bed evolution on section along the navigational channel. Sediment transport model by Van Rijn (2007) (hrun71). Horizontal line corresponds to maintenance depth and vertical lines correspond to the boundaries of the dredging site.
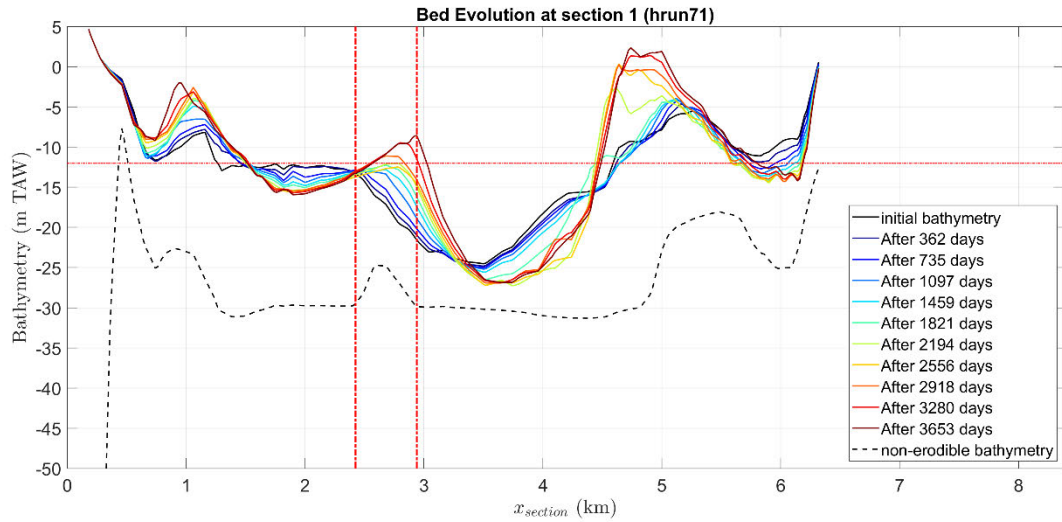
Figure 211 – Bed evolution on transect 1. Sediment transport model by VanRijn (20007) (hrun71). Horizontal line corresponds to maintenance depth and vertical lines correspond to the boundaries of the dredging site.
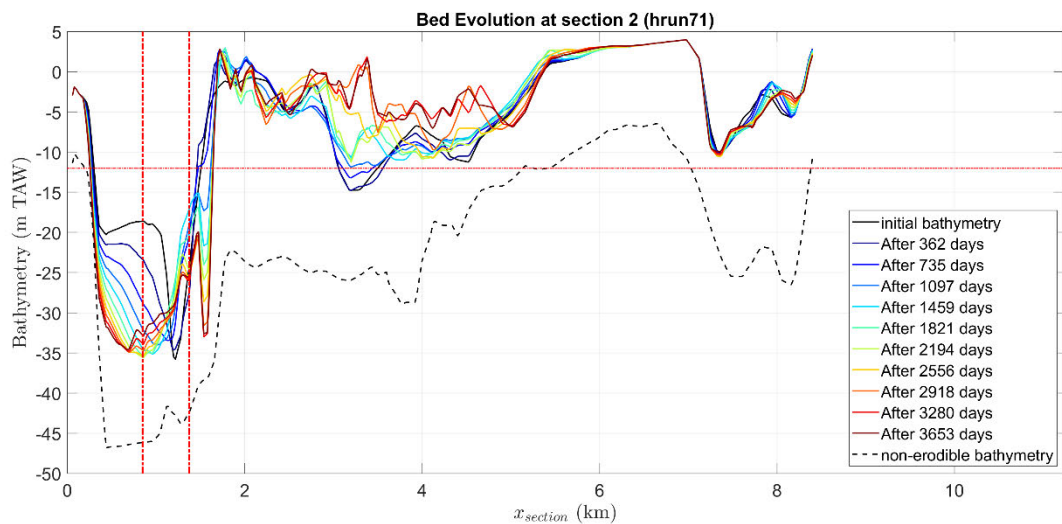

Figure 212 – Bed evolution on transect 2. Sediment transport model by VanRijn (20007) (hrun71). Horizontal line corresponds to maintenance depth and vertical lines correspond to the boundaries of the dredging site.
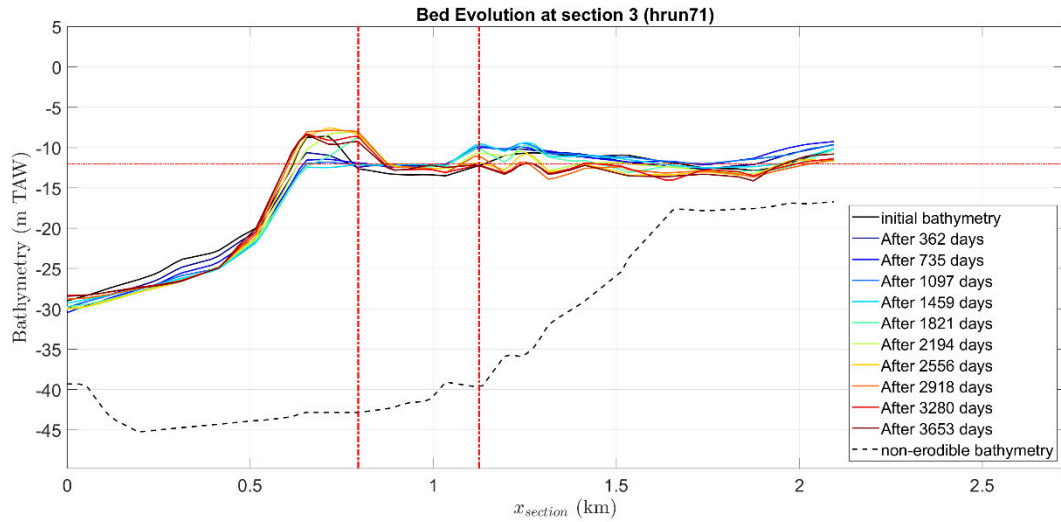
Figure 213 – Bed evolution on transect 3. Sediment transport model by VanRijn (20007) (hrun71). Horizontal line corresponds to maintenance depth and vertical lines correspond to the boundaries of the dredging site.
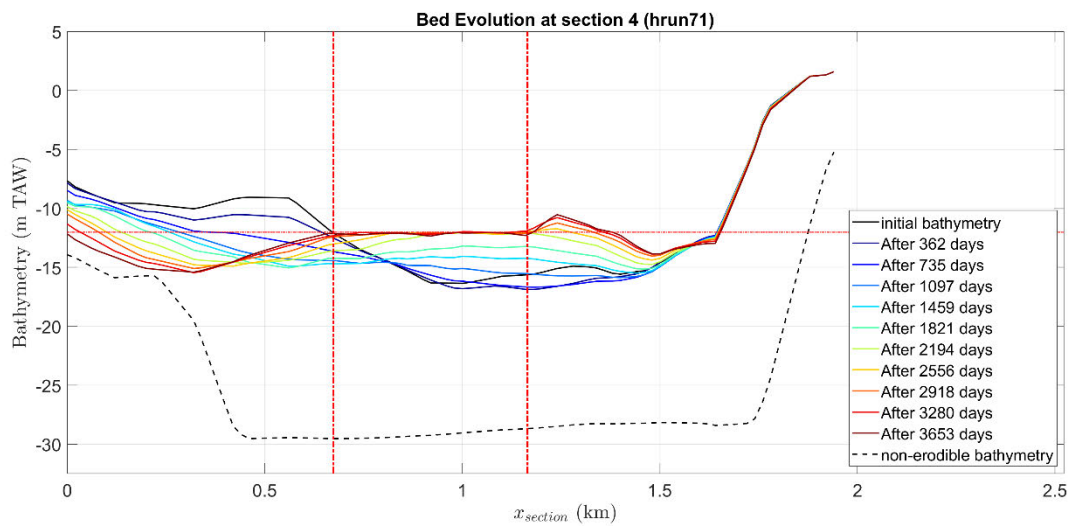

Figure 214 – Bed evolution on transect 4. Sediment transport model by VanRijn (20007) (hrun71). Horizontal line corresponds to maintenance depth and vertical lines correspond to the boundaries of the dredging site.

DEPARTMENT **MOBILITY & PUBLIC WORKS**
Flanders Hydraulics

Berchemlei 115, 2140 Antwerp
T +32 (0)3 224 60 35
F +32 (0)3 224 60 36
flanders.hydraulics@vlaanderen.be
www.flandershydraulics.be